Technische Universität Braunschweig

INSTITUT FÜR AKUSTIK

Wave-resolving aircraft cabin noise prediction

Christopher Blech

Schriften des Instituts für Akustik
Band 1, 2022
Herausgeber: Prof. Dr.-Ing. Sabine C. Langer

Schriften des Instituts für Akustik

Band 1, 2022

Christopher Blech

Wave-resolving aircraft cabin noise prediction

Shaker Verlag
Düren 2022

Bibliographic information published by the Deutsche Nationalbibliothek
The Deutsche Nationalbibliothek lists this publication in the Deutsche Nationalbibliografie; detailed bibliographic data are available in the Internet at http://dnb.d-nb.de.

Zugl.: Braunschweig, Techn. Univ., Diss., 2022

Printed in Germany.

ISBN 978-3-8440-8701-7
ISSN 2699-5336

Shaker Verlag GmbH • Am Langen Graben 15a • 52353 Düren
Phone: 0049/2421/99011-0 • Telefax: 0049/2421/99011-9
Internet: www.shaker.de • e-mail: info@shaker.de

Wave-resolving aircraft cabin noise prediction

Von der Fakultät für Maschinenbau
der Technischen Universität Carolo-Wilhelmina zu Braunschweig

zur Erlangung der Würde

eines Doktor-Ingenieurs (Dr.-Ing.)

genehmigte Dissertation

von:	Christopher Blech
geboren in (Geburtsort):	Gifhorn

eingereicht am:	07.09.2021
mündliche Prüfung am:	16.03.2022

Vorsitz:	Prof. Dr. Jan W. Delfs
Gutachter:	Prof. Dr.-Ing. Sabine C. Langer
	Prof. Dr.-Ing. Hans P. Monner

2022

TU Braunschweig – Niedersächsisches
Forschungszentrum für Luftfahrt

Berichte aus der Luft- und Raumfahrttechnik

Forschungsbericht 2022-14

Wave-resolving aircraft cabin noise prediction

Christopher Blech

TU Braunschweig
Institut für Akustik
Braunschweig

Diese Veröffentlichung wird gleichzeitig in der Berichtsreihe „NFL - Forschungsberichte“ geführt.

Diese Arbeit erscheint gleichzeitig als von der Fakultät für Maschinenbau der Technischen Universität Carolo-Wilhelmina zu Braunschweig zur Erlangung des akademischen Grades eines Doktor-Ingenieurs genehmigte Dissertation.

It only takes a spark
To get a fire going
And soon all those around
Can warm up in its glowing

Kurt Frederic Kaiser

Acknowledgements

Five years of work in the Collaborative Research Centre 880 have had a decisive influence on the topic of this thesis. I would like to thank Professor Rolf Radespiel for holding the CRC together over almost a decade and bring it to life at all. An intensive and regular exchange accompanied by numerous scientific discussions helped me to identify crucial research questions. Professor Jan Werner Delfs has guided the quarterly meetings in a very pleasant and highly scientific way. He has always driven the cabin acoustics subproject forward – many thanks for this and for taking on the chair of the doctoral committee. Many thanks goes to Christina Katharina Appel and Roland Ewert, who made great efforts in the project to resolve all emerging issues and finally have contributed significantly to the success of the cabin noise simulations. Delivering the required input data for my simulations has required the implementation of new methods on the aeroacoustics side. Last but not least, I would like to thank all research assistants in the CRC who finally breathe life into the project – it was a great time with fruitful scientific discussions as well as interesting extracurricular workshops.

The dissertation was written during my time as research assistant at the Institute for Engineering Design and the Institute for Acoustics. I would like to thank all my colleagues, who have accompanied my journey with numerous discussions on the whiteboard, coffee breaks and conference trips. (Scientific) questions and answers that arose in the meantime have contributed greatly to this work. My particular thanks go to Steffen for his unconditional support in the transport of the aircraft seats and constructive advices with regard to acoustic measurements as well as code implementations. The latter also applies to Harik, who participates significantly in the development of our in-house research code. Very special thanks go to Professor Sabine Christine Langer for the trust in 7 years of joint work, a substantial contribution to my personal development and finally the supervision of this thesis. She always sees the person behind the scientist, for which she deserves my highest appreciation. Furthermore, I would like to thank Professor Hans Peter Monner for taking on the supervision and especially for providing the aircraft seat bench for acoustic measurements at PTB. Without Volker Wittstock and Kevin Picker, impedance and reverberation time measurements would not have been possible – Many thanks for

the significant contribution to the success of these studies.
I would also like to thank my friends, who have always believed in the success of this work. Patrick and David carried out a comprehensive proofreading. They have delivered excellent linguistic corrections and identified scientific disagreements, for which I am very thankful and look forward to returning the favour. Since our studies, Sebastian and I have been on the journey of acoustics together. He is one of the few people with whom I can discuss different points of view without arguing. I am very grateful to him for that as well as the constant mutual motivation and look forward to our future joint projects.
I would not be at this point in my life without my parents. Kornelia and Andreas supported me in everything for over 30 years now and made it possible at all that I am now an engineer and scientist. My most important thanks go to Josephine, who stood by me at all times and never doubted the success of the work. She helped me to get through all difficult phases of my doctoral time and to focus on the essential things in life like our wonderful son Henry. He may not know it yet, but he has made a significant contribution by the way he looks at his father. As little as he knows about acoustics, as much he is my personal source of inspiration.

Abstract

Quiet aircraft passenger cabins contribute significantly to the well-being and health of billions of air travellers. During design, a reliable prediction of the sound pressure level is seen as crucial decision-making basis. The wave-resolving numerical simulation of sound pressure levels in the cabin is investigated within this thesis, which results in a comprehensive modelling of a typical aircraft fuselage, the efficient numerical solution and the assessment of the sound induced by a novel engine concept and the turbulent boundary layer.

A major challenge is the complexity of aircraft models including structural, acoustic and poro-elastic domains. For each relevant fuselage part, experiments are conducted and different vibroacoustic models are compared in order to choose a suitable modelling approach, repectively. The airframe, the insulation, the interior panels and the cabin are studied separately and merged into a full aircraft fuselage model. One important finding is on the glass wool insulation layer between the airframe and the interior panel, for which the need for the Biot model is shown. The modelling of structure-borne sound transmission within the glass fibres is necessary to take structural resonances within the double wall gap in the low frequency range into account. Another finding concerns the cabin domain containing seats and passengers – a global homogenised damping approach yields suitable results compared to a more detailed consideration of local surface impedances.

As the resulting finite element model incorporates millions of degrees of freedom, efficient solving approaches are studied with regard to potentially introduced errors. The combination of frequency-adaptive meshes and the admissible weak mechanical coupling assumption for the cabin above 410 Hz decreases the computational time required by 87 % for a 4.3 m fuselage section, while the reference is a constant mesh with a strong mechanical coupling between all domains. In addition, the application of the iterative solver GMRES in combination with a suitable preconditioner (Block low rank LU) is presented. The usage in blocks according to the physical domains requires significantly less computational effort compared to a direct solver. Besides, it is shown that the full length aircraft fuselage can be replaced by shorter fuselage sections without introducing significant errors above 410 Hz.

The aircraft fuselage model in combination with efficient solving approaches is applied

for two analyses. Firstly, the available acoustic excitations of two jet engines (bypass-ratio 17 and 5) are compared. The acoustic footprint of the novel engine yields significantly lower sound pressure levels in the cabin, which results in a positive assessment of the new technology. Secondly, the acoustic excitations beneath the turbulent boundary layer are modelled by a generic superposition of plane waves resulting in a deterministic snapshot of the random loading. It is demonstrated that the turbulent boundary layer generates cabin sound pressure levels lying between those of the two engine generations. Based on these results, a more distinct presence of the turbulent boundary layer acoustics within the cabin can be assumed for future aircraft generations.

The assessment of complex excitations by applying the acoustic footprint directly shows a great advantage of wave-resolving models. The developed recommendations on aircraft fuselage modelling and the derived efficient solving approaches state the major scientific contribution of this thesis, which is transferable to different aircraft and even other mobility vehicles. The obtained results represent a decisive contribution towards the development of quieter passenger cabins in future aircraft.

Kurzfassung

Leise Flugzeugpassagierkabinen tragen wesentlich zum Wohlbefinden und zur Gesundheit von Milliarden von Flugreisenden bei. In der Konstruktion wird eine zuverlässige Vorhersage des Schalldruckpegels als wichtige Entscheidungsgrundlage gesehen. Die wellenauflösende numerische Simulation von Schalldruckpegeln in der Kabine wird in dieser Dissertation untersucht. Das Ergebnis ist eine umfassende Modellierung eines typischen Flugzeugrumpfes, die effiziente numerische Lösung und die Bewertung des Schalls induziert durch ein neuartiges Triebwerkskonzept sowie die turbulente Grenzschicht.

Eine große Herausforderung ist die Komplexität der Flugzeugmodelle, die strukturelle sowie akustische und poro-elastische Gebiete umfasst. Auf Basis von Experimenten und dem Vergleich verschiedener vibroakustischer Modelle wird für jeden relevanten Teil eines Flugzeugrumpfes jeweils ein geeigneter Ansatz ausgewählt. Die Flugzeugzelle, die Dämmung, die Innenverkleidung und die Kabine werden getrennt untersucht und zu einem Gesamtmodell des Flugzeugrumpfes zusammengeführt. Für Modellierung der Glaswolle-Dämmschicht zwischen der Flugzeugzelle und der Innenverkleidung wird die Notwendigkeit des Biot-Modells als wichtige Erkenntnis gezeigt. Die Modellierung der Körperschallübertragung innerhalb der Glasfasern ist notwendig, um Strukturresonanzen innerhalb des Doppelwandspalts im niedrigen Frequenzbereich zu berücksichtigen. Eine weitere Erkenntnis gilt der Kabine, in welcher sich die Sitze und Passagiere befinden – ein globaler homogenisierter Dämpfungsansatz führt zu geeigneten Ergebnissen im Vergleich zu einer detaillierteren Berücksichtigung lokaler Oberflächenimpedanzen.

Da das resultierende Finite-Elemente-Modell Millionen von Freiheitsgraden umfasst, werden effiziente Lösungsansätze im Hinblick auf potenziell eingeführte Fehler untersucht. Die Kombination von frequenzadaptiven Netzen und der zulässigen Annahme einer schwachen mechanischen Kopplung der Kabine oberhalb von 410 Hz verringert den zeitlichen Rechenaufwand um 87 % für einen Rumpfabschnitt über 4.3 m, während ein konstantes Netz mit starker mechanischer Kopplung zwischen allen Gebieten als Referenz herangezogen wird. Darüber hinaus wird die Anwendung des iterativen Lösers GMRES in Kombination mit einem geeigneten Vorkonditionierer (Block low rank LU) präsentiert. Die Verwendung in Blöcken entsprechend der physikalischen

Gebiete bedarf deutlich weniger Berechnungsaufwand im Vergleich zu einem direkten Löser. Außerdem wird gezeigt, dass der gesamte Flugzeugrumpf durch kürzere Rumpfabschnitte ersetzt werden kann, ohne signifikante Fehler oberhalb von 410 Hz einzuführen.

Das Flugzeugrumpfmodell wird in Kombination mit effizienten Lösungsansätzen für zwei Analysen angewendet. Zum einen werden die zur Verfügung stehenden akustischen Anregungen zweier Strahltriebwerke (Nebenstromverhältnis 17 und 5) miteinander verglichen. Der akustische Fußabdruck des neuartigen Triebwerks mit Nebenstromverhältnis 17 führt zu deutlich niedrigeren Schalldruckpegeln in der Kabine, wodurch sich eine positive Bewertung der neuen Technologie ergibt. Zweitens werden die akustischen Anregungen unterhalb der turbulenten Grenzschicht durch eine generische Überlagerung von ebenen Wellen modelliert, was zu einer deterministischen Momentaufnahme der Zufallsanregung führt. Es wird gezeigt, dass die turbulente Grenzschicht Kabinenschalldruckpegel erzeugt, die zwischen denen der beiden untersuchten Triebwerke liegen. Auf Grundlage dieser Ergebnisse kann für künftige Flugzeuggenerationen von einer stärkeren Präsenz der turbulenten Grenzschichtanregung in der Kabine ausgegangen werden. Die Bewertung komplexer Anregungen durch das direkte Aufbringen des akustischen Fußabdrucks zeigt einen großen Vorteil von wellenauflösenden Modellen. Die entwickelten Empfehlungen zur Modellierung von Flugzeugrümpfen und die daraus abgeleiteten effizienten Lösungsansätze stellen den wesentlichen wissenschaftlichen Beitrag dieser Arbeit dar, der auf andere Flugzeuge und sogar andere Mobilitätsträger übertragbar ist. Die erzielten Ergebnisse stellen einen entscheidenden Beitrag für die Entwicklung leiserer Passagierkabinen in zukünftigen Flugzeugen dar.

Contents

List of symbols

Greek symbols

α_∞	Tortuosity
$\boldsymbol{\epsilon}$	Strain vector in Voigt notation
$\boldsymbol{\sigma}$	Stress vector
ϵ	Strain
ϵ_{rel}	Maximum relative error
η	Damping loss factor
γ	Coupling term (Biot model)
κ	Condition number
λ'	Thermal viscous length
λ	Wave length / Characteristic viscous length
ν	Poisson's ratio
Ω	Mechanical domain
ω	Angular frequency
Φ	Porosity
ρ	Density
σ	Stress / flow resistivity
φ	Rotational angles / Fibre volume content
Pr	Prandl number

Roman symbols

$\mathbf{A}$	System matrix
$\mathbf{b}$	Right hand side
$\mathbf{C}$	Elastic stiffness matrix
$\mathbf{f}$	Force vector

$\mathbf{L}$	Differential operator matrix
$\mathbf{L}$	Lower triangular matrix
$\mathbf{M}$	Mass matrix
$\mathbf{M}_{\mathrm{pre}}$	Preconditioning matrix
$\mathbf{N}$	Ansatzfunctions
$\mathbf{r}$	Residual vector
$\mathbf{U}$	Upper triangular matrix
$\mathbf{u}$	Displacements
$\mathbf{x}$	Solution
$\mathcal{K}_m$	Krylov subspace
$\tilde{R}$	Bulk modulus (Biot model)
A_t	Equivalent absorption area
B	Bending stiffness
c	Speed of sound
E	Young's modulus
E_{kin}	Kinetic energy
E_{pot}	Potential energy
F	Force
f	Frequency
f_s	Sampling rate
G	Shear modulus
h	Total thickness of shell structures / admittance
I	Moment of inertia of area
i	Imaginary unit
K	Bulk modulus
k	Wave number
L	Aircraft model domain length
m	Mass
n	Number of
p	Sound pressure

P_{in}	Input power
P_{out}	Output power
R	Flow resistance / Reflection coefficient
r_c	Compression rate
R_r	Reverberation time
R_s	specific flow resistivity
RH	Relative humidity
T	Total solution time / Temperature
t	Time / layer thickness
V	Volume
v	Velocity
W	External work
x, y, z	Cartesian coordinates
Z	Impedance

Indices

$\square^{\mathrm{e}}$	Finite element
$\square_{\mathrm{a}}$	Acoustic 3D domain
$\square_{\mathrm{c}}$	Passenger cabin
$\square_{\mathrm{eff}}$	Effective material parameters (equivalent fluid models)
$\square_{\mathrm{g}}$	Insulation
$\square_{\mathrm{s2}}$	Structural 2D shell
$\square_{\mathrm{s3}}$	Structural continuous 3D domain
$\square_{\mathrm{s}}$	Airframe
$\square_{\mathrm{t}}$	Interior lining
$\square_{x/y/z}$	Direction in cartesian coordinates

List of abbreviations

AMD	Approximate minimum degree
AMF	Approximate minimum fill
BEM	Boundary element method
BLR	Block-low rank
BPR5	Conventional engine with bypass ratio of 5
CFD	computational fluid dynamics
CFRP	Carbon fibre reinforced polymer
CLT	Classical laminate theory
CRC	Coordinated research centre
dB	Decibel
D-B	Delany-Bazley
dof	Degree of freedom
FEM	Finite element method
GMRES	Generalized minimal residual procedure
GFRP	Glass fibre reinforced polymer
IATA	International air transport association
ILU	Incomplete LU factorisation
JCA	Johnson-Champoux-Allard
MUMPS	Multifrontal massively parallel sparse solver
OASPL	Over all sound pressure level
PrADO	Preliminary aircraft design and optimization program
QMR	Quasi-minimal residual method
SEA	Statistical energy analysis
SPL	Sound pressure level

TBL Turbulent Boundary Layer

TL Transmission loss

UHBR Ultra-high-bypass ratio

1 Introduction

A constantly growing world population is facing many challenges in future. One of them is an increasing demand for mobility, while aeroplanes are the means of transport of choice for medium distances within Europe and long inter-continental distances. The International Air Transport Association (IATA) forecasts a doubling of passengers on the basis of three scenarios. The amount of passengers is expected to grow from 4.3 to 8.2 billion air travellers in 2037 [80]. Within the Coordinated Research Centre (CRC) 880 [37], in which this thesis is originated, efficient point-to-point connections are the basic motivation. The fundamentals of active high-lift systems are investigated in order to develop environmentally friendly future transport aircraft, which offer a low fuel consumption and short runways near cities [135]. Environmental friendliness comprises the noise that is transmitted into the passenger cabin. It highly depends on the passenger and past experiences brought along whether a sound backdrop is perceived as comfortable or disturbing. In general, the induced sensations of humans are investigated in the field of psychoacoustics based on the time- or frequency response of the sound pressure level (SPL) [164]. However, it is well known that the SPL as a physical quantity significantly contributes to the well-being and health of passengers [108]. Hence, a reliable prediction of the SPLs in the passenger cabin is one important step towards a virtual cabin noise assessment, which is conducted in this thesis clearly excluding other subsequent metrics. In Fig. 1.1 (a) (Modified from: [148]), a correlation based on simulator tests between the satisfaction of passengers and the overall SPL is shown, indicating an improvement of comfort by lower SPLs and thus the main motivation for this work. During the past decades, the SPL has been reduced as shown in Fig. 1.1 (b) (Modified from: [148]).
Keeping this trend for novel aircraft technologies and ensuring equal or less SPLs in the cabin is highly important. Simulation tools play a major role as a basis for sound reduction measures in early design phases [156].

This work contributes to the numerical prediction of passenger cabin SPLs for novel aircraft technologies by use of wave-resolving mechanical models. The major **aim of this work** is providing reliable, comprehensive modelling as well as an efficient numerical solution of the sound field in a passenger cabin of a typical aircraft fuse-

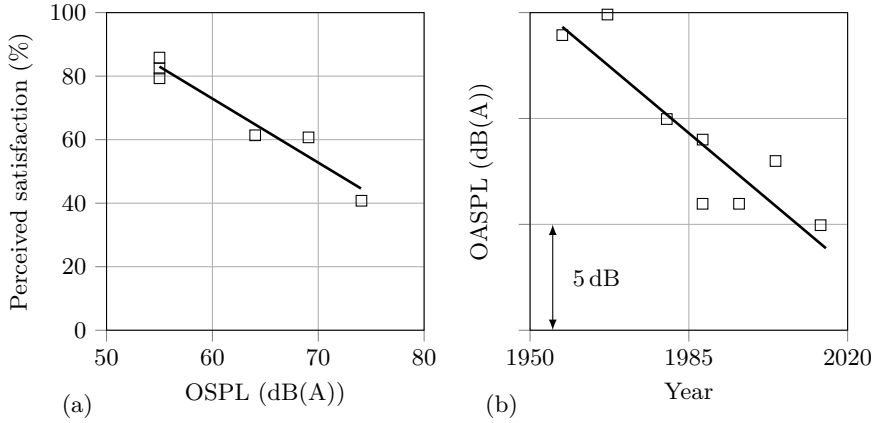

Figure 1.1: (a) Satisfaction of passengers in dependency on the overall sound pressure level OSPL in the aircraft cabin (Modified from: [148]) (b) General trend of the OSPL in narrow body aircraft cabins (Modified from: [148])

lage. Obtained results can further be used for a psychoacoustic assessment. Such detailed models help understanding the sound transmission mechanisms of different sources into the cabin. Especially novel engine concepts are of interest, as different noise sources are introduced [156]. Such new sources can only be investigated by high-fidelity models, as no profound assumptions on the dynamic behaviour have to be considered. Furthermore, high sound levels can be avoided or even lower levels can be reached by targeted acoustic measures in early design phases. As structural modifications in late design phases are rather expensive, early changes lead to more efficient solutions concerning costs or weight.

With higher frequency, the wave length decreases, which exponentially increases the computational costs for a numerical solution. The *problem of short wave lengths* [168] easily brings today's computing capacities to limits if wave-resolving approaches like the finite element method are applied. As the computing capacity increases over decades, it's worth looking into this problem again and again until the maximum solvable frequency meets the frequency range of interest. Full aircraft models are rarely available as the computational costs are still high. Instead, fuselage sections are solved up to frequencies of several hundred Hertz – in contrast, typical noise sources like the turbulent boundary layer (TBL) are present up to several thousand Hertz and affect the entire fuselage. This clearly points out the need for research and shapes the aim of this thesis. The long-term aim comprises a full aircraft model with all relevant parts for a sound transmission analysis considering all dominant sources. The requirement of a full model is motivated by large acoustic footprints of sound radiating engines on the outer skin and a changing fuselage structure over the length

of an airliner. On the frequency limit due to computing capacities (time and memory) because of short wave lengths follows a crucial need for efficiency. Efficiency in the simulation can be reached by physically motivated reductions in the mechanical models or by numerical approaches, like a reduced precision within the solver. Keeping the wave-resolving characteristics in the models is a basic requirement and challenge for this thesis. A second problem is the consideration of TBL loads [168] – in order to resolve the occurring pressure fluctuations on the outer skin of an aircraft fuselage, really fine meshes are required. This topic is addressed by the use of semi-analytical approaches.

Four major parts make up the **structure of this thesis**. Firstly, the necessary theoretical background on aircraft structures, wave-resolving vibro-acoustic models, the discretisation by finite elements and the numerical solution are studied in Ch. 2. This chapter concisely collects the essential theories and related equations. Secondly, the state-of-the-art knowledge on aircraft cabin noise by numerical and experimental investigations is documented in Ch. 3. Thirdly, the innovative core of this thesis is extensively described in Ch. 4 to 6. The focus of these chapters is an efficient modelling and solution process for a full aircraft fuselage, which is applied for the investigation of engine jet and TBL excitations. Finally, the work is concluded in Ch. 7 including an anticipation of further studies.

2 Background

The prediction of passenger cabin acoustics requires a basic knowledge about sound sources, sound propagation and sound immision in complex systems. The underlying preliminary design for an research aircraft is briefly described first. As potential sources affect, for instance, the outer skin, acoustic waves have to propagate in order to reach the the passenger ears. A proper modelling of these sound propagation paths states the core research activity of this thesis, which is why available mechanical models are introduced in Sec. 2.2 and 2.3. Accordingly, in Sec. 2.4, an FE implementation is derived in order to discretise the relevant domains of the aircraft. Besides modelling and discretisation, an efficient solving process of the system of equations is focus of this work. Therefore, the background on direct and iterative solvers appropriate for the present problem type are presented in Sec. 2.5.

2.1 Aircraft fuselage components

Aircraft configurations with a cylindrical fuselage between two wings are highly dominating [82]. As stated in [68], the conventional pressurised tube fuselage is ideal for passenger aircraft. Modern aircraft concepts mainly consider novel engines or slight adaptations of the tube wing configurations [37, 135]. A future passenger aircraft, based on a tube wing configuration, but with enhanced high lift characteristics is studied within the CRC 880, which lays the basis for this thesis [32]. The airframe of the research aircraft is focussed in order to study the sound transmission into the cabin, while the wings are neglected from the start.
Highly modern concepts like blended-wing-bodies may catch on in future, see e.g. [38], but shall not be considered within this thesis. Typical vibroacoustic characteristics like a double-wall structure are expected to stay for novel concepts, which enables a possible transfer of this work.

General airframe design The airframe of a typical cylindrical fuselage section is depicted in Fig. 2.1 (modified from: [120, p. 376]). A thin tubular fuselage skin joined with stiffening members is called a *semi-monocoque construction* [120]. As the skin is cylindrical, it withstands relatively high shear forces and the internal

cabin pressure. Combined with the stiffeners, much higher bending forces are carried by the construction. The longitudinal (or length-wise / in flow direction) stiffening members are called stringers and longerons, while the latter are stringer-like structures going through the entire fuselage. Stringers are placed between two circular frames. Circular frames and bulk-heads are transverse elements, while the latter are much more substantial than frames [120]. As depicted in Fig. 2.1, frames are systematically repeated length-wise in order to maintain the fuselage shape. Bulk-heads are placed at crucial location of high stresses like the wing mount or the ends of the pressurised tube [120]. For more and more aircraft structures, fibre-reinforced plastics are used as materials substituting conventional materials like wood or aluminium [150].

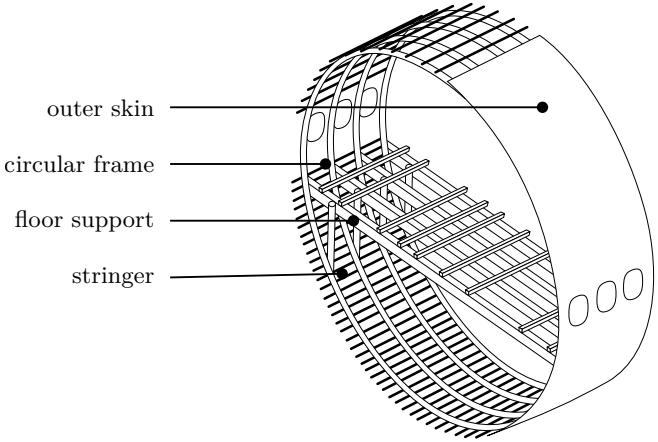

Figure 2.1: Cylindrical fuselage section of a conventional aircraft configuration (modified from: [120, p. 376])

The airframe of a conventional aircraft clearly belongs to the primary structure carrying primary loads like internal pressurization or flight loads [68]. In opposite, the secondary structure carries much lower loads. Such parts are, for instance, the interior side panels, the ceiling panels and seats [130]. However, the secondary structure of the CRC 880 research aircraft is not available as the project is located at a lower technical readiness level (components in laboratory validated). Rather preliminary design data on the primary structure is available within the project and used for the generation of the vibroacoustic model within this thesis.

Research aircraft airframe In Tab. 2.1, the main properties of the CRC 880 project's reference 3 (ref3) configuration are given. The mid-range aircraft transports 100 passengers over a distance of 2000 m. An ultra-high-bypass ratio (UHBR) engine enables short take-off and landing characteristics. This engine is studied in Sec. 6.1,

in which a comparison to a conventional jet engine with regard to cabin acoustics is conducted. The passenger cabin has a length of 16.95 m resulting in a cabin volume of 100.3 m^3 filled by 20 seat rows.

341.43343pt6.0pt

Table 2.1: Preliminary design data on the CRC 880 (ref3) research aircraft [74]

Quantity	Value	Unit
Aircraft weight	44698	kg
PAX	100	-
Mach number at cruise flight	0.78	-
Range	2000	km
Max. Length	33.176	m
Max. Width	28.783	m
Max. Height	9.849	m
Max. Diameter	3.510	m

Concerning the fuselage, the design process delivers the thickness distribution of the outer skin, the dimensions of each circular frame, the entire floor design including stiffener and the two bulk heads. Additionally, all material data is given – the entire primary structure is mainly made of carbon fibre reinforced polymer (CFRP) consisting of 10 layers. In Fig. 2.2, the thickness distribution of the outer skin is depicted. As visible, the main passenger cabin section is surrounded by a 0.7 to 4.0 mm fuselage skin. A static finite element model of the entire aircraft is delivered by the preliminary design process within the project. Based on the application of several standardised load cases, the dimensioning is obtained within the process [138]. Detailed information on the design process itself and the in-house preliminary aircraft design Code PrADO of TU-Braunschweig are available in [160]. By use of the static FE model, information like the thickness distribution is automatically extracted for the much finer resolved vibroacoustic model.

Summarising, in the CRC 880 aircraft fuselage, the following major parts are expected to be crucial in a vibroacoustic fuselage model. Some mechanical expectations are already given here and investigated in the following sections.

- A thin ($0.7 - 4$ mm) curved (radius 1.74 m) skin and a stiffened 2 mm floor both made of CFRP with anisotropic characteristics due to the layer stack, respectively.

- Directly integrated frames and stringers supporting floor and skin structures made of CFRP with anisotropic characteristics due to the layer stack.

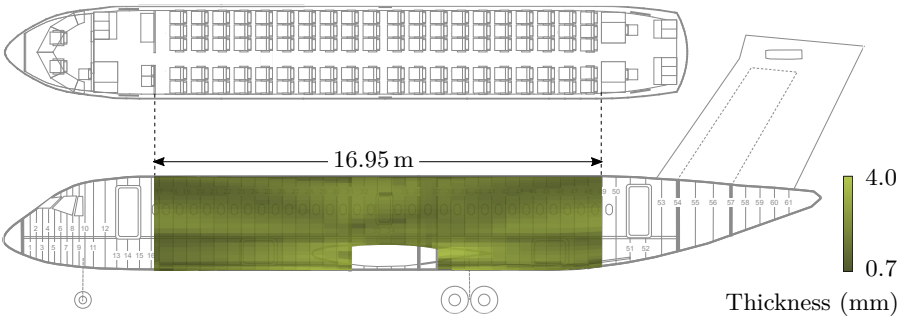

Figure 2.2: Outer skin thickness distribution of the CRC 880 ref3 configuration (aircraft sketch from: [74])

- A cabin interior trim assumed to be made of light sandwich panels with honeycomb cores (thickness approx. 10 mm) and thin GFRP covers with short fibres (thickness approx. 1 mm) fixed to the frames. The core is expected to have anisotropic characteristics due to the manufacturing process of honeycombs and its shape while the GFRP layers are expected to behave isotropically.

- Insulation material assumed to a) fill the double wall gap of 100 mm in the fuselage and assumed to be made of aircraft-grade glass wool with short fibres filled with air.

- A pressurised aircraft cabin filled with air and containing seats and people bringing in surfaces, which absorb and reflect sound waves.

Condensing the listed points, the requirement for a mechanical description of a 3D structural domain Ω_{s3} (honeycomb core), a 2D shell domain Ω_{s2} (outer skin, floor, frames) and a 3D acoustic domain Ω_a (cabin, insulation) is identified and is confirmed in Ch. 4. In Fig. 2.3 a), the domains are illustrated and assigned to a typical fuselage double wall structure. Ω_{s2} assigned to the outer skin is excited by pressure fluctuations on the boundary Γ_e and coupled on Γ_c to the adjacent fluid Ω_a assigned to the insulation. A light sandwich panel of the interior trim consists of two outer thin layers Ω_{s2} and a 3D core Ω_{s3} in between. Finally, the cabin domain is again related to an 3D acoustic domain Ω_a.
The set up is very similar to the transmission of sound through a double wall, which is indicated in Fig. 2.3 a) at the bottom. The insulation layer described by Ω_a is comparable with the (air) gap in the transmission loss problem through a double wall, while the outer skin (Ω_{s2}) and the interior trim ($\Omega_{s2} \cup \Omega_{s3} \cup \Omega_{s2}$) refer to the excited and radiating wall, respectively. The transmission loss (TL) according to Eq. (2.1) relates the input and output energies P_{in} and P_{out} [1] and thus describes

the transmitted portion of energy from the sending room ($\widehat{=}$ surrounding air) to the receiving room ($\widehat{=}$ cabin). The higher the TL, the less energy is transmitted through the double wall, which contributes to lower SPLs in the cabin [101].

$$\mathrm{TL} = 10\ \log_{10}\left(\frac{P_{\mathrm{in}}}{P_{\mathrm{out}}}\right)\mathrm{dB} \tag{2.1}$$

For a typical double wall, a frequency f_0 exists, at which a minimum can be observed in the TL curve shown in Fig. 2.3 b). The position of this frequency is qualitatively marked in the figure. The effect is attributed to a resonance of the two wall's masses and the gap as spring in between. Below this frequency, the behaviour follows the mass law by Berger (+6 dB per octave), while, above f_0, a TL-increase of 18 dB per octave is present [101]. The overall TL-magnitude and further resonance phenomena depend on the geometry and material characteristics. Similar observations are expected for an aircraft fuselage, which enables the TL problem to serve as motivation in order to study single aircraft components in detail.

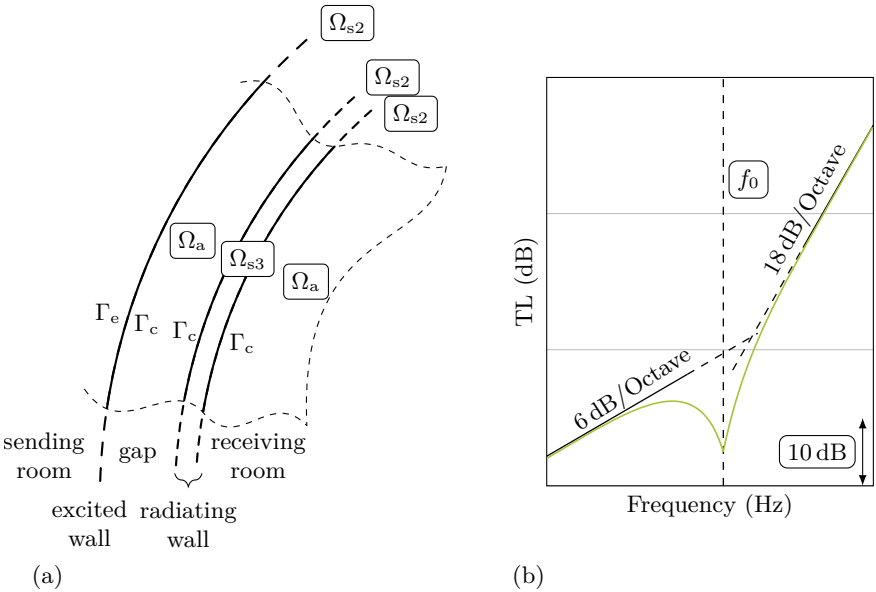

Figure 2.3: (a) Overview on required mechanical assigned to aircraft parts and (b) qualitative transmission loss (TL) curve

The displacement-strain-relations, the stress-strain-relations and the equilibrium conditions for the two structural domains Ω_{s3}/Ω_{s2} and the fluid domain Ω_a are briefly derived in Sections 2.2 and 2.3, respectively.

2.2 Sound waves in 3D structures Ω_{s3} and 2D shells Ω_{s2}

In a solid medium, the general differential operator matrix $\mathbf{L}$ connects displacements $\mathbf{u} = [u_x, u_y, u_z]$ and strains $\boldsymbol{\epsilon} = [\epsilon_{xx}, \epsilon_{yy}, \epsilon_{zz}, \epsilon_{yz}, \epsilon_{xz}, \epsilon_{xy}]^1$ are connected via according to Eq. (2.2) [101]. This is commonly referred to as **displacement-strain-relations** for the linear case.

$$\boldsymbol{\epsilon} = \mathbf{L}\mathbf{u}$$
$$\begin{bmatrix} \epsilon_{xx} \\ \epsilon_{yy} \\ \epsilon_{zz} \\ \epsilon_{yz} \\ \epsilon_{xz} \\ \epsilon_{xy} \end{bmatrix} = \begin{bmatrix} \frac{\partial}{\partial x} & 0 & 0 \\ 0 & \frac{\partial}{\partial y} & 0 \\ 0 & 0 & \frac{\partial}{\partial z} \\ 0 & \frac{\partial}{\partial z} & \frac{\partial}{\partial y} \\ \frac{\partial}{\partial z} & 0 & \frac{\partial}{\partial x} \\ \frac{\partial}{\partial y} & \frac{\partial}{\partial x} & 0 \end{bmatrix} \begin{bmatrix} u_x \\ u_y \\ u_z \end{bmatrix} \tag{2.2}$$

$\mathbf{L}$ yields the strains $\boldsymbol{\epsilon}$, which are the first order derivatives of the displacements in a general 3D domain which is shown in Fig. 2.4. For shell structures with thickness

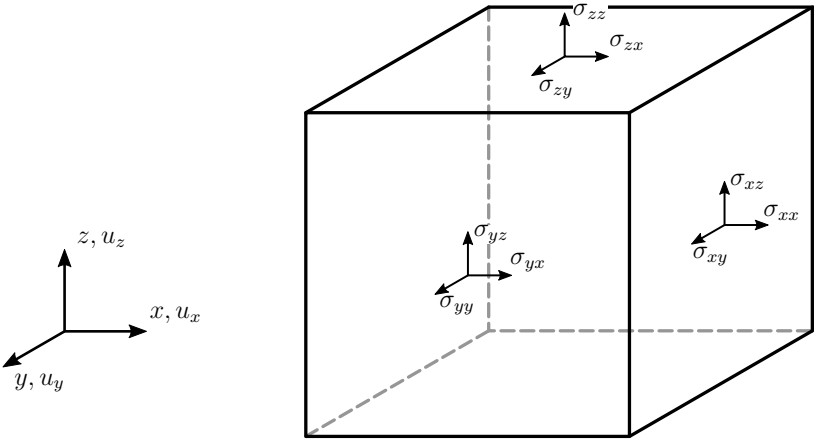

Figure 2.4: Displacements and stresses acting on an infinite small 3D cube in cartesian coordinates

h, a computationally advantageous formulation can be derived as the extension in direction of the orthonormal coordinate (local z-coordinate with $-h/2 < z < h/2$) is assumed to be smaller compared to the occurring wavelengths [101]. For such shell structures, which occur in some aircraft parts (e.g. outer skin, floor), a constant displacement u_z is considered over thickness h, ϵ_{zz} is neglected and two rotational

[1] Voigt notation with the first order assumption of small angles leading to $\epsilon_{xy} = \epsilon_{yx}$

angles φ_x and φ_y are introduced [48] as shown in Fig. 2.5.[2] These angles describe the rotation of the cross sectional area and contribute to an in-plane displacement via linear dependencies given in Eq. (2.3) [48]. Hence, φ_x and φ_y also contribute to the in-plane strains ϵ_{xx} and ϵ_{yy}. This contribution changes over thickness to maximum values at the surface.

$$\begin{aligned} u_x &+= z\varphi_y \\ u_y &+= z\varphi_x \end{aligned} \tag{2.3}$$

Under these assumptions including the novel introduced rotational degrees of free-

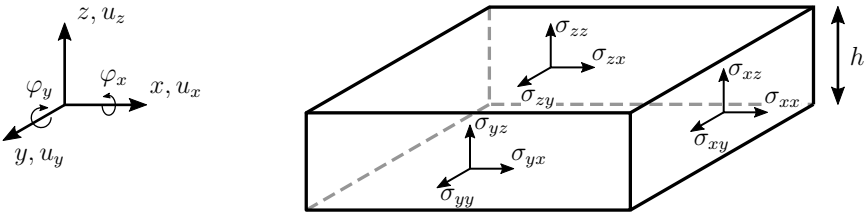

Figure 2.5: Displacements and stresses acting on an infinite small 2D structure in cartesian coordinates

dom, Eq. (2.2) becomes Eq. (2.4), in which the field values are given in the neutral plane of the shell. Restricting the explicit knowledge of field values to this neutral plane, a potential reduction of unknowns is yielded. Displacements $\mathbf{u}_{s2}$ and strains $\boldsymbol{\epsilon}_{s2}$ are connected via the differential operator matrix for shells $\mathbf{L}_{s2}$. The dashed lines indicate a disc part (in-plane waves) and a plate part (out-of-plane waves). For the disc part, only in-plane strains occur whereas in-plane *and* out-of-plane strains occur for the plate part. If the linear theory is appropriate for the shell structure, the resulting displacements $\mathbf{u}_{s2}$ should be much smaller than h [48].

$$\boldsymbol{\epsilon}_{s2} = \mathbf{L}_{s2}\mathbf{u}_{s2}$$

$$\begin{bmatrix} \epsilon_{xx} \\ \epsilon_{yy} \\ \epsilon_{yz} \\ \epsilon_{xz} \\ \epsilon_{xy} \end{bmatrix} = \left[\begin{array}{cc:ccc} \frac{\partial}{\partial x} & 0 & 0 & 0 & z\frac{\partial}{\partial x} \\ 0 & \frac{\partial}{\partial y} & 0 & z\frac{\partial}{\partial y} & 0 \\ 0 & 0 & \frac{\partial}{\partial y} & 1 & 0 \\ 0 & 0 & \frac{\partial}{\partial x} & 0 & 1 \\ \frac{\partial}{\partial y} & \frac{\partial}{\partial x} & 0 & z\frac{\partial}{\partial x} & z\frac{\partial}{\partial y} \end{array}\right] \begin{bmatrix} u_x \\ u_y \\ \hdashline u_z \\ \varphi_x \\ \varphi_y \end{bmatrix} \begin{array}{l} \\ \\ \text{disc part} \\ \hdashline \\ \\ \text{plate part} \end{array} \tag{2.4}$$

Second, going back to the general 3D case Ω_{s3} and assuming linear elasticity (*Hooke's law*), the **stress-strain relations** between $\boldsymbol{\epsilon} = [\epsilon_{xx}, \epsilon_{yy}, \epsilon_{zz}, \epsilon_{yz}, \epsilon_{xz}, \epsilon_{xy}]$ and the stresses $\boldsymbol{\sigma} = [\sigma_{xx}, \sigma_{yy}, \sigma_{zz}, \sigma_{yz}, \sigma_{xz}, \sigma_{xy}]$ are defined via the elastic stiffness matrix $\mathbf{C}$

[2] Variables are reordered compared to [48] for consistency with the in-house code elPaSo available at the institute.

according to Eq. (2.5) [118, 101, 167].

$$\boldsymbol{\sigma} = \mathbf{C}\epsilon$$

$$\mathbf{C} = \begin{bmatrix} \frac{\left(1-\nu_{yz}\nu_{zy}\right)}{D}E_x & \frac{\left(\nu_{xz}\nu_{zy}+\nu_{xy}\right)}{D}E_y & \frac{\left(\nu_{xy}\nu_{yz}+\nu_{xz}\right)}{D}E_z & 0 & 0 & 0 \\ & \frac{\left(1-\nu_{xz}\nu_{zx}\right)}{D}E_y & \frac{\left(\nu_{yx}\nu_{xz}+\nu_{yz}\right)}{D}E_z & 0 & 0 & 0 \\ & & \frac{\left(1-\nu_{xy}\nu_{yx}\right)}{D}E_z & 0 & 0 & 0 \\ & & & G_{yz} & 0 & 0 \\ & & & & G_{xz} & 0 \\ \text{sym} & & & & & G_{xy} \end{bmatrix}$$

$$D = 1 - \nu_{xy}\nu_{yx} - \nu_{xz}\nu_{zx} - \nu_{yz}\nu_{zy} - 2\nu_{xy}\nu_{yz}\nu_{zx} \tag{2.5}$$

$\mathbf{C}$ is symmetric as shear stresses and strains are symmetric as well [101]. Normally, this leads to 21 entries in $\mathbf{C}$. For the purpose of describing aircraft fuselages, a consideration of orthotropic materials is reasonable. Orthotropic materials have three perpendicular planes of symmetry concerning the stress-strain relations, which leads to the 12 considered entries in Eq. (2.5) and 9 independent variables in order to receive these entries [118]. E_i are the Young's moduli, G_{ij} are the shear moduli and ν_{ij} are the Poisson's ratios, respectively in dependency on the direction. For the latter, the relations according to Eq. (2.6) (Betti's reciprocal theorem) are valid due to the described symmetry of stresses and strains [118].

$$\frac{\nu_{xy}}{E_x} = \frac{\nu_{yx}}{E_y}; \quad \frac{\nu_{yz}}{E_y} = \frac{\nu_{zy}}{E_z}; \quad \frac{\nu_{xz}}{E_x} = \frac{\nu_{zx}}{E_z} \tag{2.6}$$

The variable D in Eq. (2.5) must be positive in order to ensure a positive definite matrix $\mathbf{C}$. This requirement is necessary in order to yield a positive strain energy [157].

For shells, σ_{zz} is almost zero [48] which is compatible with the ignored ϵ_{zz}.[3] Eq. (2.5) can still be applied by crossing out the third row and column, which yields $\mathbf{C}_{\mathrm{s2}}$. In addition, all Poisson's ratios related to z are ignored.

In the frame of vibroacoustics, structural damping can be considered within $\mathbf{C}$ by introducing a damping loss factor η in order to compute complex material parameters. For this purpose, the stiffness matrix is scaled by η according to Eq. (2.7) [94] In the equation, i is the imaginary unit. η can be frequency-dependent – a consideration of $\eta(f)$ is directly possible in frequency domain.

[3] The plane stress state allows any ϵ_{zz} in the structure in order to receive $\sigma_{zz} = 0$ – it's consideration would be more correct and induces in-plane stresses according to Eq. (2.5) but is not expected to be significant here and ignored as commonly done in literature.

$$\mathbf{C} = \mathbf{C}(1 + i\eta) \tag{2.7}$$

Summarising the two steps, a correlation is given between stresses and displacements by combining Eq. (2.2) and Eq. (2.5). If one of these fields is known, the corresponding field is known as well according to Eq. (2.8) [101].

$$\boldsymbol{\sigma} = \mathbf{CLu} \tag{2.8}$$

Third, **equilibrium conditions** are necessary. A general approach is *Hamilton's principle*, in which the variation of the mean difference between potential and kinetic energy is equilibrated with the external work according to Eq. (2.9) [48]. For a dynamic system, the mean energy difference and the external work reaches a minimum over time t [48].

$$\delta \int_{t1}^{t2} (E_{\text{kin}} - E_{\text{pot}})\,\mathrm{d}t + \int_{t1}^{t2} \delta W \mathrm{d}t = 0 \tag{2.9}$$

3D structural domain Ω_{s3} For the structural 3D case, the sum of stresses multiplied by strains yields the potential energy E_{pot} according to Eq. (2.10) [48]. The given integral in Eq. (2.10) represents the maximum deformation of the vibrating structure while no stresses occur if the kinetic energy reaches its maximum and vice versa. Eqs. (2.8) and (2.5) are inserted in matrix form in order to yield the displacement formulation which is used in this work for all structural 3D continua. For the stationary harmonic case, $\mathbf{u} = \underline{\mathbf{u}}\mathrm{e}^{i\omega t}$, which contains the complex amplitudes $\underline{u}_{x/y/z}$.

$$\begin{aligned} E_{\text{pot,s3}} &= \frac{1}{2} \int \boldsymbol{\epsilon}^{\mathrm{T}} \boldsymbol{\sigma}\ \mathrm{d}\Omega_{\text{s3}} \\ &= \frac{1}{2} \int \mathbf{u}^{\mathrm{T}} \mathbf{L}^{\mathrm{T}} \mathbf{C} \mathbf{L} \mathbf{u}\ \mathrm{d}\Omega_{\text{s3}} \end{aligned} \tag{2.10}$$

The kinetic energy E_{kin} for the general 3D case is given in Eq. (2.11) [48] already satisfying the requested displacement formulation. In addition, the time derivative is substituted by the time derivatives of $\underline{\mathbf{u}}\mathrm{e}^{i\omega t}$ for the stationary harmonic case.

$$\begin{aligned} E_{\text{kin,s3}} &= \frac{1}{2} \int \rho_s\ \dot{\mathbf{u}}^{\mathrm{T}} \dot{\mathbf{u}}\ \mathrm{d}\Omega_{\text{s3}} \\ &= \frac{\omega^2}{2} \int \rho_s\ \mathbf{u}^{\mathrm{T}} \mathbf{u}\ \mathrm{d}\Omega_{\text{s3}} \end{aligned} \tag{2.11}$$

Within the full aircraft model, 3D continua are not exposed to external work. Hence, for these domains $W = 0$.

2D structural domain Ω_{s2} In contrast to the 3D structural domain, shell structures within the aircraft model are indeed excited by an external pressure p_{e} or the sound pressure p of an adjacent acoustic domain Ω_{s2}. Both, the boundary condition on $\Gamma_{\mathrm{e}} \in \Omega_{s2}$ and the coupling condition on $\Gamma_{\mathrm{c}} \in (\Omega_{s2} \cap \Omega_a)$, are considered in Eq (2.12) [98]. $\mathbf{u}_{\mathrm{s2}}$ contains complex amplitudes $u_{x/y/z}$ and $\varphi_{x/y}$. The pressure acts on the normal displacement of the shell domain which corresponds to the third local degree of freedom u_z within $\mathbf{u}_{\mathrm{s2}}$.

$$W_{\mathrm{s2}} = \int \begin{bmatrix} 0 & 0 & p_{\mathrm{e}} & 0 & 0 \end{bmatrix} \mathbf{u}_{\mathrm{s2}} \, \mathrm{d}\Gamma_{\mathrm{e}} + \int \begin{bmatrix} 0 & 0 & p & 0 & 0 \end{bmatrix} \mathbf{u}_{\mathrm{s2}} \, \mathrm{d}\Gamma_{\mathrm{c}} \tag{2.12}$$

The potential energy $E_{\mathrm{pot,s2}}$ within Ω_{s2} (Eq. (2.13) [44]) contains two modified stiffness matrices $\mathbf{C}_{\mathrm{s2,d}}$ and $\mathbf{C}_{\mathrm{s2,p}}$, which are yielded by the integration over the shell's thickness h. As introduced above, an orthotropic material behaviour is considered throughout. Due to terms of different orders of z within Eq. (2.4), the distinction between disc and plate parts is necessary [44]. The differential operator matrix $\mathbf{L}_{\mathrm{s2}}$ is split as well as already indicated in Eq. (2.4). This approach is only valid for symmetric laminates in the frame of the classical laminate theory (CLT) [150]. The shear correction factor $k_s \approx 5/6$ is necessary in order to correct the assumptions of constant shear stresses over thickness [15].

$$E_{\mathrm{pot,s2}} = \frac{1}{2} \int \mathbf{u}_{\mathrm{s2}}^{\mathrm{T}} \left(\underbrace{\mathbf{L}_{\mathrm{s2,m}}^{\mathrm{T}} \mathbf{C}_{\mathrm{s2,m}} \mathbf{L}_{\mathrm{s2,m}}}_{\text{disc}} + \underbrace{\mathbf{L}_{\mathrm{s2,p}}^{\mathrm{T}} \mathbf{C}_{\mathrm{s2,p}} \mathbf{L}_{\mathrm{s2,p}}}_{\text{plate}} \right) \mathbf{u}_{\mathrm{s2}} \, \mathrm{d}\Omega_{\mathrm{s2}} \tag{2.13}$$

$$\mathbf{C}_{\mathrm{s2,d}} = \begin{bmatrix} \frac{h}{1-\nu_{xy}\nu_{yx}} E_x & \frac{h\nu_{xy}}{1-\nu_{xy}\nu_{yx}} E_y & 0 & 0 & 0 \\ & \frac{h}{1-\nu_{xy}\nu_{yx}} E_y & 0 & 0 & 0 \\ & & 0 & 0 & 0 \\ & & & 0 & 0 \\ \text{sym} & & & & hG_{xy} \end{bmatrix} \tag{2.14}$$

$$\mathbf{C}_{\mathrm{s2,p}} = \begin{bmatrix} \frac{h^3}{12(1-\nu_{xy}\nu_{yx})} E_x & \frac{h^3\nu_{xy}}{12(1-\nu_{xy}\nu_{yx})} E_y & 0 & 0 & 0 \\ & \frac{h^3}{12(1-\nu_{xy}\nu_{yx})} E_y & 0 & 0 & 0 \\ & & k_s h G_{yz} & 0 & 0 \\ & & & k_s h G_{xz} & 0 \\ \text{sym} & & & & \frac{h^3}{12} G_{xy} \end{bmatrix} \tag{2.15}$$

Incorporating Eq. (2.3) as angle-displacement relation and integrating over thickness h, the kinetic energy $E_{\mathrm{kin,s2}}$ is given in Eq. (2.16) [44].

$$E_{\mathrm{kin,s2}} = \frac{\omega^2}{2} \int \rho_{\mathrm{s}}\ \mathbf{u}_{\mathrm{s2}}^{\mathrm{T}} \begin{bmatrix} h & 0 & 0 & 0 & 0 \\ 0 & h & 0 & 0 & 0 \\ 0 & 0 & h & 0 & 0 \\ 0 & 0 & 0 & \frac{h^3}{12} & 0 \\ 0 & 0 & 0 & 0 & \frac{h^3}{12} \end{bmatrix} \mathbf{u}_{\mathrm{s2}}\ \mathrm{d}\Omega_{\mathrm{s2}} \tag{2.16}$$

Conducting the variation of the functional (Eq. (2.9)) for Ω_{s2}, a system of equations is received for the shell. Eqs. (2.17) and (2.18) describe in-plane waves (disc part) and are independent on Eqs. (2.19) to (2.21) representing bending waves (Mindlin plate part) [44, 111]. For the local normal displacement (Eq. (2.19)) Neumann boundary conditions are yielded by the external work W_{s2}. In general, a Neumann boundary condition defines the derivative of the field value [19]. Here, an external pressure p_{ext} or a pressure p by the acoustic fluid domain is given on Γ_{e} and Γ_{c}, respectively.

$$\begin{aligned} &\frac{hE_x}{1-\nu_{xy}\nu_{yx}} u_{x,xx} + hG_{xy} u_{x,yy} + \\ &\left(\frac{h\nu_{yx}E_x}{1-\nu_{xy}\nu_{yx}} + hG_{xy} \right) u_{y,yx} + \omega^2 \rho_{\mathrm{s}} h u_x = 0 \end{aligned} \tag{2.17}$$

$$\begin{aligned} &\frac{hE_y}{1-\nu_{xy}\nu_{yx}} u_{y,yy} + hG_{xy} u_{y,xx} + \\ &\left(\frac{h\nu_{xy}E_y}{1-\nu_{xy}\nu_{yx}} + hG_{xy} \right) u_{x,xy} + \omega^2 \rho_{\mathrm{s}} h u_y = 0 \end{aligned} \tag{2.18}$$

- -

$$\begin{aligned} &k_s h G_{xz} \left(u_{z,xx} + \varphi_{x,x} \right) + \\ &k_s h G_{yz} \left(u_{z,yy} + \varphi_{y,y} \right) + \omega^2 \rho_{\mathrm{s}} h u_z = -p - p_{\mathrm{e}} \end{aligned} \tag{2.19}$$

$$\begin{aligned} &k_s h G_{xz} \left(u_{z,x} + \varphi_x \right) - G_{xy} I \left(\varphi_{x,yy} + \varphi_{y,xy} \right) - \\ &B_x \left(\varphi_{x,xx} + \nu_{yx} \varphi_{y,xy} \right) - \omega^2 \rho_{\mathrm{s}} I \varphi_x = 0 \end{aligned} \tag{2.20}$$

$$\begin{aligned} &k_s h G_{yz} \left(u_{z,y} + \varphi_y \right) - G_{xy} I \left(\varphi_{y,xx} + \varphi_{x,xy} \right) - \\ &B_y \left(\varphi_{y,yy} + \nu_{xy} \varphi_{x,xy} \right) - \omega^2 \rho_{\mathrm{s}} I \varphi_y = 0 \end{aligned} \tag{2.21}$$

B_x and B_y are the bending stiffness's according to Eqs. (2.22) and (2.23) [15] in both flexural directions while $I = h^3/12$ is the related moment of inertia of area resulting

from the integration over thickness [44].

$$B_x = \frac{E_x h^3}{12(1-\nu_{12}\nu_{21})} \tag{2.22}$$

$$B_y = \frac{E_y h^3}{12(1-\nu_{12}\nu_{21})} \tag{2.23}$$

The required material parameters can be approximated for orthotropic composites (in aircraft) by the classical laminate theory (CLT). The theory is well-documented in basic literature like, e.g. [150]. However, the shear moduli G_{xz} and G_{yz} play an important role with increasing laminate thickness and are required for the consideration of shear within the Mindlin theory. As the CLT considers the Kirchhoff theory for the derivation of material parameters, the shear moduli are not given by standard. A simple approach in order to receive the shear moduli is a mixing rule according to Eq. (2.24) [140].

$$G = \frac{1}{t_{\text{ges}}} \sum_{j=1}^{N} G_j t_j \tag{2.24}$$

The transverse shear moduli G_j of each layer j are weighted by the layers thickness t_j and summed up resulting in an overall shear modulus G. The equation is applied for the two shear planes xy and xz in the laminate coordinate system. As the mixing rule equilibrates the influence of all layers and the stresses converge to zero at the surfaces, a reasonable extension of the mixing rule is available by Rohwer – In [140], a calculation routine is derived in order to yield the transverse shear moduli under consideration of the reduced influence of the outer layers.

2.3 Sound waves in 3D acoustic fluids Ω_a

The weak formulation for the 3D fluid acoustic domain is derived based on [98, 115]. In parallel to the shell domain, a coupling term on Γ_c is considered as given in Eq. (2.25). This way, a strong structural-acoustic coupling is enabled.

$$W_\text{a} = \int \begin{bmatrix} 0 & 0 & p & 0 & 0 \end{bmatrix} \mathbf{u}_{\text{s}2} \, \mathrm{d}\Gamma_\text{c} \tag{2.25}$$

For an isotropic medium, the acoustic potential energy $E_{\text{pot,a}}$ is expressed by the integral over the pressure fluctuation p and the relative volume change $\Delta V/V$ as given in Eq. (2.26) [115]. The Volume change is per definition expressed by p and the bulk modulus K_a in order to yield a pressure formulation for the stationary harmonic case. The bulk modulus is in turn replaced according to Eq. (2.27) [14]. k_a is the wave number as given in Eq. (2.28), which is defined as relation between angular

frequency ω and speed of sound c_a [14].

$$\begin{aligned} E_{\mathrm{pot,a}} &= \frac{1}{2}\int\ p\frac{\Delta V}{V}\ \mathrm{d}\Omega_\mathrm{a} \\ &= \frac{1}{2}\int\ \frac{1}{K}p^2\ \mathrm{d}\Omega_\mathrm{a} \\ &= \frac{1}{2\rho_\mathrm{a}c_\mathrm{a}^2}\int\ p^2\ \mathrm{d}\Omega_\mathrm{a} \end{aligned} \tag{2.26}$$

$$K_\mathrm{a} = \frac{\omega^2\rho_\mathrm{a}}{k_\mathrm{a}^2} \tag{2.27}$$

$$k_\mathrm{a} = \frac{\omega}{c_\mathrm{a}} \tag{2.28}$$

The acoustic kinetic energy $E_{\mathrm{kin,a}}$ is derived similarly to the structural domains above. For harmonic problems, Eq. (2.29) is valid based on the continuity of particle displacements [19].

$$\mathbf{u}_\mathrm{a} = \frac{1}{\rho_f\omega^2}\nabla p \tag{2.29}$$

In order to keep the pressure formulation, $\mathbf{u}$ is substituted by Eq. (2.29), which yields Eq. (2.30) [115].

$$\begin{aligned} E_{\mathrm{kin,a}} &= \frac{\omega^2}{2}\int\ \rho_\mathrm{a}\ \mathbf{u}_\mathrm{a}^\mathrm{T}\mathbf{u}_\mathrm{a}\ \mathrm{d}\Omega_\mathrm{a} \\ &= \frac{1}{2\rho_\mathrm{a}\omega^2}\int\ p\nabla^2 p\ \mathrm{d}\Omega_\mathrm{a} \end{aligned} \tag{2.30}$$

Conducting the variation of the functional (Eq. (2.9)) for Ω_a, the Helmholtz equation (2.31) with Neumann boundary condition is received [19]. Here, a particle displacement u_n from $\Omega_{\mathrm{s}2}$ is considered on Γ_c.

$$\bigtriangledown^2\ p + k_\mathrm{a}^2 p = -\rho_\mathrm{a}\omega^2 u_n \tag{2.31}$$

Besides the Neumann boundary condition, a Robin or impedance boundary condition is introduced. For Γ_a, Eq. (2.32) with the normal surface impedance Z_surf is then valid.

$$\frac{\partial p}{\partial \mathbf{n}} + i\omega k\frac{1}{Z_\mathrm{surf}}p = 0 \tag{2.32}$$

A homogenised damping loss factor η_a in a acoustic fluid domain can be considered via a complex speed of sound $\underline{c}_\mathrm{a}$ as given in Eq. (2.33) [19].

$$\underline{c}_\mathrm{a}^2 = c_\mathrm{a}^2\left(1 + i\eta_a\right) \tag{2.33}$$

Porous materials

As porous materials are multi-phase domains (structure and fluid), numerous modelling approaches exists in dependency on the actual application case and the material characteristics. For several porous materials, an equivalent fluid is sufficient to model the wave propagation on macroscopic scale. An equivalent fluid domain is governed by the Helmholtz equation (2.31) but considers complex effective material parameters [14]. The complex characteristic impedance Z_c and the effective wave number $k_{\mathrm{a,eff}}$ of porous materials like foams and fibres can be approximated by the law by Delany and Bazley as given in Eq. (2.34) and (2.35) [52].

$$Z_{\mathrm{a,eff}}(f) = \rho_{\mathrm{a}} c_{\mathrm{a}} \left(1 + 0.0570 \left(\frac{\rho_{\mathrm{a}} f}{\sigma}\right)^{-0.754} - i0.087 \left(\frac{\rho_{\mathrm{a}} f}{\sigma}\right)^{-0.732}\right) \tag{2.34}$$

$$k_{\mathrm{a,eff}}(f) = \frac{2\pi f}{c_{\mathrm{a}}} \left(1 + 0.0978 \left(\frac{\rho_{\mathrm{a}} f}{\sigma}\right)^{-0.700} - i0.189 \left(\frac{\rho_{\mathrm{a}} f}{\sigma}\right)^{-0.595}\right) \tag{2.35}$$

The formulas are fitted to measurements of many fibre materials with a porosity Φ close to 1 [14]. By the porosity Φ, the volume fraction filled by air (or any other surrounding medium) V_a is related to the total volume V_t and is obtained according to Eq. (2.36) [14]. Knowing the density of the structural frame material ρ_s, the total mass m_t and the total volume, Φ can be calculated, which is more accessible in practical laboratory situation only having a micro scale available.

$$\Phi = \frac{V_a}{V_t} = 1 - \frac{m_t}{\rho_s V_t} \tag{2.36}$$

The empirical model by Delany and Bazley requires the flow resistivity σ and frequency f as input. The flow resistivity σ is defined as length-related (to the specimen's thickness h) specific flow resistance R_s, which in turn is the flow resistance R of a specimen with an area of $1\,\mathrm{m}^2$ [4].

$$\sigma = \frac{R_s}{h} \tag{2.37}$$

The effective speed of sound $c_{\mathrm{a,eff}}$, the effective bulk modulus $K_{\mathrm{a,eff}}$ and the effective density $\rho_{\mathrm{a,eff}}$ are given by Eqs. (2.38), (2.39) and (2.40) [14]. As mentioned, all parameters generally remain as complex and frequency-dependent.

$$c_{\mathrm{a,eff}}(f) = \frac{\omega}{k_{\mathrm{a,eff}}(f)} \tag{2.38}$$

$$K_{\mathrm{a,eff}}(f) = \frac{\omega Z_{\mathrm{a,eff}}(f)}{k_{\mathrm{a,eff}}(f)} \tag{2.39}$$

$$\rho_{\mathrm{a,eff}}(f) = \frac{k_{\mathrm{a,eff}}(f) Z_{\mathrm{a,eff}}(f)}{\omega} \tag{2.40}$$

Finally, two parameters must be known in order to have a complete description of the equivalent fluid. A more sophisticated approach, compared to Delany and Bazley, is published by Johnson-Champoux-Allard (JCA-model) in [43, 83]. As given in Eqs. (2.41, 2.42), the model describes the calculation of the effective density $\rho_{a,\mathrm{eff}}(f)$ and the effective bulk modulus $K_{a,\mathrm{eff}}(f)$ and requires additional microscopic variables.

$$\rho_{a,\mathrm{eff}}(f) = \frac{\rho_a \alpha_\infty}{\Phi} + \frac{\sigma}{i\omega}\left(1 + \frac{4i + \alpha_\infty^2 \eta_a \rho_a \omega}{\sigma^2 \lambda^2 \Phi^2}\right)^{0.5} \tag{2.41}$$

$$K_{a,\mathrm{eff}}(f) = \frac{\gamma p_0}{\Phi}\left(\gamma - \frac{\gamma - 1}{1 + \frac{8\eta_a}{i\mathrm{Pr}\omega\rho_a\lambda'^2)}\left(1 + \frac{i\rho_a\omega\mathrm{Pr}\lambda'^2}{16\eta_a}\right)^{0.5}}\right)^{-1} \tag{2.42}$$

The Tortuosity α_∞ relates the squared macroscopic and microscopic velocities as defined by Johnson in [83]. α_∞ is expected near unity for common fibre materials [12]. λ and λ' symbolise the characteristic viscous and thermal lengths, respectively. Two integrals of the fluid velocities within the porous material (over volume and surface) yields λ [84] while for obtaining λ', the volume and surface of the pores are related [43]. γ is the adiabatic constant, p_0 is the static ambient pressure and Pr represents the Prandtl number.

By a consideration of the inertia of a limp frame without significant stiffness, the equivalent fluid approach is further extended. $\rho_{a,\mathrm{limp}}$ is estimated based on $\rho_{a,\mathrm{eff}}$ according to Eq. (2.43) [127].

$$\rho_{\mathrm{limp}}(f) \approx \frac{\rho_t \rho_{a,\mathrm{eff}} - \rho_a^2}{\rho_t + \rho_{a,\mathrm{eff}}(f) - 2\rho_a} \tag{2.43}$$

$$\rho_t = \rho_s + \phi\rho_a \tag{2.44}$$

ρ_s is the bulk density of the porous domain. This model is preferable for fibrous materials attached to vibrating structures and mainly influences the behaviour at low frequencies [14].

Knowing $Z_{a,\mathrm{eff}}$ and $k_{a,\mathrm{eff}}$, the acoustic fluid impedance of a porous layer at normal incidence before a hard wall is obtained by Eq. (2.45) [14]. h is the thickness of the equivalent fluid layer. For normal incidence, the entire layer can be replaced by Z_{surf} at its surface.

$$Z_{\mathrm{surf}}(f) = -iZ_{a,\mathrm{eff}}(f)\frac{\cos\left(k_{a,\mathrm{eff}}h\right)}{\sin\left(k_{a,\mathrm{eff}}h\right)} \tag{2.45}$$

Finally, in order to consider interactions between the 3D structural frame and the fluid pores with the porous domain, the Biot model is available. Especially for elastic frames, the consideration of fluid-frame interactions is reasonable and supplied by the model [19]. The Biot model is originally formulated based on structural and

fluid particle displacements [25]. As the above formulations for Ω_{s3} and Ω_a use the unknowns $\boldsymbol{u}$ and p, respectively, a suitable representation of the Biot model uses these variables as well. The according ($\boldsymbol{u}$, p) formulation is available in [20] as given in Eqs. (2.46) and (2.47). The major advantage of ($\boldsymbol{u}$, p) is that the same form of the above introduced fluid-structure coupling is met [19].

In Eq. (2.46), the first two terms equal a 3D domain's Ω_{s3} behaviour in vacuum. $\tilde{\rho}$ declares a dynamic density using three additional density parameter, which are given in [19] and are in turn based on the porosity, the frame's material density, the dynamic tortuosity and the fluid density.

In both equations, coupling terms are included, which consider the product of a coupling coefficient γ with the respective other dof. These coupling terms essentially represent the Biot theory as an extension of the two above introduced models for Ω_{s3} and Ω_a [19]. $\tilde{\rho}_{22}$ declares one of Biot's three density parameters, which depend on the geometry of the frame [14].

Finally, in Eq. (2.47), the first two terms are similar to the Helmholtz equation for an equivalent fluid. $\tilde{R}$ is the bulk modulus of the fluid phase under consideration of the volume reduced by the structural frame [19].

$$\nabla\boldsymbol{\sigma} + \omega^2\tilde{\rho}\boldsymbol{u} \overbrace{+\tilde{\gamma}\nabla p}^{\text{coupling term}} = 0 \tag{2.46}$$

$$\nabla^2 p + \frac{\tilde{\rho}_{22}}{\tilde{R}}\omega^2 p \underbrace{-\frac{\tilde{\rho}_{22}}{\Phi^2}\tilde{\gamma}\omega^2\nabla\boldsymbol{u}}_{\text{coupling term}} = 0 \tag{2.47}$$

Concluding this section, all mechanical models required for the studies on aircraft fuselages in this thesis are introduced. As indicated, a numerical solution is obtained, which is given in the following section for the three fundamental domains Ω_{s3}, Ω_{s2} and Ω_a.

2.4 Discretisation with finite elements

In order to obtain a solution for the variations of the time-integrated Lagrangian functional according to Eq. (2.9) for 3D/2D structural and 3D acoustic domains in aircraft, analytical approaches are hardly realisable. Instead of finding the exact solution $\mathbf{u}$, an approximation $\tilde{\mathbf{u}}$ is found in the frame of the finite element method (FEM). In the FEM, geometries are represented by a discretisation with finite domains (elements), which follow typical geometrical forms [19]. Shape and solution are approximated by local ansatzfunctions and associated nodes and it's dofs. Adjacent elements share their nodes at local boundaries, which finally connects the entire

domain to be solved numerically. In literature, numerical alternatives exist; for instance, a boundary integral is applied within the boundary element method (BEM), which yields a reduction of dof but dense matrices [19]. However, within this thesis, focussing on the FEM, 27-node hexahedrons are used for the 3D domains Ω_{s3} and Ω_a while 9-node quadrilaterals are applied for the 2D shell domain Ω_{s2}. The major steps of the implementation[4] are concisely described in the following. The transformation to the global coordinate system and the assembling of the system matrices are not shown in detail. The reader is referred to [44, 86] for more details or to fundamental books on FEM like [19, 24, 169].

For all domains, the local approximated solution of each finite element's domain $\tilde{\mathbf{u}}^e$ is described by polynomial ansatzfunctions $\mathbf{N} = (N_1\ N_2\ \ldots\ N_n)$ according to Eq. (2.48). Within each element $\square^e$, the unknowns of the domain define the degrees of freedom at each node, which are considered as coefficients for the polynomial ansatzfunctions [86].

$$\tilde{\mathbf{u}}^e(x,y,z) = \mathbf{N}(x,y,z)\mathbf{u}^e \tag{2.48}$$

Lagrange polynomials of second order are used for $\mathbf{N}$ within all implemented elements [44]. All integrals are calculated by a full Gauß integration.

Discretised 3D structural domain Ω_{s3} In order to discretise Ω_{s3}, hexahedron elements are applied as element type. Eqs. (2.10) and (2.11) describe both the entire domain and the local element's domain. A consideration of the ansatzfunction $\tilde{\mathbf{u}}^e$ in Eqs. (2.10) and (2.11) for a single element yields Eqs. (2.49) and (2.51). $\mathbf{B}$ is the strain matrix containing the derivations of $\mathbf{N}$. The integral is shifted, as no dependency of the node solution $\mathbf{u}^e$ on coordinates is present. Each element is integrated individually, the resulting element matrices $\mathbf{K}^e_{s3}$ and $\mathbf{M}^e_{s3}$ are called stiffness and mass matrix, respectively. Material parameters (for $\mathbf{C}$ and ρ_s) must be given while the values of the shape functions and its derivatives are dependent on the element shape.

$$E^e_{\mathrm{pot,s3}} = \frac{1}{2}\mathbf{u}^{eT} \underbrace{\int \mathbf{B}^T\mathbf{C}\mathbf{B}\ \mathrm{d}\Omega^e_{s3}}_{\mathbf{K}^e_{s3}}\ \mathbf{u}^e \tag{2.49}$$

$$\text{with}\quad \mathbf{B} = \mathbf{L}\mathbf{N} \tag{2.50}$$

$$E^e_{\mathrm{kin,s3}} = \frac{\omega^2}{2}\mathbf{u}^{eT} \underbrace{\int \rho_s\mathbf{N}^T\mathbf{N}\ \mathrm{d}\Omega^e_{s3}}_{\mathbf{M}^e_{s3}}\ \mathbf{u}^e \tag{2.51}$$

[4] The element implementations already exist within the in-house code elPaSo at the institute and applied for the aircraft applications within this thesis. Code extensions concerning pre-stressing and a separation of disc and plate material parameters are conducted by the author.

For the 3D continuum without external work, Hamilton's principle (Eq. (2.9)) yields Eq. (2.52) after inserting Eqs. (2.49) and (2.51).

$$\delta \int_{t1}^{t2} \frac{\omega^2}{2} \mathbf{u}^{\mathrm{e}\mathrm{T}} \mathbf{M}_{\mathrm{s3}}^{\mathrm{e}}\ \mathbf{u}^{\mathrm{e}} - \frac{1}{2} \mathbf{u}^{\mathrm{e}\mathrm{T}}\ \mathbf{K}_{\mathrm{s3}}^{\mathrm{e}}\ \mathbf{u}^{\mathrm{e}} \mathrm{d}t = 0 \tag{2.52}$$

After interchanging the integral and variation operators and rearranging the equation, similar to [89], Eq. (2.53) is received. In addition, the time integral is dropped as the stationary solution is studied in frequency domain.

$$\delta \mathbf{u}^{\mathrm{e}\mathrm{T}} \left(\mathbf{K}_{\mathrm{s3}}^{\mathrm{e}}\ \mathbf{u}^{\mathrm{e}} - \omega^2 \mathbf{M}_{\mathrm{s3}}^{\mathrm{e}}\ \mathbf{u}^{\mathrm{e}} \right) = 0 \tag{2.53}$$

As the variation $\delta \mathbf{u}^{\mathrm{e}\mathrm{T}}$ is of arbitrary nature, the factor besides $\delta \mathbf{u}^{\mathrm{e}\mathrm{T}}$ must be zero [89]. This way, the element description in frequency domain with three translational degrees of freedom is yielded in Eq. (2.54) [92]. A connection to Ω_{s2} is realised within the assembly process by shared nodes at which the shell displacements are identical to the continuum displacements.

$$\mathbf{K}_{\mathrm{s3}}^{\mathrm{e}}\ \mathbf{u}^{\mathrm{e}} - \omega^2 \mathbf{M}_{\mathrm{s3}}^{\mathrm{e}}\ \mathbf{u}^{\mathrm{e}} = 0 \tag{2.54}$$

Discretised 2D structural domain Ω_{s2} Similar to the 3D structural domain, an approximation $\tilde{\mathbf{u}}_{\mathrm{s2}}^{\mathrm{e}}$ is inserted in Eqs. (2.13) and (2.16) for one single shell element. This way, Eqs. (2.55) and (2.56) are yielded in which the disc part and the plate part are separated as described above. For the latter, the density ρ_{s} is assumed to be constant within one element.

$$E_{\mathrm{pot,s2}}^{\mathrm{e}} = \frac{1}{2} \mathbf{u}_{\mathrm{s2}}^{\mathrm{e}\mathrm{T}} \underbrace{\left(\underbrace{\int \mathbf{B}_{\mathrm{s2,d}}^{\mathrm{T}} \mathbf{C}_{\mathrm{s2,d}} \mathbf{B}_{\mathrm{s2,d}}\ \mathrm{d}\Omega_{\mathrm{s2}}^{\mathrm{e}}}_{\text{disc}} + \underbrace{\int \mathbf{B}_{\mathrm{s2,p}}^{\mathrm{T}} \mathbf{C}_{\mathrm{s2,p}} \mathbf{B}_{\mathrm{s2,p}}\ \mathrm{d}\Omega_{\mathrm{s2}}^{\mathrm{e}}}_{\text{plate}} \right)}_{\mathbf{K}_{\mathrm{s2}}^{\mathrm{e}}} \mathbf{u}_{\mathrm{s2}}^{\mathrm{e}} \tag{2.55}$$

$$E_{\mathrm{kin,s2}}^{\mathrm{e}} = \frac{\omega^2}{2} \mathbf{u}_{\mathrm{s2}}^{\mathrm{e}\mathrm{T}} \underbrace{\int \rho_{\mathrm{s}} \mathbf{N}^{\mathrm{T}} \begin{bmatrix} h & 0 & 0 & 0 & 0 \\ 0 & h & 0 & 0 & 0 \\ 0 & 0 & h & 0 & 0 \\ 0 & 0 & 0 & \frac{h^3}{12} & 0 \\ 0 & 0 & 0 & 0 & \frac{h^3}{12} \end{bmatrix} \mathbf{N}\ \mathrm{d}\Omega_{\mathrm{s2}}^{\mathrm{e}}}_{\mathbf{M}_{\mathrm{s2}}^{\mathrm{e}}}\ \mathbf{u}_{\mathrm{s2}}^{\mathrm{e}} \tag{2.56}$$

Accordingly, the identified stiffness matrix $\mathbf{K}^{\mathrm{e}}_{\mathrm{s2}}$ is a sum of the two mechanical parts and contains differential operators within $\mathbf{B}_{\mathrm{s2}}$ while the mass matrix $\mathbf{M}^{\mathrm{e}}_{\mathrm{s2}}$ contains the ansatzfunctions and thickness terms [44].

A discretisation of the external work $W^{\mathrm{e}}_{\mathrm{s2}}$ for one shell element yields Eq. (2.57). n symbolises the number of nodes i within the quadrilateral shell element (here $n = 9$ nodes). The first term represents a constant external pressure load p_{ext}. The integration over the shell area yields an external nodal force vector $\mathbf{f}^{\mathrm{e}}_{\mathrm{ext}}$ [44, 98]. The second term yields the coupling matrix $\mathbf{C}^{\mathrm{T}}_{\mathrm{s2a}}$ connecting the normal deflection of the shell to the pressure of the acoustic domain [44, 98]. n remains unchanged as the nodes of the adjacent 3D acoustic domain must be coincident for the underlying implementation. Hence, the pressure p_i at node i of the acoustic domain is coupled to the corresponding entries within $\mathbf{u}^{\mathrm{e}}_{\mathrm{s2}}$.

$$W^{\mathrm{e}}_{\mathrm{s2}} = \underbrace{\begin{bmatrix} 0 & 0 & p_{\mathrm{ext}} & 0 & 0 \end{bmatrix}_{(\times n)} \int \mathbf{N}_{\mathrm{s2}} \, \mathrm{d}\Gamma^{\mathrm{e}}_{\mathrm{ext}}}_{\mathbf{f}^{\mathrm{e}}_{\mathrm{ext}}} \mathbf{u}^{\mathrm{e}}_{\mathrm{s2}} + \begin{bmatrix} 0 & 0 & p_i & 0 & 0 \end{bmatrix}_{(\times n)} \underbrace{\int \mathbf{N}^{\mathrm{T}}_{\mathrm{a}} \mathbf{N}_{\mathrm{s2}} \, \mathrm{d}\Gamma^{\mathrm{e}}_{\mathrm{c}}}_{\mathbf{C}^{\mathrm{eT}}_{\mathrm{s2a}}} \mathbf{u}^{\mathrm{e}}_{\mathrm{s2}} \tag{2.57}$$

By application of Hamilton's principle similar to Ω_{s3} above, the typical FE form of a shell is derived as given in Eq. (2.58) [44, 98].

$$\mathbf{K}^{\mathrm{e}}_{\mathrm{s2}} \, \mathbf{u}^{\mathrm{e}}_{\mathrm{s2}} - \omega^2 \mathbf{M}^{\mathrm{e}}_{\mathrm{s2}} \, \mathbf{u}^{\mathrm{e}}_{\mathrm{s2}} = \mathbf{C}^{\mathrm{e}}_{\mathrm{s2a}} \begin{bmatrix} 0 & 0 & p_i & 0 & 0 \end{bmatrix}^{\mathrm{T}}_{(\times n)} + \mathbf{f}^{\mathrm{e}}_{\mathrm{ext}} \tag{2.58}$$

Within the shell, a Mindlin plate with 3 dof and a disc element with 2 dof are combined. In contrast, for a transformation to the global coordinate system, six dof are necessary. Hence, the element system is regularised by an artificial introduction of the third rotational dof (by use of a small stiffness) [24, 44]. In addition, the shell elements applied in this thesis use the *discrete shear gap* DSG method according to [31] for the plate part in order to reduce shear locking effects within thin Mindlin plates [44].

Discretised 3D acoustic domain Ω_{a} The FE implementation of Ω_{a} is taken from the literature sources [44, 98]. Assuming constant values for the speed of sound c_{a} and the density ρ_{a} within one finite element element for Ω_{a}, Eqs. (2.59) and (2.60) describe the discretised potential and kinetic energy, respectively. Again, mass and

stiffness matrices can be identified.

$$E^{\mathrm{e}}_{\mathrm{pot,a}} = \frac{1}{2\rho_{\mathrm{a}}} \mathbf{p}^{\mathrm{eT}} \underbrace{\frac{1}{c_{\mathrm{a}}^2} \int \mathbf{N}_{\mathrm{a}}^{\mathrm{T}} \mathbf{N}_{\mathrm{a}} \, \mathrm{d}\Omega_{\mathrm{a}}^{\mathrm{e}}}_{\mathbf{M}_{\mathrm{a}}^{\mathrm{e}}} \mathbf{p}^{\mathrm{e}} \tag{2.59}$$

$$E^{\mathrm{e}}_{\mathrm{kin,a}} = \frac{1}{2\rho_{\mathrm{a}}\omega^2} \mathbf{p}^{\mathrm{eT}} \underbrace{\int \nabla \mathbf{N}_{\mathrm{a}}^{\mathrm{T}} \nabla \mathbf{N}_{\mathrm{a}} \, \mathrm{d}\Omega_{\mathrm{a}}^{\mathrm{e}}}_{\mathbf{K}_{\mathrm{a}}^{\mathrm{e}}} \mathbf{p}^{\mathrm{e}} \tag{2.60}$$

As external work (Eq. (2.61)), a coupling to Ω_{s2} is realised. Similar to the shell, the discretisation considers a strong coupling between coincident nodes. For simplicity, n describes the necessary subset of all element nodes within the 27-node hexahedron.

$$W_{\mathrm{a}}^{\mathrm{e}} = \begin{bmatrix} 0 & 0 & p_i & 0 & 0 \end{bmatrix}_{(\times n)} \underbrace{\int \mathbf{N}_{\mathrm{a}}^{\mathrm{T}} \mathbf{N}_{\mathrm{s2}} \, \mathrm{d}\Gamma_{\mathrm{c}}^{\mathrm{e}}}_{\mathbf{C}_{\mathrm{s2a}}^{\mathrm{eT}}} \mathbf{u}_{\mathrm{s2}}^{\mathrm{e}} \tag{2.61}$$

Hamilton's principle yields the final form of a 3D acoustic domain as given in Eq. (2.62). Formulating $\mathbf{C}_{\mathrm{s2a}}^{\mathrm{eT}}$ on element level requires an inflation of the matrix in order to fit the 27 nodes of the hexahedron. Within the used in-house code elPaSo, the coupling matrices are separately calculated within a 9-node interface element.

$$\mathbf{K}_{\mathrm{a}}^{\mathrm{e}} \, \mathbf{p}^{\mathrm{e}} - \omega^2 \mathbf{M}_{\mathrm{a}}^{\mathrm{e}} \, \mathbf{p}^{\mathrm{e}} = \rho_{\mathrm{a}} \omega^2 \mathbf{C}_{\mathrm{s2a}}^{\mathrm{eT}} \mathbf{u}_{\mathrm{s2}}^{\mathrm{e}} \tag{2.62}$$

Discretised system Within the aircraft model, the three domains are combined by use of

- shared nodes in case of identical translational dof between Ω_{s2} and Ω_{s3}
- coupling matrices in order to link the displacement in Ω_{s2} and the pressure in Ω_{a}

The final shape of the system is qualitatively summarised within Eq. (2.63). A consideration of damping loss factors for both structural and acoustic domains generally yields non-symmetric complex matrices and thus non-Hermetian system properties. Similar effects are introduced by the inclusion of impedance boundary conditions and an equivalent fluid approach within Ω_{a}.

$$\underbrace{\left[\begin{bmatrix} \mathbf{K}_{\mathrm{s3}} & 0 & 0 \\ 0 & \mathbf{K}_{\mathrm{s2}} & -\mathbf{C}_{\mathrm{s2a}} \\ 0 & 0 & \mathbf{K}_{\mathrm{a}} \end{bmatrix} - \omega^2 \begin{bmatrix} \mathbf{M}_{\mathrm{s3}} & 0 & 0 \\ 0 & \mathbf{M}_{\mathrm{s2}} & 0 \\ 0 & \rho_{\mathrm{a}} \mathbf{C}_{\mathrm{s2a}}^{\mathrm{T}} & \mathbf{M}_{\mathrm{a}} \end{bmatrix} \right]}_{\mathbf{A}} \underbrace{\begin{bmatrix} \mathbf{u}_{\mathrm{s3}} \\ \mathbf{u}_{\mathrm{s2}} \\ \mathbf{p} \end{bmatrix}}_{\mathbf{x}} \overset{\text{shared nodes}}{\cdots} = \underbrace{\begin{bmatrix} \mathbf{0} \\ \mathbf{f}_{\mathrm{ext}} \\ \mathbf{0} \end{bmatrix}}_{\mathbf{b}} \tag{2.63}$$

By Eq. (2.63), a sparse linear system of equations is set up which is solved by direct or iterative approaches introduced in Sec. 2.5.

2.5 Solution of large sparse linear systems

The system matrix $\mathbf{A} = \mathbf{K} - \omega^2\mathbf{M}$ in Eq. (2.64) is frequency-dependent and contains the element matrices in Ω_{s3}, Ω_{s2}, Ω_a and their couplings. The discretisation by elements yields the typical sparse band structure of $\mathbf{A}$. $\mathbf{x}$ is the general solution vector containing $\mathbf{u}_{s3}$, $\mathbf{u}_{s2}$ and $\mathbf{p}$ according to the domains while $\mathbf{b}$ contains pressure loads on Ω_{s2}. Solution algorithms for such linear systems can be divided into direct and iterative solution methods [110].

$$\mathbf{A}\mathbf{x} = \mathbf{b} \tag{2.64}$$

Direct solver Direct solution methods generate a lower triangular matrix $\mathbf{L}$ and an upper triangular matrix $\mathbf{U}$ according to Eq. (2.65). This LU factorisation consists of Gaussian elimination steps [87].

$$\mathbf{A} = \mathbf{L}\mathbf{U} \tag{2.65}$$

Modern methods take advantage of the FE system's typical sparsity in order to obtain the factorisation more efficiently compared to $n-1$ elimination steps on the full matrix. Within an upstream analysis step, mainly a symbolic factorization is conducted in order to obtain the resulting fill-in during the actual elimination steps. The fill-in describes additional non-zero entries of $\mathbf{L}$ and $\mathbf{U}$ compared to $\mathbf{A}$ [87]. A reduction of the fill-in by the application of reordering schemes is a crucial step in order to reduce the memory and time effort for direct solutions [107]. Time reduction is mainly achieved by an improved parallelisation of the problem due to renumbering [66]. By use of an optimised elimination tree, system dependencies are considered through which independent eliminations are possible. This way, a parallel implementation is realised [107, 87], which is essential for the solution of large vibro-acoustic systems like aircraft. Within this thesis, the MUMPS (MUltifrontal Massively Parallel sparse direct Solver) package is applied, which implements the multifrontal method and supports numerous reordering schemes [107, 116].
For an exemplary vibro-acoustic system with approximately 100 k dofs, the computational costs of direct solvers are studied. The system is shown in Fig. 2.6 and comprises an aluminium plate domain Ω_{s2} (dimensions $0.63 \times 0.4\,\mathrm{m}^2$, thickness $t = 4\,\mathrm{mm}$) strongly coupled to an air-filled 3D acoustic domain Ω_a (dimensions $0.63 \times 0.4 \times 0.33\,\mathrm{m}^3$). The two domains are chosen as these are assumed to be dominated for the aircraft model. Especially, the interaction of Ω_{s2} and Ω_a should be put

into focus here. The mesh is chosen according to approx. 20 nodes per bending wave length in Ω_{s2} and a point force is applied at the plate's corner. The bending wave length $\lambda_b(f)$ is approximated according to Eq. (2.66) for an infinite homogeneous flat plate [94]. In the equation, B is the bending stiffness and ρ is the density.

$$\lambda_b(\omega) = \frac{2\pi}{\sqrt{\omega}} \sqrt[4]{\frac{B}{\rho t}} \tag{2.66}$$

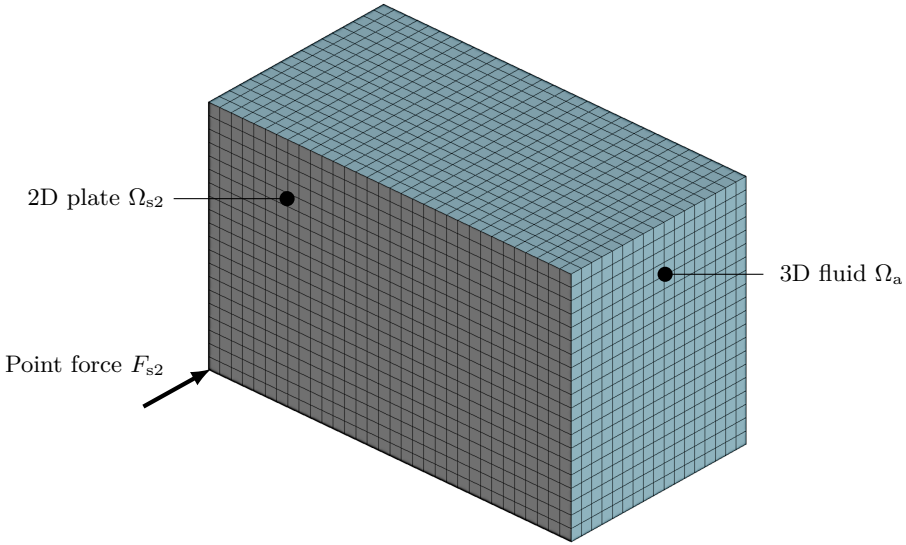

Figure 2.6: Examplary vibroacoustic system comprising a plate Ω_{s2} and fluid domain Ω_a applied for preliminary solver studies

The resulting times and memory usage for different commonly used reordering schemes are given in Tab. 2.2. The nested dissection reordering scheme yields the lowest memory usage and the second lowest computational time. Nested dissection subdivides the graph (connectivity of elements) by so called separators into smaller domains, which do not induce fill-in to other subdomains [107]. AMF (Approximate Minimum Fill) even yields a faster solution while AMD (Approximate minimum degree) is not competitive in this scenario. According to [69], METIS produces well-balanced elimination trees and therefore yields better performances in the parallel factorisation compared to AMD and AMF. METIS or its parallel implementation PARMETIS is preferred in the following settings.

By sparse direct methods for 3D problems, the numerical factorisation requires $\mathcal{O}(n^2)$ operations, while the memory effort is of $\mathcal{O}(n^{4/3})$ [87]. n symbolises the number of

Table 2.2: Maximum memory usage and total solution time (incl. i/o, reordering, analysis, factorisation and solution) for the 100 k plate-acoustic system for different reordering schemes within MUMPS (direct solver)[5]

Reordering scheme	T [s]	M [GB]
AMD	11.4	5.7
QAMD	11.4	5.7
AMF	5.3	3.3
Nested dissection (METIS)	6.0	2.5
Nested dissection (PARMETIS)	6.0	2.7

unknowns. Scaling the results of Tab. 2.2 to a similar plate-acoustic system with 10 mio dof, the required memory comprises approximately 1160 GB. The order of magnitude of several 10 mio dof can be expected for large aircraft systems, which may come up against the available system limits (even by using MPI over several nodes). The out-of-core factorisation of MUMPS may partly overcome this issue for the price of longer solution times [116].

After the numerical factorisation, $\mathbf{L}$ and $\mathbf{U}$ are applied in a forward and backward substitution, respectively, in order to receive the results [87]. This process needs $\mathcal{O}(n^{4/3})$ operations [87], which shows that the numerical factorisation phase is the decisive step in direct solutions. In addition, having obtained $\mathbf{L}$ and $\mathbf{U}$ once, many different right hand sides $\mathbf{b}$ can be considered in the solution phase [85].

Iterative solver Iterative methods converge to the solution by testing a sequence of approximate solutions $\mathbf{x}_k$ ($k \in \mathbb{N}$) starting with a chosen initial guess $\mathbf{x}_0$ [85]. The iteration rules highly differ, which results in many possible algorithms. For vibro-acoustic systems, the selection can be (almost) limited to the generalized minimal residual procedure (GMRES), which is mainly due to the non-Hermitian system property [53, 54]. The quasi-minimal residual method (QMR) is one possible alternative, but instabilities during convergence can occur [54]. Therefore, the selection is limited to GMRES within this thesis. GMRES is a Krylov subspace projection method, which spans and increases the Krylov subspace $\mathcal{K}_m$ according to Eq. (2.67) by one dimension until a convergence criterion is fulfilled [146].

$$\mathcal{K}_m(\mathbf{A}, \mathbf{v}_i) \equiv \text{span}\{\mathbf{v}_1, \mathbf{A}\mathbf{v}_2, \mathbf{A}^2\mathbf{v}_3, \ldots, \mathbf{A}^{m-1}\mathbf{v}_m\} \tag{2.67}$$

$$\mathbf{v}_1 = \mathbf{r}_0/||\mathbf{r}_0||_2 \tag{2.68}$$

[5] system (used for entire section): fat node on phoenix cluster of TU Braunschweig, 2× INTEL Xeon E5-2640v4, 8× DDR4-2400 32GB; 2 intel mpi threads and symmetrically diagonally scaled within PETSC before solving.

The dimension of the subspace m must kept much smaller than the original system's size n in order to realise an efficient iterative method. $\mathbf{v}_1$ is obtained by the residual $\mathbf{r}_0 = \mathbf{A}\mathbf{x_0} - \mathbf{b}$ normalised by its Euclidean norm $||\mathbf{r}_0||_2$ under consideration of a start vector $\mathbf{x}_0$ [146, 147]. The residual is obtained at each step k and minimised by the least squares method. The subsequent basis vectors $\mathbf{v}_{i+1}$ are obtained by the Arnoldi method (modified Gram-Schmidt orthogonalization combined with a Krylov subspace) in order to receive orthogonality of the entire basis [23]. GMRES always converges (at least at $\mathbf{v}_m$ with $m = n$), but has to save all basis vectors and therefore requires a relatively large memory space compared to other iterative methods. A restart reduces the memory effort by defining a limit for the number of vectors m and of restarts [23].

As the residual is decreased, a decrease of the field errors follows, but directly assigning error bounds for acoustic values is not possible. Hence, preliminary studies for each novel problem are conducted in order to obtain reasonable thresholds for $||\mathbf{r}||_2$. In Fig. 2.7 (a), resulting mean squared pressure values are depicted for different convergence thresholds within GMRES. The 100 k dof plate-acoustic system introduced above is applied for the study. Decreasing $||\mathbf{r}||_2$ down to 1e-6 yields a mean field error less than 0.1 dB in Ω_a, which is acceptable in the frame of the application. The curves show exemplary, that no deviation compared to the direct solver is observable. The solution time is generally increasing with sharper tolerances as shown in Fig. 2.7 (b). In addition, an increase of the solution time with increasing frequency is visible. This observation can be attributed to the increasing complexity of the deflection shapes within the two domains. From approximately 500 Hz, the direct solver is faster for the plate-acoustic example. Concerning memory usage, GMRES only occupies 24 % of the memory for this use case. If memory usage is particularly important, which is highly expected for large-scale aircraft systems, the iterative solver represents a trade-off towards the direct solver.

The convergence rate of iterative methods is sensitive to the problem type itself and the related condition number κ of the system matrix $\mathbf{A}$ [54]. An essential technique is preconditioning in order to improve the robustness and the efficiency of iterative solvers. $\mathbf{A}$ and $\mathbf{b}$ are transformed by a preconditioning matrix $\mathbf{M}_\mathrm{pre}$ according to Eq. (2.69) (left preconditioner) [146]. The received solution $\mathbf{x}$ of the preconditioned system $\mathbf{M}_\mathrm{pre}^{-1}\mathbf{A}$ remains the same and the optimal preconditioner $\mathbf{M}_\mathrm{pre} = \mathbf{A}$ is obvious. For an advantageous application of a preconditioner, κ must be reduced significantly and the calculation of $\mathbf{M}_\mathrm{pre}^{-1}$ must be simple compared to the solution of the actual system [146].

$$\mathbf{M}_\mathrm{pre}^{-1}\mathbf{A}\mathbf{x} = \mathbf{M}_\mathrm{pre}^{-1}\mathbf{b} \tag{2.69}$$

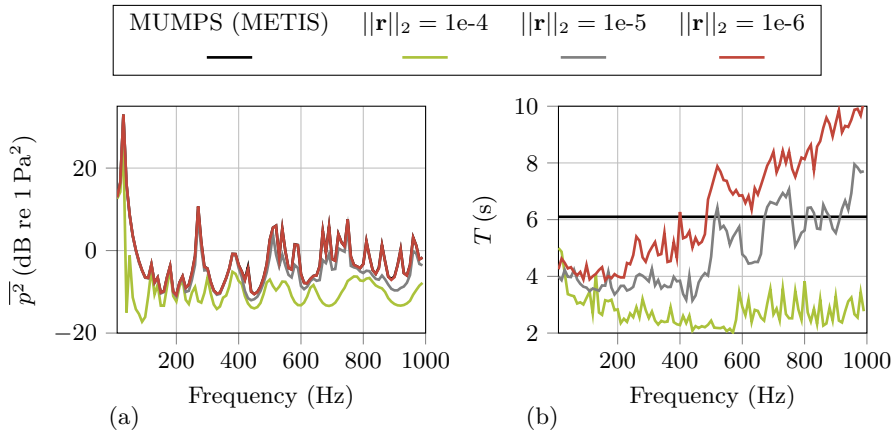

Figure 2.7: (a) Resulting mean squared pressure $\overline{p^2}$ and (b) total solution time T (incl. i/o and reordering) for the 100 k dof plate-acoustic system for different tolerances within GMRES[5,6]

A common technique to obtain $\mathbf{M}_{\text{pre}}^{-1}$ is the incomplete LU factorisation (ILU). Within the factorisation, non-zero fill elements are intentionally ignored and set to zero, which yields a preconditioning matrix $\mathbf{M}_{\text{pre}} = \mathbf{LU}$ [23]. For a full LU factorisation (within a direct solver), $\mathbf{M}_{\text{pre}}$ is optimal and yields the solution within one iteration. Incomplete LU variants are generally obtained faster and lower κ and thus the needed iterations m within GMRES. One option is an ILU(k), which considers non-zero entries defined by a level k. For $k = 0$, the non-zero pattern of $\mathbf{A}$ is reused for the factorisation [146]. Considering $k = 1$, one additional entry besides the existing pattern is accepted and referred to as level 1. Consequently, increasing k, additional memory and time is required and the quality of the preconditioner is expected to increase [146]. Similar to the direct solver, reordering schemes are highly important for ILU(k) techniques in order to spend the defined fill-in effectively [146]. The reverse Cuthill McKee ordering (RCM) is recommended as fast algorithm in the frame of an ILU [146] and therefore generally considered in the following applications of an ILU. However, ILU techniques show a poor parallel performance [23], which can be overcome by splitting the system.

As the discretised vibroacoustic system (Eq. (2.63)) has a natural block structure, domain decomposition approaches are highly suitable. Each domain Ω_{s3}, Ω_{s2} and Ω_{a} serve as one physical diagonal block, while the coupling entries are off-diagonal blocks [134]. As shown above, the structural and acoustic domains are highly heterogeneous. For this reason, the thesis concentrates on non-overlapping domain decomposition techniques [62], while individual monolithic preconditioners (e.g. ILU(0)) are applied

[6] preconditioner: Block Jacobi with 2 blocks [LU / ILU(0)] according to the physical domains

to each domain. Two basic domain decomposing preconditioners are block Jacobi and block Gauss Seidel. A block Jacobi preconditioner transfers the basic Jacobi preconditioner ($\mathbf{M}_{\mathrm{pre}} \coloneqq \mathrm{diag}(\mathbf{A})$) to blocks (domains) instead of diagonal entries [146]. The block Jacobi preconditioner for a system of two non-overlapping blocks $\mathbf{A}_1$ and $\mathbf{A}_2$ is the sum of two individual preconditioners $\mathbf{M}_{\mathrm{pre},1}$ and $\mathbf{M}_{\mathrm{pre},2}$ as given in Eq. (2.70) [166]. Two independent (and therefore parallelisable) approximations for both $\mathbf{M}_{\mathrm{pre},1}^{-1}$ and $\mathbf{M}_{\mathrm{pre},2}^{-1}$ are possible. Again, the ideal preconditioner for each block i is $\mathbf{A}_i^{-1}$, e.g. obtained by a full LU factorisation.

$$\mathbf{M}_{\mathrm{pre}} = \begin{bmatrix} \mathbf{M}_{\mathrm{pre},1} & 0 \\ 0 & \mathbf{M}_{\mathrm{pre},2} \end{bmatrix} \tag{2.70}$$

The combination of Eq. (2.70) with GMRES is referred to as block Jacobi preconditioned Krylov subspace method [166].

Recalling the plate-acoustic example problem, the plate domain $\Omega_{\mathrm{s}2}$ is much smaller (8 k dof) compared to the acoustic domain (93 k dof). Therefore, the use of a full LU factorisation as preconditioner is considered for $\Omega_{\mathrm{s}2}$, while an ILU of different levels k is considered for Ω_{a}. The relatively small size of the plate combined with a high condition number pushes for the application of LU in $\Omega_{\mathrm{s}2}$, compare e.g. [142]. The resulting solution times in Fig. 2.8 (b) show a huge benefit of the domain decomposition approach compared to a monolithic ILU(1) on one processor. For the three exemplary block Jacobi variants (LU+ILU(0), LU+ILU(1), LU+LU), the system is consequently physically distributed on the two available processors as recommended in [23]. This way, the LU factorisation on $\Omega_{\mathrm{s}2}$ and the ILU on Ω_{a} are performed in parallel. As described in [146], distributing the system matrix on several processors in a reasonable (physically motivated) way generally reduces the computational effort. This fact is reasoned by a decreased communication between processors. Besides, it is worth mentioning that the LU (performed by MUMPS) inherently delivers an initial solution vector $\mathbf{x}_{\mathrm{s}2}$ for the isolated plate.

Depicting some (possibly limiting and helpful) facts, the following observation are made for the example problem:

- The solving of the system preconditioned by a monolithic ILU(0) requires disproportionately more time (factor around 30) compared to the use of a monolithic ILU(1) and is therefore omitted.

- As $\mathbf{M}_{\mathrm{pre}}$ influences the residual, the comparison is not perfectly fair. An iterative adaptation of the tolerance is skipped in the frame of this theoretical part.

- The memory effort is lowest for the block Jacobi LU + ILU(0) and LU + ILU(1) variants (0.59 and 0.65 GB), while the monolithic ILU(1) requires 1.0 GB and the block Jacobi LU + LU variant 1.9 GB. Using two LU factorisations on the physical domains instead of one monolithic domain saves 24 % memory and requires around 33 % more time for the solution.

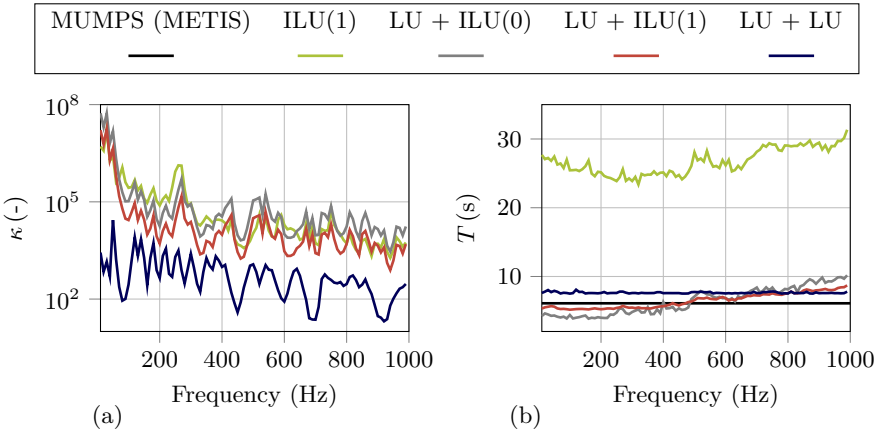

Figure 2.8: (a) Condition number κ and (b) total solution time T (incl. i/o and reordering) for the 100 k dof plate-acoustic system for monolithic and block Jacobi variants within GMRES

The according κ is depicted in dependency on frequency in Fig. 2.8 (a). A decreasing trend of κ is visible for all approaches. By choosing a potentially better (or more expensive) preconditioner, κ decreases. A remarkable fact is a similar condition number of the monolithic ILU(1) compared the the two split approaches considering an ILU(k) for Ω_a, while the total solution time T is much higher. Here, the split approaches are much faster due to its distribution on two processors and a long-lasting sequential monolithic ILU(1). In general, a strong correlation of κ and T cannot be expected as the time for obtaining $\mathbf{M}_{\text{pre}}$ is always included in T. Besides a preconditioning by $\mathbf{M}_{\text{pre}}$, κ is further improved by scaling the system matrix [54]. A preliminary scaling by the diagonal entries (similar to the basic Jacobi preconditioner [146]) is considered within all studies.

As mentioned above, block Gauss Seidel is another basic domain decomposition approach. Similar to Eq. (2.70), individual preconditioners are applied to each block. Within one iteration step using block Gauss Seidel, the domains are solved sequentially, which is the main difference to one iteration step using block Jacobi. After the application of $\mathbf{M}_{\text{pre},1}$, $\mathbf{A}_1$ is solved solely and the resulting $\mathbf{x}_1$ is considered as bound-

ary condition in the second domain by use of the coupling matrices [134]. In case of the exemplary plate-acoustic system, the plate's deflections are obtained without fluid domain first. In a second step, these results are applied as boundary condition to Ω_a and the fluid domain is solved for $\mathbf{p}$. This weakly coupled solution refers to one block Gauss Seidel iteration [134]. Performing several iterations yields equality of the interface forces between the split domains [134]. As the Gauss Seidel iteration is inherently sequential, each step must be parallelised itself. For instance, both the solution of $\Omega_{\mathrm{s}2}$ or Ω_a can be conducted using MUMPS.
In Fig. 2.9, the monolithic LU factorisation (MUMPS) is compared to 1 and 3 Gauss Seidel iterations for the 100 k plate-acoustic system. For block Gauss Seidel iterations, MUMPS is always applied for the solution of $\Omega_{\mathrm{s}2}$ while MUMPS and GMRES with ILU(0) are tested for Ω_a. The relative error in the acoustic domain according to Eq. (2.71) with respect to the direct solution $\mathbf{x}_\mathrm{dir}$ is calculated in dependency on frequency and depicted in Fig. 2.9 (a).

$$\epsilon_\mathrm{rel} = \frac{\max\left(\mathbf{x}_\mathrm{dir}, \mathbf{x}_\mathrm{iter}\right)}{\min\left(\mathbf{x}_\mathrm{dir}, \mathbf{x}_\mathrm{iter}\right)} - 1 \tag{2.71}$$

For both MUMPS + MUMPS and MUMPS + GMRES, the error decreases with frequency and drops below 1 dB above 750 Hz. Towards low frequencies, ϵ_rel increases as the coupling is stronger (compare Sections 2.2 and 2.3) and one Gauss Seidel solution inevitably differs from the strongly coupled solution. By conducting 2 more iterations, the error falls below 1 dB from around 50 Hz. Here, the MUMPS + MUMPS variant shows a higher convergence rate, which is dedicated to the precision of the direct solution in each domain. However, the block Gauss Seidel iteration is not appropriate for the lowest frequency range of the example system.
In Fig. 2.9 (b), the respective solution times are plotted. The block Gauss Seidel MUMPS + MUMPS variant requires nearly 8 s for all frequency steps, which is 25 % compared to the monolithic (and thus exact) direct solution. In contrast, the memory effort drops by 18 %. In general, the computational and the memory effort do not raise significantly in case of several iterations of this variant. As the LU matrices can be reused, the effort limits to the solution phase from the second Gauss Seidel step. For the tested variant using GMRES in the fluid domain, the time effort indeed increases significantly by each iteration. This fact is attributed to the inner iteration steps by GMRES required within each outer Gauss Seidel loop. The occupied memory falls down to 23 %. For the example system, Gauss Seidel is appropriate in order to receive a weakly coupled memory-saving solution, but shows higher computational times compared to the block Jacobi preconditioned GMRES.

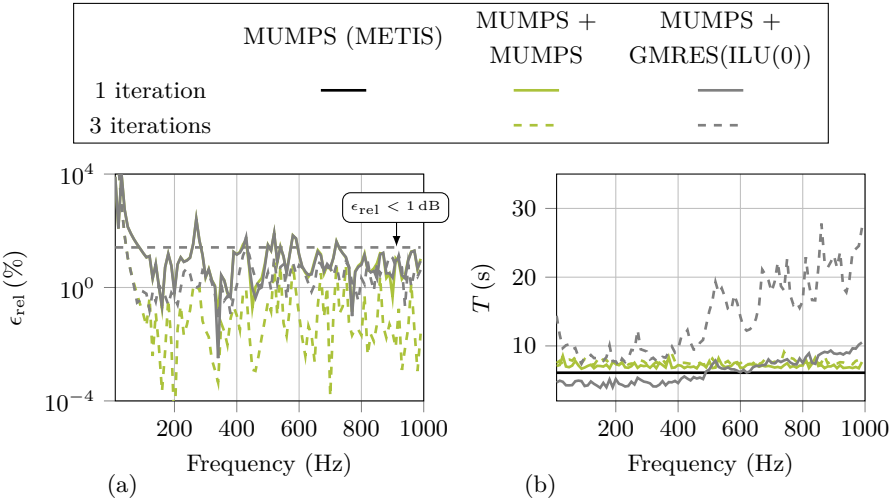

Figure 2.9: (a) Maximum rel. error ϵ_{rel} in Ω_{a} and (b) total solution time T (incl. i/o and reordering) for the 100 k dof plate-acoustic system for different block Gauss Seidel settings

Besides block Jacobian and Gauss Seidel, the following extensions are conceivable:

- overlapping blocks (e.g. additive Schwarz as extended block Jacobi or multiplicative Schwarz as extended Gauss Seidel [87]) for further substructuring of the individual domains [23],
- low-rank direct solvers (e.g. MUMPS with block-low rank (BLR)) as parallel preconditioner [107],
- multigrid methods [87] and
- recycling of information from the last frequency step(s) [105].

The latter is briefly described and tested in the following. In frequency domain calculation, the deflection shapes slightly change from one frequency step to another. This fact is rooted in a slight change of $\mathbf{A}$ due to a potentially small $\Delta\omega$ in Eq. (2.63), which indicates non-significant changes of a suitable preconditioner matrix $\mathbf{M}_{\mathrm{pre}}$ as well. Both, a previous solution $\mathbf{x}(\omega_{i-1})$ and preconditioner matrix $\mathbf{M}_{\mathrm{pre}}(\omega_{i-1})$ can be recycled at ω_i as proposed in [105].
In the frame of this theory section, the recycling of a preconditioner matrix is not studied. Results in [149] indicate a possible advantage of reusing a full LU factorisation over several frequency samples, but the performance reduces with increasing frequency. This is due to an increasing modal density, which is expected by an air-

craft system as well. Furthermore, the use of recycled information is limited in case of random input data as present in Ch. A.

The effect of reusing the previous solution $\mathbf{x}(\omega_{i-1})$ as initial guess at ω_i is depicted in Fig. 2.10 for the example system. For the block Jacobi LU + ILU(0) variant, recycling slightly decreases the solution time T by reducing the iteration steps of GMRES. In contrast, T increases for the LU + LU variant, which may be reasoned by the optimal preconditioner matrix yielding only around 7 to 9 GMRES iteration steps with an initial guess of zero anyway. The recycling of $\mathbf{x}(\omega_{i-1})$ is tested for one Gauss Seidel iteration as well, but a clear reduction of ϵ_{rel} cannot be observed for the plate-acoustic system.

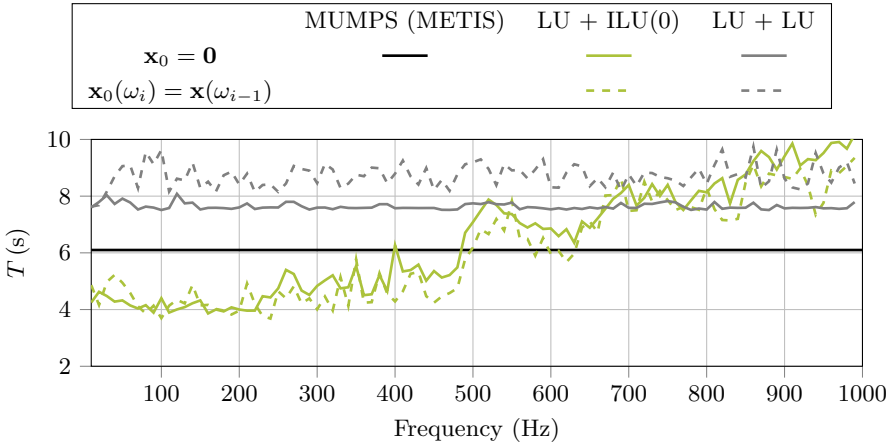

Figure 2.10: Total solution time T (incl. i/o and reordering) for the 100 k dof plate-acoustic system with and without recycling of $\mathbf{x}(\omega_{i-1})$ within GMRES

Concluding this section, direct and (block) preconditioned iterative methods are available and suitable for solving large sparse vibroacoustic systems. GMRES as a common Krylov subspace method occupying significantly less memory compared to the direct solver MUMPS, which is shown on a 100 k dof plate-acoustic system. For large aircraft systems, memory increases for GMRES with m modified Gram-Schmidt orthogonalisation steps as $\mathcal{O}(mn)$ [146]. Even for a small factor $\frac{m}{n} \approx 0.1\,\%$, as observed for the 100 k dof example at 1000 Hz, the memory usage of GMRES explodes with increasing dof. Scaling the example system to 10 mio dof, 6500 GB are necessary for the block Jacobi LU + ILU(1) variant. Therefore, a limitation of the Krylov space using a restarted version of GMRES is indispensable. As the direct solver requires around 1160GB for 10 mio dof, a restarted GMRES approach may overcome memory limits of the computing system. Concerning the solution time, the characteristics

are similar (iterative $\mathcal{O}(m^2 n)$ [146]; direct $\mathcal{O}(n^2)$ [87]). As the direct solver requires around 1 day for one frequency step of the 10 mio system, a restarted GMRES with limited m may be faster.
However, the actual memory and time effort are highly problem-dependent and must be re-investigated for the aircraft system. In addition, the structural and fluid domain blocks of large systems must be further split as an ILU is a sequential process. Otherwise, a negative effect on solution time is expected due to non existing scaling.
Having obtained the field $\mathbf{p}$ within an aircraft cabin by use of direct or iterative solver, an approximation of the sound pressure fluctuation at the potential passenger ear is available. Based on the complex amplitude describing the stationary oscillation, for instance, different aircraft configurations or different loads can be compared. In the end, the human perception of sound determines about a signal to be disturbing or comfortable. Therefore, the perception of sound is briefly described within the following section.

2.6 Perception of sound

The human perception of sound is defined by, among other things, the biological characteristics of the ear. The cochlea in the auditory canal transforms temporal state changes of the surrounding air into nerve signals. If the static pressure p_0 is superimposed by repeated changes, the human brain addresses the sense of hearing [164]. The repeated temporal change referred to as oscillation is available by the calculated sound pressure field $\mathbf{p}$ in the cabin fluid domain. A young human ear perceives oscillations in a frequency range between 16 and 20,000 Hz [164]. At 1000 Hz, the healthy human ear is able to perceive pressure amplitudes between 2e-5 and 20 Pa [94], which comprises more than 7 orders of magnitude. In this context, Weber's law is valid for the hearing sense. Transferred to a tone, Weber states by use of experiments, that the perception of sound is dependent on the change of the stimuli rather than the actual amplitude [61]. What follows is the Fechner-law giving the mathematical relation for the Weber-law [61]. By use of the Fechner law with slight acoustic-related adaptations, the component-wise absolute values of a sound pressure field $\mathbf{p}^{\mathrm{abs}}$ are generally presented as sound pressure levels (SPL) $L_{\mathbf{p}}$ in decibels (dB) as stated in Eq. (2.72) and already used in the previous sections [94].

$$L_{\mathbf{p}} = 20 \log_{10} \left(\frac{\mathbf{p}^{\mathrm{abs}}}{p_{\mathrm{ref}}} \right) \ \mathrm{dB} \tag{2.72}$$

The reference $p_0 = 2\text{e-}5\,\mathrm{Pa}$ refers to the above mentioned smallest audible amplitude at 1000 Hz [113] yielding a level of 0 dB. In Eq. (2.72), the factor of 20 is chosen in

order to yield a value of 1 dB as just barely audible amplitude change [113]. Concerning frequency, the perception of sound changes with frequency. E.g., towards high frequencies ($> 5\,\mathrm{kHz}$), the hearing ability generally decreases. In addition, the human ear is able to perceive a change of 3.6 Hz below 500 Hz and a change of 0.7 % above 500 Hz [164]. These facts are considered for the determination of necessary precisions in the frame of a model comparison or a residual threshold by iterative solvers. In a free field, phase shifts are hardly noticeable while those are well audible in cavities [164]. However, phases are not considered in level representations, but available by the numerical results.

For a rough consideration of the human perception of sound, a frequency-dependent weighting of the sound pressure level can be applied. The standardised and most commonly used A-weighting [164] is represented by Eq. (2.73) [6] and plotted in Fig. 2.11.

$$A(f) = 20\,\log_{10}\left(\frac{12194^2\ f^4}{(f^2+20.6^2)\ \sqrt{(f^2+107.7^2)\,(f^2+737.9^2)}\ (f^2+12194^2)}\right) + 2 \tag{2.73}$$

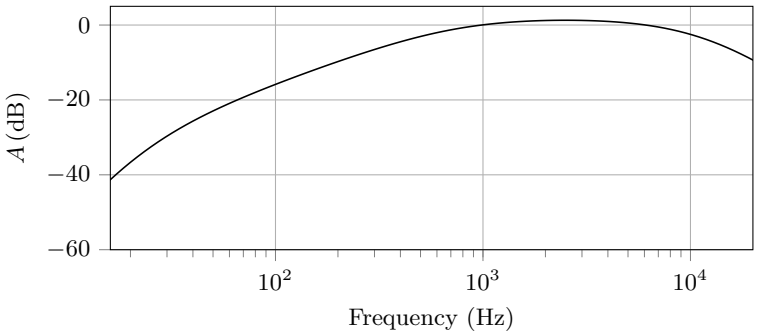

Figure 2.11: A-weighting A over frequency according to Eq. (2.73)

By this weighting, the physical oscillation levels are shifted in dependency on frequency to the supposedly perceived levels. Especially at frequencies below 1000 Hz, the human ear is much less sensitive compared to the range between 1000 and 3000 Hz. For cabin acoustic calculations, this simple correction may change the maximum SPL in aircraft cabins and hence, change the frequency range of interest. As representation of the inverse approximation of a curve of equal loudness (20 to 40 dB at 1000 Hz), the A-weighting is only a rough estimation of the human perception of sound [164]. A deeper investigation is out of scope of this thesis and attributed to the field of psychoacoustics.

For the addition of two incoherent sound pressure fields induced by different sources,

an addition of powers instead of field values is necessary. n incoherently induced pressure fields $\mathbf{p}_i$ are added according to Eq. (2.74) yielding the total SPL for incoherent sources [94]. For the level calculation of energy quantities, the factor 10 results from the basic rules for logarithms.

$$L_{\mathbf{p}} = 10 \log_{10} \left[\sum_{i=1}^{n} \left(\frac{\mathbf{p}_i^{\mathrm{abs}}}{p_{\mathrm{ref}}} \right)^2 \right] \ \mathrm{dB} \tag{2.74}$$

3 Related work

The implementation of reliable models for the numerical prediction of cabin acoustics and a reasonable interpretation of resulting frequency spectra require updated knowledge about investigations of aircraft passenger cabin noise. A suitable publication to start with is [161] by Wilby. The paper gives a review on aircraft cabin noise (sources, transmission paths, prediction methods) and covers the progress in 45 years before 1996. Wilby says that the introduction of new technologies (e.g. propulsion system) has lead to problems in interior acoustics. Therefore, more and more attention is paid to the prediction of cabin noise in order to avoid higher noise levels. Major noise sources are the power plant and the TBL [161] while the characteristic excitation of the power plant can be classified in jet engines and propeller aircraft. The interior noise of propeller aircraft is dominated by oscillations in air at the blade passing frequency and its harmonics [161]. The near field behaviour and mainly the phase between rotating propeller blades is highly important concerning cabin noise. The cabin fluid characteristics (e.g. temperature) is slightly influencing the SPL [161]. In opposite, jet noise and TBL noise introduce a broadband excitation on the aircraft's outer skin. In Fig. 3.1 (Source: [161, p. 552]), a measured vibrational response of a skin panel is shown for TBL excitation only and for both, TBL and jet noise excitation. The jet noise excitation is dominating the outer skin field vibrations in the low frequency range ($< 2000\,\mathrm{Hz}$) while at 500 to 1000 Hz the additional contribution by the engine jet is rather small. These results indicate the frequency-dependency of sources and the importance to investigate different sources and their contribution to the cabin acoustics.

In [49], Wilby further describes additional sources – besides TBL and jet excitation, fan noise contributes at low frequencies and low flight speed (e.g. start/landing) to the cabin acoustics. Furthermore, the structure-borne vibrational impact of the engines and internal noise sources emit sound into the cabin. For propeller aircraft, characteristic loadings at the blade passing frequency dominantly excite the structure [49]. Apart of induced airborne-sound forces on the outer skin near the propeller, structure-wake interactions induce vibrations at wings and stabilisers which contribute to the cabin acoustics [49].

In Sec. 3.1, relevant experimental studies from literature are summarised giving data

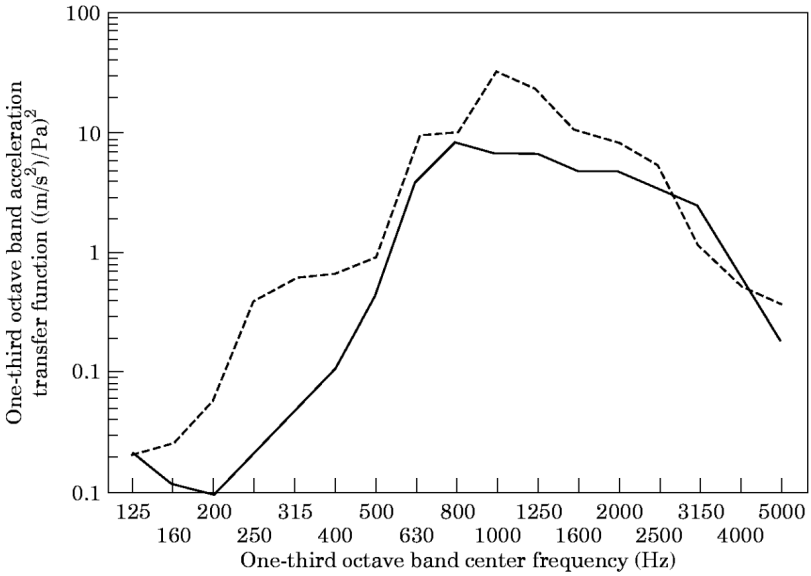

Figure 3.1: Vibrational response of an aircraft skin panel for — TBL excitation and - - - TBL + Jet excitation (Source: [161, p. 552])

on typical cabin noise spectra and relevant noise sources. Numerical investigations of aircraft structures are presented in Sec. 3.2 while detailed literature focusing on single parts (like e.g. glass wool) is introduced according to demand in the modelling sections of Ch. 4. The scientific contribution of the thesis at hand is described in Sec. 3.3.

3.1 Experimental studies of aircraft cabin noise

In-flight measurements of the SPL in an A321 cabin during two flights are conducted in [126]. Several positions are investigated – the results show around 4 dB higher noise levels at window seats compared to middle and aisle-seats. In addition, the SPL increases in the rear cabin. During cruise, SPLs spatially vary between 74 and 82 dB(A) while significant temporal variation is not measured in cruise. Maxima up to 85.5 dB(A) are observed during take-off [126].

In 2012, Pennig et al. publish, i.a., results of cabin noise assessments by 109 trial participants within a laboratory setup [133]. Different spectra have been recorded during real flights and played back within a mock-up of a Dornier Do 728 aircraft. For each spectrum, the noise level is varied as well in order to receive information on the separate effects by different spectra *and* noise levels on the passenger's comfort during a short-haul flight. It is reported that a lower SPL generally leads to more

comfort during the flight. The lowest test noise level is 66 dB(A) while the majority of the subjects accept cabin noise levels up to $70 - 73$ dB(A). Concerning the noise spectra, the recording in the front, middle and rear partition are distinguished in [133] as well. The noise in the front partition, for example, is frequently described as bright or shrill in comparison to the rear noise. According to the subjects in the study, an optimal cabin noise should be monotonous without prominent irregularities [133].

The noise sources beneath the TBL, in the jet and in the air conditioning system are investigated experimentally and ranked in [79]. Measurements are conducted at the outer skin and inside the cabin with distributed microphones in real flights of an A320 aircraft. For the TBL-induced noise, a high contribution is observed in a frequency range from 800 and 3000 Hz. With increasing flight speed, the impact of both sources put on weight. Concerning the spatial distribution, an increase in the back of the aircraft compared to measurements further to the front can be observed. In a flight level of FL $350 - 390$, jet noise and TBL-induced noise are quite similar. Cabin noise due to the air conditioning system is not that important compared to the other two sources [79].

The vibro-acoustic response of an A400M fuselage is experimentally investigated in [163]. A limit of around 140 Hz for a reasonable experimental modal analysis is identified. Based on this limit, a damping factor calculation by the input energy method is successfully applied up to 200 Hz and a robust correlation criterion based on an integrated (frequency band and skin panel) kinetic energy value is tested [163]. The A400M fuselage is further described in [93] besides a collection of state-of-the-art test stands for vibro-acoustic measurements. The test stands contain single panels, a wooden mock up and an aluminium cylinder while the paper focuses on experimental activities in active noise control (ANC) [93]. A fuselage section without trim is built up in the Acoustic Flight-LAB demonstrator in Hamburg The demonstrator comprises 17 frames (8.5 m) of a short-range aircraft and is made of aluminium. The major goal of the test stand is a validation of FE models up to 300 Hz on the basis of experimental data [162]. First experimental results are shown at few frequencies in [162] by use of $11,406$ measurement positions and 3 points excited by an electrodynamic shaker. Structural intensities (STI) are calculated bases on several assumptions in order to visualise the energy flow. Dominated energy paths cannot be identified but the suspension points are clearly visible as energy sinks [162].

In [99], the fact of a reduced sound absorption performance of glass wool with decreasing frequency is stressed. A plate-type acoustic metamaterial embedded in aircraft grade glass wool is tested in order to improve the transmission loss (TL) of a 40 mm setup below 1000 Hz. The results show an increased TL (better than mass law) but a

high dependency on the position of the metamaterial in the glass wool layer [99]. This again indicates a need for complex models in which such investigations are possible.

3.2 Numerical analysis of aircraft cabin noise

As indicated before, a clear focus is laid on wave-resolving methods, while the FEM is applied within this work. For the literatur study, the BEM is included as alternative wave-resolving approach and the statistical energy analysis (SEA) is partly considered to briefly depict the non-wave-resolving alternative.

In 1992, Roozen solves an aircraft fuselage section by the FEM [143]. The degrees of freedom are limited to around 20,000 and the frequency band to a maximum of 120 Hz. Among other things, relevant effects of the strong coupling between internal fluid and fuselage structure are demonstrated and modal reduction techniques are successfully studied. The use of wave-resolving aircraft models is emphasised and shown on the example of structural modifications (e.g. de-tuning by a changed frame thickness) leading to reduced SPLs. The outlook of his thesis [143] underlines the consideration of doors, windows, trim panels and interior parts.

In [34], a cylindrical shell structure without stiffeners is investigated considering porous and visco-elastic materials as damping measure. The model is solved by the FEM (NASTRAN) using a modal approach whereby a good agreement to measurements can be observed. The importance of the structure-fluid coupling effects is stressed in the paper as modes within the acoustic cavity at appreciably higher eigenfrequencies than the maximum investigated frequency must be taken into account [34]. These results underline the fact that a direct solution is more suitable instead of considering that many modes in modal space. Furthermore, frequency-dependency is a problem as indicated in [130] as well which makes a direct solution preferable.

Cylindrical structures with frames and stringers are investigated in [39] by use of FE models and compared to experiments up to 1 kHz. Similar comparisons are conducted in [76] resulting in a good agreement up to 200 Hz. In both references [39, 76], the insulation and the cabin side-wall panels have been neglected in order to focus the investigation on a validation of the primary structure.

A hybrid FEM/SEA approach is applied in [124] on the example of a stiffened outer skin panel under diffuse field and TBL loading. The TL in third octave bands is computed by a periodic approach shown in [47] in which the FE structure is solved with appropriate boundary conditions and serve as input for a periodic SEA formulation. The periodic approach is applicable for early design phases in order to generally rate different design concepts – in [124], the effect of frame spacings are investigated exemplary. The contribution [95] also aims for an acoustic design within the preliminary

design phases by use of models integrated in a Design & Engineering Engine (DEE). A stiffened test cylinder is solved by NASTRAN and the use of automatised scripts in order to study the vibrations of different fuselage designs [95].

In [67], the TL of a fuselage section is calculated based on the FEM. The results show a good agreement in frequency ranges above 400 Hz. The limp model for glass wool is discussed in detail and efficient solution approaches are given. Firstly, non-coincident meshes are used as the structural and fluid domain have different wave lengths. For this purpose, an automatised interface generation is implemented. Secondly, the modal basis in the fluid and structural domains are calculated separately by use of an iterative solver. The iterative solver works well for the fluid part (Helmholtz equation) but has strong problems solving the structural part. Shell elements are used here causing high condition numbers [67].

A three-step approach for the numerical prediction of cabin SPLs is presented in [8]. First, pressure fluctuations beneath the TBL and by the engines are considered by semi-empirical models (Goody and Corcos) and accumulated plane waves with certain angles of incidence, respectively. Second, the excitations are applied on a FE model of a flat fuselage panel. Finally, the response of the panel serve as excitation of the internal fluid in which the SPL is simulated using a ray-tracing method. The flat panels are repeated and arranged in order to enclose the passenger cavity [8]. Ray-Tracing is also applied in [136] on generic test rooms with aircraft cabin materials. An acceptable agreement to measurements can be observed above 1000 Hz.

An analytical approach for cabin noise predictions of a blended wing body configuration under TBL loading is shown in [139]. The model calculates the SPL at different seat positions in dependency on a certain number of vibrating panels. It considers the panels of the ceiling and the cabin fluid in an analytical modal solution space [139].

The TL of an aircraft double wall panel is calculated in [112] by use of the FEM. The outer skin including stiffeners, glass wool insulation and the trim panel are considered in a fully coupled system. Statistically distributed point sound sources are applied to generate a diffuse field excitation. This method, shown in detail in [131], enables TL-calculations by the FEM with one frequency response only instead of a consideration of many angles of sound incidence. The TL-results in [112] agree fairly well (deviation < 5 dB) in a frequency range between 200 and 1000 Hz compared to measurements [112].

In order to reduce computational costs and uncertainties by manufacturing, a hybrid FEM/SEA implementation is proposed in [132]. An FE solution of a generic aircraft model under point force load is varied in its frame dimensions and compared to a SEA solution. The resulting mean SPL in third octave bands between 300 and 700 Hz agree

well [132].

In [125], three different wave-based methods (Transfer matrix method (TMM), periodic cell method, waveguide finite elements) are applied for the TL calculation of a double wall and a sandwich panel. The first two methods are fast in application and help during design phases on the basis of parameter studies. The waveguide finite elements are computationally more expensive but seems to have a high potential to assess waveguiding structures acoustically [125]. All methods are faster alternatives to classical FE solutions, but come along with specific inflexibilities (e.g. periodicity) [125]. The TMM is also used in [155] from 2016 within an internal toolbox by Airbus in order to optimize the application of insulation material. The method is applied to a side-wall section to increase the TL by considering constraints as weight, costs and available space. The insulation material (glass wool) is considered as limp model using six material parameters.

In [114], a recent status by Airbus is shown solving the entire cabin fluid, but only the back of the structural aircraft part. A solution in frequency domain at harmonics of the blade passing frequency is presented in order to investigate different configurations in early design phases. However, a wave-based approach for full aircraft models still results in massive computational cost [114]. Optimisation in early design is also aimed for in [151], in which a 1-frame section of the A350 fuselage made of CFRP is optimised with regard to the equivalent radiated sound power (ERP). As outlook, the authors indicate an improvement of the studies by more complex models including seats, passengers and trim panels. This way, the SPL at the passenger ears can be considered as continues frequency response instead of mean values in time and space [151].

In [51], the TL of an aircraft fuselage section is numerically calculated using the FEM in comparison with the statistical energy analysis. The model (shown in Fig. 3.2; Source: [51, p. 6106]) comprises the outer skin, the insulation and the side-wall panel and is solved by NASTRAN. Results by measurements, SEA and FEM are comparable, but show significant differences above 400 Hz which is attributed to the isolation in the test stand. In addition, a weakly coupled simplified aluminium double wall is compared to the strongly coupled solution showing a non-significant difference in the sound transmission above 500 Hz [51]. In order to save computational costs, this approach might be reasonable for a full fuselage as well.

In [50], a hybrid approach for a fuselage model (14 m long King Air 350 turboprop) is shown using the FEM for the structure and the BEM for the cabin fluid. A NASTRAN FE model of the structure is imported to SYSNOISE in which the BE model of the cavity is added in order to compute a strongly coupled solution. On the basis of a fan noise excitation received by the Ffowcs Williams-Hawkings equation,

Figure 3.2: Detailed FE model of a realistic fuselage section including the outer skin, the insulation and inner side-wall panels (Source: [51, p. 6106])[7]

the effects of synchrophasing and absorptive noise treatments (vibration absorbers tuned to the harmonics) on cabin noise are studied. The BEM approach is also applied in [104] to the cabin fluid of an aircraft section. The investigation focuses on a new nanofiber textile for damping and a new seat shape for lower SPLs in the cabin. The numerical model is compared to experiments showing differences up to 10 dB above 100 Hz. Below 100 Hz, higher differences are observed which is mainly attributed to the neglected influence of the surrounding structure [104]. The need for a consideration of adjacent structure in the cabin is also stressed in [49]. Besides, the paper [104] documents frequency-dependent absorption coefficients of the floor, seats and panels.

A comparison of wave-resolving (deterministic) methods like the FEM and statistical approaches like the SEA is shown in [130]. For low frequencies, deterministic approaches are appropriate while in high frequency ranges, statistics shall be considered. The Helmholtz number He in Eq. 3.1 represents the ratio between the geometric dimension L and the wave length λ. This value can be used to choose an appropriate solution method [130]. The suggestion is a Helmholtz number of 10 in order to change over to stochastic methods as the system's response is highly sensitive to small modifications.

[7] The author thanks Koen De Langhe for the permission to reuse this figure.

$$\mathrm{He} = \frac{L}{\lambda} \tag{3.1}$$

In addition, Peiffer (Airbus Group Innovations) shows an overview of a simulation strategy for vibro-acoustic aircraft models in [130] which is shown here in Fig. 3.3 (Source: [130, p. 33]). In general, between 200 and 400 Hz, a hybrid FEM/SEA solution is proposed for fuselage sections. While at lower frequencies the FEM is applied, SEA models are used in higher frequency ranges. A full aircraft model is only present in low frequency regions. According to [130], some typical deficiencies of this simulation chain are the modal coupling for large size aircraft, frequency-dependent material parameters and the application of loads. Some of these deficiencies are seen as challenges within the scope of this thesis as explained in the following section.

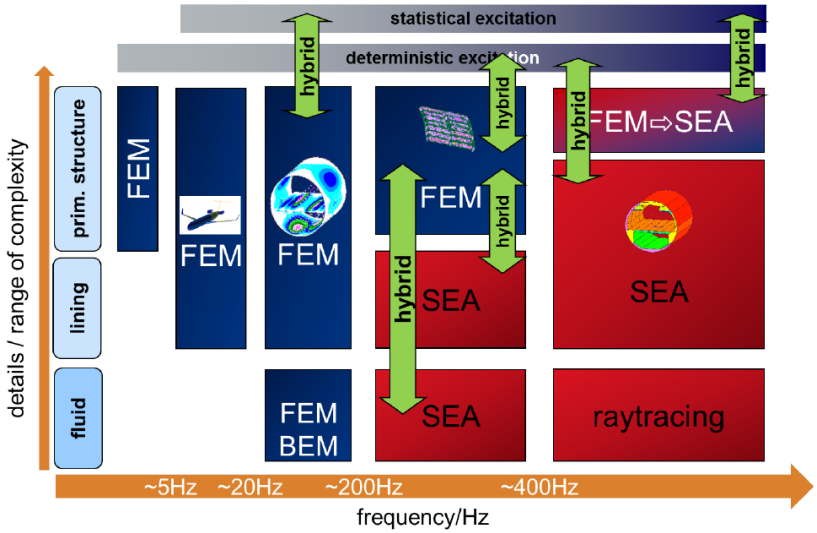

Figure 3.3: Simulation strategy for aircraft structures (Source: [130, p. 33])[8]

[8] The author thanks Alexander Peiffer for the permission to reuse this figure.

3.3 Contribution of this thesis

In general, the need for detailed models for cabin sound predictions is stressed in many sources like, e.g., in [104, 158]. To the knowledge of the author, there is no literature source documenting a comprehensive procedure of a full wave-resolving aircraft model including structural and fluid domains. The importance of cabin sound predictions for future aircraft and the need for research are again underlined in [123] (2016) with the aim to derive design recommendations for, e.g., engines in order to reduce cabin sound pressure levels in early design phases. For this thesis, a stochastic transition, as given by the Helmholtz number He, is (temporary) neglected and wave-resolving models are focused instead. The major challenge is the combination of a high model complexity in combination with the computational effort for the solution. If the model complexity can be handled and a solution up to a certain frequency without significant error is possible, the potential of a wave-resolving system is assumed to be high if uncertainties are taken into account.

The innovative core of this thesis is a comprehensive numerical simulation of the sound field in a passenger cabin of a typical aircraft fuselage with both, views on the modelling aspects and efficient solving approaches (Ch. 4 and 5). The mechanical models of all relevant aircraft parts are characterised using experimental data, which is obtained within this thesis as well. The considered aircraft parts are chosen in a way that the modelling aspects and solving approaches are entirely transferable to a specific aircraft configuration in industry. For the solving process of the discretised aircraft fuselage, a flow chart is developed in order to identify an efficient approach to solve fuselage models.

In addition, two application cases for a future aircraft concept are shown in Ch. 6. Firstly, a simulation chain is established in cooperation with scientists from DLR Braunschweig in the frame of the CRC 880. Using an interface implemented in this thesis, pressure fluctuations from realistic jet excitations are considered as input for the aircraft fuselage model. The chain yields the cabin SPLs due to jet excitations of a novel ultra-high-bypass ratio engine (UHBR) compared to a conventional engine. This comparison has not been conducted before and is also published by the author in [29]. Secondly, an extension of the simulation chain to a consideration of pressure fluctuations beneath the TBL is implemented in this thesis. Existing semi-empirical models are transferred for an application into FE models. The resulting SPL of a full aircraft due to TBL sources in comparison to engine jet sources represents new insights [30]. Summarising, the present thesis increases the frequency limits for the wave-resolving solution of full fuselage models and underlines the need for such models by the application of complex loads and sound reduction measures.

4 Characterisation of aircraft components

A wave-resolving aircraft fuselage model comprises the consideration of many aircraft parts. Inaccurate modelling of single parts may result in relevant error propagation into the finally predicted SPLs in the cabin. The methodology applied in this thesis is *bottom-up*, as characterisation of single typical aircraft parts is provided in the following sections. A validation of the finally predicted SPL in the cabin of the full aircraft is not realised as no experiments in a real aircraft are conducted in the frame of this thesis, or rather, the CRC 880 project.

The aim of this thesis is *not* a model for a specific real aircraft. Rather, with some orientation to the CRC 880 research aircraft, typically occurring aircraft parts, which are expected to have an influence on the vibroacoustic response, are considered in order to identify crucial modelling aspects. The selection of components is motivated by the TL problem through a double wall (see Sec. 2.1), which is similar to a double-walled fuselage:

- The airframe (Sec. 4.1) comprises stiffeners and outer skin fields, which are directly excited by fluid loadings (compare excited wall in Fig. 2.3).
- The insulation (Sec. 4.2) serves as gap within the TL problem and significantly affects the sound transmission
- The interior lining (Sec. 4.3) represents the second, radiating wall of the TL problem.
- The passenger cabin (Sec. 4.4) substitutes the free field radiation of the radiating wall. Instead, the closed domain is coupled to the interior lining, which finally increases the complexity of the entire problem.

Major differences between the TL problem and the aircraft fuselage are the closed cavity instead of a free field as well as the curvature of the tube. Nevertheless, holding on to this comparison shall remain to serve as motivation. In each of these 4 sections, a vibroacoustic characterisation is conducted by use of experiments. One challenge is finding an experimental setup which ensures a focused study of one domain only, excluding most of the possible side effects or boundary influences. On the basis of the experimental results, several modelling approaches are discussed for each aircraft part,

resulting in recommendations for the full aircraft model, which is finally assembled in Sec. 4.5.

4.1 Airframe

According to the sound transmission through double-walls, the outer skin is the equivalent to the excited wall. The airframe (outer skin, circular frames, stringers, etc.) is directly affected by pressure fluctuations beneath the turbulent boundary layer or sound radiated by the jet stream. As the input energy to the outer skin is expected to be crucial for the resulting cabin SPL, an appropriate modelling of the waves within the airframe is essential. In Ch. 6, pressure excitations by a turbulent boundary layer and an engine jet are investigated as examples. Frames and stringers are expected to influence the vibrations of the outer skin significantly and to transmit structure-borne sound into the interior lining directly.
Exemplary, a typical (metallic) airframe is shown in Fig. 4.1. Given by the preliminary design data within the CRC 880, for this thesis, the aim is an appropriate model for a CFRP airframe which can be transferred to many different aircraft configurations (e.g. with different thickness, fibres or layer stacks). For instance, the airframe of the Airbus A350 is made of CFRP while as much fuselage sections as possible are composed within one component [122]. For lightning protection, a metallic mesh, which is not considered here, is included in the layer stack [122] . For both civil aircraft, the A350 and also the Boeing 787, the airframes are made of around 50 % CFRP while the tendency is increasing towards higher percentages of CFRP use in transport aircraft [159].
In principle, the structure of a CFRP airframe is similar to a metallic one, while less joints are required due to a more monolithic design [122, 121]. Frames and stringers are integrated, as for instance realised in the "black fuselage" concept [75]. Hence, from the mechanical modelling point of view, a domain Ω_s is assumed for an airframe section and joining technologies are neglected within the scope of this thesis. Ω_s describes a flat or curved structure composed of several (CFRP) layers bearing bending and in-plane forces.

Experiment

For the characterisation process, the experimentally investigated dynamic response of a CFRP structure serves as basis. Rectangular curved CFRP plates are manufactured according to the design data in Tab. 4.1. The radius of the plates is half the radius compared to the available aircraft design data (Sec. 2.1). This way, a significant effect due to the curvature is ensured in the experiments. The layer stack consists

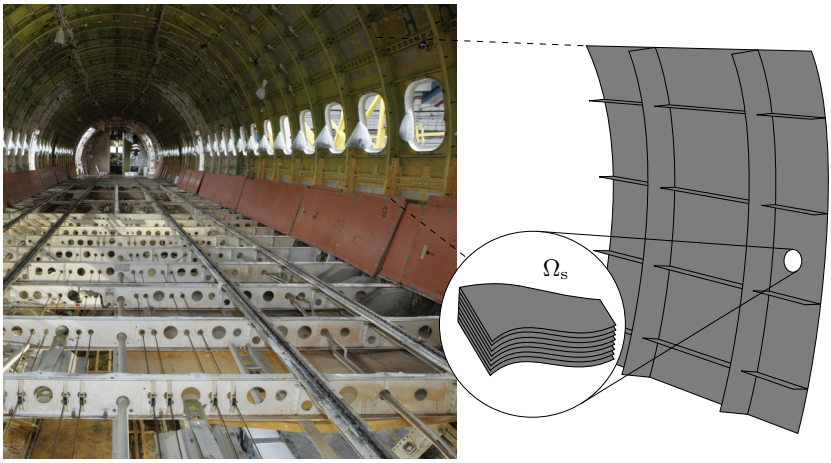

(a) (b)

Figure 4.1: (a) Typical primary structure of a commercial passenger aircraft (Source: Chalabala/istockphoto.com) and (b) generalised problem for the generic aircraft model

of uni-directional layers and the thickness of all layers is identical. Three plates of different total thickness with high occurrence in the aircraft design data are selected. Due to manufacturing tolerances, each plate shows a slight ripple on one side which leads to a local variability in the thickness. Hence, according to the mesh shown in Fig. 4.2 (top right), in Tab. 4.1, the mean value of the thickness measured at 28 marginal positions is given together with the standard deviation. Furthermore, each curved plate is manufactured two times in order to investigate the deviation between two nominally identical plates.

Table 4.1: Investigated curved CFRP plates.

Plate	Length a (m)	Width b (m)	Thickness t (mm)	Stack	Radius R (m)	Density ρ_s (kg/m^3)
1	0.402	0.298	3.89 ($\pm$0.15)	$[0/90]_{5s}$	0.85	1523.6
2	0.401	0.296	4.14 ($\pm$0.10)	$[0/90]_{5s}$	0.85	1444.8
3	0.400	0.298	3.13 ($\pm$0.18)	$[0/90]_{4s}$	0.85	1527.8
4	0.402	0.298	3.20 ($\pm$0.11)	$[0/90]_{4s}$	0.85	1477.0
5	0.401	0.300	1.99 ($\pm$0.09)	$\left[[0/90]_2/0\right]_s$	0.85	1545.5
6	0.400	0.301	1.95 ($\pm$0.08)	$\left[[0/90]_2/0\right]_s$	0.85	1575.9

In Fig. 4.2, the experimental setup is shown on the example of plate 5. In order to minimise influences by the test stand, the plates are suspended by thin nylon

threads. A point excitation is realised by an electrodynamic shaker (The Modal Shop SmartShaker) with a force sensor (PCB 208C01, weight 0.024 kg) at the tip. The velocity of the face sheet is measured using a laser scanning vibrometer (Polytec PSV-400) at the positions shown in Fig. 4.2 at the top right. The measuring points are chosen in an equidistant grid and serve as locations for the model comparison. The vibrometer is placed in the focus of the curved plates in order to measure the orthonormal velocity at all points. For this purpose, the angle correction by the system is disabled in x-direction and enabled in y-direction. The green spots are colourings of the mould used in the manufacturing process. In Tab. 4.2, data on the experimental setting is collected.

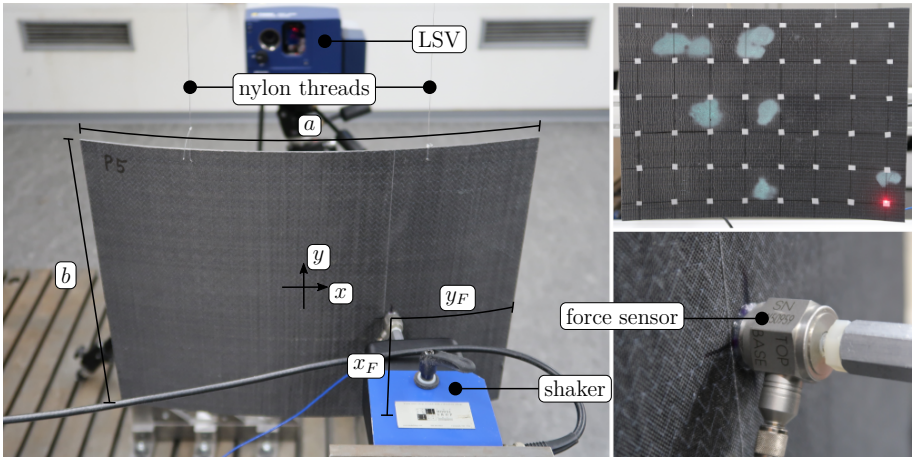

Figure 4.2: Experimental setup of the investigated curved CFRP plates

Table 4.2: Settings for the experimental investigation on curved CFRP plates.

Quantity	Variable	Value	Unit
Sampling rate	f_s	3200	Hz
Frequency lines	n_{lines}	3200	–
Averages	n_{avg}	6	–
Number of measuring points (front)	n_{points}	48	–
Force position (backside)	$[x_F, y_F]$	$[0.125, 0.125]$	m
Temperature	T	17	°C
Relative humidity	RH	38	%

By the experiments, the frequency response of the force between the shaker tip and the plates and the frequency response of the velocity at 48 points on the plate's surface are given. Both, force and velocity, are measured in orthonormal direction

to the plate's surface. In Fig. 4.3, the mean squared admittance $\overline{h^2}(f)$ according to Eq. (4.1) is plotted for plates 1 and 2 with thickness $t = 4\,\mathrm{mm}$.

$$\overline{h^2}(f) = \frac{1}{n_{\mathrm{points}}} \sum_{i=1}^{n_{\mathrm{points}}} |\underline{h}_i(f)|^2 \tag{4.1}$$

Two nominally identical plates are compared. *Nominally identical* means that the same thickness has been aimed for in the manufacturing process. Up to 500 Hz, a good agreement can be observed between the dynamic responses. With increasing frequency, differences get higher as the wave lengths are smaller and manufacturing tolerances are more relevant to the dynamic response.

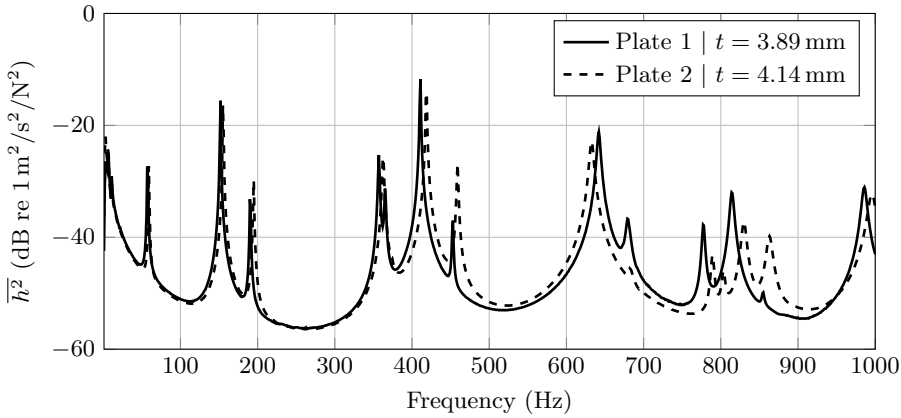

Figure 4.3: Experimental results for the mean squared admittance $\overline{h^2}(f)$ of 4 mm curved CFRP plates

In Fig. 4.4 and 4.5, the mean squared admittance for plates 3 to 6 is shown. Similar to the two plates with $t = 4\,\mathrm{mm}$, deviations can be observed in the upper half of the frequency range for the thinner plates as well. With a smaller thickness, even higher deviations seem to occur as the modal density is higher. For smaller wave-lengths, similar manufacturing tolerances have a higher impact on the dynamics. This impact is important with respect to the model assessment.

As described before, a slight ripple leads to a variability in thickness of all plates. On material level, further manufacturing tolerances are expected which may lead to the visible differences between two responses. Consequently, each manufactured plate will lead to different optimal modelling parameters. However, the reproducibility of a measurement of the same plate is reliable in comparison to the observed differences between two different but nominally identical plates. A description of the reproducibility is given in the appendix, Sec. A. On this basis, the different responses can

be mainly attributed to manufacturing tolerances.

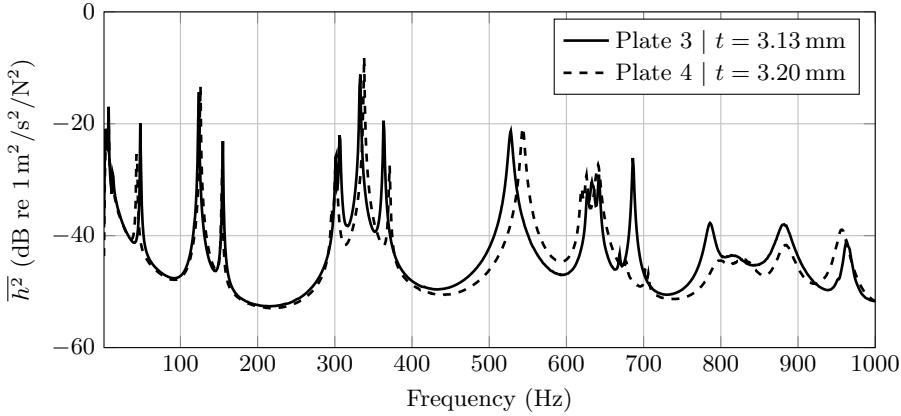

Figure 4.4: Experimental results for the mean squared admittance $\overline{h^2}(f)$ of 3 mm curved CFRP plates

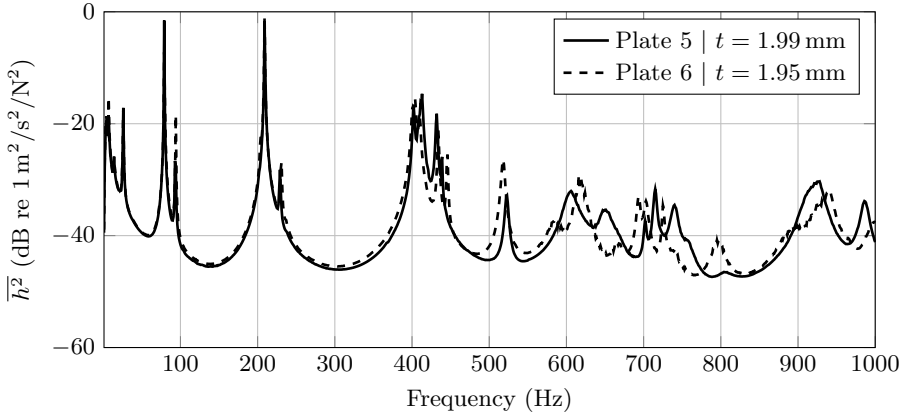

Figure 4.5: Experimental results for the mean squared admittance $\overline{h^2}(f)$ of 2 mm curved CFRP plates

As the model for the curved CFRP plates is assumed to be linear, linearity is demonstrated on the example of the thinnest plate 6. An explanation and the dynamic response can be found in Sec. A. On this basis, linearity is proven for the experiments conducted. Of course, this assumption holds true for the investigated curved CFRP plates and is not shown for the excitation of an aircraft skin in-flight. Investigations on non-linearities are out of the scope for this thesis and must be conducted in future studies.

Within the frequency range of interest, clearly separated resonances are given. At

these frequencies, the half band method according to [118] is applied in order to receive the damping loss factor $\eta(f)$. $\eta(f)$ is calculated by an automatised script for the measured mean squared admittance, respectively. In Fig. 4.6, all received values are plotted. The values of $\eta(f)$ are slightly below 1 % over a wide frequency range. In the low frequency range, the values increase significantly while a slight increase can be observed to higher frequencies. The overall picture seems to follow a trend of a classical Rayleigh damping curve of the basic form $\eta(f) = \frac{a}{f} + bf$. For this form, a fitting curve (least squares method) is given for each nominal thickness. The parameters are shown in Tab. 4.3.

Table 4.3: Curve fitting parameters for the damping loss factor $\eta(f)$ of the CFRP plate in dependency on thickness

Quantity	Variable	Value Plate 1/2	Value Plate 3/4	Value Plate 5/6	Unit
Curve fitting parameter	a	1.209	1.155	1.0112	-
Curve fitting parameter	b	6.6e-6	6.7e-6	10.9e-6	-

In the frequency range below 200 Hz, significant differences between the curve fittings cannot be observed. Above that frequency range, a trend to higher damping loss factors with smaller thickness is observable. The curve fitting for plates 5 and 6 shows the highest values in the frequency range above 400 Hz which manifests itself in a highest parameter b. Here, $\eta(f)$ takes values up to 1.5 % A reason for that might be the layer stack which has two zero layers in the symmetry plane. Another reason can be more complex deflection shapes as the modal density is higher for these plates. With complex deflection shapes, more changes between maxima and minima occur which might increase the damping performance. However, the three curve fittings are used as basis for the plate models, respectively.

Model

For a model of the curved CFRP plate, a shell formulation seems appropriate, which is a combination of a Mindlin plate according to Eqs. (2.19) to (2.21) and a disc according to Eqs. (2.17) and (2.18). An FE formulation for a general shell domain Ω_{s2} is given in Sec. 2.2. The shell ensures a possible combined occurrence of flexural waves (including shear) and in-plane waves in the curved structure. For each uni-directional layer, an orthotropic material behaviour according to Eq. (2.5) is assumed. The layer stack with changing fibre orientations yields a homogenised orthotropic material behaviour. The linear orthotropic elastic material finally requires nine independent variables. In Tab. 4.4, available data by the suppliers of the carbon fibres and the

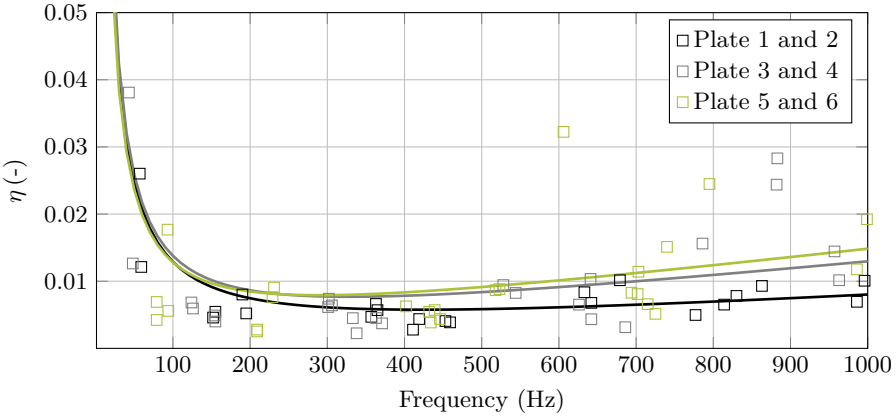

Figure 4.6: Damping loss factors for CFRP plates 1 to 6 based on experimental results in Fig. 4.3, 4.4 and 4.5 and curve fitting ($a = 1.135$, $b = 7\text{e-}6$)

epoxy matrix are given.

Table 4.4: Material data on carbon fibres (Zoltek PX35 HT fibre) and the epoxy matrix (HP-E3000RI + HP-E300RI) [170, 78, 154]; Marked (*) data is estimated on the basis of mean data given in [150]

Carbon fibre parameters	Variable	Value	Unit
Young's modulus (length-wise)	$E_{\text{fibre}\parallel}$	242e9	N/m^2
Young's modulus (transverse) *	$E_{\text{fibre}\perp}$	28e9	N/m^2
Poisson ratio*	$\nu_{\text{fibre}\perp\parallel}$	0.23	-
Shear modulus*	$G_{\text{fibre}\perp\parallel}$	50e9	N/m^2
Density	ρ_{fibre}	1810	kg/m^3
Fibre volume content	φ_{fibre}	45	%
Epoxy matrix parameters	**Variable**	**Value**	**Unit**
Young's modulus (isotropic)	E_{ep}	3e9	N/m^2
Poisson ratio*	$\nu_{\text{fibre}\perp\parallel}$	0.35	-
Density	ρ_{ep}	1100	kg/m^3
Glass transition temperature	T_g	83	°C

By use of the micromechanical modelling assumptions within the classical laminate theory (CLT) according to [150], homogenised orthotropic material parameters are calculated (results are given in Tab. 4.5). This material data of one uni-directional CFRP layer is nominally applicable for each layer in all six plates.

Considering the layer stack of each plate, the CLT is applied in order to obtain the necessary homogenised orthotropic elastic material parameters. In Tab. 4.6, the resulting parameters are listed. Separated homogenised parameters are considered

Table 4.5: Material data of one uni-directional CFRP layer based on the CLT

Quantity	Variable	Value	Unit
Young's modulus (parallel to fibre)	$E_{\parallel}$	110.5e9	N/m^2
Young's modulus (transverse to fibre)	$E_{\perp}$	7.6e9	N/m^2
Poisson ratio	$\nu_{\parallel\perp}$	0.296	-
Shear modulus (fibre planes)	$G_{\parallel\perp}$	3.3e9	N/m^2
Shear modulus (normal plane to fibre)	$G_{\perp\perp}$	2.7e9	N/m^2

for bending and in-plane deflections, respectively. As all layer stacks are symmetric, a mechanical coupling between these parts does not occur [150]. The mindlin plate formulation considers a shear influence for which the transverse shear moduli G_{xz} and G_{yz} are needed. The mixing rule according to Eq. (2.24) equilibrates all layers in order to receive homogenised shear moduli. For the same layer count in each direction (0/90), this approach delivers identical shear moduli (plates 1 to 4). For plate 5/6, the layer weighting us slightly asymmetric and thus also the shear moduli. Compared with this, a more sophisticated approach by Rohwer [140] mentioned in Sec. 2.2 considers a realistic shear stress distribution. A reduced influence of the outer layers on the homogenised shear moduli is expected as these layers bear less shear loads, which yields different values for G_{xz} and G_{yz} as given in Tab. 4.6. A little further back in this section, a comparison between the approaches is conducted.
Finally, damping is considered by a damping loss factor $\eta(f)$ based on the curve fitting in Fig. 4.6. The mesh is refined in x and y-direction in order to ensure a small discretisation error. A mean relative error below 1 dB is realised by halving the mesh size for plate 5 with 2 mm thickness. Between two meshes, the error is calculated considering 200 frequency samples with $\Delta f = 5\,\mathrm{Hz}$. The resulting mesh size for plate 5 is 6.25 mm, which is applied for all plates studied in this section. The resulting FE model and the converged response for the converged mesh are depicted in Fig. 4.7 a) and b), respectively. The mesh considers approx. 50 nodes per bending wave[9] length in x-direction, which is the crucial direction as the structure is stiffened for bending waves in y-direction due to the curvature. For plate 5, an increased mesh size in the local y-direction does not introduce a significant discretisation error according to the criterion. The resulting possible mesh size corresponds to 12.5 nodes per bending wave length, based on a flat infinite plate which depicts the influence of the curvature on the actually required mesh. For a realistic aircraft structure, a reduced mesh size in the aircraft's axial direction can be considered due to the stiffening effect of the curvature. Furthermore, frames and stringers lead to further stiffening effects.
In Fig. 4.8, the resulting mean squared velocity is plotted for plate 1 according to the

[9] Based on Eq. (2.66) for an infinite plate, a wave length of $\lambda_b = 0.159\,\mathrm{m}$ is calculated

Table 4.6: Homogenised material data of three CFRP layer stacks based on the CLT [150] and two approaches for the transversal shear moduli [140]

CLT parameters	Variable	Value Plate 1/2	Value Plate 3/4	Value Plate 5/6	Unit
Young's modulus (bending)	E_{bx}	67.1e9	69.0e9	74.6e9	N/m^2
Young's modulus (bending)	E_{by}	51.6e9	49.6e9	44.0e9	N/m^2
Young's modulus (membrane)	E_{mx}	59.3e9	59.3e9	69.7e9	N/m^2
Young's modulus (membrane)	E_{my}	59.3e9	59.3e9	49.0e9	N/m^2
Poisson ratio (bending)	ν_{xy}	0.044	0.044	0.051	-
Poisson ratio (membrane)	ν_{xy}	0.038	0.038	0.046	-
Shear modulus (bending)	G_{xy}	3.3e9	3.3e9	3.3e9	N/m^2
Shear modulus (membrane)	G_{xy}	3.3e9	3.3e9	3.3e9	N/m^2
Mixing rule parameters					
Shear modulus	G_{xz}	3.0e9	3.0e9	3.1e9	N/m^2
Shear modulus	G_{yz}	3.0e9	3.0e9	2.9e9	N/m^2
Rohwer parameters					
Shear modulus	G_{xz}	2.6e9	2.6e9	2.8e9	N/m^2
Shear modulus	G_{yz}	4.7e9	4.5e9	6.0e9	N/m^2

two approaches for the transverse shear moduli. In addition, an infinite shear stiffness is applied for comparison (like a Kirchhoff plate *with* rotational inertia effects). Plate 1 is chosen exemplary, as a higher influence of the shear stiffness is expected with increasing thickness.

The results do not show any significant differences. Only above 800 Hz, slight deviations can be observed – here, an infinite stiffness shows resonances at slightly higher frequencies. The transverse shear modulus does not have a crucial impact on the vibrational response of a curved CFRP plate with 4 mm thickness. For the following models, the approach by Rohwer is applied.

The experimental and numerical responses of plate 1 are compared in Fig. 4.9. The *first model* is the FE result considering the material data from Tab. 4.6. Measurement and model response show a similar overall course but considerable deviations in some resonance peaks. A study of the deflection shapes shows that mainly the

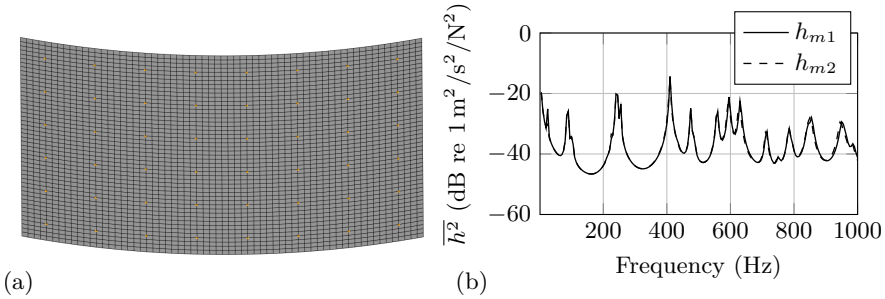

Figure 4.7: (a) Finite element model with a mesh size of $h_m = 6.250\,\text{mm}$ and highlighted measuring nodes; (b) $\overline{h^2}(f)$ for $h_{m1} = 6.250\,\text{mm}$ and $h_{m2} = 3.125\,\text{mm}$ for CFRP plate 5

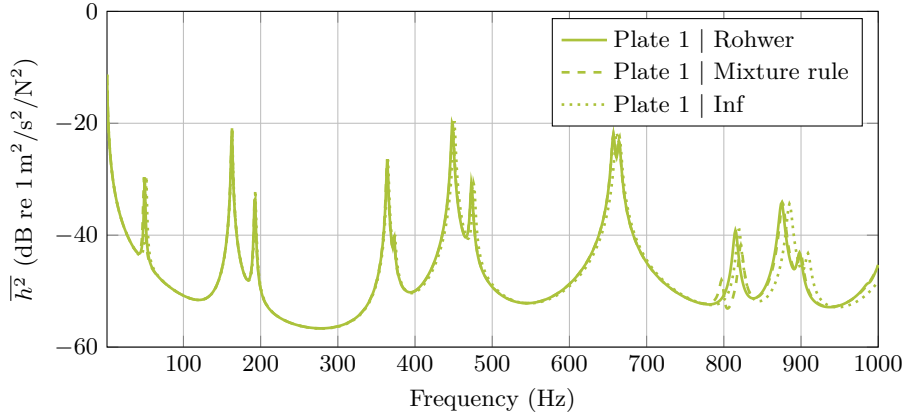

Figure 4.8: Numerical results for mean squared admittance $\overline{h^2}(f)$ of curved CFRP plates comparing three models for transverse shear moduli

bending modes in local x-direction are shifted to higher frequencies. Due to the curvature of the plate, a high influence of the shape itself is expected for bending modes in y-direction. In opposite, as the plate is not additionally stiffened in in local x-direction, a higher influence of manufacturing tolerances is expected. The CLT underlies numerous ideal assumptions like plane and parallel layers with a constant thickness [150]. Another point is a neglection of cracks or air-inclusion by the CLT. The parameters derived above apply among these (and more) assumptions. As mentioned, the investigated plates have a slight ripple on the surface leading to thickness deviations while internal *defects* cannot be investigated in the frame of this thesis. Furthermore, the fibres are not perfectly parallel which can be seen on the surface of the two outer layers (see Fig. 4.2). Hence, a reduced layer stiffness is expected in order to find more suitable material parameters and test the applicability of the

model. The Young's moduli of each layer (Tab. 4.5) are reduced within a parameter study and the final homogenised parameters (Tab. 4.6) are recalculated for each sample. The optimal curve is identified as minimum absolute error between experimental and numerical result. The difference is summed up over frequency in order to get a scalar criterion. The response of the fitted model is shown in Fig. 4.9. A 12 % reduction of the Young's moduli of each uni-directional layer yields this result. The experimental and numerical responses clearly match better after the stiffness reduction. Shifts in resonance peaks are significantly reduced while deflection shapes with a wave propagation in local x-direction are particularly affected by the reduced layer stiffness. Further deviations between the model and the real CFRP plate may be introduced by influences of humidity, temperature, a locally varying fibre volume content or an inhomogeneous fibre distribution [150]. Deeper investigations of these factors are out of scope – on the basis of the current results, the shell model with an orthotropic linear elastic material and material parameters by the CLT seem to be appropriate. Deviations between model and measurements can mostly be expected in manufacturing tolerances.

In Fig. 4.9, the experimental and numerical results for the thinner plate 3 (3 mm) are shown as well. Again, *first model* is the response of the CLT material parameter while *fitted model* describes the response under consideration of a decreased layer stiffness (here: 14 %). Compared to plate 1, a similar description of the curves holds true – the overall course is comparable while the resonance peaks show deviations. A decreased layer stiffness yields a much better fitting up to 550 Hz. At higher frequencies, the deviations remain. Manufacturing tolerances as mentioned above are expected to have stronger effects in thinner structures. For instance, if the fibre distribution in one layer is inhomogeneous, the influence on the stiffness of the entire stack decreases with the total number of layers. Therefore, a mean reduction of the layer stiffness is expected to work better for thicker plates. For thinner plates, more *adjustments* of the material parameter seem necessary. The responses for the even thinner 2 mm plate 5 are shown in Fig. 4.9 at the bottom. As described above, the deviation between experiment and model increases again – an appropriate fitting can be achieved up to 450 Hz. The layer stiffness is reduced by 12 % for plate 5. This value is similar for all three modelled plates and leads to better results in all cases.

The results of all three plates show that the finding of appropriate material parameters gets more complex with decreasing thickness or increasing frequency. However, the shell model itself seems to capture the dynamic response of a CFRP plate while a slightly reduced layer stiffness improves the results compared to the CLT. For thinner plates, more measures are necessary, which are expected to be realisable by a further

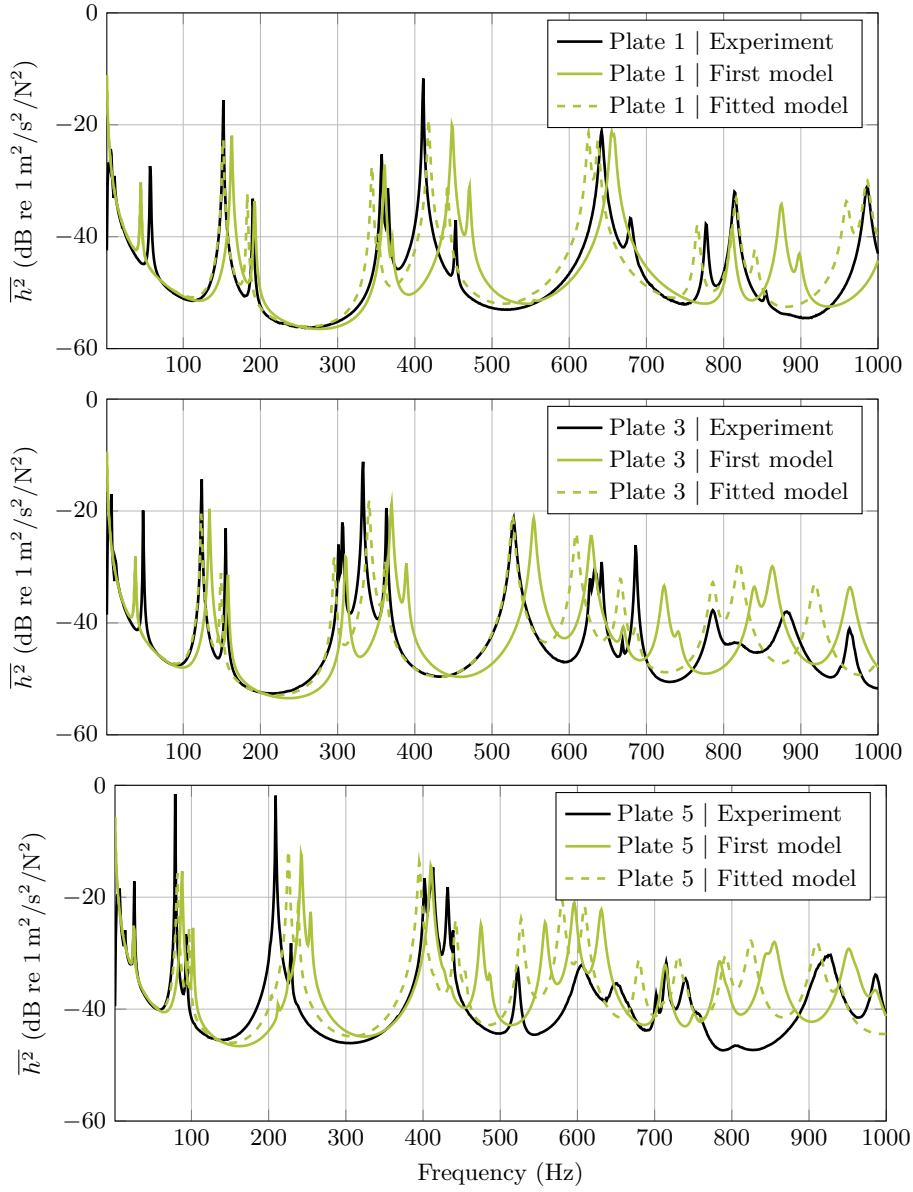

Figure 4.9: Experimental and numerical mean squared admittance $\overline{h^2}(f)$ for the curved CFRP plates 1, 3 and 5

adaptation of the parameters. Therefore, the shell model is used for the aircraft model with the knowledge that an error is expected for thin skin fields.

The actual airframe mainly consists of the outer skin fields stiffened by a combination of length-wise stringers and circular frames as introduced in Sec. 2.1. While the outer skin carries the overpressure in the cabin and shear forces, the stiffeners mainly increase the bending stiffness. Overpressure induces a pre-stressing, which again increases the stiffness of the system. These factors basically shift the frequency response to higher frequencies and thus shifts the highest expected modelling errors to higher frequencies as well. In order to assess the effect of pre-stressing and stiffeners, a realistic cut-out of a fuselage is studied in the following.

The model is shown in Fig. 4.10. The marked central skin field shall be of interest here. A plane wave load (45 deg incidence angle on the central skin field) is applied only in this central skin field and the mean squared velocity is computed for this field as well. The 14 surrounding fields including the stiffeners serve as boundary condition while the entire cut-out is clamped at the surrounding nodes. The final material parameters of plate 5 (with 12 % layer stiffness reduction) are applied and all skin fields, frames and stringers have a thickness of 2 mm as well. The frames are placed with a typical distance of $\Delta_{\text{frames}} = 0.52\,\text{m}$ and size (I-shape, height $h_{\text{frame}} = 0.05\,\text{m}$, width $b_{\text{frame}} = 0.03\,\text{m}$) according to the preliminary design data available within the CRC 880, see Sec. 2.1. The stringer positions are available as well while a typical distance of $\Delta_{\text{stringers}} = 0.18\,\text{m}$ is adopted for the model of the cut-out investigated here. A mesh study is conducted for the panel. As the radius is larger (1.75 m) than the radius of the CFRP plates above, a doubled mesh size in y-direction is not possible under the same criteria (though the error of 1.4 dB is quite small). Less curvature introduces less stiffening effect, towards an infinite radius, the result converges to a flat structure. For a flat plate, only differences in the bending stiffness remains which finally declares the required mesh size. For stringers and frames, a much coarser mesh is suitable without a violation of the error criterion explained above. The usage of shell elements (compared to, e.g., beam elements) is necessary for the stiffeners in order to capture the dynamic behaviour [58].

In Fig, 4.11, the response of the central skin panel is shown with and without a consideration of pre-stressing. The overpressure in the cabin is given and documented in Tab. 4.14. Under the assumption of a closed cylinder under pressure Δp, pre-stresses per unit length can be calculated according to Eqs. (4.2,4.3) [119].

$$T_x = \Delta p \frac{R}{2} \tag{4.2}$$

$$T_y = \Delta p R \tag{4.3}$$

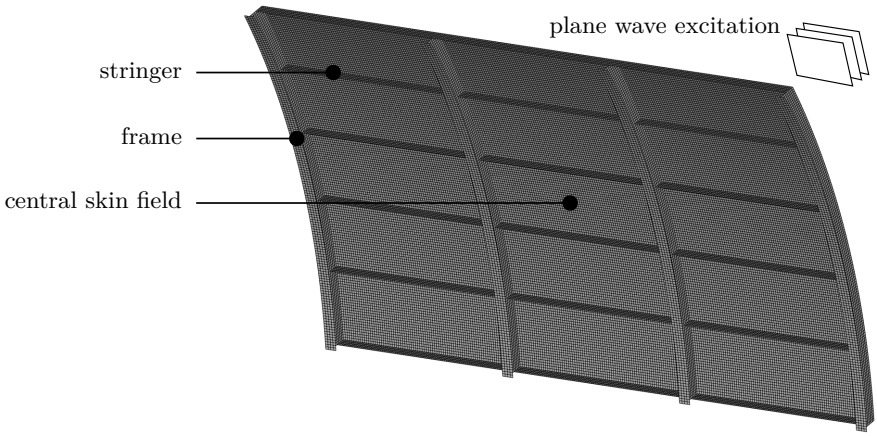

Figure 4.10: FE model of a stiffened panel section

$T_x = 54668\,\mathrm{N/m}$ is the axial (length-wise / flow direction) stress per unit length while $T_y = 109337\,\mathrm{N/m}$ is the stress per unit length in lateral direction. The results in Fig. 4.11 show a significant shift of the field response to higher frequencies as the panel is stiffer due to the applied pre-stressing. The first resonances at around 200 Hz occur at almost doubled frequency. Furthermore, the dynamic is higher up to 1000 Hz as all resonances are shifted to higher frequencies. Similar to the free CFRP plates, higher damping performances can be observed with higher frequency *and* more complex deflection shapes. By the stiffening effect, more complex deflection shapes are expected at even higher frequencies. These changes in vibration levels and resonance locations are expected to be crucial for the cabin SPL as well. Hence, the pressurisation must be considered within the aircraft model. In order to receive a more detailed stress-distribution within the stiffened structure, a static analysis in advance is recommended for future investigations. Within this thesis, the overall effect is considered based on the closed-cylinder assumption above.

The stringer shape and size is not available in the early design stage of the CRC 880. In order to basically study the effect of stringers, a simple unflanged stringer [120] is chosen. As the material is CFRP, frames and stringers are perfectly integrated and connected in the structure, similar to the "black fuselage" concept studied in [75]. Of course, such assumptions influence the dynamic response of the panel. But a neglection of stringers is expected to distort the result to an extent worse than a consideration and study of *typical* stringers fitting to the given frames. In Fig. 4.12, the response of the panel under variation of the stringer height relative to the frame height $h_{\mathrm{frame}} = 0.05\,\mathrm{m}$ (25, 50 (reference) and 75 %) is plotted. All three panel variants respond on a similar level to the plane wave load, while mainly resonance

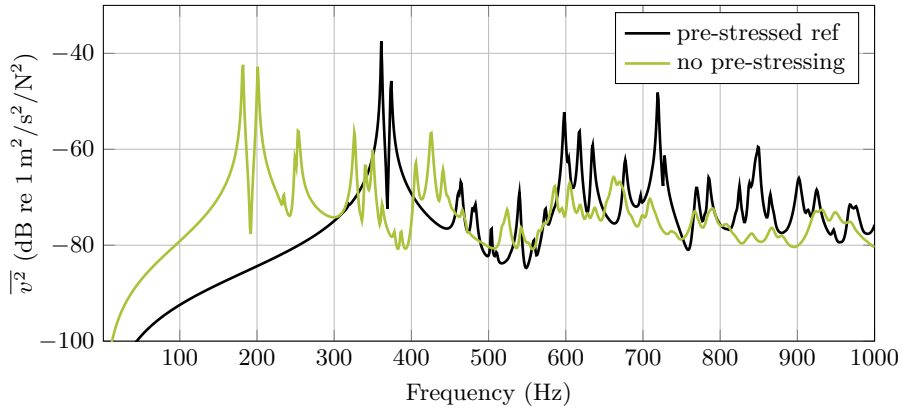

Figure 4.11: Numerical response of the central skin field within a stiffened panel section with and without pre-stressing due to cabin overpressure

shifts can be observed. Comparing 25 and 50 % stringer height, a significant shift in frequency is given, especially the first resonance frequencies are affected by the stiffness of the surrounding stringers. Comparing 50 and 75 % stringer height, the change is much smaller. A convergence in the panel stiffness can be expected as the panel's response is not changing crucially if the stringer height is already increased to a certain extend. The stringers may rather behave as boundary condition to the skin field than vibrating structure which corresponds to the coarser mesh appropriate for the stringers. However, the stringer height (and finally the shape) will have a noticeable effect on the outer skins vibrational response. As the outer skin is a major part of the separating component in the sound transmission into the cabin, which kind of declares the energy input and directly interacts with the insulation, a noticeable effect on the cabin is expected as well. Hence, a cautious recommendation can be given to study the stringer shape and height within uncertainty studies with regard to cabin acoustics of preliminary designs. For the underlying thesis, an assumptions on the stringers must be made in order to conduct the aircraft model analyses. The influence of the stringer shape must be kept in mind for the interpretation of results. Of course, as the level is similar but the resonances are shifted, the influence is not that critical for broadband excitations (e.g. turbulent boundary layer) as for tonal excitations (e.g. propeller).

The stringer thickness in the reference panel is 2 mm (identical with the frame thickness). A variation (1 and 3 mm) is conducted in order to study the influence on the central skin's response which is shown in Fig. 4.13. For the three studied stringer thicknesses, the results are really similar and the changes in frequency and amplitude are much smaller compared to the stringer height. This fits the expectation that

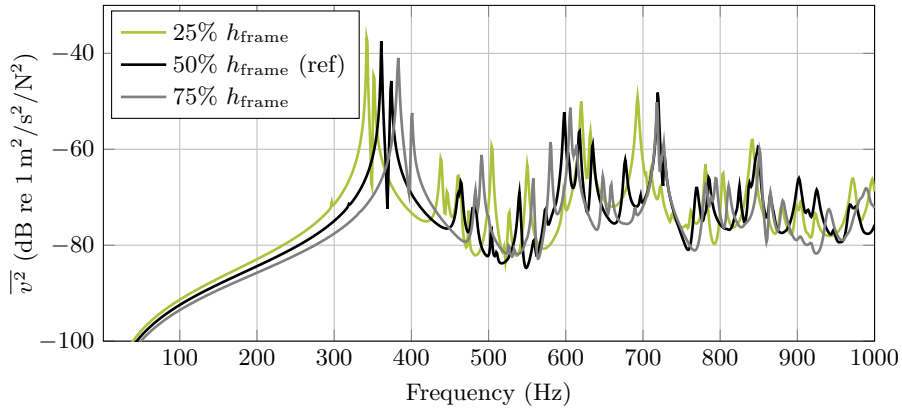

Figure 4.12: Numerical response of the central skin field within a stiffened panel section under variation of the stringer height relative to the frame height $h_{\text{frame}} = 0.05\,\text{m}$

the height of stringers has a cubic contribution to the moment of inertia while the dependency on thickness is linear. As the effect on the panel response is small for the realistic panel, a small influence on the cabin SPL is expected as well. If the stringer thickness is not known in detail by preliminary design data, a value can be assumed and shall not be in focus of uncertainty investigations. Rather the shape and height is of primal relevance for the skin field vibrations.

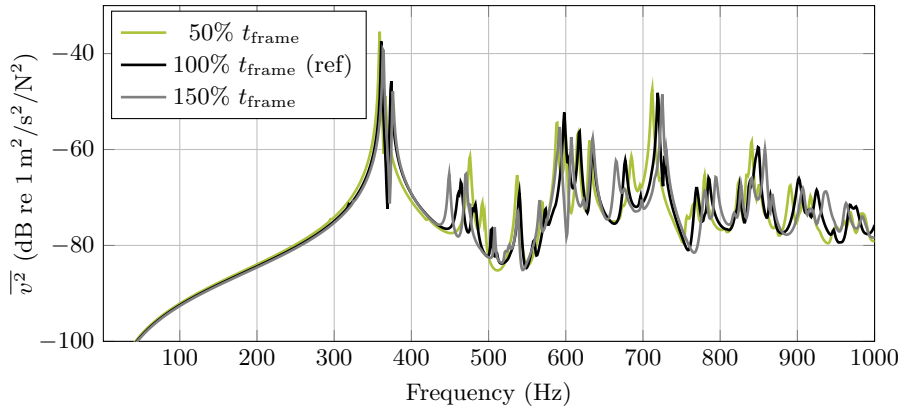

Figure 4.13: Numerical response of the central skin field within a stiffened panel section under variation of the stringer thickness relative to the frame thickness $t_{\text{frame}} = 2\,\text{mm}$

Concluding the section on CFRP plates and panels, the following statements are derived considered for the aircraft model:

- The CLT is appropriate for linear orthotropic material parameters of curved CFRP structures in the outer aircraft skin which is shown for plates between 2 and 4 mm. With decreasing thickness and increasing frequency, larger deviations in the dynamic response due to manufacturing tolerances can be expected, which cannot be easily covered by the model.
- No crucial impact of the transverse shear moduli on the vibrational response of a curved CFRP plate with 4 mm thickness is observed. As outlook, this parameter is rather a minor source of uncertainty in the model.
- A consideration of different mesh sizes in axial and lateral direction of the aircraft's outer skin is basically reasonable as the shells are stiffened by the curvature which can save computational costs.
- The effect of pre-stress due to a pressurisation of the passenger cabin is crucial to the skin field vibrations and must be considered in the aircraft model
- The effect of frames and stringers is obvious in the response of a realistic panel section and acts similar to a boundary condition. In opposite to frames, a dimensioning of stringers is not available in the early design stage. The height of an unflanged stringer has turned to have a significant influence on the dynamic response of a skin field while its thickness plays a minor role. For the full aircraft in this thesis, assumptions are made on the stringer dimensioning. For further studies, a study of varying stringers is a recommended option.

4.2 Insulation

According to a technical report by the federal aviation administration (faa), fibreglass insulation is extensively used in the double-wall structures of commercial aircraft [106]. The two purposes are thermal and acoustic insulation, while the latter is important for the vibroacoustic model. Thermal acoustic insulation blankets are applied between the outer skin and the interior trim panels. These blankets consist of fibreglass encapsulated in plastic moisture barrier film coverings [106, 155], which can be seen in the example of an A320 aircraft in Fig. 4.14 (a). Obviously, insulation blankets can be placed at the interior trim panel *and* the airframe. In aircraft design, the application of insulation is mainly limited by weight, costs and space [155]. This leads to numerous possible and individual distributions of insulation. Instead of considering all individual layers or a specific configuration, a homogenisation of the double-wall gap is carried out in order to meet the generic requirements and ensure more general results. Of course, in industry, more detailed models may be reasonable to investigate specific aircraft configurations. These models might include a specific

distribution of insulation material, e.g. gaps due to pipes or electrical wires. For the generic aircraft model, a 3D domain Ω_g filled with glass wool is applied in order to reasonably consider the influence of insulation material in the transmission loss problem. Ω_g corresponds to the air gap within the double wall sound transmission problem. The insulation material is attached to the airframe and the interior lining connecting which creates a wave transmission path.

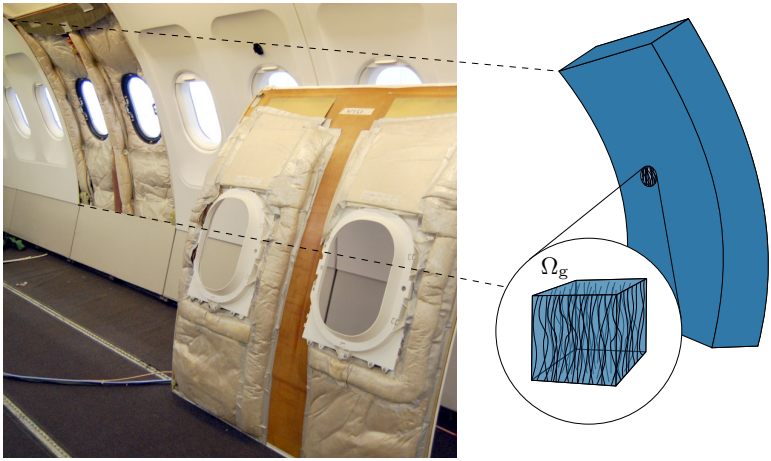

(a) (b)

Figure 4.14: (a) Typical insulation of a commercial passenger aircraft and (b) generalised problem for the generic aircraft model

Experiment

In order to obtain structural and material data for the model, four established standard measurements are conducted on aircraft grade glass wool. Experiments on the absorption coefficient α, local characteristic impedances $\underline{Z}$ and the flow resistivity σ are carried out using an impedance tube, a reverberation chamber and a flow resistivity meter. For the impedance tube and the flow resistivity meter, circular specimens are required and cut out as shown in Fig. 4.15. The material has a thickness of $t_g = 20\,\text{mm}$ and comes along with additional plastic moisture barrier film coverings. An area of $A_g = 12\,\text{m}^2$ is used for the reverberation measurements and can be seen in Fig. 4.15 as well.

In Tab. 4.7, relevant data on the investigated aircraft grade glass wool is listed. The mass of several specimens is measured with a micro balance in order to compute the bulk density. The calculated bulk density is close to the value for the standardised *type 1 class AA grade B* according to ASTM C800-14 [40]. Based on literature values [16,

152], the density of glass fibres $\rho_{gf} = 2500\,\mathrm{kg/m^3}$ is applied in Eq. (2.36), yielding the porosity given in Tab. 4.7. Tests under flight conditions are not conducted – hence, experiments under laboratory conditions serve as validation basis while flight conditions (e.g. a different air density) can be considered for the aircraft model as input parameters.

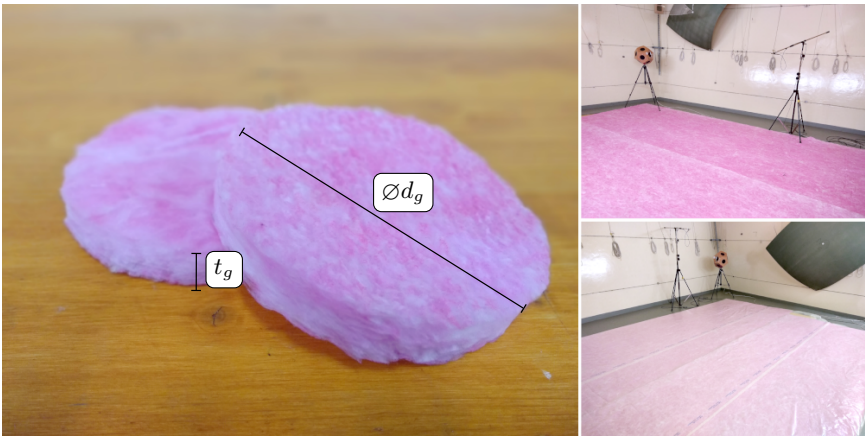

Figure 4.15: Circular specimens ($t_g = 100\,\mathrm{mm}$) of aircraft grade glass wool applied as insulation material and glass wool blankets with and without plastic moisture barrier film coverings in reverberation chamber

Table 4.7: Data on glass wool specimens including laboratory conditions and directly obtained material data

Quantity	Variable	Value	Unit
Thickness	t_g	20	mm
Diameter	d_g	100	mm
Bulk density	ρ_g	7.68	$\mathrm{kg/m^3}$
Porosity	Φ_g	99.7	%
Temperature	T	17	°C
Relative humidity	RH	38	%

The first experimental study is a determination of the absorption coefficient $\alpha(f)$ under normal sound incidence by use of an impedance tube (AED AcoustiTube®) according to DIN EN ISO 10534-2 [2]. $\alpha(f)$ allows an easily accessible comparison of modelling to experimental results in the following section. Two microphone distances are applied in order to cover a frequency range from 57 to 1981 Hz. In the overlapping frequency range (228 to 517 Hz), a linear transition is conducted between the results obtained with an increased microphone distance for low frequencies and those ob-

tained with a shorter microphone distance for high frequencies. Different thicknesses of specimens are investigated by stacking the circular samples. In Fig. 4.16, $\alpha(f)$ is shown for different stacks with a total thickness t_g. As expected, the absorption coefficient is increasing with frequency and thickness. For three stacked glass wool specimens resulting in $t_g = 60\,\text{mm}$, an absorption near 1 can be expected around 1000 Hz. The aircraft double wall gap in the preliminary design data has a thickness of 0.1 m, which allows for a placement of such stacks. Hence, for the sound transmission through the fuselage, the transmission path through the glass wool may play a minor role at high frequencies (similar to a high transmission loss in the double wall problem). Rather, the sound waves within the glass wool are absorbed instead transmitted. At frequencies towards 1000 Hz, a dominating transmission is expected through the structural part in which the interior trim panels are directly attached to the frames. A slight compression of the glass wool is not avoidable as the material is packed into bags and pressed against the outer skin and the interior trim panel. In Fig. 4.16, $\alpha(f)$ is shown for a 60 mm stack, but compressed by a rate of $r_c = 1 - \frac{t_g}{t_{g0}} = 50\,\%$. An increase of the absorption capacity can be observed at low frequencies while a slight reduction at higher frequencies is visible. These results are qualitatively comparable with literature on general glass wool absorption measurements [17, 97]. Fluctuations of $\alpha(f)$ at low frequencies ($< 200\,\text{Hz}$) can be ascribed to measurement noise rather than to the material physics. The obtained results serve as basis for a model characterisation under normal sound incidence.

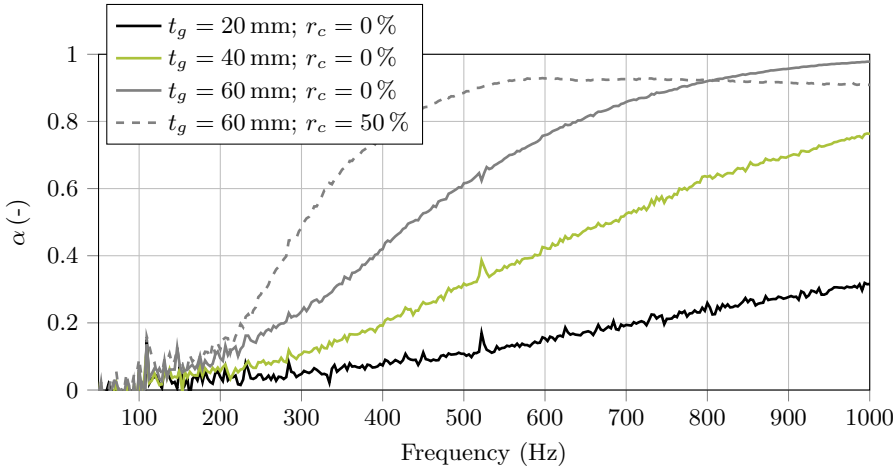

Figure 4.16: Experimental results for the absorption coefficient $\alpha(f)$ of glass wool of different thickness t_g and compression rates r_c (normal sound incidence)

In addition to the impedance tube measurements under normal sound incidence, $\alpha(f)$

is measured according to DIN ISO 354 [5] within a diffuse field. The experiments are conducted in the reverberation chamber of the PTB Braunschweig. The results are shown in Fig. 4.17 for the raw glass wool as well as the glass wool covered by plastic moisture barrier film coverings. In the frequency range below 1000 Hz, a rather insignificant influence of the plastic covering can be observed. The absorption coefficient increases by around 0.1 at 1000 Hz, which can be neglected in the following models. At frequencies above 1000 Hz, the influence is more significant and should be considered in aircraft models. Especially above 2000 Hz, the application of the covering results in much lower absorption coefficients. Shorter wave lengths occur and the waves seem to interact with the thin covering, partly leading to reflections and decreasing the sound incidence in the glass wool. As clarified in further chapters, the computational cost of the aircraft model is increasing crucially with higher frequencies. This fact postpones investigations at high frequencies (>1000 Hz) to future when wave-resolving models and the required FE meshes can be solved. Compared with impedance tube measurement under normal sound incidence, the absorption coefficient is higher under oblique sound incidence from all directions in the reverberation chamber's diffuse sound field. A factor of around 2 can be observed at 500 to 1000 Hz. As the sound incidence is diffuse, all directions influence the macroscopically observed absorption characteristics of the glass wool blanket. It can be expected that the wave propagation length within the glass wool blanket is longer for oblique sound incidence, yielding a higher absorption. Furthermore, it is known that glass wool has anisotropic properties due to an orientation of the glass fibres within the blankets [11, 14]. Again, compared to normal sound incidence, a wave travel out of the normal direction might lead to a higher absorption. For the aircraft structure, a circumferential wave propagation within the double wall gap can be expected. Within the frame of this thesis, an isotropic material model for the glass wool is applied and investigations of anisotropic effects are postponed to further studies.

Further measurements are conducted within a transmission loss setup of the impedance tube according to ASTM E2611-09 [55]. Compared to the 2-microphone measurement (yielding $\alpha(f)$ only), the 4-microphone measurement applied here allows for the calculation of material parameters by use of the transfer matrix method. Under the assumptions of normal sound incidence and normal sound transmission, the characteristic impedance Z_c of the glass wool is obtained (shown in Fig. 4.18). Three compression rates r_c are tested in order to get Z_c in dependency on r_c. The magnitude of both the real and the imaginary part tends to increase in a wide frequency range as the glass wool is compressed. A gedanken experiment of an infinitely compressed glass wool blanket suggests an infinite impedance in this case. Hence, a convergence towards large values of Z_c is reasonable. The overall course of Z_c is approximately

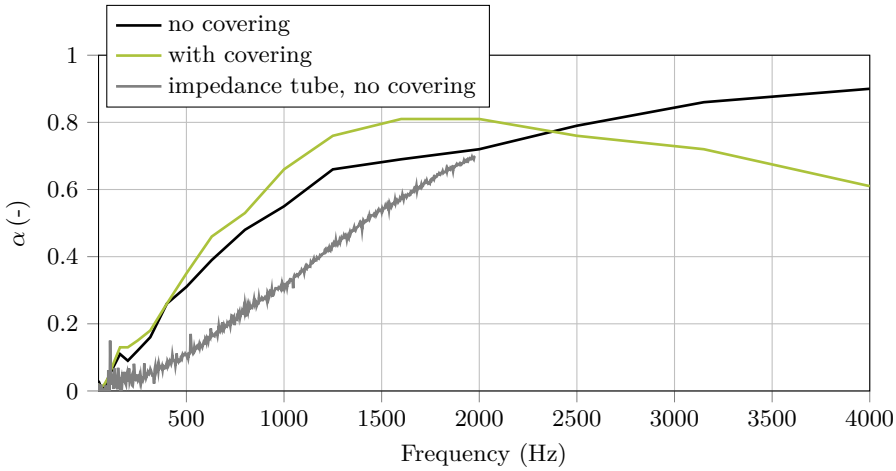

Figure 4.17: Experimental results for the absorption coefficient $\alpha(f)$ of glass wool ($t_g = 20\,\text{mm}$) in the reverberation chamber (oblique sound incidence)

constant (around 600 to 1000 Ns/m^3) within a wide frequency range.

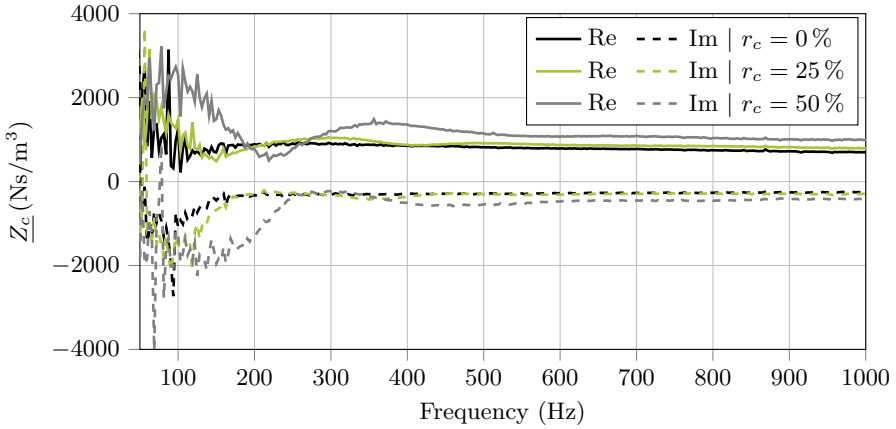

Figure 4.18: Experimental results for the characteristic impedance $\underline{Z_c}$ of aircraft grade glass wool

Besides Z_c, the transfer matrix method delivers the wave number $\underline{k}$ which is plotted in Fig. 4.19. Similar to Z_c, the three investigated compression rates are shown for the real and imaginary part, respectively. Again, the magnitudes of both parts are increasing with r_c within a wide frequency range. In the low frequency range between 200 and 300 Hz, fluctuation can be observed, which is typically for porous materials. However, a smooth (despite some measurement noise below 150 Hz) and reasonable course is obtained for k_c. In [70], the speed of sound c is given for aircraft grade

glass wool. Comparing the results, the real part of c is similar while the imaginary part shows higher magnitudes here. The two characteristic parameters Z_c and k_c are required as input for the equivalent fluid model applied below within this section.

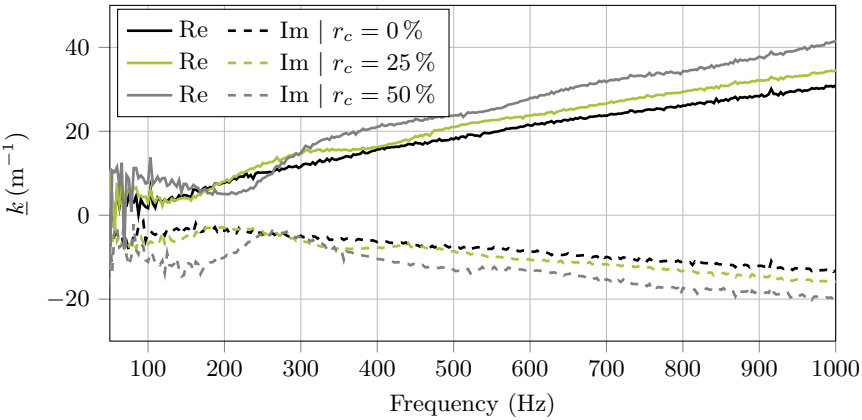

Figure 4.19: Experimental results for the wave number $\underline{k}$ of aircraft grade glass wool

As basic parameter, the flow resistivity σ is required by many material models for porous materials. σ is measured according to DIN EN 29053 [4] by use of the alternating flow method (Norsonic Nor1517A) in normal (out-of-fibre) direction. As mentioned, the insulation blankets are exposed to a static pressure leading to higher density. Hence, the density of the glass wool within a 60 mm stack (three specimens) is increased significantly within a closed cylinder in order to yield σ as a function of the density. The results are shown in Fig. 4.20 and show an exponentially increasing flow resistivity with increasing density, which qualitatively correlates with literature results [152]. A measurement of single specimens yields similar results, but does not allow for precise compression. On the x-axis, the compression rate r_c is given, which corresponds to the increase of density. For $r_c = 50\,\%$ (equivalent to a doubled density), a flow resistivity of $\sigma = 41000\,\mathrm{Ns/m^4}$ can be observed, which is around four times higher than in original condition. This fits well with a simple modelling assumption ($\sigma_{\mathrm{compr}} = \sigma/(1-r_c)^2$) by Castagnède et al. [42], for which the plot is given as well. The sensitivity of σ on r_c is assumed to be important for the aircraft model as a dependency of Z_c and k_c is proposed by all models. Hence, an effect on the sound transmission can be expected. For the aircraft model in this thesis, $r_c = 25\,\%$ is assumed as a reasonable value under installation conditions. The flow resistivity serves as input in the following modelling part.

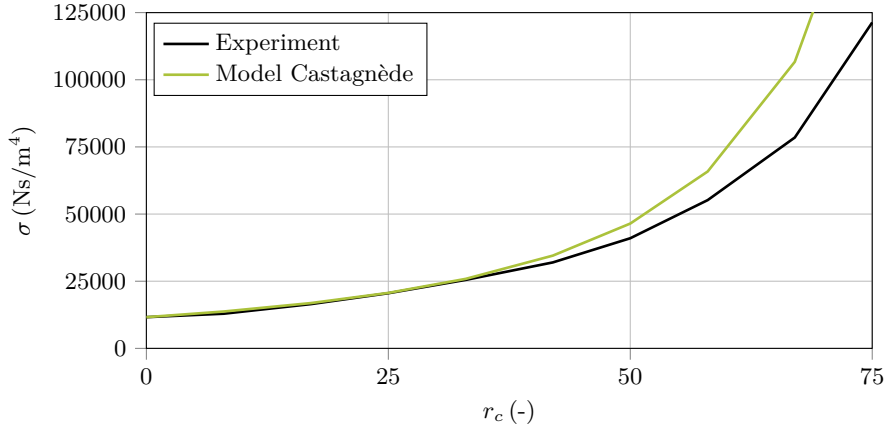

Figure 4.20: Experimental results for the flow resistivity σ of a 60 mm stack of aircraft grade glass wool in dependency on the compression rate r_c compared to a model by Castagnède [42]

Model

The domain Ω_g is filled by glass wool which can be described by porous material models briefly introduced in Sec. 2.3 for the general acoustic domain Ω_a. The simplest modelling approach is an equivalent fluid domain with complex and frequency-dependent parameters $\underline{c}(f)$ and $\underline{\rho}(f)$ in the Helmholtz Eq. (2.31). This approach is applied first and compared to the experimental results under normal sound incidence. The two parameters are calculated using the complex wave number $\underline{k}$ and the complex characteristic impedance $\underline{Z_c}$ according to Eqs. (2.38,2.40). The following modelling approaches are applied in order to receive these parameters:

- Semi-empirical Delany-Bazley model (**D-B**; Eqs. (2.34,2.35)) [52] using the flow resistivity measurements according to DIN EN 29053 [4] shown in Fig. 4.20.
- Semi-empirical Johnson-Champoux-Allard model (**JCA**; Eqs. (2.41,2.42)) [43, 83] using the flow resistivity measurements according to DIN EN 29053 [4] shown in Fig. 4.20, the porosity Φ from Tab. 4.7 and the additional parameters tortuosity $\alpha_\infty = 1.1$, viscous characteristic length $\lambda = 140\,\mu m$ and thermal characteristic length $\lambda' = 500\,\mu m$ from literature [14].
- Limp model (**JCA-limp**, Eq. (2.43)) [127] extending $\rho_{eff}(f)$ calculated by JCA using the same parameters.
- Parameter conversion based on the Transfer-Matrix-Method results according to ASTM E2611-09 (**ASTM**) [55] shown in Fig. 4.18 and 4.19.

It is advantageous to have a model using microscopic parameters in order to study

different glass wool types in aircraft design. The experimental results for $\underline{c}(f)$ and $\underline{\rho}(f)$ can also be used directly, but these results do not perfectly fit the absorption measurements either as shown below.

As an advantage, the Delany-Bazley model only requires the measured flow resistivity as a parameter. In opposite, the Johnson-Champoux-Allard model considers more parameters which might be more accurate and flexible, for instance, in order to consider the effect of compression on several parameters as done below. In [127], a limp model is compared to a rigid frame model for fibrous materials. A limp model considers the mass of the frame (in our case glass fibres), but no frame stiffness. On the other hand, a rigid frame model considers no frame motion at all. Especially in low frequency ranges, the results shown in [127] are in a better agreement with impedance measurements. Using a limp model for glass wool is also considered in [67, 81, 130] and recommended instead of the much more complex and computationally expensive Biot model [25], which considers the structural phase as a coupled linear elastic domain. Besides computational expenses, more parameters must be determined which brings in additional error sources and effort. Nevertheless, the Biot model is used in [96] for 65 mm glass wool applied to a panel and the computed FE response of the sound transmission fits well to measurements.

The resulting effective speed of sound $\underline{c}_{\text{eff}}$ on the basis of the above mentioned models is shown in Fig. 4.21 (a) for the uncompressed material. The values are calculated every 25 Hz while the results based on ASTM E2611-09 are smoothed (mean value at sampling points ±10 Hz). Compared to air ($c_0 = 341.5\,\text{m/s}$ under experimental conditions), a sound wave propagates about half as fast in the glass wool. Furthermore, a strong frequency-dependency can be observed as expected from previous experiments. All four curves follow a similar trend and show comparable magnitudes. With lower frequency, the JCA-limp model considering the frame density yields a higher real part of $\underline{c}$. The ASTM measurement is not correlating well to the models which might be rooted in a suitability of the models in different frequency ranges. In general, the curves of the uncompressed glass wool compare well to results in [130] calculated by the JCA-limp model. This indicates a reasonable input parameter basis.

Under compression, modelling assumptions by [42] are considered in order to calculate the necessary parameters with $r_c = 50\,\%$ as given in Eqs. (4.4)–(4.8).

$$\sigma_{\text{compr}} = \sigma/(1 - r_c)^2 \tag{4.4}$$

$$\Phi_{\text{compr}} = 1 - (1 - r_c)^{-1}(1 - \Phi) \tag{4.5}$$

$$\alpha_{\infty,\text{compr}} = 1 - (1 - r_c)^{-1}(1 - \alpha_\infty) \tag{4.6}$$

$$\lambda_{\text{compr}} = \lambda(1 - r_c) \tag{4.7}$$

$$\lambda'_{\text{compr}} = \lambda'(1 - r_c) \tag{4.8}$$

$$\rho_{g,\text{compr}} = \rho_g/(1 - r_c) \tag{4.9}$$

The bulk density ρ_g is linearly increased by compression (Eq. (4.9), which leads to lower wave speeds as shown in Fig. 4.21. The ASTM and JCA-limp results fit well above 300 Hz for the real and imaginary part. Below this frequency, a measurement or modelling error can be expected in one of the curves. Significant deviations in the real part can be observed for the Delany-Bazley and the JCA model compared to the ASTM and JCA-limp model.

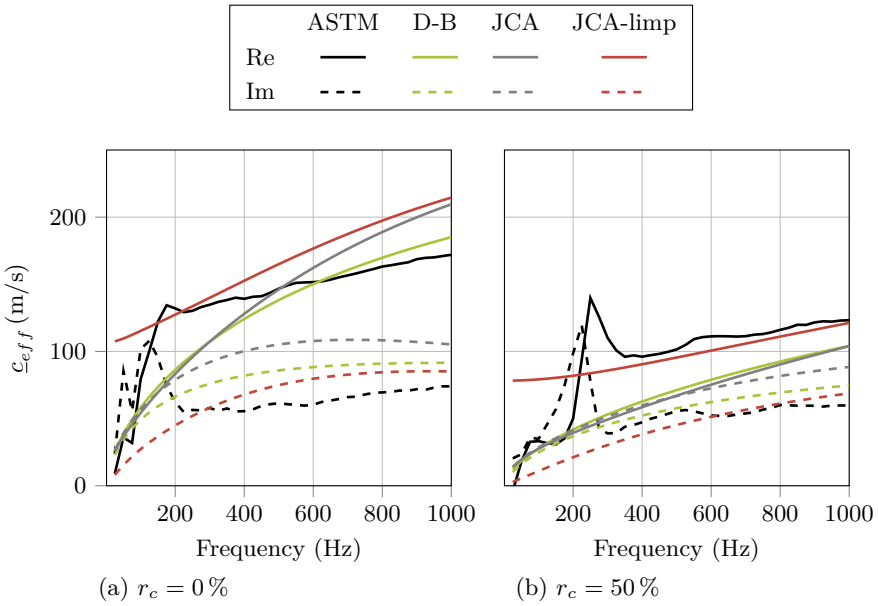

(a) $r_c = 0\,\%$ (b) $r_c = 50\,\%$

Figure 4.21: Comparison of modelling approaches for the effective speed of sound $\underline{c}_{\text{eff}}$ of aircraft grade glass wool under different compression rates r_c

The second parameter for the equivalent fluid model is the effective density ρ_{eff} shown in Fig. 4.22 (a) without compression. All curves have a similar trend of decreasing magnitudes with increasing frequency. Below 200 Hz, the JCA-limp model yields a deviation compared to D-B and JCA due to the consideration of the frame density. Again, compared to the JCA-limp model applied in [130], the curves are in a good agreement.

In Fig. 4.22 (b), $\underline{\rho}$ is displayed for the compressed case. A clear similarity between the ASTM and JCA-limp models can be seen while the D-B and JCA models have a

significant broadband deviation. The increase in density by compression is captured well by the JCA-limp model which can be seen in the entire frequency range comparing with the uncompressed case.

In summary, by the studied models for an equivalent fluid, higher deviations with compression and in lower frequency regions are depicted. Compression is important if the assembly considers more glass wool blankets compared to the double wall gap or if glass wool is laid around stringers and frames. The low frequency range is important for applications like propeller noise – here the model must be well-chosen. In opposite, a low absorption is expected in these regions which might decrease the importance of the insulation model within the fuselage system.

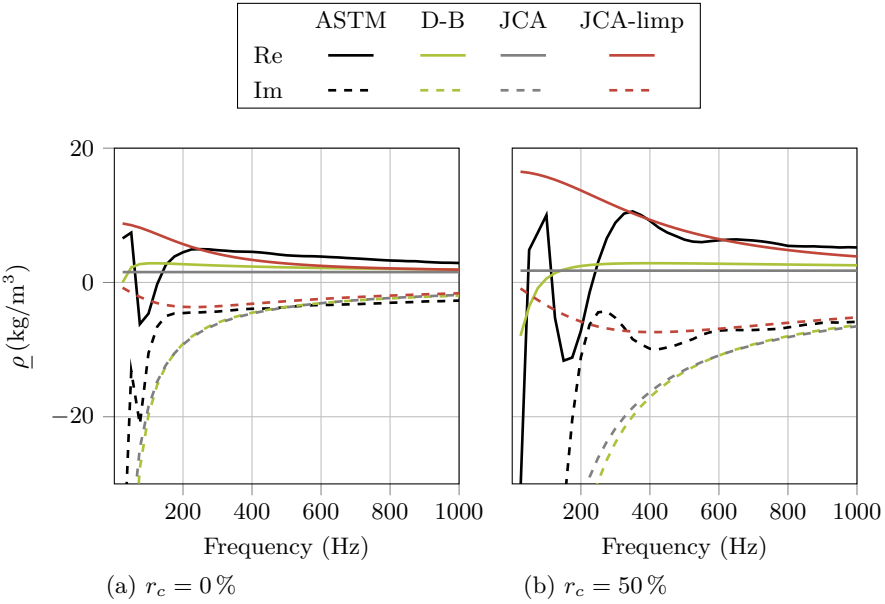

(a) $r_c = 0\,\%$ (b) $r_c = 50\,\%$

Figure 4.22: Comparison of modelling approaches for the effective density $\underline{\rho}_{\text{eff}}$ of aircraft grade glass wool under different compression rates r_c

In order to study the absorption behaviour of insulation stacks represented by the above models, an FE model of a tube shown in Fig. 4.23 is used. At the left end, a Neumann boundary condition is applied introducing a particle velocity similar to the loudspeaker in an impedance tube. At the right end, the domain Ω_g is represented by the porous material models. Ω_0 is a real-valued Helmholtz domain (air). According to [2], the sound pressure is evaluated at two microphone positions in order to calculate $\alpha(f)$. A comparison of $\alpha(f)$ indicates a valid modelling under sound incidence. For the mesh, 27-node hexahedrons with quadratic ansatzfunctions are used which are

implemented in the in-house code elPaSo and used in the aircraft model as well. The frequency domain is sampled by a step size of 25 Hz in order to get smooth absorption curves.

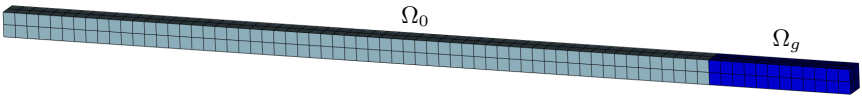

Figure 4.23: FE model of the impedance tube using 27-node hexahedron elements

The resulting absorption coefficients $\alpha(f)$ for the numerical impedance tube calculations are shown in Fig. 4.24. The above mentioned partly estimated parameters are used. Without compression (Fig. 4.24 (a)), a good agreement is observed with a maximum deviation of 0.15 by the JCA model at around 700 Hz. Surprisingly, the D-B model fits well though only one parameter is required. Reasons might be the fact that the D-B model is developed for fibrous material and that the characteristic lengths are estimated for the JCA model. The latter may introduce additional errors, which is always the trade off considering more parameters. By the JCA-limp model and by the direct ASTM measurements, a comparable result in the low frequency range is obtained.

Under compression (Fig. 4.24 (b)), the JCA-limp model yields the best result with a slight frequency shift to lower frequencies. The results of the JCA and of the D-B model do not show a similarity to the measured curve any more. The increased density seems to introduce significant effects as the consideration of a limp mass is the major difference in the JCA-limp model. These results indicate that at least the mass of the frame plays an essential role. The ASTM results fit well up to 400 Hz. Above this frequency, $\alpha(f)$ is lightly underestimated (up to 0.15). In conclusion, the JCA-limp model and the ASTM measurement can be used to model compressed glass wool by an equivalent fluid under normal sound incidence.

As the $\alpha(f)$ in the limp model based on the JCA approximation fits well to the experimental curves and offers high flexibility (compared to ASTM), a parameter fitting is conducted for this model. The two parameters λ and λ' are taken from literature and not explicitly known for the glass wool applied here. The inverse fitting of porous material parameters is described in [21, 128]. For this simple setup of a porous layer backed by a rigid wall under normal sound incidence, $\alpha(f)$ can also

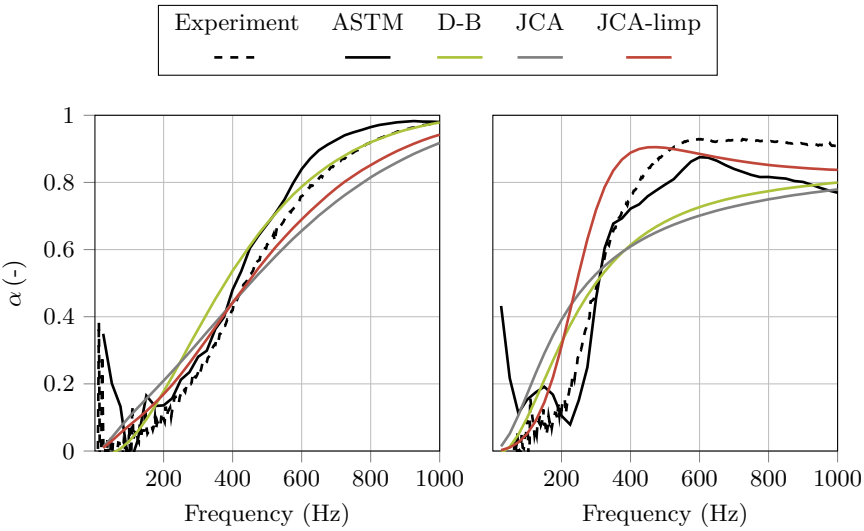

(a) $t_g = 60\,\text{mm}$ $r_c = 0\,\%$ (b) $t_g = 60\,\text{mm}$ $r_c = 50\,\%$

Figure 4.24: Numerical results for the absorption coefficient $\alpha(f)$ of aircraft grade glass wool for different compression rates r_c under normal sound incidence in comparison to impedance tube measurements

be computed analytically by Eqs. (4.10) to (4.12) [14].

$$\alpha = 1 - |R|^2 \tag{4.10}$$

$$R = \frac{Z - Z_{c,0}}{Z + Z_{c,0}} \tag{4.11}$$

$$Z = -iZ_{c,g}\frac{\cos(k_g t_g)}{\sin(k_g t_g)} \tag{4.12}$$

R is the reflection coefficient, Z is the impedance at the glass wool surface, $Z_{c,0}$ and $Z_{c,g}$ are the characteristic impedances of air and the glass wool, respectively, and k_g is the wave number within the glass wool layer. $Z_{c,g}$ and k_g are calculated based on $\underline{c}$ and $\underline{\rho}$ given by the JCA-limp model and its parameters above. This way, the same α is obtained as by the FE-model[10]. Hence, this setup is used for a parameter variation of λ and λ' in combination with a least squares objective function. For the uncompressed glass wool, the identified optimal parameters are $\lambda = 41\mu\text{m}$ and $\lambda' = 596\mu\text{m}$, yielding $\alpha(f)$ shown in Fig. 4.25 (a). The curve almost perfectly fits the measurement.

In opposite, for the compressed glass wool, the identified parameters change to

[10] Though the method is fast and suitable for the parameter study, the final results are calculated by the FEM in order to show the validity as the same implementation is used in the aircraft model.

$\lambda = 69\mu m$ and $\lambda' = 3848\mu m$. The according $\alpha(f)$ is shown in Fig. 4.25 (b). Also, the curve for the compressed state shows a high quality with a maximum deviation below 0.1 at the highest frequency. Of course, a change of the identified characteristic lengths is not expected by compression as Eqs. (4.7) and (4.8) are applied. The parameters are not expected to change if the model perfectly covers the effect of the compression. Alternatively, the compression model may not cover properly the change of fibre directions due to compression or the JCA-limp model may allow different parameter combinations yielding similar results. However, the JCA-limp model is capable of reproducing the absorption behaviour under normal sound incidence and can be applied for this case if the characteristic lengths are re-fitted for the compressed case.

In addition to all above mentioned models, the **Biot** model according to Eqs. (2.46) and (2.47) considers the elasticity of the skeleton's structural phase and the coupling of the skeleton to the surrounding air within Ω_g. The Biot model allows for the propagation of longitudinal and shear waves in Ω_g. A first comparison between the JCA-limp model and the Biot model is reasonable at this point. In [153, 137], the elastic behaviour of glass wool is described as transversally isotropic. In [153], accordingly, two Young's moduli E_1 and E_3 are measured, including derived damping loss factors. The latter belongs to the softer direction perpendicular to the glass wool blankets relevant under normal sound incidence. The entire parameter set for the Biot model is summarised in Tab. 4.8, which is an extension of the JCA-limp model parameters by elasticity parameters. A frequency-dependency of the elastic parameters is observed in [153] but neglected here for simplicity. Reasons are that the values for E_1 are almost constant above 60 Hz, which can be observed for E_3 above 20 Hz as well. The measured material is similar to the aircraft grade glass wool investigated here. For the Poisson ratio ν, [137] states a value of zero which is adopted here. By use of these parameters within the tube model, $\alpha(f)$ shown in Fig. 4.25 (a)/(b) are yielded. The absorption behaviour of the two models almost perfectly agrees. The consideration of the structural phase by the Biot model introduces a non-relevant additional absorption at frequencies below 500 Hz for the uncompressed model. For the compressed model, a slight difference can be observed up to 1000 Hz, which is induced by the higher density due to compression. Under normal sound incidence, the Biot model does not introduce a significant change in the resulting absorption curves and should not be considered for this case as the model requires three additional dof for the structural phase.

Nevertheless, the results under fluid excitation are a positive indicator for the valid application of the model in a fuselage double wall. The thin outer skin is directly

Table 4.8: Biot parameters of uncompressed aircraft grade glass wool [153, 137].

Quantity	Variable	Value	Unit
Young's modulus (in-plane/in-fibre)	E_1	12.0e3	N/m^2
Young's modulus (normal)	E_3	2.6e6	N/m^2
Poisson ratio	ν	0	-
Bulk density	ρ_g	7.68	kg/m^3
Flow resistivity (normal)	σ	11617	Ns/m^4
Porosity	Φ_g	99.7	-
Tortuosity	α_∞	1.1	-
Viscous char. length	λ	41.0e−6	m
Thermal char. length	λ'	596.0e−6	m

exciting the structural *and* the fluid phase of the glass wool due to its transversal deflection induced by occurring bending waves. Similarly, the interior lining is directly excited by the structural phase of the glass wool. Hence, a double wall model is built on the basis of the stiffened and fixed CFRP panel section (see Sec. 4.1) in order to investigate the influence of the glass wool's elasticity in a more realistic setup. For this purpose, the stiffened CFRP panel section is extended by a trim consisting of 0.1 m thick glass wool and a typical sandwich panel representing the secondary structure. For sake of simplicity, the sandwich panel is homogenised by the sandwich theory [15] and orthotropic parameters are taken from [10]. This representation is assumed to be valid for an assessment of different porous material models. Detailed studies on the interior lining are conducted within the next section. The double wall model is shown in Fig. 4.26 – the interior and outer structures are connected by the glass wool insulation only. As excitation, a plane wave is generated using identical parameters compared to Sec. 4.1, but exciting the entire outer skin. All three domains Ω_s, Ω_g and Ω_t are meshed by quadratic elements (9-node quadrilaterals for the shells and 27-node hexahedrons for the 3D equivalent fluid/porous domain) and a strong coupling is considered between adjacent domains. The mean squared velocity $\overline{v^2}$ of the interior trim panel is evaluated for the assessment. As the particle velocity in the cabin fluid of the aircraft model is mechanically coupled with the interior trim panel's velocity (in the following chapters), $\overline{v^2}$ is expected to be a meaningful measure for the model assessment conducted here.

The insulation domain Ω_g is modelled by the JCA-limp and the Biot model. The latter is considered as isotropic within the structural domain (E_3 from Tab. 4.8 is used). In Fig. 4.27 (a), the resulting $\overline{v^2}$ of the interior lining is shown for the two modelling approaches. Though a similarity in the overall curve shape can be observed,

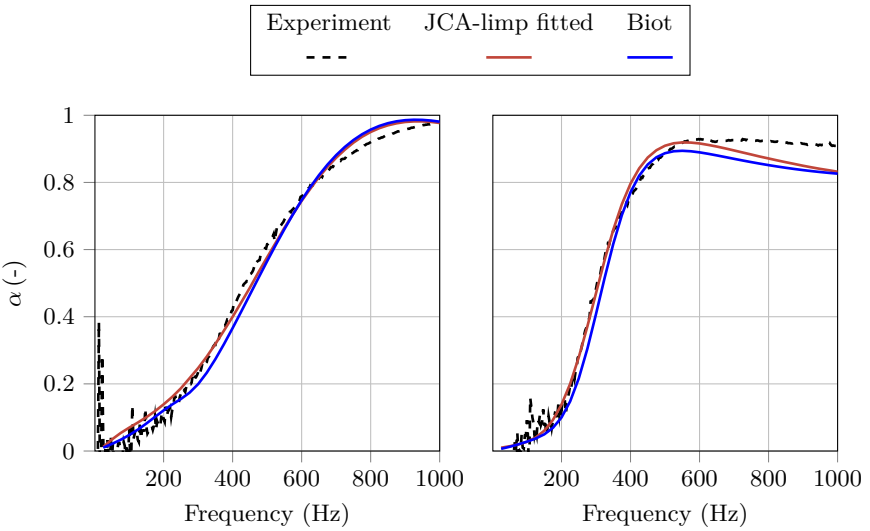

(a) $t_g = 60\,\text{mm}$ $r_c = 0\,\%$ (b) $t_g = 60\,\text{mm}$ $r_c = 50\,\%$

Figure 4.25: Fitted numerical results for the absorption coefficient $\alpha(f)$ of aircraft grade glass wool for different compression rates r_c under normal sound incidence in comparison to impedance tube measurements

the interior trim panel vibrates less in the entire frequency range if the Biot model is applied. The resonances of the panel are more clearly visible within the section considering the JCA-limp model, which indicates a significant effect of the structural phase covered by the Biot model. For instance, at 100 Hz, the (2x2) resonance of the interior trim panel is completely suppressed if the Biot model is applied. At this frequency, a dominant deflection shape within the structural phase of Ω_g occurs. The effect seems to be similar to a vibration absorber. This underlines the necessity for considering the structural phase for this setup. In this example, half the wavelength fits the gap thickness of the double wall. Of course, a crucial dependency on the geometry and the material parameters is present. In literature, frequency-dependent Young's moduli on glass wool are scarcely available despite the above used references. In [153], strong dependencies on frequency and density are indicated. Hence, a deeper study of elastic parameters for glass wool is recommended for further investigations. In addition, the effect of compression is assumed to play an important role.

Coming back to Fig. 4.27 (a), an increase of damping and a decrease of the admittance is visible with higher frequency. The overall difference between the models is smaller above 700 Hz. Deviations up to 5 dB are visible, which is still more than a doubling of the structure-borne sound energy carried by the interior trim panel. At lower frequencies, especially at 100 Hz, significant differences up to 15 dB are observable

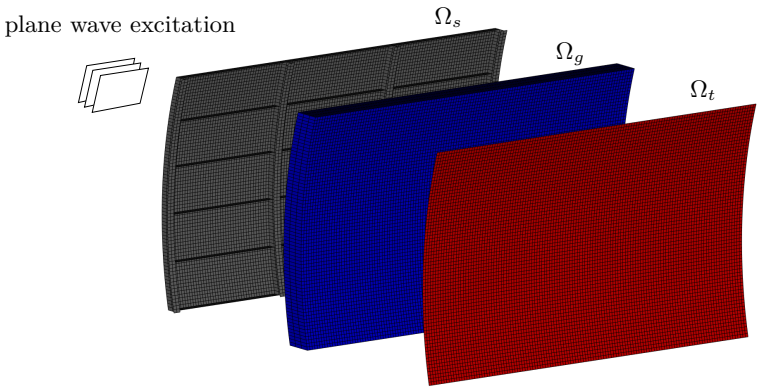

Figure 4.26: FE model of a trimmed stiffened panel section

between the two modelling approaches. Compared to the fluid excitation used above (impedance tube setup), the present results clearly depict significant differences using the Biot model for this setup. Apparently, this can not be shown by numerical impedance tube tests only.

Compressed glass wool is considered in parallel to the above described procedure using Eqs. (4.4)–(4.9). Only the characteristic lengths are taken by the fitting results. In the model, the Young's modulus is assumed to be constant under compression. As fibres are oriented by compression, a reduction of the Young's modulus is expected, while an increase of the Young's modulus is expected by approaching adjacent fibres. The change of the Young's modulus is not available in literature and can not be measured easily. However, the comparison of the models (assuming a constant Young's modulus) is shown in Fig. 4.27 (b). The deviations between the two approaches are similar to the uncompressed results. Again, the Biot model predicts higher damping performances yielding smaller amplitudes over the entire frequency range. As the mass is higher, the difference falls below 5 dB already at 500 Hz.

Concluding the comparison of the JCA-limp and the Biot model, the latter shall be preferred in the aircraft model as the models induce significantly different vibrations to the interior trim panel. Deviation between the two models generally reduces with increasing frequency, which indicates a lower influence of the structural domain. In addition, the difference is slightly reduced by compression which means a smaller difference is expectable at lower frequencies. Nevertheless, these studies must be taken with care as, especially for the structural phase, a specific parameter set is chosen from literature. Furthermore, one major aspect is the assumption of a entirely filled air gap between the outer skin and the interior lining. If glass wool blankets are attached to both sides (compare Fig. 4.14), a wave propagation within the structural

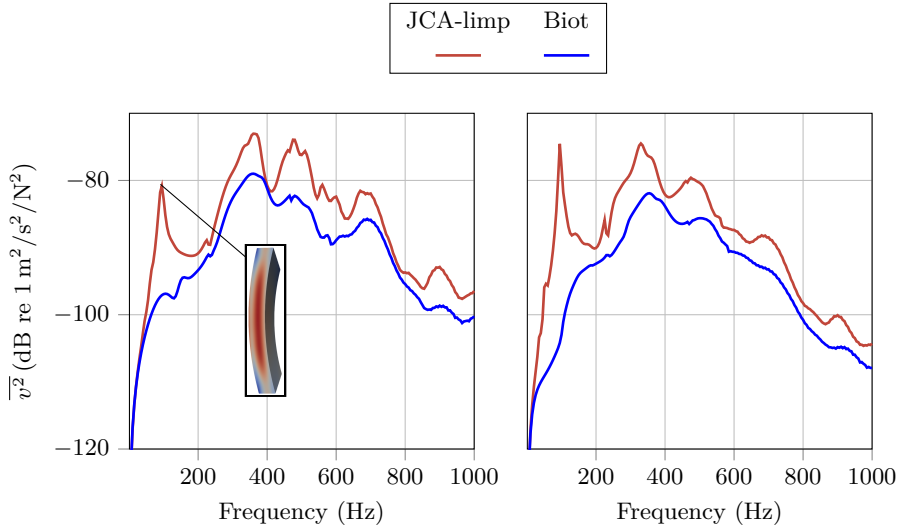

(a) $t_g = 100\,\text{mm}$ $r_c = 0\,\%$ (b) $t_g = 100\,\text{mm}$ $r_c = 50\,\%$

Figure 4.27: Numerical results for the mean squared velocity $\overline{v^2}$ of the interior trim panel under plane wave excitation of the primary structure for different compression rates r_c and different models for the insulation domain

phase is interrupted. Hence, a model considering an air gap with one third of the entire double wall gap is investigated exemplary. This air gap is placed centrally between the two glass wool domains adjacent to the structures, respectively. The resulting $\overline{v^2}$ is plotted in Fig. 4.28 for the two modelling approaches. The induced change by the air gap within the JCA-limp model is rather small as a similar curve shape can be noted and deviations of less than 5 dB are prominent in the entire frequency range. If the JCA-limp model is applied to a configuration with or without air gap, detailed knowledge of the glass wool application and the dimension of the gap does not seem to be decisive for the result. For the Biot model, the induced change by the air gap is slightly higher (up to 7 dB). For the configuration with air gap, the difference between the models is slightly smaller above 200 Hz compared to the completely filled air gap. Below 200 Hz, distinct differences can be observed, which again are expected to be highly dependent on the material parameters of the structural phase. Between 550 and 750 Hz, the deviation increases locally up to 6 dB, while above 750 Hz, a difference below 2 dB is visible. An additional air gap leads to a smaller difference by neglecting the structural phase. This might be an option to save computational costs, keeping the potential modelling error in mind. Again, the material parameters of the structural phase must be taken with care as they definitely induce parameter errors.

For the aircraft model, the JCA-limp model must be used as the uncertainty of the structural material parameters cannot be clarified in the frame of this thesis. Furthermore, the Biot model requires drastically more dof and additional couplings between them. This fact increases the computational costs crucially, which limits the frequency range. This can not be investigated on the available server capabilities.

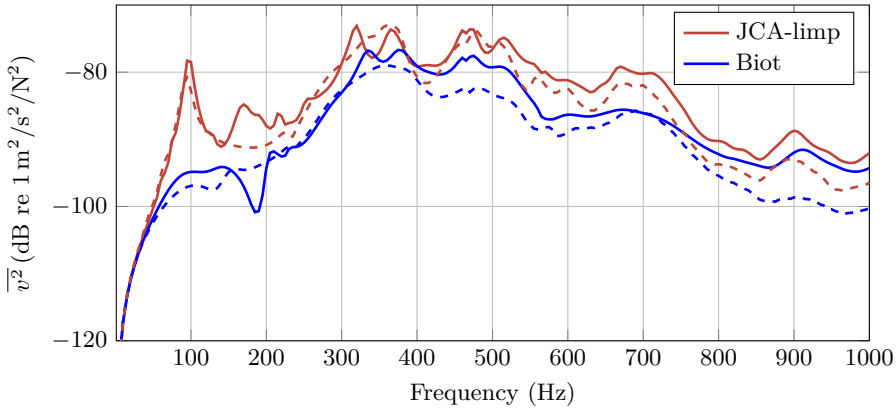

Figure 4.28: Numerical results for the mean squared velocity $\overline{v^2}$ of the interior trim panel under plane wave excitation of the primary structure for different models for the insulation domain including an air gap (dashed lines: results without air gap)

Concluding the section on aircraft grade glass wool insulation, the following statements are derived and considered for the full aircraft model:

- A glass wool stack of 60 mm yields absorption coefficients near 1 at 1000 Hz under normal sound incidence. Compression of the material even increases $\alpha(f)$ at low frequencies, while a compression of 50 % yields values around 0.9 at 500 Hz. In general, oblique incidence of sound further increases $\alpha(f)$. Testing a model with neglected transfer path through the insulation at high frequencies might be successful in saving computational costs as off-diagonal coupling terms are reduced.
- The influence of plastic moisture film coverings on the absorption behaviour of the glass wool is not significant below 1000 Hz.
- Compression of the insulation mainly leads to a higher flow resistivity σ, significantly influences the absorption behaviour and shall be considered if relevant in the assembly. Here, a compression rate of 25 % is considered.
- A direct measurement of equivalent fluid parameters or the JCA-limp model yields good results under normal sound incidence for different compression rates,

while the D-B and the JCA model fail predicting the behaviour under high compression.

- In opposite, if the glass wool is applied between two vibrating structures (distance 0.1 m; completely filled; no compression; specific material parameter set from literature) similar to an aircraft double wall, the Biot model is necessary up to 700 Hz. This is due to significant differences in the vibration of the second panel that can be observed when compared to the JCA-limp model. Above 700 Hz, the difference of the structure-borne sound energy of the interior trim panel is around 5 dB. Under compression, the differences slightly decrease and a use of the JCA-limp model is rather possible at lower frequencies.
- If an air gap (1/3 of the double wall distance) is present between two glass wool layers, the picture slightly changes to an even smaller difference between the models. The material parameter uncertainties, especially those of the structural phase, and a visible difference up to 6 dB above 200 Hz remain. Nevertheless, assuming the model to be representative, in low frequency ranges, the Biot model is necessary because of the above reasons.
- The findings clearly point out the need for
  - the Biot model *and*
  - further studies on the structural material parameters of glass wool in order to precisely consider local resonance effects, especially in low frequency ranges

  The combination of uncertain material parameters and high computational costs for the Biot model creates the constraint of using the JCA-limp model for the full aircraft model within this thesis, as explained above.

4.3 Interior lining

Typical representatives of the interior lining (interior trim) of an aircraft cabin are side panels, ceiling panels or luggage compartment doors. As motivated, these structures are directly coupled to the cabin fluid resulting in a sound propagation through these panels into the passenger cabin and vice versa. Hence, an appropriate modelling of the interior lining is expected to be crucial for the aircraft model. In this section, experimental studies on the dynamic response of a typical structural design are conducted. On this basis, several modelling approaches are identified and tested. Finally, the selected model is considered within a realistic aircraft section in order to show investigate the behaviour within a usual system environment.

A typical interior trim panel consists of honeycomb sandwiches combining a lightweight core and thin face sheets made of glass fibre reinforced plastics [56]. Alternatively, CFRP is used for the covering layers [130]. For the generic aircraft model in this thesis, a valid model of such a sandwich structure is aimed for. In Fig. 4.29 (a), a side panel of an Airbus A320 aircraft including two windows is shown. On the right hand-side (b), the derived modelling problem is sketched. Any windows and joints are excluded for the validation process in order to get an appropriate model for the basic structure which is expected to be mainly relevant for the transmission of sound. Again (similar to the previous parts), the basic model of a sandwich without details like windows and joints allows a derivation of general findings (on modelling and solution efficiency) and enables a transferability to real aircraft configurations in industry.

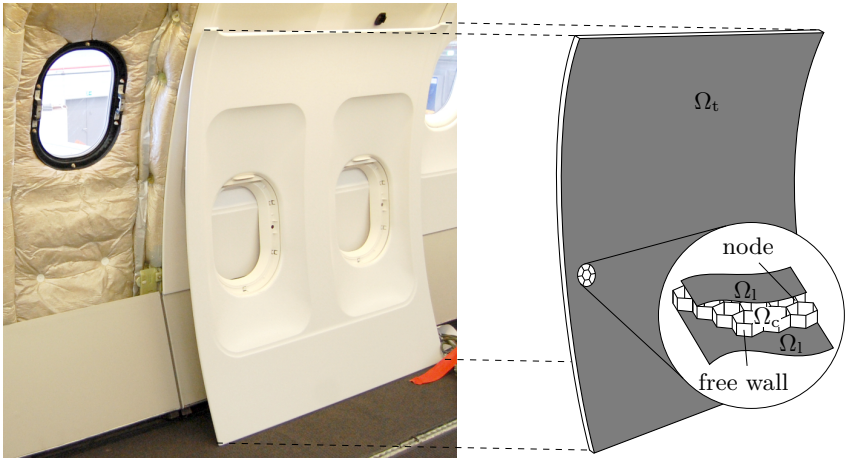

(a) (b)

Figure 4.29: (a) Typical inner side panel of a commercial Airbus A320 passenger aircraft[11] and (b) generalised problem for the generic aircraft model

In the sketch (Fig. 4.29 (b)), the sandwich is split into two domains: Ω_c for the core and Ω_l for the GFRP layers. In the manufacturing process of the honeycomb core, thin aramid fibre reinforced plastic layers are coated partially by adhesives and stacked on top of each other [56]. The adhesive strips are applied with a distance of half the cell width, resulting in a doubled thickness at these positions in the final regular honeycomb core. While the glued walls of doubled thickness are called *nodes*, the others are called *free walls* [33]. After a heated pressing of the stack with partially glued foils, an expansion of the stack results in a honeycomb web as shown in Fig. 4.29

[11] The author thanks Sebastian Deubler (DLR Braunschweig) for the opportunity to take photos of the Airbus A320-232 D-ATRA [9] interior.

(b) [56]. In order to yield required mechanical properties, these *green honeycombs* are dipped into a phenolic coating which is cured [56]. A prominent commercial example is Nomex® [56]. Between the two outer layers and the honeycomb core, an adhesive is used, which may – in dependency on the manufacturing procedure – cover the cell walls as well [56]. As a first general assumption, the mechanical effect of the adhesive is neglected or rather expected to be considerable within the two domains Ω_c and Ω_l.

Experiment

For an experimental characterisation of a typical interior lining structure, a flat 6 mm honeycomb sandwich plate with GFRP layers is available within the CRC 880 project and shown in Fig. 4.30. The decoration foil is typically used as finish in aircraft interior trim panels and therefore considered in the experiments as well. Data of the full plate is given in Tab. 4.9. The 5 mm thick honeycomb core contains free walls and nodes (double thickness) and is made of an aramid fibre composite similar to Nomex® paper. The 0.5 mm thick GFRP layers are composed by fabrics and an epoxy matrix. Of course, many variants of core and face sheet combinations occur in different aircraft configurations. The flat 6 mm plate serves as example in order to demonstrate appropriate modelling options.

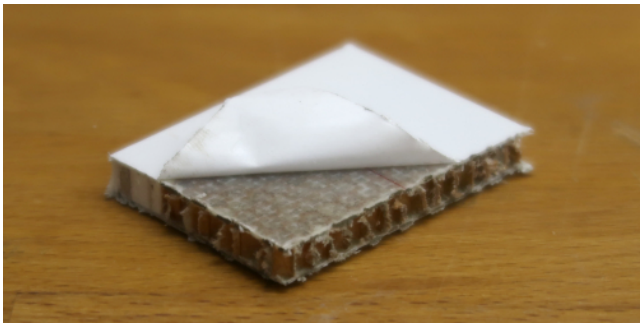

Figure 4.30: Cut out piece of the investigated honeycomb sandwich plate with aramid core, GFRP layers and decoration foil

The experimental setup for measuring the dynamic response of the plate is shown in Fig. 4.31. Similar to the CFRP plates, the sandwich plate is suspended by thin nylon threads on a traverse realising an almost free vibration. The normal direction of the nodes points into the depicted global y-direction of the plate (along width b) which is important for the modelling part. A point excitation is realised by an electrodynamic shaker (type "The Modal Shop SmartShaker") with a force sensor (type "PCB 208C01", weight 0.024 kg) at the tip. A 5 mm drilling hole for a threaded rod made of plastics allows a fixed connection between the sensor and the plate.

Table 4.9: Investigated honeycomb sandwich plate

Quantity	Variable	Value	Unit
Length	a	0.740	m
Width	b	0.305	m
Total thickness	t	6.00	mm
Total density	ρ_s	390.7	kg/m^3
Core thickness	t_c	5.00	mm
Free wall thickness	t_w	0.1	mm
Free wall width	b_w	2.0	mm
Node thickness	t_n	0.2	mm
Node width	b_n	2.0	mm
Layer thickness	t_l	0.50	mm
Decoration film thickness	t_d	0.1	mm

The velocity of the face sheets is measured by a laser scanning vibrometer (type "Optomet SWIR SLDV"). An equidistant grid of 55 vibrometer measuring points is used according to Fig. 4.31 at the top right. The same locations are considered for the model comparison assuming that a valid admittance at these points ensure a valid overall dynamic behaviour of the plate. For completeness, all relevant data on the experimental setting is collected in Tab. 4.10.

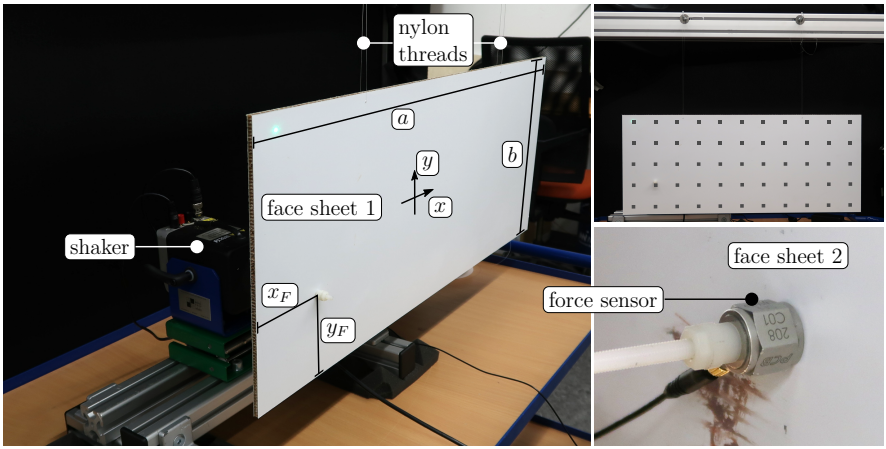

Figure 4.31: Experimental setup of the investigated honeycomb sandwich plate

Two main measurements are conducted, for which the orientation of the sandwich is flipped (excitation and velocity measurement). In Fig. 4.32, the mean squared admittance $\overline{h^2}(f)$ according to Eq. (4.1) is plotted for both orientations. Ideally, the

Table 4.10: Settings for the experimental investigation of a honeycomb sandwich plate.

Quantity	Variable	Value	Unit
Sampling rate	f_s	3200	Hz
Frequency lines	n_{lines}	3200	–
Averages	n_{avg}	3	–
Number of measuring points (front)	n_{points}	55	–
Force position (backside)	$[x_F, y_F]$	$[0.1, 0.1]$	m
Temperature	T	19	°C
Relative humidity	RH	62	%

dynamic response is expected to be identical as the plate is symmetric. In the entire frequency range, an almost equal course is visible with occasional deviations up to 6 dB in the resonances. A slightly higher damping performance within the dynamic response can be observed for the setup in which face sheet 2 is measured (compare Fig. 4.31). The resonance frequencies fit well and can be observed in both setups. For the model assessment, similar deviations must be accepted at minimum as the manufacturing process itself seems to bring along uncertainties.

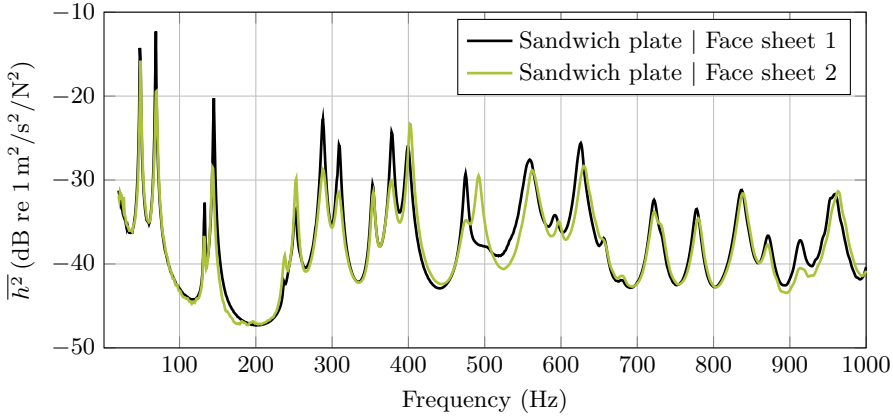

Figure 4.32: Experimental results for mean squared admittance $\overline{h^2}(f)$ of the 6 mm honeycomb plate's two face sheets in comparison

Crucial sources for such deviations are not expected in the measuring setup as the reproducibility is tested and documented in the appendix, Sec. A. For this test of reproducibility, the dynamic response is measured again after reinstalling the entire measuring setup including the specimen (as done for the side-change as well). The results clearly does not show significant deviations. Hence, the differences between the two measurements are expected to be introduced by a non-symmetry of the sandwich

due to manufacturing tolerances.

As the model is assumed to be linear, linearity is demonstrated similar to the CFRP plate. An explanation and the dynamic response can be found in Sec. A. On this basis, linearity is proven for the conducted experiments. Again, this assumption holds true for the investigated specimen and is not shown for the vibration of an interior trim panel in flight. However, from flight experiences, deflections significantly higher than the panel thickness are not expected by the side-walls or ceilings in commercial aircraft under normal flight conditions.

Analogous to Sec. 4.1, the half band method according to [118] is applied for calculating the damping loss factor $\eta(f)$ on the basis of the measured dynamic response. The method is applied for both measured orientations resulting in frequency-dependent values shown in Fig. 4.33. Again, the approximation $\eta(f) = \frac{a}{f} + bf$ is used in order to receive a curve fitting for the model. The parameters a and b are given in Tab. 4.11. The values of $\eta(f)$ roughly vary between 1 and 3 % over the investigated frequency range. Slight tendencies of higher values at frequencies below 100 Hz and towards 1000 Hz can be observed. The fitting curve follows this trend, but a large mismatch of some outliers is visible which is ignored at this stage.

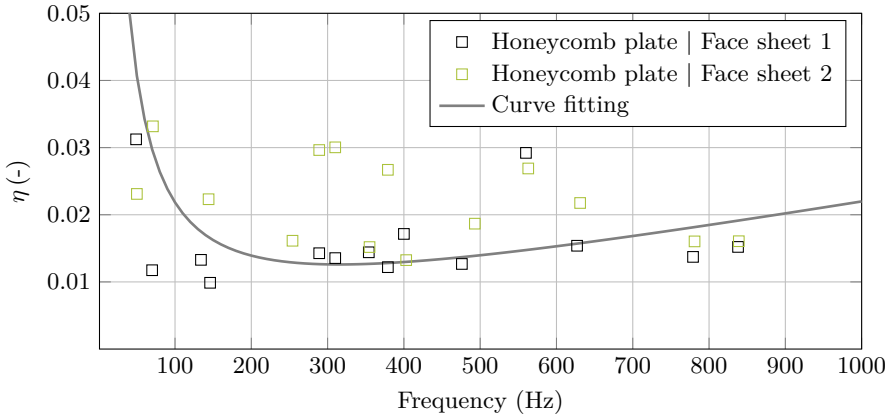

Figure 4.33: Damping loss factors $\eta(f)$ for the honeycomb sandwich plate based on experimental results in Fig. 4.32 and curve fitting ($a = 1.984$, $b = 2.45\text{e-}5$)

Model

Within the sandwich structure, the two relatively stiff GFRP layers are separated by a lightweight core. While the honeycomb core contributes mainly to the required shear stiffness, the outer layers carry most of the stresses induced by bending modes of the

Table 4.11: Curve fitting parameters for the damping loss factor $\eta(f)$ of the sandwich plate

Quantity	Variable	Value	Unit
Curve fitting parameter	a	1.984	-
Curve fitting parameter	b	2.45e-5	-

plate [15]. A mix of shear and bending forces occur within the entire sandwich so that an explicit consideration of the core and the layers is expected to be important for the model. In order to identify the required model complexity for the aircraft model to potentially save computational costs, three modelling variants are compared in the following, for which a sectional view is sketched in Fig. 4.34.

- **3D model** | The full 3D continuum model serves as reference and is shown in Fig. 4.34 on the left. The honeycomb core *and* the two GFRP layers are considered as homogenised continua, for which the FE formulation (general 3D continuum Ω_{s3}) is given in Sec. 2.2. This model already considers assumptions like the homogenisation of core/face sheet and a neglected adhesive.
- **2D/3D model** | The 3D model is reduced by replacing the 3D continuum of the GFRP continuum by a shell formulation perfectly coupled to the core. In Sec. 2.2, the FE formulation for a 2D shell domain Ω_{s2} is given. The core is meshed by 27-node hexahedrons while the face sheets are meshed by 9-node quadrilateral elements (Fig. 4.34 centre). Bending and membrane stiffness of the GFRP shells are treated separately in order to consider the offset of $t_l/2$ correctly (as the nodes are shared with the hexahedrons). The Young's moduli used for the bending stiffness are increased based on the *parallel axis theorem*. For the membrane part, pure bending of the entire sandwich is assumed in order to increase the Young's modulus by the relative change of the distance $(t_c + t_l)/t_c$ to the neutral plane. This way, the shift of the neutral plane within the shells is corrected yielding an error for pure membrane forces, which are not expected in the first line.
- **2D model** | The entire sandwich is modelled by a shell formulation[12] meshed by 9-node quadrilateral elements with quadratic ansatzfunctions (Fig. 4.34 right). Material parameters are received based on the CLT for the Young's moduli and the approach by Rohwer [140] for the shear moduli. Rohwer considers a realistic shear stress distribution with vanishing stresses at the surfaces. This fact is crucial for the sandwich structure with relatively thin face sheets not

[12] The membrane part of the shell is not affected for the experimental setup – nevertheless the element type is used as the membrane part is relevant for curved panels applied later.

contributing significantly to the shear stiffness. Vice versa, the thin face sheets are mainly contributing to the bending stiffness as the distance is maximum and the honeycomb core has significantly lower in-plane Young's moduli.

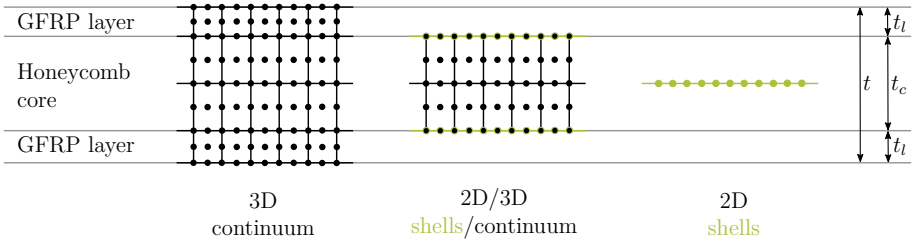

Figure 4.34: Sectional view of the modelling approaches for the honeycomb sandwich plate

GFRP layers (face sheets)

The two GFRP layers are made of two layers of E-Glass filament fabrics with twill weave within an epoxy matrix. The filaments are arranged in $[+45/-45]$ and $[0/90]$. The dominating effect with respect to the bending stiffness of the sandwich is expected to be the combination of the separating honeycomb core and the relatively high membrane stiffness of the face sheets. Hence, each GFRP layer is considered with a transversal isotropic material behaviour with in-plane quasi isotropy and non-symmetric effects of the stack are neglected. As parameters, the in-plane Young's modulus E, Possion ratio ν and the shear moduli G are required besides the known thickness. For the full 3D model, the out-of-plane Young's modulus is required as well.

Similar to Sec. 4.1, micromechanical modelling assumptions within the classical laminate theory (CLT) according to [150] and Eq. (2.24) are used in order to predict homogenised material parameters given in Tab. 4.12. As the specific materials are not known and the elastic material parameters for E-Glass and epoxy are taken from literature [150], the resulting values are expected to be uncertain. In addition, the fibre undulation of the twill weave and manufacturing tolerances are expected to create softening effects within the GFRP structure. Based on this fact, the material data given can be seen as upper bounds.

The calculated density is based on the measured density of the entire sandwich (Tab. 4.9) and the estimated core density (Tab. 4.13). Taking the density of E-Glass ($2540\,\mathrm{kg/m^3}$ [150]) and epoxy ($1100\,\mathrm{kg/m^3}$ [150]), the fibre volume content φ is iteratively accessible according to Eq. (4.13) [150].

$$\rho_l = \rho_{\mathrm{fibre}}\varphi + \rho_{\mathrm{matrix}}(1-\varphi) \tag{4.13}$$

Table 4.12: Material data on the GFRP layer of the sandwich plate based on CLT and base material data in [150]

Quantity	Variable	Value	Unit
Young's modulus (bending)	$E_{bx/by}$	20.0e9	N/m^2
Young's modulus (membrane)	$E_{mx/my}$	21.0e9	N/m^2
Young's modulus	E_z	13.4e9	N/m^2
Poisson ratio (bending)	ν_{xy}	0.129	-
Poisson ratio (membrane)	ν_{xy}	0.129	-
Poisson ratio	$\nu_{xz/yz}$	0.275	-
Shear modulus (bending)	G_{xy}	7.4e9	N/m^2
Shear modulus (membrane)	G_{xy}	7.8e9	N/m^2
Shear modulus	$G_{xz/yz}$	3.3e9	N/m^2
Density	ρ_l	1930.7	kg/m^3
Fibre volume content	φ	0.577	-

Honeycomb core

The resolution of all honeycombs within one panel is possible but currently not conceivable for an entire aircraft fuselage due to extremely high computational costs to be expected. Therefore, a homogenisation approach (e.g. also used in [59]) is applied for the core. Instead of modelling the cell walls explicitly, a 3D continuum is considered between the two GFRP layers. A significant local interaction with the honeycomb web is expected if the wave length has a similar dimension as the combs. The regular combs have a side length of 2 mm which is much below a wave length aimed for within the frame of this thesis.

The geometry of the combs and the orthotropic material behaviour of the base material itself [63] induce an orthotropic material behaviour of the homogenised 3D continuum which requires 9 independent parameters. In [103], an analytical approach for the prediction of these homogenised material parameters is given. It follows theory by Gibson and Ashby [64] and especially improves the direction dependency of the shear moduli for regular honeycombs with nodes of double thickness due to the manufacturing process. The models are implemented within this thesis and require the material parameters of the base material and the comb geometry. The Young's moduli $E_{\text{base},\parallel} = 3.18\text{e}9\,N/m^2$ and $E_{\text{base},\perp} = 1.96\text{e}9\,N/m^2$, the Poisson ratio $\nu_{\text{base}} = 0.24$ and the shear modulus $G_{\text{base}} = 1.26\text{e}9\,N/m^2$ of the base aramid fibre material are taken from experimental data on Nomex® paper in literature [145]. Only few sources are available, but the considered (latest) source [145] is comparable with data from [63]. The honeycomb core of the measured plate is made of a composite highly similar to the Nomex® paper.

In Tab. 4.13, the calculated homogenised material parameters of the honeycomb core are given. The Young's moduli in x and y direction are almost equal as the comb's nodes have hardly any influence. Dominated by the comb geometry, the web almost keeps its volume under tension load which yields an in-plane Poisson ratio near 1. As the out-of-plane Young's modulus is naturally much higher than the in-plane moduli, the out-of-plane Poisson ratios are near 0 according to [103]. However, setting 1 and 0 for ν_{xy} and $\nu_{xz/yz}$, respectively, crucially increases the sensitivity of the element stiffness matrix as D gets small according to Eq. (2.5). For the shear moduli, the out-of-plane parameters are known to be influential to the vibrational behaviour of the sandwich plate. The predicted parameters for G_{xz} are higher than for G_{yz}, which is reasonable as the comb's nodes are tilted only by xy shear forces and are loaded by xz shear forces. In [165], shear moduli of a similar honeycomb (density 80 kg/m^2) are measured – the results are almost equal, which supports the theory. Furthermore, the frequency-dependent behaviour is investigated in [165]. As a deviation less than 10 % is visible up to 1000 Hz, frequency-dependency is neglected here.

Table 4.13: Homogenised material data on the honeycomb core of the sandwich plate based on [103] and base material data in [145]

Quantity	Variable	Value	Unit
Young's modulus (in-plane)	E_x	990.7e3	N/m^2
Young's modulus (in-plane)	E_y	987.2e3	N/m^2
Young's modulus (out-of-plane)	E_z	142.6e6	N/m^2
Poisson ratio (in-plane)	ν_{xy}	0.97778	-
Poisson ratio (out-of-plane)	ν_{xz}	0.00167	-
Poisson ratio (out-of-plane)	ν_{yz}	0.00167	-
Shear modulus (in-plane)	G_{xy}	246.9e3	N/m^2
Shear modulus (out-of-plane)	G_{xz}	58.3e6	N/m^2
Shear modulus (out-of-plane)	G_{yz}	36.0e6	N/m^2
Density	ρ_c	82.7	kg/m^3

Lu and Xin show in [102] that the airborne sound path (in between the combs) in typical sandwich panels is not significant for the transmission loss of the system. Almost all energy is transmitted through the structural part of the core. Hence, in all following models, the air within the combs is explicitly modelled.

The decoration foil is assumed to contribute to the mass and damping properties only. The mass is taken into account by the overall density of the plate yielding the densities of the core and the two GFRP layers. The loss factor $\eta(f)$ of the overall sandwich measured above (see Fig. 4.33) includes the contribution of the damping foil. For

all three models, $\eta(f)$ is applied globally as homogenised parameter, a distinguishing between core and sheets is not conducted.
As the sandwich structure is a lightweight part, half of the sensor mass including the mount is considered as point mass at the force position for all three models. For the full 3D model and the 2D/3D model, the force is divided and separately applied to the two GFRP layers. For the 2D model, the force is applied at one node as the shells do not explicitly have a thickness.
For the full 3D continuum model and the honeycomb core Ω_c in the 2D/3D model, 27-node hexahedron elements with quadratic ansatzfunctions are used (see Fig. 4.34). For the shell domains in the 2D/3D model and the 2D model, quadratic 9-node quadrilateral elements are applied. To ensure a small numeral error, a mean relative error below 1 dB is realised by halving the mesh size (similar to Sec. 4.1 with 200 frequency samples with $\Delta f = 5\,\mathrm{Hz}$).

In Fig. 4.35, the dynamic response of the three models is depicted. For the FE calculation, the material parameters described above are used. The 3D model and the 2D/3D model yield almost equal responses of the plate over the entire frequency range. With regard to computational costs, a use of the 3D model is not reasonable and the face sheets can be modelled by 2D shells. For a curved panel within an aircraft section, a necessity for a 3D model is also not expected. The other way around, the result of the 3D model verifies the implementation of the 2D/3D model.
Up to 450 Hz, the 2D model agrees reasonably well with the 2D/3D model. Above, significant frequency shifts and level deviations occur for the 2D model. As the wave length decreases with frequency, it approaches the honeycomb size and core thickness. These facts generally increase the influence of the core's microstructure and its shear stiffness, which explains the larger deviations by the simplifications within the Mindlin plate (as part of the shell). As shown in Eqs. (2.19) to (2.21), the Mindlin formulation considers the shear stiffness and rotating inertia only by additional linear terms. A non-linear stress distribution over thickness is not considered within the neutral plane. However, slight deviations may be compensated by a material parameter fitting.

The experimental results of face sheet 1 exemplary serve as validation basis. Both, the 2D and the 2D/3D model are too stiff compared to the experiment (appx. Fig. A.5) which is why a parameter study is conducted considering the expected reduced stiffness by the filament fabrics with twill weave. Hence, for the 2D/3D model the Young's moduli of the two GFRP layers are equally lowered. In parallel, the two shear moduli G_{xz} and G_{yz} of the honeycomb core are decreased equally in order to consider

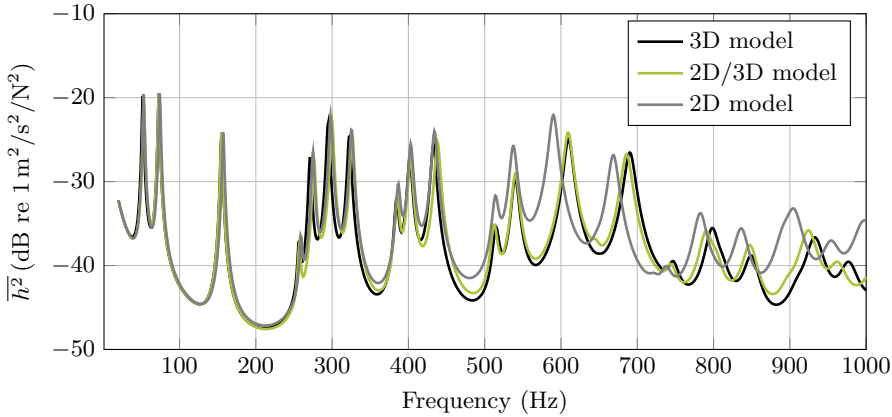

Figure 4.35: Numerical results for the mean squared admittance $\overline{h^2}(f)$ of the 6 mm honeycomb plate – Comparison of three modelling approaches with initial material parameters

systematic uncertainties in the applied models for the core homogenisation. For the 2D model, the homogenised Young's moduli and the shear moduli are reduced directly. This way, a 2D parameter space is spanned and investigated for both models. The step size for each parameter is 2.5 % of the initial parameters down to 50 %. In Fig. 4.36, the dynamic response of the 2D/3D model with fitted material parameters in comparison to the experimental results is shown. The best parameter combination is chosen based on the minimum absolute mean error. The shown result is yielded for Young's moduli decreased by 7.5 % and core shear moduli lowered by 30 % (2D/3D model). For the 2D model, in the best result, only the Young's moduli are decreased by 15 % while the shear moduli are not affected. Under this parameter fitting, both models are capable of reproducing the frequency response of the experiment appropriately to the overall aim of simulating aircraft interior sound pressure levels. Crucial deviations can not be observed in the damping performance. Some isolated resonance peaks are significantly changed in amplitude or shifted in frequency. For example, the model's resonance peak at 500 Hz is hardly visible in the experiment. Compared to Fig. 4.32, this peak can be seen for face sheet 2, which indicates a manufacturing or measurement issue. The deflection shapes within the resonances are compared to the experiment. An appropriate consistency over the entire frequency range can be determined. Above 700 Hz, the 2D/3D model agrees slightly better with the experimental result. One reason is certainly the higher influence of the core for shorter wave lengths. In general, the 2D model captures the experiment almost equally compared to the 2D/3D model under a mechanically justified material parameter fitting.

Both, the 2D and the 2D/3D model are shown to be well suited for the freely sus-

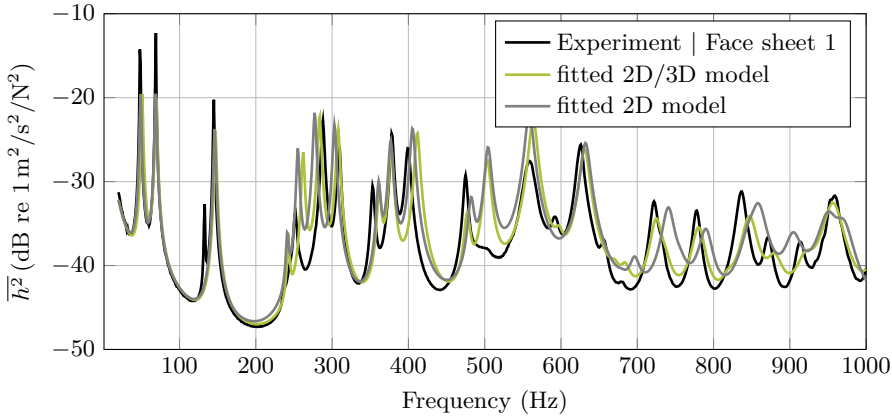

Figure 4.36: Numerical results for the mean squared admittance $\overline{h^2}(f)$ of the 6 mm honeycomb plate – Fitted material parameters of the 2D/3D model

pended flat honeycomb sandwich under point force excitation. The 2D model saves a lot of computational costs and delivers similar results despite visible resonance shifts above 700 Hz. In order to compare the approaches under more realistic conditions, an aircraft section is considered. The section is shown in Fig. 4.38. It is identical to the model with airgap applied in Sec. 4.2 while the following differences are introduced:

- Larger dimension of $1.30 \times 1.04\,\mathrm{m}^2$ are chosen in order to consider a typical size of an interior trim panel. As visible in Fig. 4.29, an interior trim panel covers a distance of two frames which is realised here as well. The height of 1.30 m is yielded by combining data by the CRC 880 and a picture of an Airbus A320. E.g., a comparable interior trim panel is investigated in [112]. Windows are not considered at all. The surrounding outer skin fields serve as boundary condition while all skin fields below the interior trim panel are excited by the plane wave. Insulation material with airgap is considered below the interior trim panel only as depicted in Fig. 4.38.
- Ideal fixture of the interior trim panel to the circumferential frames at the 4 edge positions. This way, the panel shall be excited on the dominating paths in dependency on frequency. In photographs of an Airbus A320 aircraft (Fig. 4.37), typical plastic clips in order to hold the panel can be seen. These clips are idealised by perfectly linked nodes within the FE model. The fixture is comparable to investigations in [112] as well. A major difference again are the windows, which are neglected within this thesis. Hence, the additional fixture of the windows is not considered as well.
- Consideration of the interior trim panel as 2D/3D model besides the 2D model

Figure 4.37: Typical joints of the inner side panel of an Airbus A320[11]

with the finally fitted material parameters

Similar to all previous models, a convergence study is conducted in order to ensure a mean error below 1 dB comparing to the halved mesh size.

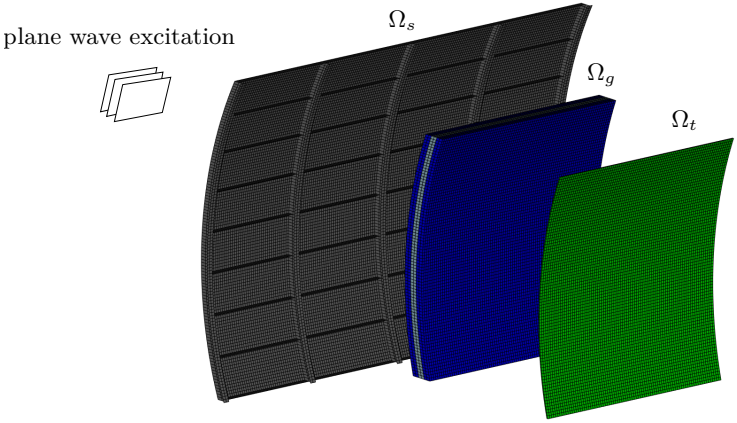

Figure 4.38: FE model of a stiffened panel section with focus on the interior trim panel

In Fig. 4.39, the resulting $\overline{v^2}$ of the interior trim panel is shown comparing the two modelling approaches. For both models, the general decreasing trend of the curves is similar and the values agree reasonably well up to 150 Hz. With increasing frequency, the deviations between the models increase up to 9 dB. From 310 Hz, the 2D model yields systematically higher vibration levels (2-9 dB) of the interior trim panel. Though the 2D model and the 2D/3D model behave quite similar for the flat plate, the larger differences in the aircraft section model may be originated in the curvature

and the embedding into the aircraft section. As the interior trim panel is directly coupled to the cabin fluid, a crucial influence on the resulting SPL is expected. On this basis, the 2D/3D model is finally chosen for the aircraft model.
The perfectly linked nodes between frames and interior trim panel are chosen at the panel's edges for both models. For the 2D model, the node lays within the neutral plane, which is due to the Mindlin theory. Hence, for the 2D/3D model, the central node within the 3D continuum (27-node hexahedrons) of the core is chosen. A selection of a node within one of the GFRP layers leads to high differences below 100 Hz. Comparing with Fig. 4.37, the joints are mounted at the outer surface which can be considered by the 2D/3D model only. However, these facts indicate a need for the 2D/3D model and that further investigations of the joints are reasonable apart from the underlying work. A detailed modelling of non-symmetric joint is only possible within the 2D/3D model. In addition, the 2D/3D model is expected to be even more advantageous if the core thickness increases as the shear effects increase or shift to lower frequencies.

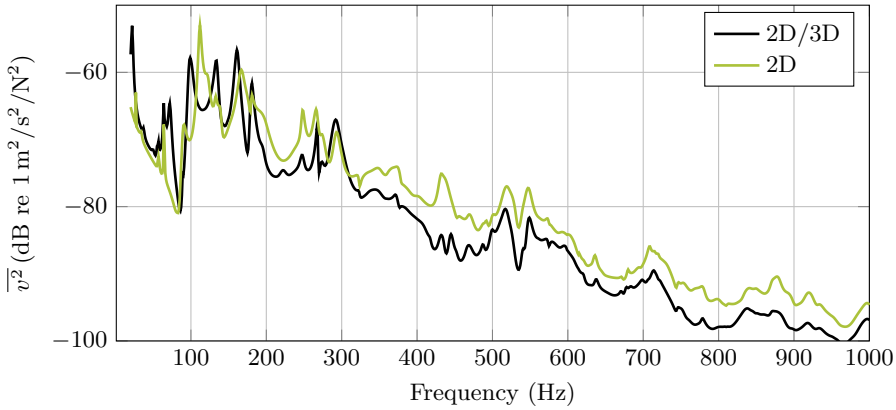

Figure 4.39: Numerical results for the mean squared velocity $\overline{v^2}$ of the interior trim panel under plane wave excitation of the primary structure for two different models for the interior trim panel domain

Concluding the section on the interior lining, the following statements are derived and considered for the aircraft model:

- A pure 2D shell model is capable to capture the vibrational behaviour of an experimentally investigated 6 mm sandwich plate up to 700 Hz. Above, a model considering a 3D continuum core and 2D shell for the two face sheets is reasonable. A full 3D continuum model is not needed. Initial material parameters (CLT and approach by Rohwer) yield reasonably well results up to 450 Hz, which can be improved by a parameter study.

- The material parameters for the GFRP layers can be calculated based on the CLT delivering appropriate results and the material parameter of the core can be calculated based on [103]. For the face sheets, the membrane stiffness is crucial, while the shear moduli are most important for the honeycomb core.
- However, on the basis of a realistic aircraft section, the necessity of the 2D/3D model is shown for a 6 mm sandwich panel (5 mm core and 0.5 mm face sheets).
- For the aircraft model, the 2D/3D model is recommended and considered with the parameter set for the GFRP layers and the honeycomb core of the investigated specimen.

4.4 Passenger cabin

A typical passenger aircraft cabin is shown in Fig. 4.40. As the surrounding structures of the cabin (interior panels, floor) are explicitly considered and strongly coupled to the cabin fluid, the dynamic effects of these domains are covered. Within the cabin fluid itself, seats and passengers are mainly expected to further influence propagating sound waves. Therefore, the focus is laid on the modelling of seats and passengers within this section. As the sound pressure distribution in the cabin represents the final result to be assessed, an appropriate modelling is expected to be essential. A reasonable separation of the cabin domain Ω_c into the pure fluid domain Ω_cf and the seat domain Ω_cs is assumed. While the air itself does not require deep investigations, the domain Ω_cs can be expected to (at least partly) consist of porous materials like foam or fabrics. In dependency on the seat model, air-filled volumes and mechanical springs with a fabric coverage are possible as well. Within the CRC 880 project, a seat bench with homogeneously foam-filled cushions is available. In order to keep the modelling effort realisable and balanced to the overall aim, the following general assumptions on Ω_c are considered:

- A cut-out within the region of typical overhead luggage racks assuming perfectly reflecting boundary conditions and a neglection of the rack's dynamic behaviour
- A neglection of the seat construction and its fixture to the floor

Typical properties of air within a passenger aircraft cabin in cruise are shown in Tab. 4.14. The atmospheric conditions at flight level must be compensated by the aircraft systems yielding an overpressure within the cabin. In addition, the air is dryer than on ground level. For the structural fluid coupling by the inner lining to the cabin fluid, especially the slightly reduced density has to be considered.

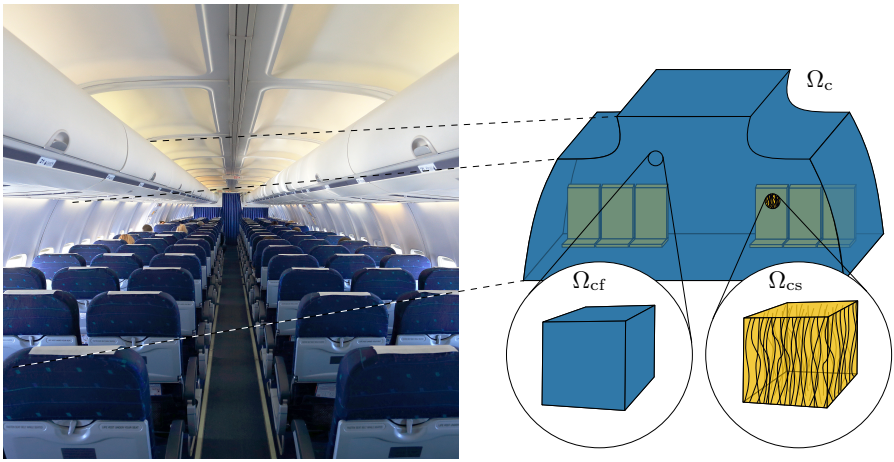

(a) (b)

Figure 4.40: (a) Typical passenger cabin of a commercial passenger aircraft (Source: dimarik/istockphoto.com) and (b) generalised problem for the generic aircraft model

Table 4.14: Typical air properties in aircraft passenger cabins from [117, 74] and by use of mathematical descriptions of ideal gases [35]

Quantity	Variable	Value	Unit
Temperature	T	$23-24$	°C
Relative humidity	RH	$14-19$	%
Static pressure (in cruise)	p_0	75035	$\mathrm{N/m^2}$
Overpressure (in cruise)	Δp	62300	$\mathrm{N/m^2}$
Density	ρ_f	0.88	$\mathrm{kg/m^3}$
Speed of sound	c_f	345.6	m/s

Experiment

The available three aircraft seats[13] are characterised experimentally and shown in Fig. 4.41. The assembly consists of a supporting structure and two cushions for the sitting surface (foam with thickness $t_{\mathrm{sit}} = 0.10\,\mathrm{m}$) and the backrest (foam with thickness $t_{\mathrm{back}} = 0.05\,\mathrm{m}$). The cushions are covered by a fabric and fixed by Velcro at a hard plastic back. Two acoustic measurements are conducted: Reverberation time and impedance measurements within the non-rectangular reverberation chamber (volume $V_{\mathrm{rev}} = 204\,\mathrm{m^3}$) at the PTB (Physikalisch-Technische Bundesanstalt) Braunschweig. This bench shall serve as example in order to show a possible consideration

[13] The author thanks Thomas Haase and Hans Peter Monner for providing the seat bench; Cushions by Greiner PURtec, 2016.

within the aircraft model. Of course, a database of several aircraft seats (certainly with slightly different requirements on the model) is necessary to characterise different cabins properly.

Figure 4.41: Experimental setup for characterisation of aircraft seats within the non-rectangular reverberation chamber at PTB Braunschweig; (a) Empty seats in central position, (b) seats with three passengers[14] and (c) intensity probe above the sitting surface

The reverberation time $T_r(f)$ describes the time in which the sound energy drops to one millionth after the sound source is switched off [113]. $T_r(f)$ is measured within the reverberation chamber equipped by the seat bench according to DIN ISO 354 [5]. A B&K 2270 measurement system with 4 microphones (2x B&K 4165, 2x Norsonic 1220) is used and the average of 5 measurements is considered. By use of the seat's total surface area $A_{\text{seat}} = 2.02\,\text{m}^2$, the equivalent absorption area $A_t(f)$ is computed based on [5]. $A_t(f)$ is a hypothetical quantity of a fully absorbent area, yielding a similar $T_r(f)$ as the measured object [5]. In Fig. 4.42, A_t is shown for the empty and occupied seat bench consisting of three seats. For the occupied case, two colleagues offered their help besides the author himself. Of course, this configuration is not representative.

With increasing frequency, the equivalent absorption area increases in both cases as the sound wave length decreases and the absorption performance of the seat cushions or the passengers increases. Below 200 Hz, A_t drops below $1\,\text{m}^2$, which is out of the recommended range and may bring along uncertainties. At 1000 Hz, the curve approaches a value of $3\,\text{m}^2$. By placing the three shown passengers on the seats, A_t is slightly increased above 300 Hz. In the lower frequency range, A_t is slightly reduced

[14] The author thanks Sebastian and Steffen for supporting the experiment and permitting the usage of this photo.

by placing passengers on the seats. The absorption by passengers depends to a certain extend, among other factors, on the body size and the clothes. On the one hand, the seat surfaces are covered by the passengers. On the other hand, the passenger introduces damping. The two curves give an idea of the relatively small magnitude in which A_t is influenced. A small influence on the cabin SPL is assumed on the basis of these results.

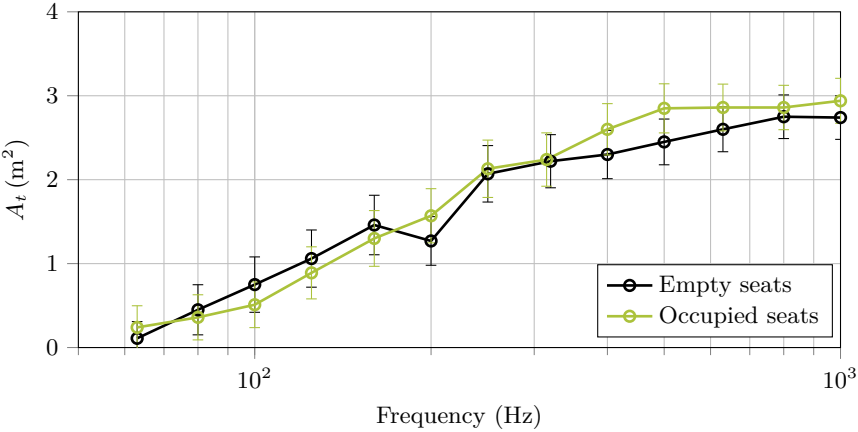

Figure 4.42: Experimental results for the equivalent absorption area A_t of three aircraft seats with and without passengers including reproducibility standard deviations according to [3]

In addition, the surface impedance $\underline{Z}_n$ at normal incidence near the surface of the two cushions is calculated by use of the measured sound pressures of an intensity probe (measuring system Oros or38 with 2 x B&K 4197 microphone pair) as proposed in [13]. The two major assumption for the measurement are:

- Plane waves similar to impedance tube measurements
- Far field conditions, meaning $\underline{Z}_n = \underline{p}/\underline{v}_n$ with the measured sound pressure $\underline{p}$ and the normal particle velocity $\underline{v}_n$ [113]
- Equality of $\underline{Z}_n$ calculated in the centre of the two microphones and the actual surface impedance of the cushion (compare Fig. 4.41; distance between seat surface and centre is 0.06 m)

The first assumption is especially expected to introduce measuring errors at low frequencies as waves enter equally from all directions. In addition, the measurement of the finite gradient between the pressure signals gets more difficult with increasing wave length. However, the authors state an applicability above 500 Hz [13].

$\underline{Z}_n = \underline{p}/\underline{v}_n$ is finally calculated based on the two pressure amplitudes $\hat{p}_1$ and $\hat{p}_2$ measured at the two microphones, respectively, and the phase difference $\Delta\varphi$. The amplitudes are calculated by averaging 750 signals while $\Delta\varphi$ is obtained from the cross-spectrum between the two microphone signals. By use of the finite pressure gradient and the Euler equation, v_n is calculated according to Eq. (4.14) [13, 36].

$$\underline{v}_n = \frac{\hat{p}_2 - \hat{p}_1 \mathrm{e}^{i\Delta\varphi}}{i\rho_f \omega d} \tag{4.14}$$

In Eq. (4.14), i is the imaginary unit, ρ_f is the fluid density during the measurement and d is the spacer distance of the intensity probe. In order to calculate the particle velocity, the first order derivative is used as usual for intensity measurements. Taking the mean pressure value $\underline{p}_a = (\hat{p}_1 + \hat{p}_2)/2$, Eq. (4.15) is yielded.

$$\underline{Z}_n(f) = -\frac{i\omega\rho_f d}{2} \frac{\hat{p}_1 \mathrm{e}^{i\Delta\varphi} + \hat{p}_2}{\hat{p}_2 - \hat{p}_1 \mathrm{e}^{i\Delta\varphi}} \tag{4.15}$$

The resulting surface impedances are shown in Fig. 4.43. Both the backrest and the sitting area are approximately measured according to the described procedure. In the low frequency range ($< 200\,\mathrm{Hz}$), significant variations can be observed in the values which is consistent with the mentioned findings in [13, 36]. In these frequency ranges, rather smooth curves are expected which can be shown by comparing with porous material models or impedance tube measurements. With increasing frequency, the real part of the impedance converges towards the impedance of air ($Z_0 \approx 410\,\mathrm{Ns/m^3}$) and deviates much less. The convergence is physically reasonable as the absorption performance of the seat cushion is expected to increase with reduced wave lengths towards an ideal absorption.

Furthermore, a measurement of the flow resistivity of the two cushions is performed in order to characterise the porous foam material. Due to the cushion's dimensions, a setup according to DIN EN 29053 [4] with sealed sides is not possible. Hence, the results shown in Tab. 4.15 shall be taken with care. Especially for the measurement of the sitting area with its thickness of $t_{\mathrm{sit}} = 0.10\,\mathrm{m}$, significant lateral flows are expected. This may explain the slightly higher value σ_{back} as the backrest is thinner.

Table 4.15: Flow resistivity of seat cushions

Quantity	Variable	Value	Unit
Sitting area	σ_{sit}	31389	$\mathrm{N/m^4/s}$
Backrest	σ_{back}	34500	$\mathrm{N/m^4/s}$

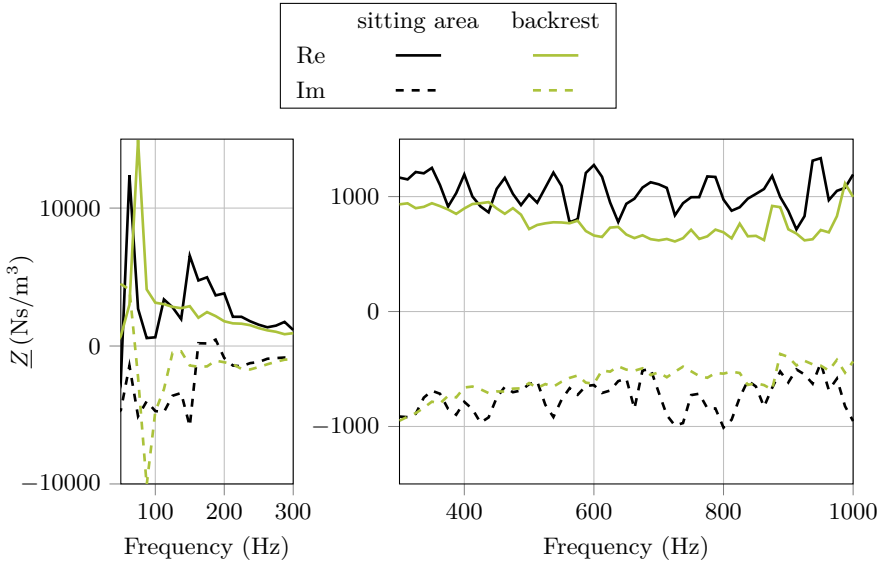

Figure 4.43: Experimental results for the impedance of aircraft seats

Model

The aircraft cabin is filled with air in which solely a propagation of longitudinal (sound) waves is assumed. This assumption is based on the viscosity of air causing non-significant shear stresses [86]. Along with the shear stresses also transversal waves are neglected. In addition, linearity and homogeneity (constant static density and speed of sound) are assumed [87]. Hence, the Helmholtz Eq. (2.31) with properties in Tab. 4.14 is applied for Ω_c. The according finite element formulation is derived for the general acoustic 3D domain Ω_a in Sec. 2.3.

As described above, the passenger cabin is mainly equipped with seats, which locally introduce damping, refraction at edges and reflection at the surfaces. Using the experimental results for the equivalent absorption area A_t and the complex seat impedances $\underline{Z}_n$, a *global* modelling approach and a *local* one are compared and assessed.

- **Global model** | The entire fluid domain is damped by a global damping loss factor $\eta_c(f)$ yielding a complex speed of sound $\underline{c}$ according to Eq. (4.16) [19]. $\underline{c}$ is considered within the Helmholtz equation. Within the seat regions, the mesh is removed, while the sitting area and the backrest are generically modelled with a constant thickness. Based on the preliminary design data, the CRC 880 research aircraft has a non-symmetric seating plan with 5 seats per row (2 on the left, 3 one the right). Here, a continuous bench with a length of 2.5 seats

is considered[15]. The seat height and depth fit the experimentally investigated seat bench. With the domain boundaries at the sitting area and the backrest, Neumann boundary conditions are introduced (totally reflecting with $\frac{\partial p}{\partial \mathbf{n}} = 0$).

$$\underline{c}^2 = c^2 \left(1 + i\eta_c\right) \tag{4.16}$$

- **Local model** | The local effect of the seat cushions is considered with the help of impedance boundary conditions, while the surrounding fluid domain is not damped (constant real-valued speed of sound c according to Tab. 4.14). For this approach, the mesh within the seat regions is removed as well. In difference, both the sitting area and backrest's surfaces pointing to the passenger are assigned with impedance (Robin) boundary conditions according to Eq. (2.32). The experimentally determined complex impedance $\underline{Z}_n$ can be used directly. Besides the impedances at the front of each cushion, the further surfaces (sides and back of the seats) remain as perfectly reflecting (due to the removed meshes). This fits the hard back of each seat on which the cushion is fixed. A similar approach within a boundary element model is investigated in [104].

The FE model of an aircraft section in Sec. 4.3 is extended by Ω_c in order to have a realistic setup for the investigation of the two modelling approaches. Between both models, excitation (plane wave) and mesh are not changed, which keeps the focus on the consideration of damping. The following further changes are considered compared to the section model in Sec. 4.3.

- The section is changed in size to cover three seat rows which equals six circular frames in the chosen aircraft part.
- The interior panel is fixed (by its face sheet pointing outwards) at each frame, respectively. As interior panels cannot be identified easily within the generic model, this setup is chosen and kept for the full aircraft model as well. Furthermore, for the investigation of different tube lengths (Ch. 5), a fixture at every second frame introduces undesired discontinuities.
- The numerical effort increases drastically by the addition of the cabin fluid. In order to use less elements (compare Sec. 4.2), the double wall gap is completely filled by glass wool (homogeneous domain) and no additional air gap is modelled within the insulation.

The resulting FE model is shown in Fig. 4.44. Similar to the insulation domain Ω_g, the mesh in the cabin domain Ω_c consists of 27-node hexahedrons. The above

[15] Symmetry is a necessary major assumption for an efficient solution, see Ch. 5

mentioned seat regions are visible in Fig. 4.44, as well. All domains are strongly coupled as given in Eq. (2.63).

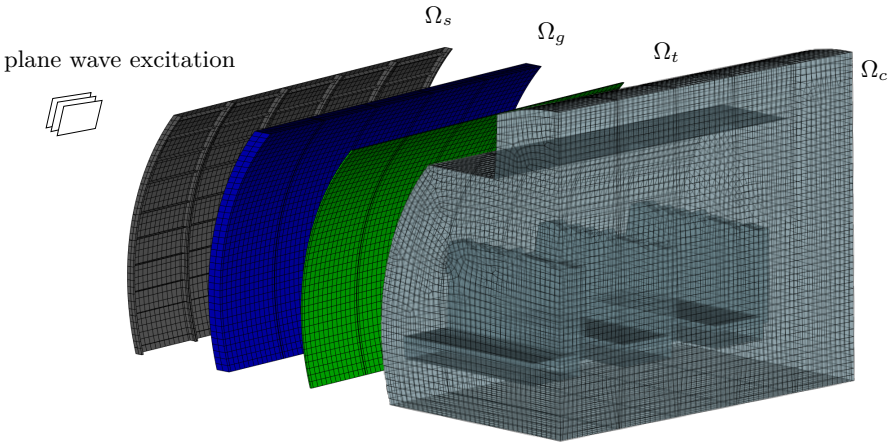

Figure 4.44: FE model of a generic aircraft section with focus on the seat modelling within the cabin fluid

In addition, the passengers themselves influence the wave propagation within Ω_c. With regard to damping, the two results for the equivalent absorption area (Fig. 4.42) are considered as two different inputs for the homogenised damping. This investigation shall give first hints on the importance of a passenger consideration in the cabin model and is statistically not reliable as three specific people participate in the experiment. A detailed modelling of passengers is clearly out of scope of this thesis.

For the aircraft cabin with 100 seats, the reverberation time is (re)calculated according to Eq. (4.17) [5], but now the properties of the passenger cabin shown in Tab. 4.14 are inserted. The measured equivalent absorption area A_t for three seats is linearly scaled to 100 seats. Interactions between seat rows which might influence the global attenuation are neglected.

$$T_r(f) = \frac{55.3 V_c}{(A_t(f) + 4 V_c m_c)\, c} \tag{4.17}$$

$V_c = 118.4\,\mathrm{m}^3$ is the cabin fluid volume and m_c is the absorption coefficient in the cabin according to [7]. Finally, a homogenised loss factor $\eta_c(f)$ is related to $T_r(f)$ as given in Eq. (4.18) [118].

$$\eta_c(f) = \frac{2.2}{f T_r(f)} \tag{4.18}$$

The resulting $\eta_c(f)$ is shown in Fig. 4.45 and serves as parameter input for the global model. This way, a consideration of damping properties by seats and passengers

is possible. The reproducibility standard deviation significantly increases at lower frequencies due to the inversely proportional dependency of A_t on f. As visible, the ranges by both the empty and occupied seat curves clearly overlap within all frequency regions. Hence, a consideration of these values can only give a first idea on the influence of passengers.

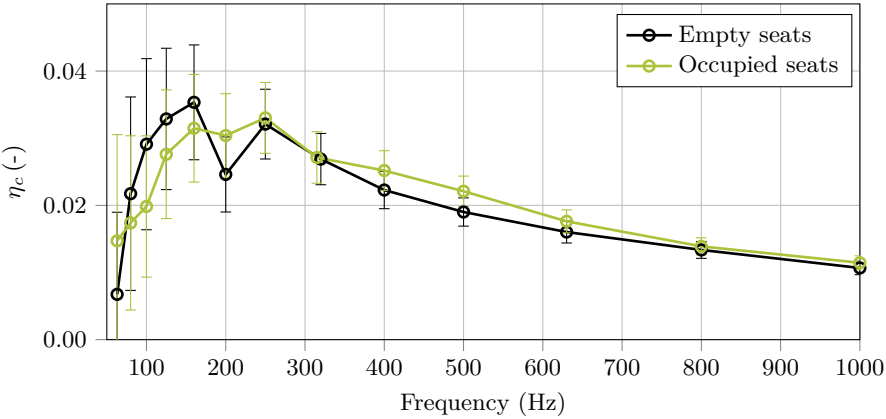

Figure 4.45: Homogenised damping loss factor η_c for 100 aircraft seats within a cabin fluid of volume $V_c = 118.4\,\mathrm{m}^3$, including reproducibility standard deviation according to [3] and error propagation in Eq. (4.17) and (4.18)

A consideration of the local damping behaviour of seats is aimed for in the local model. Similar to [104], the experimentally determined impedance $\underline{Z}_n$ is applied in the fluid domain as impedance boundary condition according to Eq. (2.32). In addition, by use of the measured flow resistivity σ and the laws by Delany and Bazley (Eq. (2.34) and (2.35)), the effective complex characteristic impedance $\underline{Z}_n$ and the effective complex density ρ_{eff} of the cushion material is approximated. By Eq. (2.38) and (2.40), c_{eff} and ρ_{eff} for an equivalent fluid domain are received (results given in Sec. A). Applying Eq. (2.45) yields the surface impedance $\underline{Z}_n$ for the D-B model. The obtained impedances by measurements are compared to the model in Fig. 4.46. Though the climate conditions between the reverberation chamber and the passenger cabin in cruise differ, the analytical approach does not introduce significant differences. Hence, only the results under cruise conditions are shown for the D-B model. The D-B model requires only the flow resistivity, what makes the setup more simple compared to the measurement of impedances. From 300 Hz, both the experimental and model data are relatively stable and comparable. At lower frequencies, the mentioned (non-physical) strong fluctuations are visible in the measurement. In contrast, the model result is smooth. The imaginary parts are in a much better agreement with the experimental curves, while for the real parts, large differences are observable

below 300 Hz. The curves of the real part are not comparable at all in this frequency region. However, deviations in low frequency ranges can be investigated in further studies and certainly reduced by a more complex measuring setup.

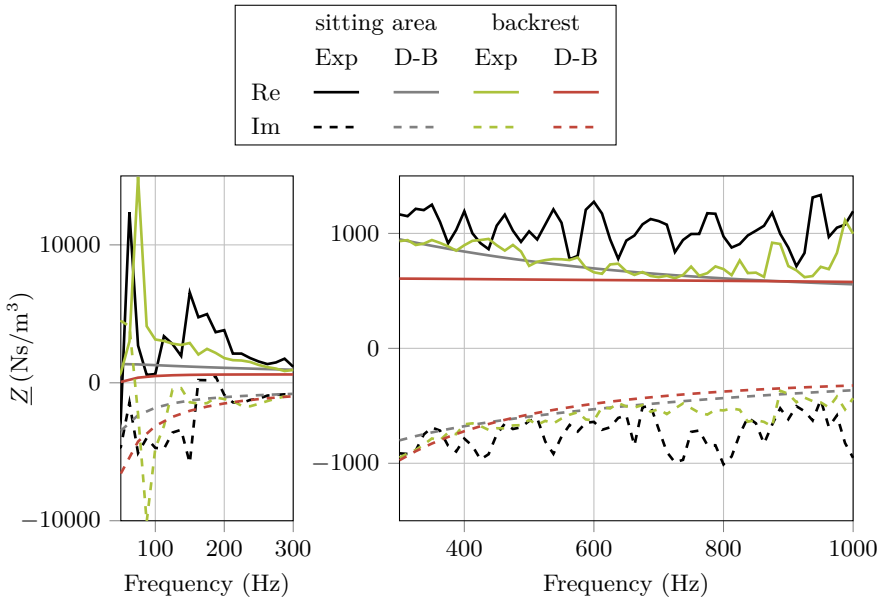

Figure 4.46: Analytical results under cruise conditions for the surface impedance $\underline{Z}_n$ of aircraft seats compared to experimentally received results under conditions of the reverberation chamber

Numerical results for the two modelling approaches are shown in Fig. 4.47. For the global model, $\eta(f)$ for empty seats is applied. For the local model, the experimental data is applied. Similar to the mean squared admittance/velocity, the mean squared pressure $\overline{p^2}(f)$ is chosen as acoustic quantity. Within a *potential head region*, the pressures $\underline{p}_i(f)$ at all nodes n_{points} are summed up according to Eq. (4.19). A line parallel to the central seat bench with 0.1 m distance to the backrest at the backrest's top height serves as centre for the volume. Along that line, the *potential ear region* is defined by a rectangular box with a square cross section (side length 0.1 m).

$$\overline{p^2}(f) = \frac{1}{n_{\text{points}}} \sum_{i=1}^{n_{\text{points}}} \left|\underline{p}_i(f)\right|^2 \tag{4.19}$$

The overall decreasing trend of both curves agree reasonably well. The introduction of local impedances compared to perfectly reflecting boundaries and a global damping

does not significantly change the appearance of resonances and anti-resonances. Concerning damping performance, both approaches are comparable within a tolerance of around 5 dB. The mean error yields 1.8 dB which is near the convergence criterion. The largest differences occur below 400 Hz, which may be dedicated to the mentioned measurement uncertainties of the impedances for low frequencies within the diffuse sound field. In total, the two approaches yield similar results of the FE model. Based on the fact of uncertain impedance measurements versus a standardised measurement of the reverberation time, the global damping approach is further used in the aircraft model. As positive side effect, the modelling effort is less as no boundary surfaces must be identified.

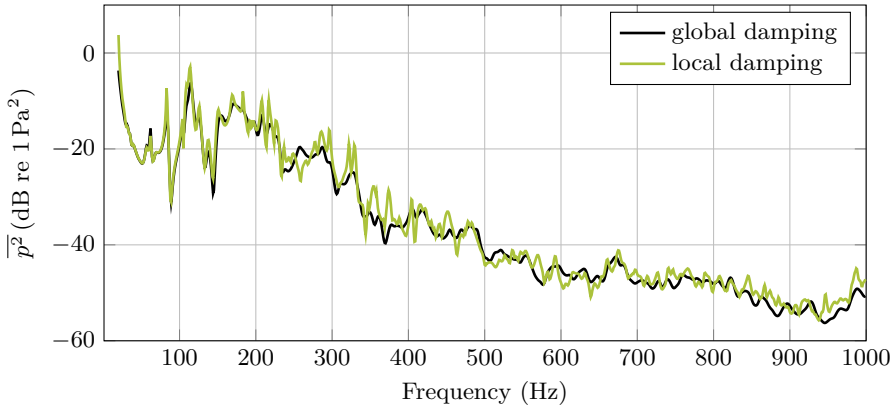

Figure 4.47: Numerical results for the mean squared pressure $\overline{p^2}$ within the cabin (passenger ear region) under plane wave excitation of the primary structure for two different models for the cabin fluid and the seats

A similar investigation of an aircraft section under TBL-load with the two modelling approaches examined here is shown in the author's contribution [27] as well. The same input data is applied for an impedance boundary condition in comparison to a global loss factor. The main difference is a neglection of the seat region for the global model (the mesh is not removed). This fact yields significant higher differences between the resulting SPL curves compared to the results above. Hence, the modelling of seats and especially their hard back (introducing reflection) is recommended as a crucial modelling detail.
Concluding the section on the passenger cabin, the following statements are derived and considered for the aircraft model:

- The equivalent absorption area $A_t(f)$ is measured for empty and occupied seats, yielding slight differences of the damping loss factor $\eta_c(f)$. The maximum

deviation occurs at low frequencies ($< 250\,\mathrm{Hz}$), at which the standard deviation of the experiment significantly increases. A meaningful further comparison of the two data sets is not possible as the trust intervalls largely overlap. Hence, the basic gain in information on a slight change of $\eta_c(f)$ due to passengers is left at that.

- Based on the comparison of a global (use of damping loss factor $\eta(f)$) and a local damping approach (use of surface impedances $\underline{Z}_n$) for aircraft seats within a representative aircraft section model, the resulting SPL in the cabin does not differ significantly. The global approach is finally chosen as significant deviations occur in the results of the local seat impedances at frequencies below 200 Hz.
- A set of material parameters for an equivalent fluid model is derived and compared to the measured surface impedances. The results are similar at high frequencies but differ significantly in their real parts below 300 Hz. Further investigations of local poro-elastic domains (including the Biot model) are shifted to future studies, keeping the global aim of this thesis in mind.

4.5 Assembled aircraft model

Within the aircraft model assembly, the findings on aircraft components by Sec. 4.1 to 4.4 are brought together and combined with the project-related preliminary design data. As introduced in Sec. 2.1, a mid-range 100 pax aircraft is investigated as a tube wing configuration with two different engine concepts. The design data mainly comprises dimensions of the airframe including its material data. Close to the aircraft section models in Sec. 4.1 to 4.4, the setting is finally extended to a symmetric airframe tube with floor and the secondary structures of the entire cabin. A symmetry boundary condition is considered from the start and explained in more detail at the beginning of Ch. 5.

In Fig. 4.48, a section of the resulting full aircraft FE model is shown, in which the four domains Ω_s, Ω_g, Ω_t and Ω_c are marked. While the full passenger cabin length comes up to 16.9 m, this *core* model has a length of 4.3 m. A significantly shorter section is considered as the full model requires tremendously more computational time, which hardly allows studies on solution efficiency in Ch. 5. The insights on the solution process are expected to be transferable – the linear scaling by lengthen the modelled tube domain is specifically studied in Sec. 5.5.
The core model includes 11 frames right behind the wing box and 5 seat rows. As two engines are mounted at the wings and the highest pressure excitation for the

conventional engine is known to be behind the wings (detailed explanation in Ch. 6), this fuselage section is chosen as starting point. The central seat row is considered as reference, while two seat rows in each direction (front/back) shall serve as buffer to the hardly reflecting boundaries in the cabin. Similar to the aircraft sections before, a plane wave excitation is applied on the outer skin motivated by the assumed transferability of the findings to realistic loads.

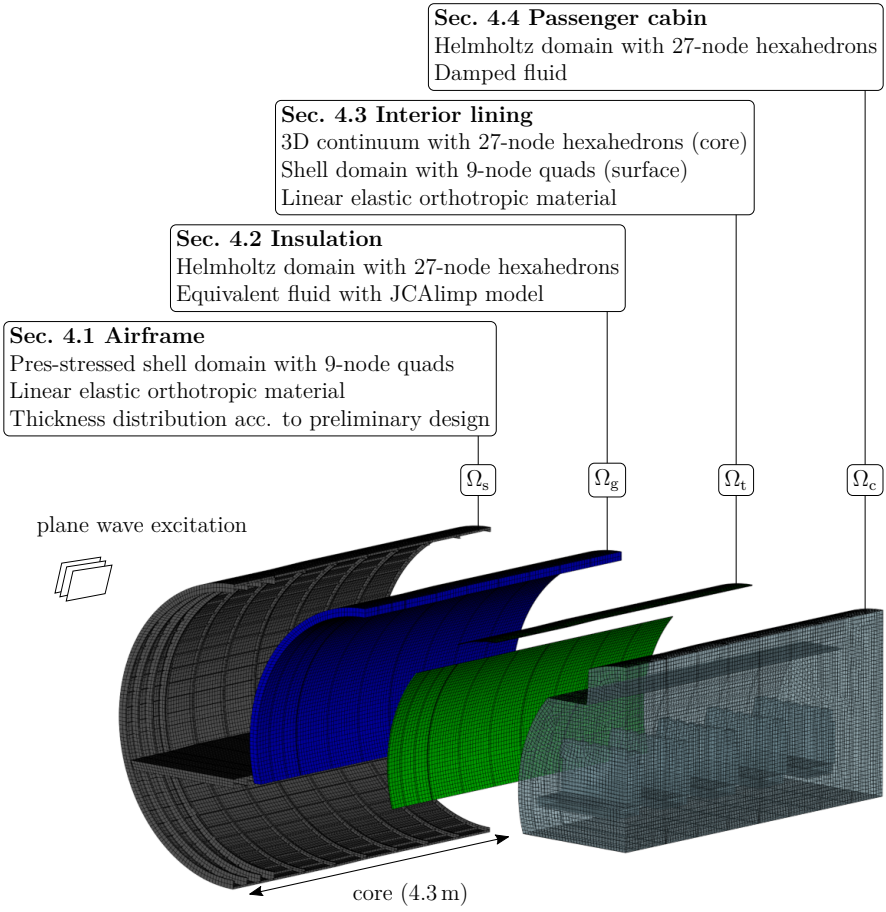

Figure 4.48: FE core model of the full aircraft fuselage

For the **airframe** domain $\mathbf{\Omega_s}$, a pre-stressed shell meshed by 9-node shell elements is considered as shown in Sec. 4.1 for curved plates. Frames and stringers are considered in $\mathbf{\Omega_s}$, while the latter's heights are set to 0.025 m. The constant value is chosen smaller compared to the frame heights as visible in typical airframe designs. However, as indicated before, this value is expected to have a significant influence on

the sound transfer into the cabin, but is not explicitly given within the preliminary design. Linear elastic orthotropic material parameters are derived based on the CLT in combination with the approach by Rohwer for the shear moduli and applied to the outer skin, frames/stringers and the floor section. CFRP material data for the research aircraft is available within the CRC 880 project, based on a T300 15k / 976 (fibre / matrix) composite, which is also applied in [138]. In order to apply the Rohwer approach for the shear moduli G_{xz} and G_{yz}, the shear modulus $G_{\perp\perp}$ (normal plane to fibre) of an unidirectional layer is additionally taken from [77]. The layer orientations within the stack are constant $((0/45/90/-45/0)_s)$ for the outer skin and the total thickness scales all layers uniformly within the preliminary design process [138, 160]. The resulting material parameters for the outer CFRP skin are shown in Tab. 4.16.

Table 4.16: Homogenised material data of the outer CFRP skin based on preliminary design data by use of the CLT [150] and Rohwer [140] for the transversal shear moduli

Quantity	Variable	Value	Unit
Young's modulus (bending)	E_{bx}	69.2e9	$\mathrm{N/m^2}$
Young's modulus (bending)	E_{by}	48.6e9	$\mathrm{N/m^2}$
Young's modulus (membrane)	E_{mx}	61.0e9	$\mathrm{N/m^2}$
Young's modulus (membrane)	E_{my}	61.0e9	$\mathrm{N/m^2}$
Poisson ratio (bending)	ν_{xy}	0.166	-
Poisson ratio (membrane)	ν_{xy}	0.201	-
Shear modulus (bending)	G_{xy}	13.6e9	$\mathrm{N/m^2}$
Shear modulus (membrane)	G_{xy}	15.8e9	$\mathrm{N/m^2}$
Shear modulus	G_{xz}	3.9e9	$\mathrm{N/m^2}$
Shear modulus	G_{yz}	1.9e9	$\mathrm{N/m^2}$

The **insulation $\Omega_\mathbf{g}$** is modelled as Helmholtz domain with frequency-dependent complex material parameters (equivalent fluid) based on the JCA-limp model in accordance with investigations of aircraft-grade glass wool in Sec. 4.2. The domain is discretised by 27-node hexhedrons and approximated by quadratic polynomial ansatzfunctions. In general, the domain is completely filled by glass wool under exclusion of any moisture film covering, as the influence below 1000 Hz has shown to be non-significant. The consideration of an equivalent fluid brings along the fact (compare Sec. 4.2), that a significant difference can be expected compared to the Biot model, which explicitly considers the structural phase of the glass wool. Due to extensive computational costs and high uncertainties in the material parameters, the application of the Biot model to a full aircraft is not considered within this work. However,

the material parameters for the JCAlimp model are calculated for a compression of 25 % based the measured inputs in Sec. 4.2.

A combination of a 3D continuum for the honeycomb core and a 2D shell for the surface layers is realised for the **interior lining** domain $\mathbf{\Omega_t}$ in line with studies of a honeycomb sandwich plate in Sec. 4.3. The linear elastic orthotropic material parameters of the two subdomains remain unchanged compared to the optimised parameter sets of the section model in Sec. 4.3. The thickness of the honeycomb core is slightly increased to 0.01 m and the thickness of the layers to 1 mm, which is more realistic for a commercial aircraft cabin. This value is estimated based on observations in real aircraft and not given within the preliminary design data. This fact raises the need for uncertainty studies under the assumption of reasonable thickness ranges in future studies.

The **passenger cabin** is a homogenised Helmholtz domain $\mathbf{\Omega_c}$ with constant density and frequency-dependent complex speed of sound (Eq. (2.33)), which is in compliance with investigations on a real aircraft seat bench in Sec. 4.4. The entire cabin fluid is meshed by 27-node hexahedrons, while the seat volumes are omitted. As shown in detail in Sec. 4.4, a comparison of the measured global loss factor to local damping (seat impedances) on the example of a section model shows deviations below 200 Hz. As large fluctuations occur in the in-situ impedance measurements below 300 Hz, the global damping approach is finally preferred as more reliable variant.

Respectively, a strong coupling according to Eq. (2.63) is considered between

- the insulation and both the outer skin and the interior lining and between
- the passenger cabin fluid and both the floor and the interior lining.

The resulting sparsity pattern of the system matrix for the core model is plotted in Fig. 4.49. The form corresponds to Eq. (2.63) and can be solved with appropriate iterative or direct solvers. For the purpose of illustrations and the use of domain decomposition approaches (Sec. 2.5), the four domains are renumbered within assigned ranges. In addition, the domains are marked according to the FE model above. The relation of dof between the domains changes with decreasing mesh size as the domains have different dimensions. In dependency on frequency limits, different mesh sizes are identified in Ch. 5, which accordingly yields different domain block sizes for Ω_s, Ω_g, Ω_t and Ω_c. All blocks are sparse, while a renumbering (e.g. nested dissection) yields the well known band structure during the solution process. The solution of the shown system matrix at each frequency sample of interest is generally challenging

due to the diversity of the domains and the size of the matrices. The next chapter introduces efficient solution approaches for the aircraft core model in order to pursue the long-term goal of parameter studies in early design stages.

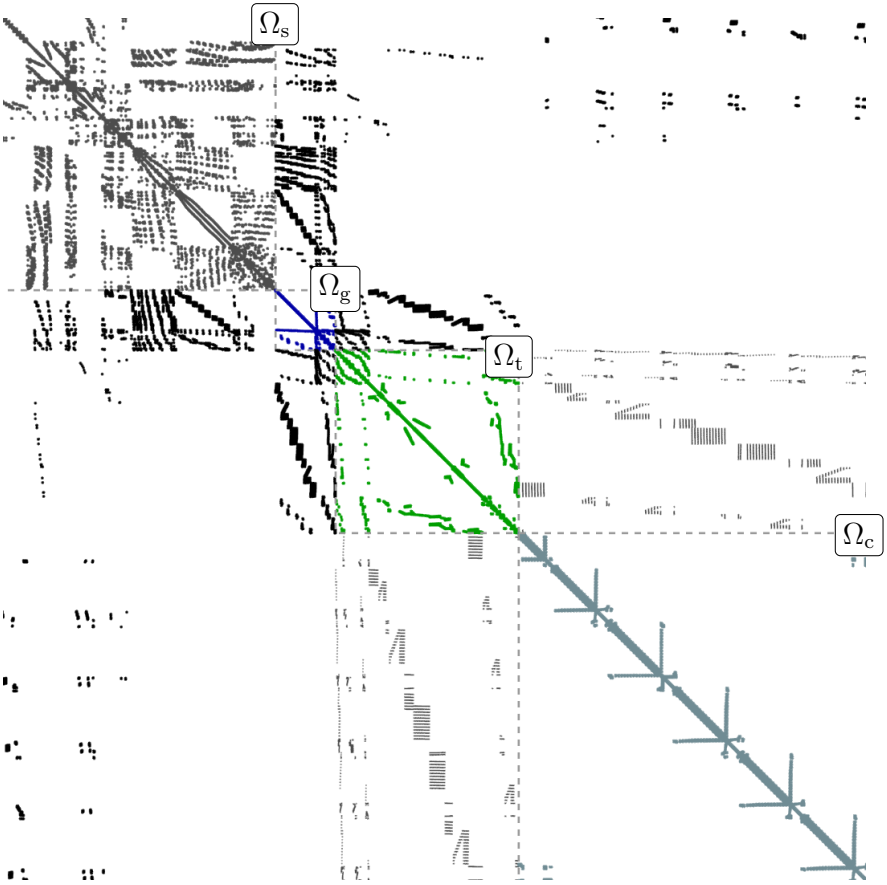

Figure 4.49: System matrix of the core aircraft model, reordered according to aircraft parts

5 Efficient solving approaches

As motivated, the applied wave-resolving approach has the advantage that the modelling of the wave propagation through the entire fuselage does not underlie numerous assumptions. All significant wave types are explicitly represented by differential equations given in Sec. 2.2 and 2.3. The discretisation of the aircraft fuselage shown in Sec. 4.5 comprising all discussed aircraft parts leads to a linear system of equations (Eq. (2.64)) shown in Fig. 4.49.

The problem is defined in frequency domain, hence, the solution can be received at any frequency f_i of the continuous spectrum. As standard, the sound pressure level L_p over frequency is received by a direct solution with a specified frequency step size Δf. In early aircraft design stages, parameter studies, uncertainty quantifications or sensitivity analyses are useful to find a design reducing L_p in the cabin. Scaling the core model to the total length of 16.95 m and realising a mesh size appropriate for the maximum frequency of 1000 Hz leads to a large model, which is computationally too expensive in the frame of many parameter samples. Therefore, an efficient solving process is aimed for within this chapter in order to benefit from the preceding effort within every potential parameter sample. Mechanical modelling assumptions (symmetry, weak coupling and shorter domain lengths) as well as numerical measures (frequency-adaptive meshes, scalability and solver settings) are addressed within the chapter in order to increase the calculation efficiency.

5.1 Symmetry

The airframe design of the the CRC 880 research aircraft configuration follows a typical cylindrical fuselage with two main wings carrying one engine, respectively. A mirror symmetry is identified within the x-z plane of the tube. In Fig. 5.1, a cross-sectional view of the interior passenger cabin is depicted indicating the assumed symmetry plane. For a consideration of the symmetry to the FE model, only one half of the fuselage is meshed and the boundary conditions according to Eq. 5.1 must be applied on Ω_s and Ω_t. On the boundaries of Ω_g and Ω_c, a particle velocity v_n of zero is inherently given by the formulation for the Helmholtz domains and satisfies the

symmetry boundary condition.

$$u_y = 0 \quad \varphi_x = 0 \quad \varphi_z = 0 \tag{5.1}$$

As visible in Fig. 5.1 (Source: [74]), the aircraft's seating plan is non-symmetric with 5 seats per row as already introduced in Ch. 4.4. In order to balance the effect of damping in the frame of the assumption of symmetry, a continuous bench with a length of 2.5 seats is considered. As a side note, details such as potentially non-symmetric emergency exits, luggage loads or interior furnishing are generally not considered in the model and therefore not affected by the symmetry assumption. Rather, the effect on applied loads is important. Excitations are assumed to be symmetrised as well (e.g. jet noise on outer skin). The phase is switched by π, which equals an addition of two coherent sound sources yielding an SPL in the cabin, which is 6 dB higher compared to incoherent loads. Sound sources like the TBL or the engine jet are originated in flows and therefore rather incoherent while the amplitude on both sides is assumed to be similar. According to Eq. 2.74, the addition of two incoherent sound sources of similar amplitude increases the SPL by 3 dB compared to one source. Therefore, for the aircraft model considering the symmetry boundary condition, a correction factor of -3 dB for the finally calculated SPL in the cabin is applied.

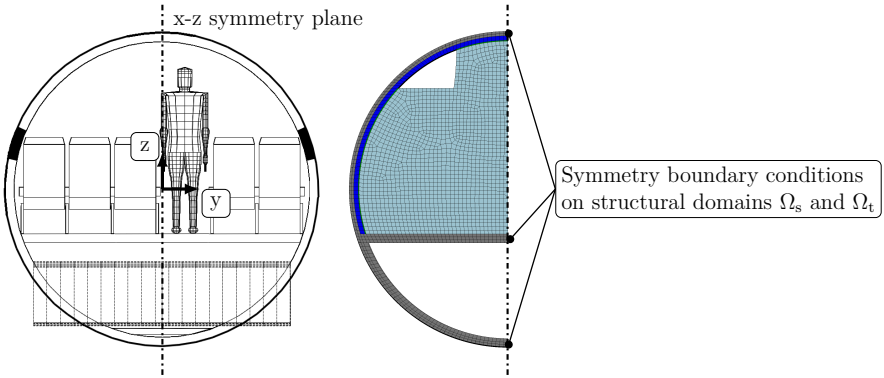

Figure 5.1: Identified symmetry plane in the fuselage of the research aircraft configuration (left; Source:[74]) and consideration in FE model (right)

Concluding, the assumption of symmetry introduces modelling errors if non-symmetric details are considered or the correlation of two-sided excitation is explicitly known. The advantage of significantly reduced computational costs due to the halving of the dof clearly prevails these points. In case of a block-jacobi preconditioner in combination with an iterative GMRES solver, based on the convergence study conducted

before, the time saving is estimated to around 63 % and the memory saving is expected to be approximately 55 %. The assumption of symmetry is applied to all following numerical calculations and to the calculations in Sec. 4.4.

5.2 Frequency-adaptive meshes

In the wave-resolving aircraft model, the unknown displacement and pressure fields are discretised by finite elements. A certain number of nodes are required to yield convergence of all occurring wave types in all domains shown in Ch. 4. So far, a constant mesh has been used for the entire frequency range, which suffices the required resolution at the maximum frequency. As wave lengths decrease with frequency, coarser meshes can be applied towards lower frequencies inducing similar discretisation errors. A meshing technique adaptive to the occurring wave lengths yields such coarser meshes and saves computational costs to the price of preceding modelling effort. As the aircraft model is built using automatised scripts and the long-term aim are parameter studies of such large and complex systems, a frequency-adaptive refinement of the mesh is expected to be indispensable.

In Fig. 5.2, estimations for the dominating wave lengths within the four domains are plotted over frequency. For Ω_s and Ω_t, the bending wave length λ_b within an infinite flat plate is calculated according to Eq. 2.66 as pessimistic and simple case (similar to Sec. 4.1). Within the airframe domain Ω_s, the thinnest outer skin field (1 mm) is chosen as reference. For the interior lining, the bending stiffness is calculated according to the CLT. The curves clearly show that the shortest wave lengths can be expected within the thin skin field of the airframe. This is valid for the frequency range of interest up to 1000 Hz – as the fluid domains Ω_g and Ω_c have a lower gradient (according to Eq. 2.28), an intersection of the curves (coincidence frequency) will occur with increasing frequency. Up to this intersection, a further saving in dof can be realised by the use of non-conforming meshes as the 3D cabin domain has the largest share on the total dof. However, within the frame of this thesis, non-conforming meshes cannot be implemented and the thinnest outer skin field is considered for the realisation of frequency-adaptive coincident meshes.

For the distance of two stringers ($\Delta_\mathrm{stringers} = 0.18\,\mathrm{m}$) within the airframe, divisors between 2 and 8 shell elements are applied, which defines the global mesh size. By the automatised scripts, an exact fulfilment of these divisors between the stringers is ensured. Relating the bending wave length in the thinnest CFRP skin field to the global mesh size, the number of nodes per wave length are yielded, which are plotted in Fig. 5.3. For the following investigations, 10 nodes per wave lengths are exemplarily considered as lower quality limit. According to the curves, the mesh

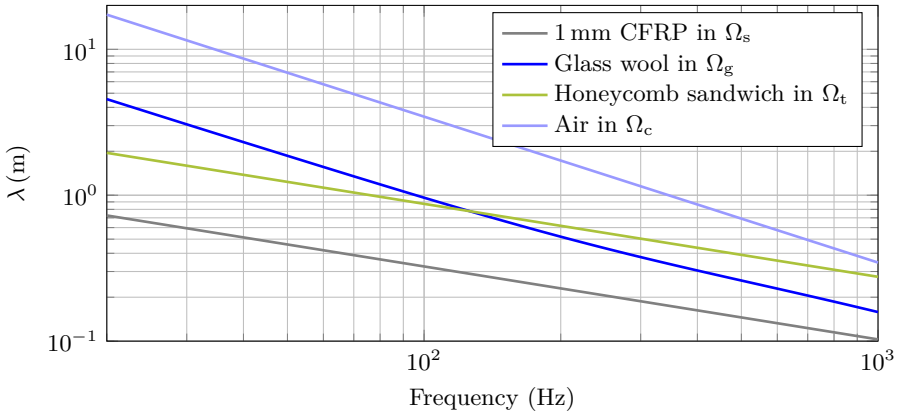

Figure 5.2: Estimation of wave lengths in different aircraft domains

"8" (8 elements between stringers) can be applied for the entire frequency range without falling below the limit of 10. As the number of nodes increase towards lower frequencies, the discretisation error changes over frequency. A more constant error and the above mentioned computational savings are reached by an application of the meshes "2" to "8" as marked in Fig. 5.3 at the bottom.

Having a closer look to Fig. 5.3, jumps can be seen from one mesh to another. For instance, switching from mesh "3" to mesh "4" at 140 Hz induces an abrupt change from 10 to 13 nodes per λ_b. This jump may exclude eigenfrequencies around 140 Hz from the entire calculation if an eigenfrequency is located above 140 Hz for mesh "3" and below 140 Hz for mesh "4". This exclusion can be crucial as these eigenfrequencies may induce critical resonances in the passenger cabin. For a safe application of different meshes, a smooth transition or a clear convergence must be realised. Both approaches are expected to be realisable, but out of scope for this thesis. Therefore, the plotted curves are not connected between two different meshes in the following, keeping in mind this consequential question.

The finally identified meshes are summarised in Tab 5.1 with the associated total dof and computational costs. For the 2D and 3D domains, the dof follow a quadratic and cubic increase, respectively. Hence, the total dof grow potentially over linearly increasing mesh sizes as well. For comparison, the finest model, which is used between 810 and 1000 Hz, comprises 19 times more dof than the coarsest model, which is applied below 60 Hz. The computational time T in Tab. 5.1 is taken as mean value over frequency samples for an execution on 6 nodes of the Phoenix cluster of the TU Braunschweig. A bijacobian preconditioner with two blocks is used – the first block combines the domains Ω_s, Ω_g and Ω_t, while the cabin domain Ω_c represents the second block (compare Fig. 4.48 and Sec. 2.5). For each block, an LU factorisation

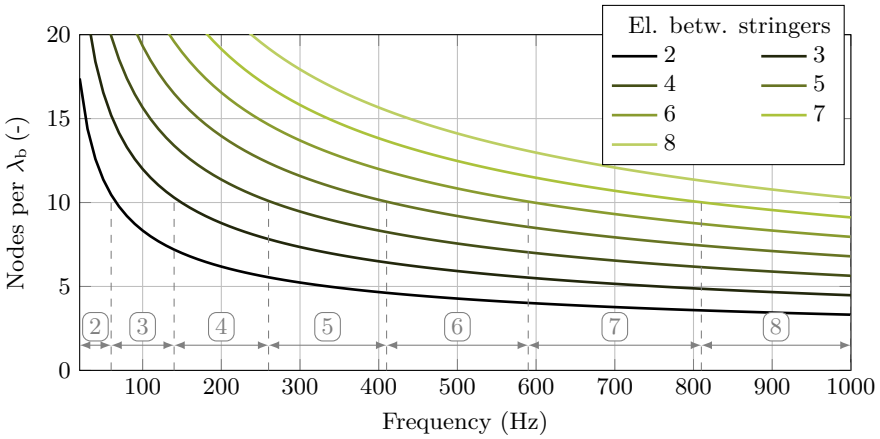

Figure 5.3: Frequency-dependent meshes (declared by number of shell elements between two stringers) for 10 nodes per wave lengths within thinnest CFRP panel

is conducted, which represents the optimal preconditioner for each block. Using the GMRES iterative solver, as described in Sec. 2.5, the exact solution is obtained. If a frequency-constant mesh "8" is contrasted with the frequency-adaptive meshes, a saving of 58 % in time is yielded under usage of the current solver setting. In addition, the memory savings allow a usage of less computing nodes *or* a usage of computing nodes with less memory. Besides the symmetry assumption, the 7 different meshes shown here are applied in the following computations.

Table 5.1: Mesh sizes, corresponding frequency ranges and mean solution times T as well as memory requirements $M_{\max}$ with block jacobi preconditioner (LU + LU)[16] and GMRES for the core model

Elements between stringers	dof	T [s]	$M_{\max}$ [GB]	$f_{\max}$ [Hz]
2	0.7 mio	38	5 (fuselage)	60
3	1.5 mio	86	9 (fuselage)	140
4	2.7 mio	185	18 (cabin)	260
5	4.3 mio	398	40 (cabin)	410
6	6.4 mio	693	74 (cabin)	590
7	9.5 mio	1459	150 (cabin)	810
8	13.5 mio	2404[17]	246 (cabin)[17]	1060

[16] per used node with one mpi process each; dominating block indicated
[17] estimation based on polynomial extrapolation as memory is not sufficiently given on 6 nodes for bijacobian (LU+LU) preconditioner

5.3 Weak coupling

With increasing frequency, a large number of dof compared to the total system size is attributed to the passenger cabin Ω_c (49 % for mesh "4"; 67 % for mesh "8"). In addition, the system matrix for Ω_c provides a significantly better condition number than the total system and the trimmed airframe consisting of Ω_s, Ω_g and Ω_t. Both facts motivate a splitting from the solver point of view, as iterative solvers work much better for the fluid domain in comparison to the shell domains. From the modelling viewpoint, a weak coupling splits the cabin domain from the remaining mesh, which sets the pressure forces by the fluid to the shells to zero. The coupling is considered in one direction only, which allows a solution of the trimmed airframe first and a solution of the fluid part in a second solution step. Within this second step, the displacement of the structure serves as excitation (right hand side). For the aircraft, Ω_s, Ω_g and Ω_t are solved first as trimmed airframe and the resulting displacements are applied to Ω_c in the second step. Comparing with the plate-cavity example in Sec. 2.5, this weak coupling corresponds to one block Gauss Seidel iteration.

In [18], Eq. (5.2) is applied in order to estimate a parameter λ_c indicating the need for a strong coupling. $\lambda_c \ll 1$ can indicate a validity of weak coupling, but must be taken with care in case of cavities. However, with increasing frequency, the tendency of a decreasing need for strong coupling is given by the equation as ω occurs within the denominator. For the coupling of the sidewall panel within the aircraft model, λ_c drops below 0.01 at 620 Hz.

$$\lambda_c = \frac{\rho_f c_f}{2\rho_s t\omega} \tag{5.2}$$

In Fig. 5.4, the solution of the core model under consideration of a weakly coupled passenger cabin domain Ω_c is compared to the strongly coupled reference solution. For the calculation, both the symmetry assumption and the frequency-adaptive meshes are applied. In (a), the mean squared pressure of the central seat row backrest's top front edge is plotted. As different meshes yield different node distributions in the previously considered volume, this clear geometry-motivated line of nodes is chosen for the full aircraft. Below 400 Hz, significant deviations are visible, which indicates a relevant influence of the cabin fluid on the trimmed airframe. With increasing frequency, the differences decrease and are largely located below a relative error of 1 dB. The relative error over the entire frequency range is plotted in Fig. 5.4 (b). The comparison matches the predicted trend of a decreasing need for a strong coupling with increasing frequency, as given by Eq. (5.2). Putting the results in relation to the observed deviations in Ch. 4 resulting from measurements, modelling and parameter

uncertainties, the induced error by the assumption of a weakly coupled cabin is accepted from around 400 Hz in the frame of this thesis and for the underlying aircraft. Above this value, all frequency samples yield an error below 3 dB in $\overline{p^2}$, while errors below 1 dB are dominating. Besides Eq. (5.2), the cabin's dimensions are expected to influence the coupling strength. For smaller aircraft cabins, a stronger coupling will occur and vice versa, which shifts the transition frequency (in compliance with the chosen acceptable error).

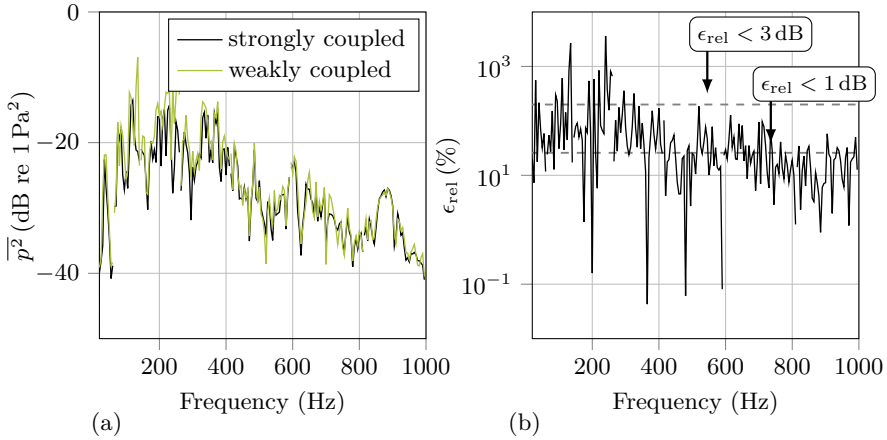

Figure 5.4: (a) Numerical results for the mean squared pressure $\overline{p^2}$ within the cabin (passenger ear region of central seat row) and (b) rel. error ϵ_{rel} of a weakly coupled passenger cabin domain Ω_{c} compared to the strongly coupled reference solution

Concluding, the assumption of weak coupling introduces a relative error decreasing with increasing frequency. From a certain frequency, the split calculation is justifiable. In the following, weak coupling is assumed above 410 Hz, which is in accordance with the start frequency of mesh "6". Additional savings in computational costs for the largest meshes "6" to "8" within their according frequency ranges are yielded by the measure. Times and memory efforts are given in Tab 5.2 for 6 computing nodes and amount to a total time saving of 23 %, while a memory reduction of 39 % is yielded for mesh "8". The latter is obvious consequence of the sequential consideration of all acquired computing nodes (here: 6) for both the trimmed airframe and the cabin partial solve. The combined consideration of frequency-dependent meshes and weak coupling decreases the computational effort by 87 % in time and is considered for all following computations in addition to the symmetry assumption. The presented values are bound to the chosen solver and computer configuration, which potential

improvements are studied in the next section.

Table 5.2: Mean solution times T and memory requirements $M_{\max}$ with block jacobi preconditioner (LU + LU)[16] and GMRES for the weakly coupled core model

Elements between stringers	dof	T [s]	$M_{\max}$ [GB]	$f_{\max}$ [Hz]
6	6.4 mio	577	41 (cabin)	590
7	9.5 mio	1004	83 (cabin)	810
8	13.5 mio	1845	149 (cabin)	1060

5.4 Scalability and solver setting

So far, GMRES in combination with a block jacobian preconditioner (LU + LU) is applied on 6 computing nodes in order to realise the cost assessments for the above described frequency-adaptive meshes and the weak coupling assumption. Actually, the number of computing nodes and the solver set-up themselves further influence the time and memory requirements, which offers potential improvements. For all time and memory measurements within this thesis, the system matrices are saved to disk by the in-house code elPaSo, which excludes the assembling time of the matrices and allows a fair assessment of the solution process only. The matrices are loaded by an external PETSC [22] program and solved on n computing nodes by use of intel MPI (version 2020). Preliminary studies show an optimal performance with 1 or 2 mpi processes per computing node for the processor architecture (INTEL Xeon E5-2640v4) having two sockets with 10 physical cores, respectively. A significant difference cannot be identified between 1 or 2 processes. Increasing the number of mpi processes per node towards 20 always results in a growth of time *and* memory requirements – hence, 1 process per node is chosen by standard for this thesis. For the 20 physical cores per node, 20 local openmp processes with shared-memory are automatically occupied by PETSC for the solution process. The combination of mpi and openmp processes is called *hybrid mode* and supported by the direct MUMPS solver and GMRES within PETSC, which both take advantage of the local scaling. In the following, the parallel scaling is tested for all meshes of the core model under different solver settings.

The two cases of strong and weak coupling must be distinguished as the conditioning of the entire system matrix is worse for the full system compared to a separated cabin part. This fact yields a possible beneficial usage of an iterative GMRES procedure

for the cabin part.

Starting with the **strongly coupled core model**, which has up to 4.3 mio dof, a direct LU factorisation serves as reference. For the renumbering, ParMETIS (Parallel Graph Partitioning and Fill-reducing Matrix Ordering [129]) is considered in MUMPS as it shows the best performance in Sec. 2.5 and is capable of parallel scaling. In Fig. 5.5, the solution times for meshes "2" to "5", for which the strongly coupled solution is obtained, are shown over 6, 12, 18 and 24 occupied computing nodes. For the full domain LU reference, shorter calculation times can be observed for the meshes "4" and "5" with increasing number of nodes. Doubling the used nodes for the two meshes from 6 to 12 yields a speed-up of 30 % and 50 %, respectively. As frequency steps can be solved independently, which corresponds to a speed-up of 100 %, only memory limitations can justify an increase of computing nodes. For the coarser meshes "2" and "3", no benefit from more than 6 mpi processes can be observed at all. Rather T is partly increased, which indicates a communication overhead between the nodes. Besides, all results underlie a certain fluctuation in the order of a few percent related to the current load on the HPC cluster. As both network controller and storage are shared by all running jobs and all computers, limitations in data transmission influence the timing and might induce such increases.

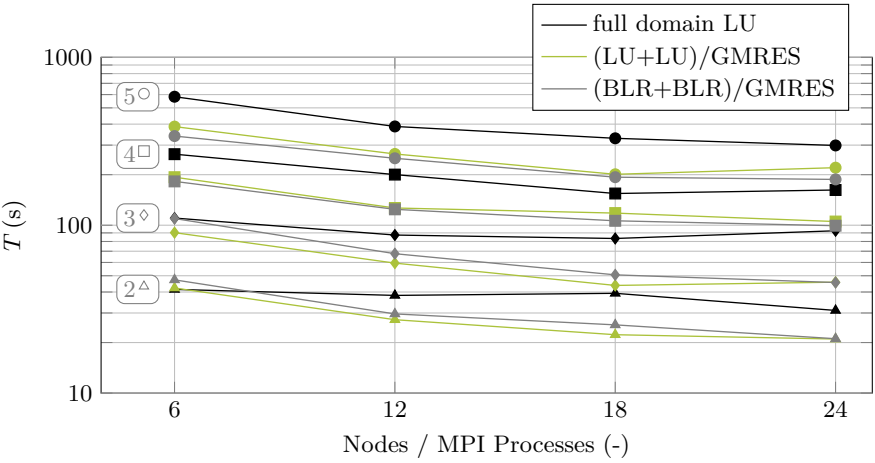

Figure 5.5: Scaling performance (time) for different solver settings below 410 Hz (strong coupling)

The computational time T for the GMRES solver in combination with a block jacobian preconditioner (LU+LU) is shown in Fig. 5.5 as well (green curves). Again, two blocks are assigned – one for the trimmed airframe and one for the cabin fluid Ω_c. For each block, the optimal full LU preconditioner is calculated by MUMPS. While the scaling

performance is similar to the full domain LU decomposition, a significant shortening of T can be measured for meshes "4" and "5" by use of GMRES. The improvement amounts to 37 and 50%, respectively. Below, similar timings are measured at 6 occupied nodes, which shows no benefit for the iterative procedure concerning the two meshes "2" and "3" with less than 2 mio dof. As the aircraft core model is extended in length in Sec. 5.5, a reasonable direct solution of the entire domain can already be excluded at this point.
As third setting building on the iterative approach, a cheaper preconditioner is desirable for the two blocks. An ILU preconditioner, as shown in Sec. 2.5, works sequentially and is therefore not scalable. Instead, a block low rank (BLR) version of the LU factorisation is available within MUMPS and applied here. The feature implements a truncated QR factorization with column pivoting resulting in a compression of so called BLR blocks [116, 107]. It runs within the parallel implementation of MUMPS' full LU decomposition and is therefore highly scalable, which is an essential criterion for large aircraft systems. Steering is provided by an absolute threshold parameter ϵ – the higher the value, the earlier the QR factorization is stopped. The compressed blocks represent an LU approximation (non-optimal preconditioner) and generally yield a reduced calculation complexity and memory usage [116, 107]. In Sec A, a preliminary study on ϵ is shown, which results in ϵ = 1e-6 set for the results in Fig. 5.5 (gray curves). The enabling of BLR for the two LU preconditioner decreases the quality of the preconditioner and thus also the convergence rate of GMRES. However, in the chosen setting, BLR does not significantly influence the total computational time of all 4 meshes.

Concerning the memory consumption of the strongly coupled model, the BLR feature indeed lowers the costs noticeably for meshes "4" and "5", which is depicted in Fig. 5.6. Similar to the previous figure, the three solver settings explained above are shown. For mesh "5", the memory consumption on 6 computing nodes is decreased by 45 % through enabling the BLR feature (gray curve) instead of using a full LU factorisation as preconditioner (green curve). For mesh "4", the saving amounts to 36 %. As the solution time is similar with and without BLR, a clear recommendation can be given to use the feature for the underlying aircraft models. Generally, for more computing nodes, the advantage of the BLR feature slightly vanishes. At the same time, the compression loses its effect towards less dof (meshes "2" and "3") or even brings a slight disadvantage. Finally, the full domain LU is not competitive against GMRES concerning memory usage as well.

The meshes "6" to "8" are used for the **weakly coupled core model** above 410 Hz.

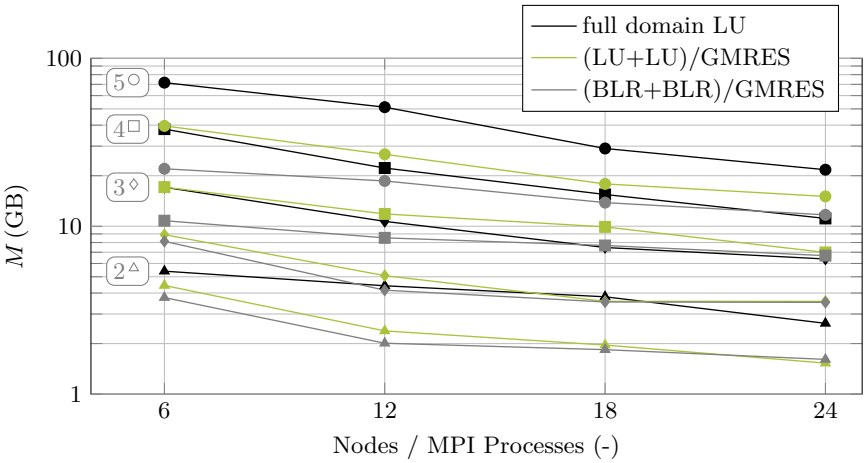

Figure 5.6: Scaling performance (memory) for different solver settings below 410 Hz (strong coupling)

As described above, the trimmed airframe is solved first and the received displacements are successively applied as external load to the cabin domain Ω_c. Each frequency steps is therefore split into two separated solver runs. In Fig. 5.7, the total computational time for two solver settings is compared for a different number of occupied computing nodes:

- Two complete LU decompositions (MUMPS) for the two sequential calculations
- A full LU decomposition for the trimmed airframe and an iterative solution (GMRES) with an LU preconditioner with enabled BLR for the cabin part. Again, the parameter ϵ is tested and an effective value is identified based on Fig. A.8.

The latter option is motivated by significantly improved system characteristics of the homogeneous cabin (Helmholtz) domain compared to the full matrix. GMRES is excluded for the trimmed airframe as the condition number is too high and the full LU solve is relatively fast compared to the much larger cabin domain. Furthermore, the memory consumption for the cabin part is critical as already indicated in Tab. 5.2 and intended to be lowered by BLR.
Having a look at the scalability in Fig. 5.7, a similar picture as for the strongly coupled meshes emerges. With increasing number of computing nodes, the actual speed up vanishes. For instance, the computing time T of mesh "7" is decreased by 30 % using 3 times more nodes ($6 \rightarrow 18$) for the LU+LU setting. Facing the two solver settings, a clear advantage of the LU+BLR/GMRES setting can be observed for both all meshes and all numbers of computing nodes. For the 3 meshes "6", "7" and "8",

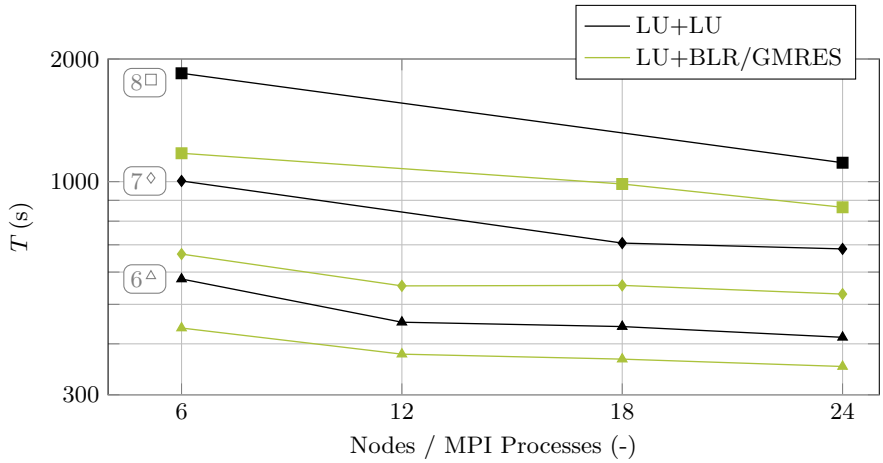

Figure 5.7: Scaling performance (time) for different solver settings above 410 Hz (weak coupling)[18]

the time saving amounts to 24, 34 and 36 % for 6 nodes. The advantage tends to decrease with increasing number of computing nodes. However, the usage of a BLR-driven LU decomposition as preconditioner with GMRES for the cabin part clearly saves computing time and therefore can be recommended without limitation. The weakly coupled meshes naturally split two large domains and make up the main part of time and memory costs of an entire frequency domain calculation – two reasons for which this setting is ideally suited for future studies on further solver settings. Several reasonable links are briefly explained in the conclusions below.

The memory consumption of meshes ”6” to ”8” is plotted in Fig. 5.8. As shown for the smaller meshes above, the memory saving using the BLR feature increases with dof. This trend continues here – the required memory per node is decreased by 36 to 41 % on 6 nodes. Again, with increasing computing nodes, the advantage vanishes as mpi communication overheads are dominating. On Phoenix, computing nodes with 64 GB memory are extensively available, while larger memory capacities are only given for up to 8 equal nodes. The example shows that a solver choice and the choice of the number of processes/nodes is related to the individual computing resources. As the speed up through an increase of computing nodes is rather small concerning computation time, a selection of the minimum required number of nodes for a possible usage of the extensively available small 64 GB nodes is reasonable. In addition, frequency steps can be solved independently. For instance, the solution of mesh ”7” should be conducted on around 12 nodes, which enables the start of many independent frequency steps simultaneously, each on 12 further small nodes.

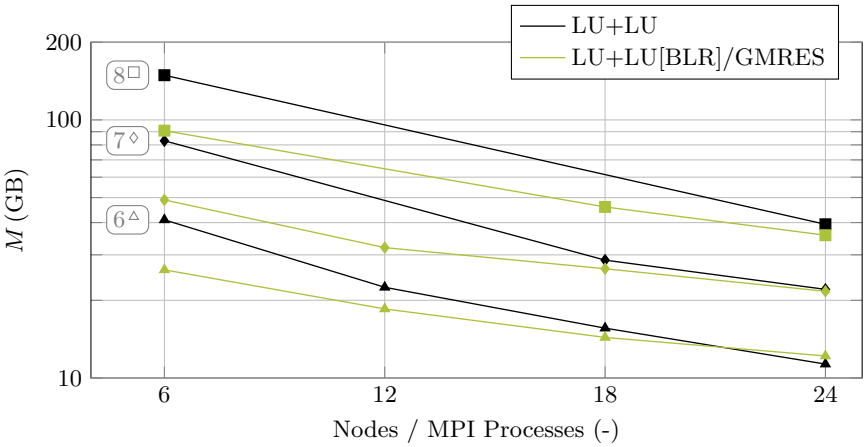

Figure 5.8: Scaling performance (memory) for different solver settings above 410 Hz (weak coupling)[18]

5.5 Domain length

With the assumptions on symmetry, frequency-adaptive meshes, weak coupling, and improved solver settings, the solution of the core model is efficiently realisable up to 1000 Hz. For the application in Ch. 6, the core model must finally be extended towards the full length of 16.95 m. Several preliminary tests before have shown, that a one-dimensional extension linearly scales time and memory requirements during solution. Within this section, a study on the necessity of a full aircraft length is conducted in order to potentially save the 4 times higher computational costs.
With increasing frequency, wave lengths generally decrease in all domains and damping performance increases. As a result, the wave attenuation increases as well. If the constant aircraft length is high compared to the wave lengths and attenuations, this may lead to a locality effect increasing with frequency. An excitation in the back of the aircraft may not have a significant effect in the front an vice versa as the wave's energy is significantly reduced over length. As a gedankenexperiment – for an infinite aircraft length no length-wise reflections occur, induced waves vanish completely and a significantly vibrating finite length can be identified. Truncating the non-significant domains is then expected to yield similar results.

The core model's length is extended stepwise in order to compare the SPL of the full length aircraft fuselage (16.95 m) to the results of smaller lengths (4.3 m [core

[18] For mesh "7" and "8", several numbers of computing nodes are possible due to memory limitations of the used HPC Cluster Phoenix. The 6 node run is possible on nodes with extended memory, but more than 8 nodes are not available with more than 64 GB memory, which does not allow the mentioned solution for the cabin part using LU (with BLR).

model], 9.0 m and 13.2 m). In Fig. 5.9, the 4 model variants are sketched. The chosen lengths result from frame positions within the preliminary design data and extensions of around 4 m compared to the respective predecessor. The 9.0 m model already comprises the back end of the passenger cabin and the area affected by jet noise in Ch. 6, despite slight structural extensions explained in this very chapter. The two following variants are extended unilaterally. For the excitation, here, a plane wave load applied to the actual fuselage length is considered. This can be compared to a TBL load affecting the entire fuselage (see Ch. 6).

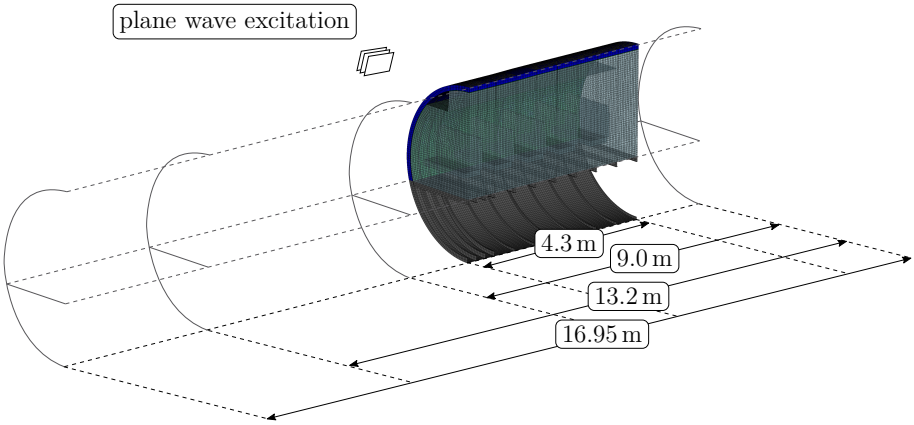

Figure 5.9: Extension steps of the core model

For the application of jet noise in Ch. 6, a clear local maximum in the excitation affecting the outer skin can be identified, which is expected to yield even smaller differences of shorter variants compared to the full length. On seat rows near the maximum, a more dominating sound immision by the direct transmission path through the double wall can be expected. Therefore, an application of a similar loading (plane wave) to the entire fuselage is assumed to deliver transferable results.

At the two ends of the considered fuselage length, no special boundary conditions are applied. This yields totally reflecting characteristic in all domains, which is seen as a worst case scenario.

Numerical results for the mean squared pressure $\overline{p^2}$ of all 4 aircraft lengths are shown in Fig. 5.10. Again, the mentioned region of the passenger ears within the central seat row of the core model is considered for the results. More precisely, the seat row is not changed due to an increase of length. Starting from 20 Hz, the 16.95 m model (red curve) is contrasted with the 13 m model (gray curve) up to 410 Hz. Due to

a limitation of the current implementation of the in-house code elPaSo[19], the 17 m model cannot be solved for finer meshes. Similarly, mesh "7" cannot be solved with 13 m length and mesh "8" is restricted to the core model's length of 4.3 m. The arising frequency limits are marked (×) in Fig. 5.10. Coming back to the lower frequency

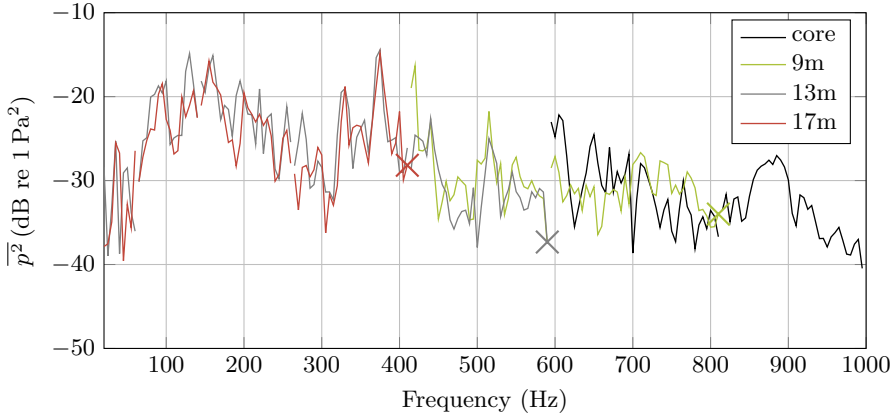

Figure 5.10: Numerical results for the mean squared pressure $\overline{p^2}$ within the cabin (passenger ear region of central seat row) under consideration of different aircraft lengths and local plane wave load

range, despite the limitation, the above introduced locality effect can already be observed. Both the 13 m and the 17 m model yield similar results towards 410 Hz, which is accepted as transition frequency within this work. Above 410 Hz, similar results are expected for the two lengths in the chosen seat row, which justifies the use of the 13 m model. For the comparison of 13 and 9 m, a slight convergence can be seen towards 590 Hz as well. Again, this frequency is used as transition between the two length for the application chapter. For the 9 m model compared to the core model, similarities cannot be clearly identified towards the limit of 810 Hz. As mesh "8" is only solvable for the core variant, the comparison can only be conducted until 810 Hz. The core model's length is similar to the aircraft's diameter (3.4 m) – therefore, a convergence can hardly be expected. Besides the lack of convergence, relevant excitations occur in the back of the aircraft. This applies in particular to the novel UHBR engine concept and the TBL. The use of a shorter domain for mesh "8" above 810 Hz neglects this excitation and does not allow for a fair comparison of engine concepts. A solution above 810 Hz must be conducted with the 9 m model and is restricted to mesh "7" in Ch. 6 (application), keeping a slightly reduced number of

[19] Non-zero entries within the system matrix are stored within a sparse format in PETSC. More than 2 billion non-zero entries yield an overflow of the integer variable increasing per entry. A 64 bit implementation of this function requires several adaptations as multiple packages are affected.

nodes per wave length in mind (9.1 Nodes per λ_b at 1000 Hz).
Concluding, a reasonable limitation to a local domain due to wave attenuation can be observed for the present aircraft model. Therefore, a general statement motivating the use of aircraft sections above certain frequencies can be derived. In the following chapter, the domain lengths summarised in Tab. 5.3 are applied. Of course, if the SPL within the entire passenger cabin is of interest, the full length has to be solved. In case of focusing a seat row with potentially high sound pressure levels, this measure linearly saves computational time and memory. Concerning the applications of TBL and jet noise, focusing a back seat row is reasonable as higher SPLs can be expected.

Table 5.3: Identified aircraft model domain lengths L in dependency on the applied frequency range

Elements between stringers	L (m)	dof	coupling condition	$f_{\max}$ (Hz)
2	16.95	2.8 mio	strong	60
3	16.95	5.7 mio	strong	140
4	16.95	10.3 mio	strong	260
5	16.95	16.6 mio	strong	410
6	13.20	19.6 mio	weak	590
7	9.00	19.4 mio	weak	1000[20]

5.6 Conclusions and further ideas

The studies in Ch. 5 reveal significant potentials concerning an efficient solution of large wave resolving aircraft models. The assumptions of symmetry, a reduced domain length and a weak coupling condition above a certain frequency in combination with frequency-dependent meshes easily save more than 90 % of the computational effort. The underlying basic idea is a well balanced error concerning modelling, discretisation and solution. E.g., an induced error below 1 dB due to a weak coupling condition can be accepted in the frame of large material parameter uncertainties of thin vibrating panels.
In addition, the choice of appropriate solver settings further reduces the computational costs of potential parameter studies. Generally, an iterative solver setting with a block preconditioner can be recommended for aircraft models. From several mio dof, a physically-motivated block definition using a parallel LU approximation clearly performs better than a full domain LU.

[20] Less than 10 nodes per bending wave length used above 810 Hz

Going towards uncertainty quantifications or optimisations requires thousands of solutions in frequency domain. Hence, additional studies building on the present work are reasonable. The following ideas shall be mentioned as logical next steps:

- Assuming a certain shape of typical SPL curves in frequency, so called transfer function estimators as shown in [100] can be used to accelerate the sampling over frequency. By consideration of an estimator, the frequency sampling points can be set more efficiently to reach a convergence of the curve under usage of less samplings. However, for random loads (like a TBL load), this approach is not feasible.
- An application of non-conforming (domain-adaptive) meshes in addition to the shown frequency-adaptivity reduce the cabin dof up to a certain frequency. Furthermore, the frequency-adaptivity can be steered by established multigrid methods, in which a new transition frequency can be identified automatically within each (automatised) refinement. A decisive research question is expected to lay in the stable/smooth and reliable error criterion in frequency domain.
- The application of appropriate impedance boundary conditions at the tube's ends may allow a further length reduction towards lower frequencies.
- For the iterative solution with GMRES, two large blocks are currently used – one for the trimmed airframe and one for the cabin. A further splitting of the trimmed airframe into 3 blocks may introduce further benefits as a more specific preconditioning can be conducted and GMRES may converge faster. In addition, instabilities of alternative iterative solvers (e.g. QMR) can be treated by better preconditioners and further save memory compared to GMRES. Besides a physically-motivated block definition, smaller blocks may lead to a more general and better scalable iterative setting (e.g. overlapping additive Schwarz preconditioner)
- A testing of alternative direct solvers (e.g. CPardiso, Strumpack, SuperLU_dist), especially as block preconditioner can increase speed or enable further low rank options for memory reductions. Additionally, the expensively calculated LU approximations can be recycled at further frequency steps [149, 105].

6 Application

Reliable and comprehensive aircraft models in combination with an efficient numerical solution of the sound field in a passenger cabin are set as major aims at the very beginning of this thesis. Ch. 4 and 5 address these objectives comprehensively, which results in a vibroacoustic aircraft fuselage model for the research aircraft of the CRC 880. The opportunity to study different sound sources arises, which is conducted within this chapter. The derived aircraft model (Sec. 4.5) is used for the investigation of jet and TBL excitations under consideration of the proposed efficient solution approaches (Ch. 5). Both loadings are already identified in Ch. 3 as two important sources of potential cabin noise besides excitations by

- fans during take-off and by compressors and turbines during landing (for jet aircraft) [115],
- propellers with dominant tonal components (for propeller driven aircraft) [115] and
- the air conditioning system, which plays a minor role according to measurements in [79].

These sources are not considered within this thesis, the same way structure-borne excitations by the mentioned sources are not taken into account. A detailed consideration of structures such as the engine mount or the wings is outside the scope of this thesis. Nevertheless, an extension by the mentioned excitations (if available) is easily possible for the wave-resolving aircraft model as any structure-borne and airborne waves can be applied.

For the consideration of jet and TBL loadings on the outer skin, a simulation chain is implemented. The chain depicted in Fig. 6.1 is jointly established with R. Ewert, C. K. Appel and J. W. Delfs from DLR Braunschweig (Institute of Aerodynamics and Flow Technology) in the frame of the CRC 880 and published in [28, 29, 30]. This thesis documents contributions to steps IIb and III of the simulation chain as highlighted in Fig. 6.1. The previously used plane wave load is finally substituted by pressure fluctuations of the two load cases in frequency-domain to calculate the according SPLs in the cabin. As simulation results from step IIa are available in

time domain on 83,000 positions for the BPR5 engine (UHBR: 53,000), interfaces are implemented within this thesis providing the data in frequency domain at element centres.

RANS (Reynolds-Averaged-Navier-Stokes equations) computations in **Step I** serve as data basis for both computational aeroacoustic analyses (CAA) of engine jet excitations (step IIa) and generic sound field generations beneath the TBL (step IIb). The CFD analysis of the CRC 880 research aircraft is conducted by DLR Braunschweig and delivers the necessary flow field.

Within **Step IIa**, the DLR Braunschweig applies a CAA computation in combination with the Fast Random Particle Mesh method (FRPM) [60] in order to deliver pressure fluctuations on the outer skin, induced by the engine jet of two different engines. A detailed publication on this step is available in [29], which comprises the CFD calculation as well. Within the thesis at hand, the pressure fluctuations are weakly coupled to the full aircraft model (step III) – the procedure and the results can be found in Sec. 6.1. Within **Step IIb**, a generic superposition of plane waves is considered as approximation of the TBL excitation. The sound field is computed based on semi-analytical approaches [91, 73] building upon models by Goody and Efimtsov [65, 57]. Similar to the jet excitations, the TBL loading is considered in step III as described in Sec. 6.2.

Step III essentially represents the core of this thesis - the application of a wave-resolving fuselage model in combination with efficient solving approaches. The simulation directly delivers the sound field in the passenger cabin and the aircraft model remains unchanged for the three load cases of two different engine jets and the TBL. While the latter load data is directly calculated for each finite element's central node, a 3D nearest neighbour search is implemented for the assignment of the above men-

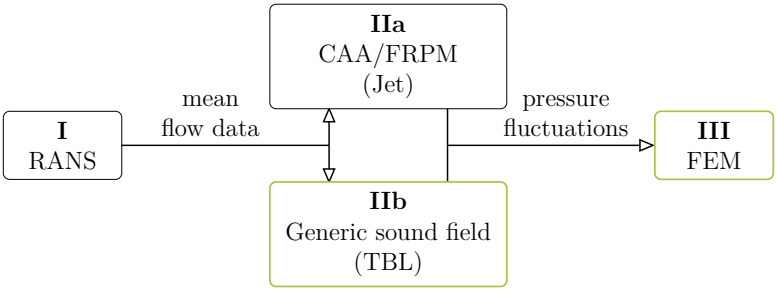

Figure 6.1: Numerical simulation chain for passenger cabin acoustic calculations comprising CFD, CAA and FEM simulations [30]

tioned spatial sampling points within the CAA simulation of the two jets. Different load cases only change the right hand-side of the system in Eq. (2.63), which raises advantages of a direct solution, as the LU factorisation can be reused. In this case, the memory requirements are significantly lower for an iterative solution with GMRES (see Sec. 5.4), which is why the iterative procedure is kept and normal computing nodes of the HPC system are used.

6.1 Jet excitation by two different engines

The introduction of new engine technologies may serve as an important step towards lower SPLs within the cabin. In contrast, higher SPLs have to be clearly excluded by SPL estimations as conducted here. Within the CRC 880, an over-the-wing ultra-high-bypass Ratio (UHBR) engine with a bypass ratio of 17 is investigated as novel engine concept for the research aircraft. The high bypass ratio is yielded by a larger diameter of the UHBR engine. Basically, a UHBR engine brings potentials in the direction of improved take-off characteristics, low fuel consumption and highly reduced noise emissions compared to a conventional engine. Exemplary, an engine with a bypass ratio of 5 (BPR5) is considered. In the first line, the BPR5 engine acts at higher rotation speeds, which generally yields a higher sound emission induced by the mixing of the actual jet flow with the surrounding flow [41]. In opposite, the UHBR engine is mounted closer to the passenger cabin and in a different length-wise position. These facts lead to a non-trivial scientific question concerning the actual transmission of sound waves into the cabin.
For the purpose of a fair comparison, two similar configurations shown in Fig. 6.2 (Source: [74]) are designed and provided within the CRC 880 by W. Heinze (Institute of Aircraft Design and Lightweight Structures, TU Braunschweig) [74]. Details on the design process by use of the preliminary aircraft design Code PrADO are given in [160].

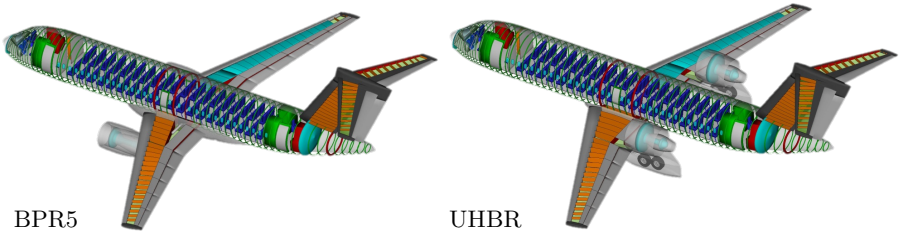

Figure 6.2: CRC 880 research aircraft configurations with conventional BPR5 and novel UHBR engine configuration (Source: [74])

For an investigation of the two aircraft configurations with regard to cabin acoustics

during cruise flight induced by the jet, the simulation chain introduced above is applied in cooperation with the DLR Braunschweig. Results from a similar aircraft model are published in [29]. For the thesis at hand, the CAA results from step IIa are taken as starting point.

In Fig. 6.3 (aircraft sketch from: [74]), the resulting overall sound pressure levels OSPL (sum levels) are plotted over the outer skin of the research aircraft. As engine designs and positioning fundamentally vary, different sound pressure level ranges and thus sum levels are predicted by the CAA calculation. The maxima in OSPL are marked by white circles and show a difference of 20 dB. For the conventional BPR5 engine, the maximum is located closer to the wing box ($x = 16.9\,\mathrm{m}$), while the maximum of the UHBR engine can be found in the back ($x = 21.5\,\mathrm{m}$). The airframe structure changes over the length and is designed much stiffer close to the wing box. In this context, as the sound transmission is expected to significantly influence the resulting sound pressure levels within the cabin, the advantage of an UHBR engine is not necessarily valid in the cabin.

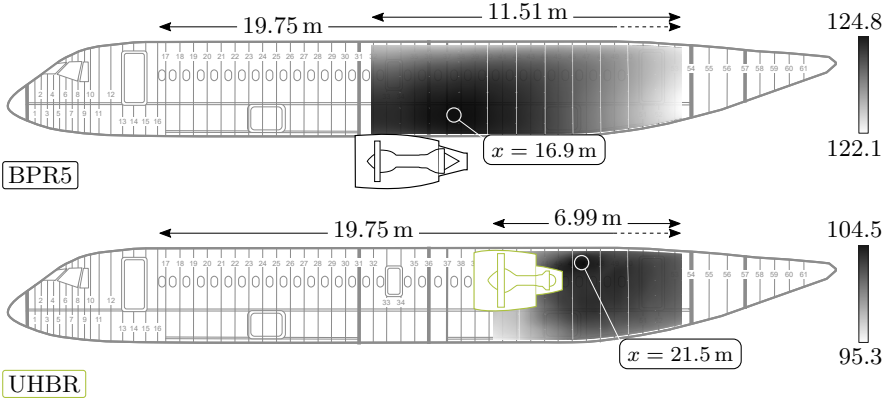

Figure 6.3: Overall sound pressure levels (OSPLs in dB re 2e-5 Pa) by BPR5 and UHBR engine jet excitations of CRC 880 ref3 configuration based on CAA results from DLR Braunschweig [74, 29]; Maxima are marked by circles (aircraft sketch from: [74])

Besides, it has to be mentioned that the passenger cabin ends at 22.6 m as considered in the previous chapter and comprises the maximum of the UHBR excitation. Nevertheless, both CAA domains exceed this cabin end as indicated by the dashed line in Fig. 6.3. In order to consider the entire CAA domain of both the BPR5 and UHBR jet by the structure, the airframe domain Ω_s is extended by 2.8 m under the assumption of non-existing trim (Ω_g and Ω_t). This way, structure-borne sound within the stiffeners and the outer skin and thus the sound power input is generally

considered. Behind the cabin end at 22.6 m, a passenger entrance area exists with the aircraft door, which is clearly separated by room-dividing furnishing and is therefore not considered here.

For the location of maximum OSPLs indicated by white circles in Fig. 6.3, the frequency response (delivered by the DLR Braunschweig) is plotted in Fig. 6.4. The BPR5 engine is clearly dominating the entire frequency range and largely excites the outer skin with SPLs between 90 and 100 dB. In opposite, the novel UHBR engine largely yields SPLs between 70 and 80 dB, which is a significantly reduced excitation at the maximum position.

The pressure spectra at all spatial sampling points within the CAA domain are directly applied to the aircraft model according to the simulation chain in Fig. 6.1 (step III). Based on the mentioned nearest neighbour search, the local CAA data is picked, transformed to frequency domain and considered as element-wise excitation (right hand-side) in the FE model. Solving the system under consideration of all documented assumptions and measures with regard to efficiency (Ch. 5), the sound pressure field within the cabin is available for the excitation by both engine concepts.

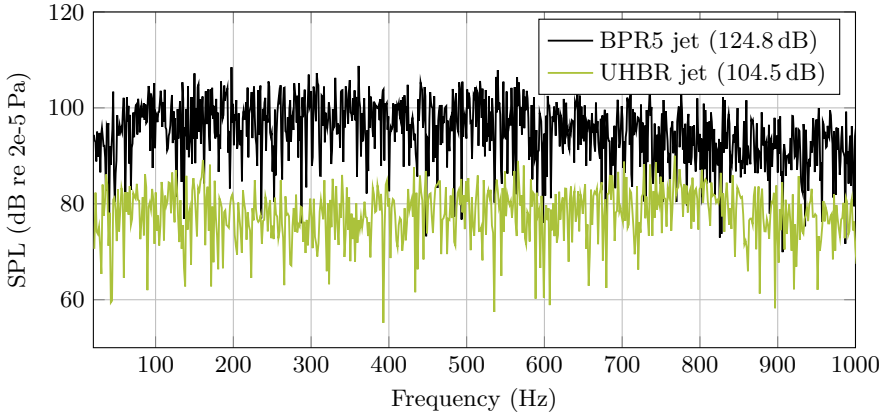

Figure 6.4: Jet excitation spectra at maximum sum level location on the outer skin based on CAA results from DLR Braunschweig [29]

In Fig. 6.5, the resulting mean squared pressure $\overline{p^2}$ for the seat row at $x = 18$ m is plotted for the BPR5 and UHBR jet excitations. The seat row is chosen, because it corresponds to the central seat row of the actual core model's section and the efficiency study on different aircraft lengths (Sec. 5.5) is conducted using the results from this very seat row. Additionally, the maximum of the BPR5 jet excitation is located close to it. The mean value is computed equally as within Ch. 5.

Both curves show stochastic characteristics as the actual sources within the jet stream

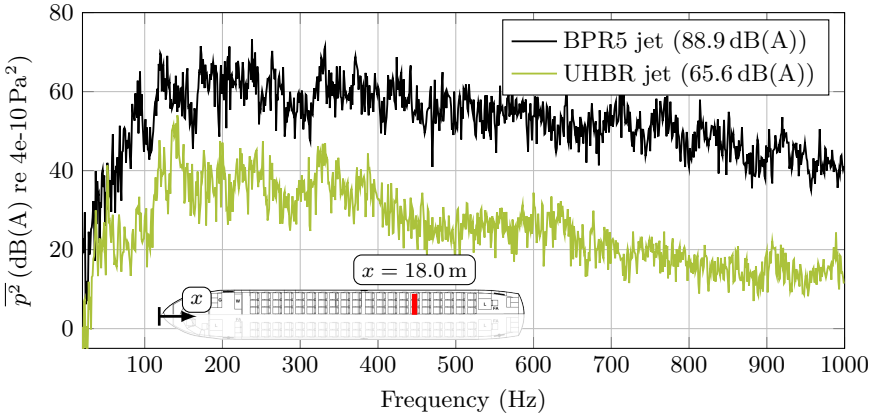

Figure 6.5: Numerical results for the mean squared pressure $\overline{p^2}$ within the cabin (passenger ear region of seat row at $x = 18\,\mathrm{m}$) under jet excitation (aircraft sketch from: [74])

are modelled stochastically within the FRPM method (step IIa) [30]. The OSPL shows a significantly lower sound pressure level induced by the UHBR engine's jet stream (65.6 dB(A) instead of 88.9 dB(A)). The BPR5 engine's jet is dominating over the entire investigated frequency range. As both curves have a decreasing trend, higher frequencies are not expected to contribute significantly to the sound pressure level. As the fuselage acts as filter for the sound transmission and an A-weighting according to Eq. (2.73) is applied, the pretty constant excitation levels by Fig. 6.4 is not visible in the cabin. Global maxima in $\overline{p^2}$ are formed between 100 and 400 Hz, whereby the UHBR engine's jet induces its maximum sound pressure levels ($> 50\,\mathrm{dB(A)}$) close to 140 Hz.

The maximum OSPL of the UHBR engine lies close to the last seat row, which results are therefore plotted in Fig. 6.6. As expected, the OSPL induced by the UHBR jet increases (+2.0 dB(A)). As the BPR5 jet's induced OSPL increases little less (+0.6 dB(A)), the difference between the two engine jets is smaller at this lengthwise position, but still significantly high. For the last seat row, the BPR5 engine jet dominates over the entire frequency range as well and similar curve trends are visible. Generally, the sound pressure levels induced by engine jets are expected to decrease towards the front part of an airliner. As shorter aircraft regions are applied above 410 Hz, the OSPL in the front seat row ($x = 6.5\,\mathrm{m}$) can be computed up to 410 Hz. For the UHBR, an OSPL of 53.3 dB(A) is yielded up to this frequency, which is a reduction of 14.0 dB(A) compared to the OSPL in the back seat row ($x = 22.0\,\mathrm{m}$; up to 410 Hz). The same comparison yields a OSPL reduced by 11.7 dB(A) for the BPR5 engine in the fron seat row. This underlines the dominating jet engine excitation in

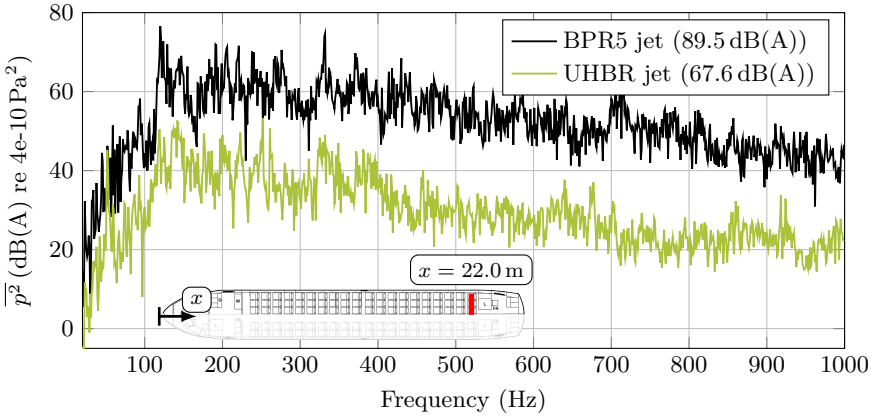

Figure 6.6: Numerical results for the mean squared pressure $\overline{p^2}$ within the cabin (passenger ear region of seat row at $x = 22\,\mathrm{m}$) under jet excitation (aircraft sketch from: [74])

the back of an airliner, as similarly depicted in [79]. In addition, the application of a short region for higher frequencies and a focus on the back region is assumed to be retrospectively justified.

As the results on engine jet excitations show significantly lower cabin sound pressure levels induced by the novel UHBR concept, the question about different possibly dominating sound sources arises. In [90], the turbulent boundary layer (TBL) is motivated as dominating sound source in passenger aircraft driven by modern engines. Therefore, the TBL is studied within the following section and applied to the fuselage model as well.

6.2 Turbulent boundary layer excitation

Beneath a turbulent boundary layer (TBL), acoustic pressure fluctuations arise on the outer skin, which are induced by the turbulent structures. The mechanisms of origin are of random nature and highly complex [41]. In literature, analytical models are available, which approximate

- location-dependent auto-spectra (power spectral density (PSD)) on the outer skin and
- location-dependent normalised wavenumber-spectra serving the occurring wavenumbers k [90].

Caused by the random nature of turbulence, a range of wave numbers occurs at each frequency. The combination of a normalised wavenumber-spectrum with an auto-

spectrum model is possible and delivers a full characterisation of the acoustic field beneath the TBL [90]. For the usage within the full aircraft FE-model, a deterministic snapshot with nodal forces is required for the right-hand side of the system in Eq. (2.63). The auto-spectra and wavenumber-spectra are introduced in the following for the generation of this snapshot. For this purpose, a superposition of plane waves under consideration of coherence length approximations below the TBL is aimed for, as similarly published in [30].

Auto-spectra approximations by analytical models are extensively studied and compared to experimental data in [91, 90]. The publication by Klabes ends up with extensions of the Goody model [65]. The modifications of the model yield an improved fitting to in-flight measurements on the outer skin of an Airbus A320. As the aircraft is similar to the CRC 880 research aircraft, the model is considered within this thesis. In Eqs. (6.1) to (6.3), the approximated auto-spectrum $\Phi(\omega)$ is given in dependency on the angular frequency ω [65].

$$\Phi(\omega) = \frac{\delta_l \tau_w^2 a \left(\frac{\omega \delta_l}{u_e}\right)^b}{u_e \left[\left(\frac{\omega \delta_l}{u_e}\right)^c + d\right]^e + u_e \left[f R_t^g \frac{\omega \delta_l}{u_e}\right]^h} \tag{6.1}$$

$$R_t = \frac{\delta_l}{u_e} \Big/ \frac{\nu}{u_\tau^2} \tag{6.2}$$

$$u_\tau = \sqrt{\tau_w / \rho} \tag{6.3}$$

This model with its auxiliary parameters R_t and u_τ is evaluated at each position of the fuselage yielding frequency-dependent and location-dependent auto-spectra. Numerous flow parameters are required for the model, which are explained in the following:

- The parameters $a - h$ are introduced by Goody as constants [65] and adjusted by Klabes et al. in [91]. After fittings to in-flight measurements, new constants or functions are partially yielded, which are given in Eq. (6.4) [91].

$$\begin{aligned}
a &= \left(\frac{\mathrm{TKE}_{\max}}{10\,\mathrm{m^2/s^2}}\right)^{\left[1.74 - 592.71 c_f\right]\left[\Delta_\delta \frac{u_e}{\nu}\right]^{0.01}} & b &= 0.5 \\
c &= 1.35 + 3\frac{\delta_l}{q}\frac{\mathrm{d}p}{\mathrm{d}x} & d &= \left(\frac{\delta_l u_e}{\nu}\right)^{0.174} - 6.7 \\
e &= 1.55 - 0.11428\frac{\Delta_\delta}{q}\frac{\mathrm{d}p}{\mathrm{d}x} & f &= 1.1 \\
g &= -0.57 & h &= 7.0
\end{aligned} \tag{6.4}$$

A detailed derivation of the equations and the fitting process can be found in [91].

- The local TBL thickness δ_l is measured according to the total pressure criterion documented by Klabes in [90]. The TBL evolves towards the back [91], which is represented by an increasing δ_l.
- At the same location (total pressure criterion), the boundary layer edge velocity u_e is considered in the model [91].
- c_f and τ_f declare the friction coefficient and the wall shear stress, respectively [91].
- The local density is given by ρ and ν is the kinematic viscosity [91].
- TKE stands for the turbulent kinetic energy, whose maximum is considered for the parameter a [91].
- The pressure gradient $\frac{\mathrm{d}p}{\mathrm{d}x}$ and the dynamic pressure q are required for the parameters c and e [91].
- Finally, $\Delta_\delta = \delta_l \sqrt{2/c_f}$ is a modified parameter by Rotta and Clauser [144, 45], which originally uses the displacement thickness. Klabes et. al declare in [91] the consistent usage of a scaled δ_l instead.

As the parameters are changing over the fuselage length, location-dependency is taken into account accordingly. In Fig. 6.7, the predicted auto-spectra are plotted for different longitudinal locations x on the research aircraft fuselage. For the derivation of flow parameters, the fuselage CFD dataset used for the jet noise excitation above and published in [29] is considered. Similar to measurements in [91] and [90], a shift of the maximum can be observed towards lower frequencies with increasing x. As the boundary layer thickness is increasing towards the back of the aircraft, larger wave lengths can evolve. In addition, the absolute maximum is visible in the middle of the aircraft. Nevertheless, the assumption of a shortened aircraft region is assumed to hold true as the amplitudes differ by $2-3\,\mathrm{dB}$. Furthermore, the shortest model starts at $x = 13\,\mathrm{m}$ (length of $9\,\mathrm{m}$) and is applied above $590\,\mathrm{Hz}$, which ensures a coverage of the maximum in the $x = 14\,\mathrm{m}$ curve.

Normalised wavenumber-spectra are available in large numbers in literature, a comprehensive documentation can be found in [90]. Beneath these models, the Efimtsov model [57] has proven in [73] to correctly represent in-flight measurements of coherence lengths in longitudinal (length-wise / flow / x) and lateral (span-wise / y) direction $\lambda_{x/y}$ under certain parameter adjustments. As Haxter and Spehr applied their fittings in [73] to in-flight data of an A320, which again fits the research

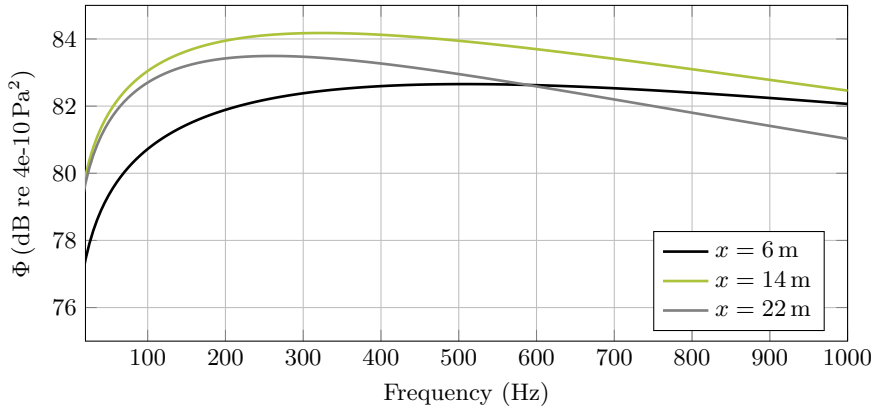

Figure 6.7: Auto-spectra (Goody-DLR) beneath TBL at different length-wise locations

aircraft, the modified Efimtsov model is selected for this thesis. In Eq. (6.5) [90], the normalised form of the model is given.

$$\Phi_{\mathrm{norm}}(\mathbf{k},\omega) = \frac{4\alpha_x\alpha_y}{\left[\alpha_y^2 + \left(k_y\frac{u_c}{\omega}\right)^2\right]\left[\alpha_x^2 + \left(k_x\frac{u_c}{\omega} - 1\right)^2\right]} \tag{6.5}$$

$$\alpha_{x/y}(\omega) = \frac{u_c}{|\omega|\,\Lambda_{x/y}} \tag{6.6}$$

The normalised spectrum $\Phi_{\mathrm{norm}}(\mathbf{k},\omega)$ in Eq. (6.5) expresses the occurrence of the inserted wave number vector $\mathbf{k}(\omega,\mathbf{x}) = [k_x(\omega,\mathbf{x}), k_y(\omega,\mathbf{x}]$ and yields 1 after integration over $\mathbf{k}$. The parameters $\lambda_{x/y}$ are coherence lengths in longitudinal (x) and lateral (y) direction, which are given in Eqs. (6.7) and (6.8).

$$\Lambda_x(\omega) = \delta_l\left[\left(\frac{a_1\mathrm{Str}}{u_c/u_\tau}\right)^2 + \frac{a_2^2}{\mathrm{Str}^2 + (a_2/a_3)^2}\right] \tag{6.7}$$

$$\Lambda_y(\omega) = \delta_l\left[\left(\frac{a_4\mathrm{Str}}{u_c/u_\tau}\right)^2 + \frac{a_5^2}{\mathrm{Str}^2 + (a_5/a_6)^2}\right] \tag{6.8}$$

Additional flow parameters required by the Efimtsov model are

- the Strouhal number $\mathrm{Str} = \omega\delta_l/u_\tau$ [57],
- the convective velocity u_c calculated according to [72] with values between $0.75u_\infty$ and $0.9u_\infty$ in dependency on frequency and
- constant parameters $a_{1\ldots6}$.

The latter were taken into account for the fitting in [73], which results in a new parameter set $a_{1...6} = (0.071, 4.1, 0.26, 0.66, 39, 9.9)$ considered in this thesis. The coherence lengths $\Lambda_x(\omega)$ and $\Lambda_y(\omega)$ are plotted in Fig. 6.8 for different longitudinal locations x on the fuselage based on the CFD data introduced above. Over the airliner's length, $\Lambda_x(\omega)$ and $\Lambda_y(\omega)$ increase towards the back, respectively. As the TBL thickness increases, larger turbulent structures can evolve, which allows larger coherence lengths in the back at low frequencies [73]. With increasing frequency, $\Lambda_x(\omega)$ and $\Lambda_y(\omega)$ approach similar values at all locations with a decreasing trend, respectively. Here, short wave lengths are the correlation-limiting factor, which replaces the TBL thickness at low frequencies [73].
Generally, the longitudinal coherence lengths $\Lambda_x(\omega)$ show a significantly higher order of magnitude over the entire frequency range. In Sec. 5.2, bending wave lengths between 0.1 and 0.7 m within a 1 mm CFRP skin field within the outer skin are depicted in Fig. 5.2. This value is considered as minimum in Sec. 5.2 in order to define the frequency-dependent meshes. As obvious in Fig. 6.8, the lateral coherence lengths λ_y cannot be resolved by the mesh as the approximated values are significantly smaller than the occurring bending wave lengths. Nevertheless, there is no need to refine the mesh in lateral direction as a significant excitation of bending waves by much shorter coherence lengths is not expected. A poorly correlated wave field within the length of a bending wave is more likely to have a destructive effect. Hence, as long as the structure is well-resolved (current value is a minimum of 9 nodes per wave length), the major part of the induced sound energy by any TBL excitation is assumed to be considered automatically. The same thread of thoughts is valid for the longitudinal coherence lengths λ_x, even if these are well resolved by the mesh as all values exceed the mentioned bending wave lengths.

In Fig. 6.9, the normalised wavenumber spectrum according to Eq. (6.5) is exemplary plotted for 300 Hz and $x = 14$ m over normalised coordinates $k_{x/y}/k_\omega$ with $k_\omega = \omega/u_c$. As introduced above, k_c declares the convective velocity calculated according to [72]. This value highly dominates the occurring wavenumbers in flow direction k_x [90] as visible in the contour plot. However, the entire domain must be considered in the integral as a high energy input is expected if the wave number beneath the TBL fits the bending wave number within the outer skin fields.

A superposition of plane waves, similar to [46, 88], is applied in order to generate a representative sound field snapshot beneath the TBL. The combination of available autospectra $\Phi(\omega, \mathbf{x})$ (Goody-DLR model) and normalised wavenumber-frequency spectra Φ_{norm} (Efimtsov model with adjusted parameters) allows to construct plane waves

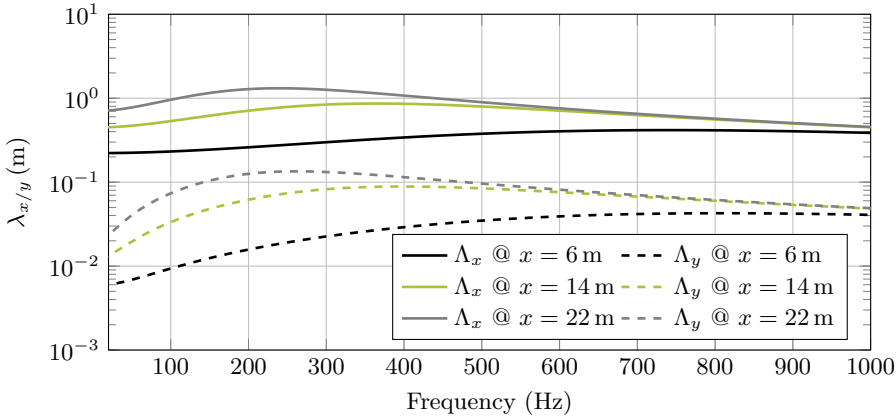

Figure 6.8: Coherence lengths beneath the TBL of the CRC 880 research aircraft according to Efimtsov [57] in combination with fitted parameters by Haxter and Spehr [73]

according to Eq. (6.9) [30], in which the amplitude is expressed by $\sqrt{\Phi(\omega, \mathbf{x})}$ [109] and the phases in longitudinal and lateral direction are generated based on the wave number vector $\mathbf{k}(\omega, \mathbf{x})$. In the numerically performed integration, Φ_{norm} serves as weighting factor yielding a superposition of normalised plane waves. The resulting phase information at $\mathbf{x}$ is dependent on the dominating wave numbers and finally multiplied by the amplitude of the Goody-DLR auto-spectrum $\sqrt{\Phi(\omega, \mathbf{x})}$.

$$p_1(\omega, \mathbf{x}) = \sqrt{\Phi(\omega, \mathbf{x})} \int \Phi_{\text{norm}}(\mathbf{k}, \omega) \mathrm{e}^{i\mathbf{k}\mathbf{x}} \mathrm{d}\mathbf{k} \tag{6.9}$$

Eq. (6.9) is evaluated within a frequency- and location-dependent coherence grid set upon the outer skin of the fuselage. The coherence grid is generated independently on the actual FE mesh and follows a 2D coordinate system on the outer skin using the longitudinal and lateral directions. Each rectangular grid area has the dimensions of the lateral and longitudinal coherence lengths $\Lambda_x(\omega, \mathbf{x})$ and $\Lambda_y(\omega, \mathbf{x})$, what provides the requirement for frequency- and location-dependent grids. Within each grid area, coherence is assumed, which is realised by a constant origin of the local coordinate system. Between any two grid areas, the normalised plane waves are uncorrelated as the origin of the local coordinate system is randomly redefined for each of them. In other words, a coherent sound field is generated within each grid area, which is incoherent to all other grid areas.

Similar to the engine jet excitation in Sec. 6.1, a complex pressure distribution is thereby available on the outer skin defining the right-hand side's input of the aircraft

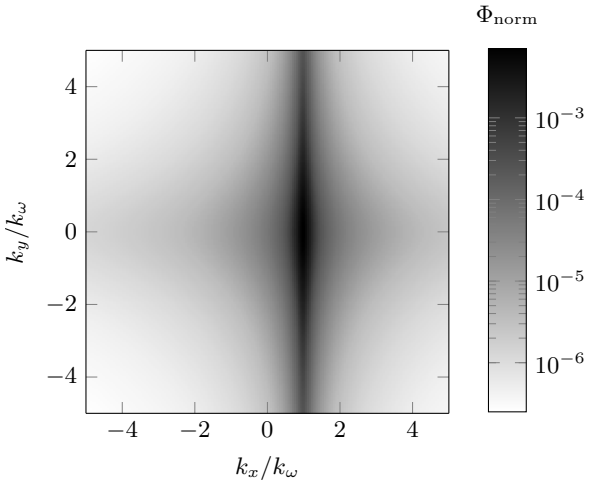

Figure 6.9: Normalised wavenumber spectrum $\Phi_{\mathrm{norm}}(\mathbf{k}, \omega)$ over normalised wavenumbers $k_{x/y}/k_\omega$ at 300 Hz and $x = 14$ m

system. The solution of the system under consideration of all efficiency measures in Ch. 5 yields the sound pressure field within the passenger cabin.

In Fig. 6.10, the resulting mean squared pressure $\overline{p^2}$ for the central seat row is plotted in comparison with the BPR5 and UHBR jet excitations from the previous section. With 70.2 dB(A), the OSPL of the generic TBL excitation is located within the OSPLs of the two jets. Dedicated to the random generation of the frequency-dependent grids' origins, each frequency sample is unique and the curves are not smooth. A regeneration of the excitation would deliver a different snapshot of the TBL loading and therefore a deviant result. Nevertheless, over the entire frequency range, these variations are not expected to change the overall assessment of the excitation type.

Between 100 and 400 Hz, the TBL excitation induces levels clearly above 40 dB(A) in the continuous spectrum. The global maxima are located similar to the jet excitation's induced levels, but from 400 Hz towards higher frequencies, the curve's descent is significantly lower. Rather, the TBL induces SPLs of nearly 40 dB(A) up to 1000 Hz. While the BPR5 results drop towards a similar value, the UHBR result already levels off at around 20 dB(A). It can be expected from these results, that the SPLs by the TBL contribute to the OSPL at even higher frequencies as well. Future studies are required to investigate higher frequencies (with finer meshes) and deliver more expressive OSPLs for the TBL. In [79], a similar OSPL contribution by the TBL and a conventional jet engine is reported at flight levels FL350–390. Based on simulations towards higher frequencies and an averaging within the cabin, a comparison with the measurement data is possible.

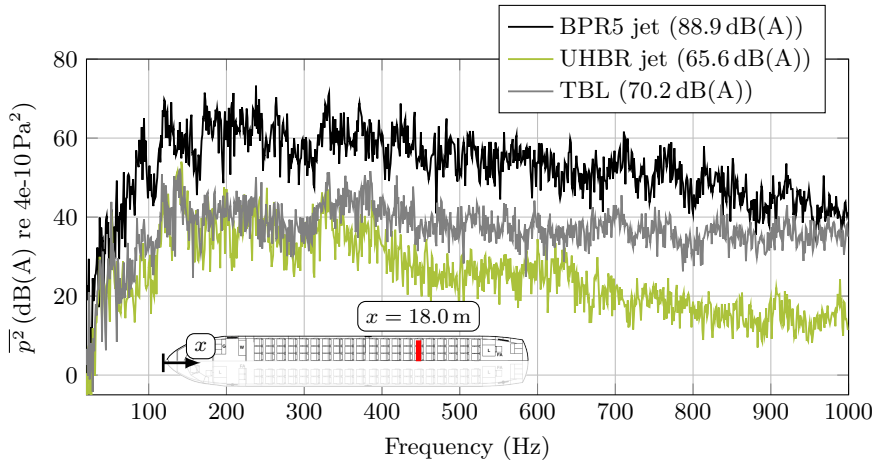

Figure 6.10: Numerical results for the mean squared pressure $\overline{p^2}$ within the cabin (passenger ear region of seat row at $x = 18$ m) under TBL excitation in comparison with engine jet excitations (aircraft sketch from: [74])

Similar to the previous section, an OSPL for the front seat row can be computed up to 410 Hz. A difference of 4.2 dB(A) is yielded between the front and back seat row under TBL excitation. The according frequency response is given in Fig. 6.11. The difference is of significantly lower order compared to the jet excitation as the entire fuselage is excited by the TBL. This indicates a clear domination of TBL excitations in front seat rows compared to the UHBR engine. Besides, the increased OSPL towards the back of the aircraft is dedicated to a thicker boundary layer. In [79], 3 to 4 dB increased OSPL due to TBL excitations when moving from a central cabin position to the back are reported. However, a quantitative comparison is only possible for the same aircraft, the entire cabin domain and a converged OSPL with regard to the maximum frequency.

Concluding, the shown results based on a generic TBL excitation point out a possibly increased relevance of this excitation type as the jets of novel engines are expected to be a non-dominating sound source. The proposed procedure can be transferred to any structure with available RANS data and is therefore highly flexible. However, a validation with measurement data or high-fidelity simulations is meant for future studies. In addition, the random character of a TBL loading can be considered by an evaluation of many snapshots.

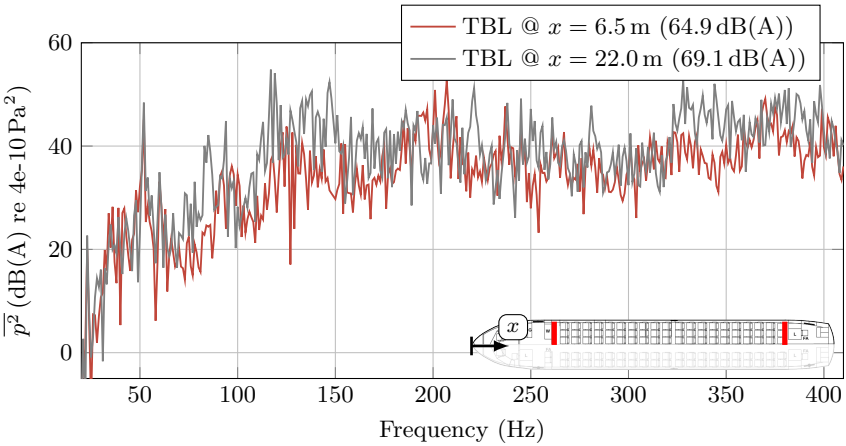

Figure 6.11: Numerical results for the SPL within the cabin (passenger ear region) under TBL excitation for two different length-wise positions (aircraft sketch from: [74])

7 Summary and outlook

Motivated by the well-being and health of billions of future air travellers, the numerical prediction of passenger cabin SPLs is investigated within this thesis. The key findings are manifold and presented with three major chapters investigating an aircraft fuselage model, its efficient solving and application examples. The latter introduces a simulation chain considering RANS and CAA results for the prediction of cabin acoustics.

The final step of the chain is constituted by a comprehensive, wave-resolving **fuselage model** including the sound field within the passenger cabin. The full aircraft fuselage model comprises the airframe, the insulation, the interior lining and the passenger cabin, which are individually characterised on the basis of experiments conducted. One important finding of the modelling chapter is on the glass wool insulation layer between the airframe and the interior panel. The Biot model, which considers the structure-borne sound transmission within the glass fibres, is necessary to take structural resonances within the double wall gap in the low frequency range into account. On this basis, a clear motivation for future studies on structural anisotropic material parameters of glass wool is given (frequency- and compression-dependent).
A second key finding on the modelling part is on the cabin fluid domain containing seats and passengers. A global damping approach using a homogenised damping loss factor shows deviations up to 5 dB in the frequency response compared to a consideration of local seat surface impedances. If the wave propagation near seats shall be modelled more detailed, precise impedance measurements of the seat surfaces or a poro-elastic modelling of the seat material are reasonable next steps based on this thesis.
Besides the described insights concerning the acoustic domains, the structural domains (airframe, interior lining) bring along difficulties regarding manufacturing tolerance of widely applied carbon and glass fibre reinforced plastics. For a consideration of uncertainties [71], parameter studies with thousands of samples are necessary. For this purpose, mathematical model order reduction techniques (e.g. Krylov subspace methods [141]) can built upon the aircraft model developed within this thesis. In addition, a significant effect of pre-stress due to pressurisation is crucial for the skin

field vibrations. For this purpose, the in-house code elPaSo is extended by a closed cylinder model considering pre-stress in skin fields, circular frames and length-wise stringers.

The numerical solution of the wave-resolving aircraft model is conducted by the FEM, for which **efficient solving** approaches are investigated. The combination of frequency-adaptive meshes and a justified weak coupling assumption decreases the computational time required by 87% for a fuselage section of 4.3 m, while the time reference is the mesh required for the maximum frequency and a strong coupling condition within the entire frequency range. The assumption of a weakly coupled passenger cabin domain above 410 Hz introduces errors below 3 dB in the fuselage section model, while errors below 1 dB are dominating. The iterative solver GMRES linked with a physically-motivated block LU preconditioners is shown to perform significantly better than the direct MUMPS solver. The application of the MUMPS solver with activated block low rank feature as preconditioner within the blocks saves memory and nevertheless allows an exact solution by the iterative full domain solution process. Implementations based on PETSC [22] are conducted for the parallel solver studies and the weak coupling solution, which are available with the thesis. Finally, in order to further increase efficiency, a locality effect due to wave attenuation allows the use of shorter aircraft sections with increasing frequency. The reduced fuselage length countermeasures the mesh refinement and therefore impedes the exponential increase in the dof and thus solution effort.

As the sound pressure field in the cabin is delivered by the fuselage model, a direct comparison of aircraft concepts with regard to cabin acoustics is accessible. The sound induced by the jet of both a conventional and a novel UHBR engine within the **application** chapter shows a clearly decreased SPL of the UHBR engine up to 1000 Hz. For the application of the jet-induced sound, a simulation chain considering RANS, CAA and FEM simulations is established in collaboration with the DLR Braunschweig, while the FEM is applied here to solve the vibroacoustic fuselage model. Besides jet excitations, a superposition of plane waves based on semi-analytical models is shown in order to generate a deterministic snapshot of the random loading beneath a TBL. The introduced approximation of a TBL excitation delivers similar SPLs as the UHBR concept up to 400 Hz in back seat rows. For front rows and generally above 400 Hz, a dominance of the TBL excitation is expected for future aircraft generations. In order to complete the picture of source impacts, different sources of jet planes like the fan must be focused in further studies as well.

Concluding, the obtained results represent a decisive contribution towards the realisation of quieter passenger cabins in future aircraft. The application on jet and TBL excitations finally demonstrates that a simulation tool for technology assessment is available now delivering the sound at the passenger ear. By transferring the mechanical modelling assumptions and its numerical solution on different aircraft and even other mobility vehicles, the performance of sound reduction measures can be estimated, novel technologies can be assessed or parameter studies can be conducted in early design stages. The author can additionally imagine the following mid- and long-term research topics:

- As the model is not subjected to deep assumptions and resolves the linear propagation of sound waves, it may serve as benchmark for testing novel numerical methods.
- The resulting SPL within the passenger cabin under realistic loading can be considered as objective function within a design or optimisation process. An appropriate example is the application of passive damping measures in early design stages, like e.g., acoustic black holes, which potentially reduce SPLs and mass in parallel. In [26], the author studies the effect of acoustic black holes on the transmission loss and shows a visible increase.
- The fuselage model can be solved at any number of frequency samples, which serves a continuous frequency spectrum of the sound pressure including the phase information. By an inverse fast Fourier transformation (ifft), an auralisation is accessible, which can be used for listening tests and thus for a psychoacoustic assessments.

Bibliography

[1] DIN EN ISO 10140-2. *Akustik–Messung der Schalldämmung von Bauteilen im Prüfstand – Teil 2: Messung der Luftschalldämmung*. DIN German Institute for Standardization. 2010.

[2] DIN EN ISO 10534-2:2001. *Akustik - Bestimmung des Schallabsorptionsgrades und der Impedanz in Impedanzrohren - Teil 2: Verfahren mit Übertragungsfunktion (ISO 10534-2:1998); Deutsche Fassung EN ISO 10534-2:2001*. DIN German Institute for Standardization. 2001.

[3] DIN EN ISO 12999-1. *Akustik - Bestimmung und Anwendung der Messunsicherheiten in der Bauakustik - Teil 1: Schalldämmung (ISO 12999-1:2014); Deutsche Fassung EN ISO 12999-1:2014*. DIN German Institute for Standardization. 2014.

[4] DIN EN 29053:1993-05. *Akustik, Materialien für akustische Anwendungen, Bestimmung des Strömungswiderstandes (ISO 9053:1991), Deutsche Fassung EN 29053:1993*. DIN German Institute for Standardization. 1993.

[5] DIN EN ISO 354:2003. *Akustik - Messung der Schallabsorption in Hallräumen (ISO 354:2003); Deutsche Fassung EN ISO 354:2003*. DIN German Institute for Standardization. 2003.

[6] DIN EN 60651:1994-05. *Schallpegelmesser (IEC 60651:1979 + A1:1993); Deutsche Fassung EN 60651:1994 + A1:1994*. DIN German Institute for Standardization. 1993.

[7] ISO 9613-1. *Akustik; Dämpfung des Schalls bei der Ausbreitung im Freien; Teil 1: Berechnung der Schallabsorption durch die Luft*. ISO International Organization for Standardization. 1993.

[8] M. Abele, M. Rescheleit and O. von Estorff. "Integrated Simulation Model for Cabin Acoustics". In: *Aircraft System Technologies, AST 2013*. mub-bib. Hamburg, 2013.

[9] *Airbus A320-232 D-ATRA*. Accessed: 2nd Aug 2021, `https://www.dlr.de/content/de/artikel/luftfahrt/forschungsflotte-infrastruktur/dlr-flugzeugflotte/airbus-a320-232-d-atra.html`.

[10] A. Alich. *Homogenisierte vibroakustische Modelle für Honeycomb-Sandwich-Strukturen in Flugzeugen*. Studienarbeit, Institute for Engineering Design, TU Braunschweig. 2018.

[11] J.-F. Allard, R. Bourdier and A. L'Esperance. "Anisotropy effect in glass wool on normal impedance in oblique incidence". In: *Journal of Sound Vibration* 114 (1987), pp. 233–238, 1987.

[12] J.-F. Allard and Y. Champoux. "New empirical equations for sound propagation in rigid frame fibrous materials". In: *Journal of the Acoustical Society of America* 91.6 (1992), pp. 3346–3353, 1992.

[13] J.-F. Allard and B. Sieben. "Measurements of acoustic impedance in a free field with two microphones and a spectrum analyzer". In: *Journal of the Acoustical Society of America* 77.4 (1985), pp. 1617–1618, 1985.

[14] J. Allard and N. Atalla. *Propagation of sound in porous media: modelling sound absorbing materials 2e*. John Wiley & Sons, 2009.

[15] H. Altenbach and J. Altenbach. *Mechanics of composite structural elements*. Springer, 2004.

[16] B. Arnold. *Werkstofftechnik für Wirtschaftsingenieure*. Springer, 2017.

[17] S. Aso and R. Kinoshita. "Sound absorption coefficient of glass wool". In: *Journal of the Textile Machinery Society of Japan* 12.3 (1966), pp. 101–106, 1966.

[18] N. Atalla and R. J. Bernhard. "Review of numerical solutions for low-frequency structural-acoustic problems". In: *Applied Acoustics* 43.3 (1994), pp. 271–294, 1994.

[19] N. Atalla and F. Sgard. *Finite element and boundary methods in structural acoustics and vibration*. CRC Press, 2015.

[20] Noureddine Atalla, Raymond Panneton and Patricia Debergue. "A mixed displacement-pressure formulation for poroelastic materials". In: *The Journal of the Acoustical Society of America* 104.3 (1998), pp. 1444–1452.

[21] Y. Atalla and R. Panneton. "Inverse acoustical characterization of open cell porous media using impedance tube measurements". In: *Canadian acoustics* 33.1 (2005), pp. 11–24, 2005.

[22] S. Balay et al. *PETSc Web page*. Accessed: 2nd Aug 2021, `https://www.mcs.anl.gov/petsc`.

[23] R. Barrett et al. *Templates for the solution of linear systems: building blocks for iterative methods*. SIAM, 1994.

[24] K.-J. Bathe. *Finite-Elemente-Methoden*. Springer, 2002.

[25] M. A. Biot. "Generalized theory of acoustic propagation in porous dissipative media". In: *Journal of the Acoustical Society of America* 34.9A (1962), pp. 1254–1264, 1962.

[26] C. Blech and S. C. Langer. "Aircraft cabin noise reduction by means of acoustic black holes". In: *INTER-NOISE and NOISE-CON Congress and Conference Proceedings*. Institute of Noise Control Engineering. Hong Kong, China, 2017.

[27] C. Blech and S. C. Langer. "Wave-resolving aircraft fuselage model for cabin noise predictions under distributed fluid loadings". In: *Proceedings of the International Conference on Structural Dynamic (EURODYN)*. European Association for Structural Dynamics (EASD). Athens, Greece (virtual conference), 2020.

[28] C. Blech et al. "Numerical prediction of cabin noise due to jet noise excitation of two different engine configurations". In: *Proceedings of the 24th International Congress on Sound and Vibration (ICSV24)*. International Institute of Acoustics and Vibration. London, Great Britain, 2017.

[29] C. Blech et al. "Numerical prediction of passenger cabin noise due to jet noise by an ultra–high-bypass ratio engine". In: *Journal of Sound and Vibration* 464 (2020), pp. 114960, 2020.

[30] C. Blech et al. "Wave-resolving Numerical Prediction of Passenger Cabin Noise Under Realistic Loading". In: *Radespiel, R., Semaan, R.: Fundamentals of High Lift for Future Civil Aircraft: Papers Contributed to the Final Symposium of the Collaborative Research Center 880, December 17-18, Braunschweig, Germany 2019*. Springer, 2020.

[31] K.-U. Bletzinger, M. Bischoff and E. Ramm. "A unified approach for shear-locking-free triangular and rectangular shell finite elements". In: *Computers & Structures* 75.3 (2000), pp. 321–334, 2000.

[32] J. Blinstrub, L. Bertsch and W. Heinze. "SFB 880 Vehicle Concepts and Comparative Noise Assessment". In: *in Final Symposium of the Collaborative Research Centre 880 - Fundamentals of High Lift for Future Civil Aircraft* (2020).

[33] T. Blitzer. "Introduction, Honeycomb Technology". In: *Materials, design, manufacturing, applications and testing, first edition, Chapman & Hall* (1997).

[34] S. Boily and F. Charron. "The vibroacoustic response of a cylindrical shell structure with viscoelastic and poroelastic materials". In: *Applied Acoustics* 58.2 (1999), pp. 131–152, 1999.

[35] F. Bošnjaković and K.-F. Knoche. *Technische Thermodynamik Teil II*. Springer, 1997.

[36] E. Brandão, A. Lenzi and S. Paul. "A review of the in situ impedance and sound absorption measurement techniques". In: *Acta Acustica united with Acustica* 101.3 (2015), pp. 443–463, 2015.

[37] TU Braunschweig. *Collaborative Research Center 880*. Accessed: 24th Jul 2018, `tu-braunschweig.de/sfb880`.

[38] TU Braunschweig. *SE²A - Sustainable and Energy-Efficient Aviation*. Accessed: 12th Feb 2021, `tu-braunschweig.de/se2a`.

[39] R. D. Buehrle et al. "Finite element model development for aircraft fuselage structures". In: *Proceedings of XVIII International Modal Analysis Conference*. Society for Experimental Mechanics. San Antonio, TX, United States, 2000.

[40] ASTM C800-14. *Standard Specification for Fibrous Glass Blanket Insulation (Aircraft Type)*. ASTM American Society for Testing and Materials. 2014.

[41] R. Camussi. *Noise sources in turbulent shear flows: fundamentals and applications*. Vol. 545. Springer Science & Business Media, 2013.

[42] B. Castagnède et al. "Parametric study of the influence of compression on the acoustical absorption coefficient of automotive felts". In: *Comptes Rendus de l'Académie des Sciences-Series IIB-Mechanics* 329.2 (2001), pp. 125–130, 2001.

[43] Y. Champoux and J.-F. Allard. "Dynamic tortuosity and bulk modulus in air-saturated porous media". In: *Journal of applied physics* 70.4 (1991), pp. 1975–1979, 1991.

[44] D. Clasen. "Numerische Untersuchung der akustischen Eigenschaften von trennenden und flankierenden Bauteilen". Braunschweiger Schriften zur Mechanik Nr. 64-2008, Me-chanik-Zentrum, TU Braunschweig. PhD thesis. 2008.

[45] F. H. Clauser. "Turbulent boundary layers in adverse pressure gradients". In: *Journal of the Aeronautical Sciences* 21.2 (1954), pp. 91–108, 1954.

[46] A. Clement, C. Audoly and J.-A. Astolfi. "Finite element study of the vibroacoustic response of a structure, excited by a turbulent boundary layer". In: *INTER-NOISE and NOISE-CON Congress and Conference Proceedings*. Vol. 253. 1. Institute of Noise Control Engineering. 2016, pp. 6996–7006.

[47] V. Cotoni, B. Gardner and P. Shorter. "Vibro-acoustic analysis of aircraft fuselage panels using a periodic SEA subsystem formulation". In: *INTER-NOISE and NOISE-CON Congress and Conference Proceedings*. Institute of Noise Control Engineering. Shanghai, China, 2008.

[48] L. Cremer and M. Heckl. *Körperschall: physikalische Grundlagen und technische Anwendungen*. Springer, 2013.

[49] M. J. Crocker. *Handbook of noise and vibration control*. John Wiley & Sons, 2007.

[50] I. Dandaroy et al. "Passive interior noise reduction analysis of King Air 350 turboprop aircraft using boundary element method/finite element method (BEM/FEM)". In: *Journal of the Acoustical Society of America* 118.3 (2005), pp. 1888–1889, 2005.

[51] K. De Langhe et al. "Sound Transmission Loss predictions of aircraft panels: an update on recent technology evolutions". In: *INTER-NOISE and NOISE-CON Congress and Conference Proceedings*. Institute of Noise Control Engineering. Hamburg, Germany, 2016.

[52] M. E. Delany and E. N. Bazley. "Acoustical properties of fibrous absorbent materials". In: *Applied acoustics* 3.2 (1970), pp. 105–116, 1970.

[53] J. W. Demmel. *Applied numerical linear algebra*. SIAM, 1997.

[54] W. Desmet. "Mid-frequency vibro-acoustic modelling: challenges and potential solutions". In: *Proceedings of ISMA*. Vol. 2. 2002. Citeseer. 2002, pp. 12, 2002.

[55] ASTM E2611-09. *Standard Test Method for Measurement of Normal Incidence Sound Transmission of Acoustical Materials Based on the Transfer Matrix Method*. ASTM American Society for Testing and Materials. 2009.

[56] S. Ebnesajjad. *Handbook of adhesives and surface preparation: technology, applications and manufacturing*. William Andrew, 2010.

[57] B. M. Efimtsov. "Characteristics of the field of turbulent wall pressure-fluctuations at large Reynolds-numbers". In: *Soviet Physics Acoustics-USSR* 28.4 (1982), pp. 289–292, 1982.

[58] O. von Estorff and T. König. "Influence of different stiffening types of the aircraft body structure on the noise exposure in the cabin". In: *25th Congress of International Council of the Aeronautical Sciences Proceedings*. Hamburg, Germany, 2006.

[59] O. von Estorff and M. Wandel. “Numerical modelling of sound transmission loss of interior aircraft lining elements”. In: *Proceedings of the 10th International Congress on Sound and Vibration (ICSV10)*. International Institute of Acoustics and Vibration. Stockholm, Sweden, 2003.

[60] R. Ewert et al. “CAA broadband noise prediction for aeroacoustic design”. In: *Journal of sound and vibration* 330.17 (2011), pp. 4139–4160, 2011.

[61] G. T. Fechner. *Elements of psychophysics. Vol. I.* Holt, Rinehart and Winston, 1966.

[62] X. Feng and Z. Xie. “Domain decomposition methods for a coupled vibration between an acoustic field and a plate”. In: *Proceedings of the 12th International Conference on Domain Decomposition Methods*. ddm.org. 1999.

[63] C. C. Foo, G. B. Chai and L. K. Seah. “Mechanical properties of Nomex material and Nomex honeycomb structure”. In: *Composite structures* 80.4 (2007), pp. 588–594, 2007.

[64] L. J. Gibson and M. F. Ashby. “The mechanics of honeycombs”. In: *Cellular Solids: Structure and Properties*. 2nd ed. Cambridge Solid State Science Series. Cambridge University Press, 1997.

[65] M. Goody. “Empirical spectral model of surface pressure fluctuations”. In: *AIAA journal* 42.9 (2004), pp. 1788–1794, 2004.

[66] A. Grama and A. H. Sameh. *Parallel Algorithms in Computational Science and Engineering*. Springer, 2020.

[67] F. P. Grooteman. *Transmission Loss analyses on fuselage panels*. Report no. NLR-TP-2006-479, National Aerospace Laboratory NLR. 2006.

[68] S. Gudmundsson. *General aviation aircraft design: Applied Methods and Procedures*. Butterworth-Heinemann, 2013.

[69] A. Guermouche, J.-Y. L’Excellent and G. Utard. “On the memory usage of a parallel multifrontal solver”. In: *Proceedings International Parallel and Distributed Processing Symposium*. IEEE. 2003, 8–pp, 2003.

[70] A. Gündel, S. Häusler and S. Marburg. “Vergleich verschiedener Absorbermodelle zur Berechnung von Fluginnenlärm unter Beachtung poröser Materialien”. In: *Fortschritte der Akustik – DAGA 2007*. Deutsche Gesellschaft für Akustik e.V. (DEGA). Stuttgart, Germany, 2007.

[71] S. Guruprasad et al. “Uncertainty Quantification of numerical transmission loss calculations of an aircraft fuselage section”. In: *Fortschritte der Akustik – DAGA 2018*. Deutsche Gesellschaft für Akustik e.V. (DEGA). Munich, Germany, 2018.

[72] S. Haxter and C. Spehr. “Two-dimensional evaluation of turbulent boundary layer pressure fluctuations at cruise flight conditions”. In: *Proceedings of the 18th AIAA/CEAS Aeroacoustics Conference*. American Institute of Aeronautics and Astronautics (AIAA). Colorado Springs, CO, United States, 2012.

[73] S. Haxter and C. Spehr. “Comparison of model predictions for coherence length to in-flight measurements at cruise conditions”. In: *Journal of Sound and Vibration* 390 (2017), pp. 86–117, 2017.

[74] W. Heinze and T. Weiss. *Main Data Sheet, A/C Type: SFB880 Reference Aircraft REF3-2015*. Internal CRC 880 document,Institute of Aircraft Design and Lightweight Structures, TU Braunschweig. 2015.

[75] L. Herbeck, H. Wilmes and M. Kleineberg. “Material and processing technology for CFRP fuselage”. In: *Proceedings of the 49th international SAMPE symposium and exhibition*. Society for the Advancement of Material and Process Engineering. Long Beach, CA, United States, 2004.

[76] P. C Herdic et al. “The vibro-acoustic response and analysis of a full-scale aircraft fuselage section for interior noise reduction”. In: *Journal of the Acoustical Society of America* 117.6 (2005), pp. 3667–3678, 2005.

[77] H. Hosseini-Toudeshky, M. S. Goodarzi and B. Mohammadi. “Prediction of through the width delamination growth in post-buckled laminates under fatigue loading using de-cohesive law”. In: *Structural Engineering and Mechanics* 48.1 (2013), pp. 41–56, 2013.

[78] *HP-Textiles – 158 g/m^2 Unidirektional Carbongelege | HP-U158/122C*. Accessed: 22nd Mar 2020, `shop.hp-textiles.com/shop/de/158g-m-Unidirektional-Carbongelege-HP-U158C.html` .

[79] N. Hu et al. “Contributions of different aeroacoustic sources to aircraft cabin noise”. In: *Proceedings of the 19th AIAA/CEAS Aeroacoustics Conference*. American Institute of Aeronautics and Astronautics (AIAA). Berlin, Germany, 2013.

[80] IATA. *IATA Forecast Predicts 8.2 billion Air Travelers in 2037*. Press Release No: 62 (2018), Accessed: 13th Jan 2020, `iata.org/en/pressroom/pr/2018-10-24-02`.

[81] K. U. Ingard. “Locally and nonlocally reacting flexible porous layers; a comparison of acoustical properties”. In: *Journal of Engineering for Industry* 103.3 (1981), pp. 302–313, 1981.

[82] L. Jenkinson, P. Simpkin and D. Rhodes. *Civil jet aircraft design*. American Institute of Aeronautics and Astronautics, Inc., 1999.

[83] D. L. Johnson, J. Koplik and R. Dashen. “Theory of dynamic permeability and tortuosity in fluid-saturated porous media”. In: *Journal of fluid mechanics* 176 (1987), pp. 379–402, 1987.

[84] D. L. Johnson, J. Koplik and L. M. Schwartz. “New pore-size parameter characterizing transport in porous media”. In: *Physical review letters* 57.20 (1986), pp. 2564, 1986.

[85] M. Jung and U. Langer. *Methode der finiten Elemente für Ingenieure*. Springer, 2013.

[86] M. Kaltenbacher. *Numerical simulation of mechatronic sensors and actuators*. Vol. 3. Springer, 2015.

[87] M. Kaltenbacher. *Computational Acoustics*. Springer, 2018.

[88] M. Karimi et al. “A hybrid numerical approach to predict the vibrational responses of panels excited by a turbulent boundary layer”. In: *Journal of Fluids and Structures* 92 (2020), pp. 102814, 2020.

[89] J. Kim, G. F. Dargush and Y.-K. Ju. “Extended framework of Hamilton’s principle for continuum dynamics”. In: *International Journal of Solids and Structures* 50.20-21 (2013), pp. 3418–3429, 2013.

[90] A. Klabes. “Aircraft fuselage vibration excitation by turbulent boundary layer flow in cruise”. Deutsches Institut für Luft-und Raumfahrt, TU Braunschweig. PhD thesis. 2017.

[91] A. Klabes, M. Herr and S. Callsen. “Fuselage excitation during cruise flight conditions: a new CFD based pressure point spectra model”. In: *INTER-NOISE and NOISE-CON Congress and Conference Proceedings*. Institute of Noise Control Engineering. 2016.

[92] K. Knothe and H. Wessels. *Finite Elemente – Eine Einführung für Ingenieure*. Springer, 2017.

[93] C. Koehne, D. Sachau and M. Schaedlich. “Vibro-acoustic research on a full-scale aircraft structure”. In: *Topics in Modal Analysis, Volume 7*. Springer, 2014, pp. 67–76, 2014.

[94] F. G. Kollmann. *Maschinenakustik: Grundlagen, Meßtechnik, Berechnung, Beeinflussung*. Springer, 2011.

[95] L. Krakers et al. "A Design & Engineering Engine to Investigate Acoustics in Preliminary Fuselage Design". In: *Proceedings of the 9th AIAA/CEAS Aeroacoustics Conference and Exhibit*. American Institute of Aeronautics and Astronautics (AIAA). Hilton Head, SC, United States, 2003.

[96] P. Lamary. "Aircraft friendly cabin environment-Enhancement acoustic and vibro- acoustic numerical methods for trimmed fuselage models". In: *Proceedings of the XI International Symposium on Dynamic Problems of Mechanics (DINAME)*. Brazilian Society for Mechanical Sciences and Engineering (ABCM). Ouro Preto, Brazil, 2005.

[97] P. Lamary, O. Tanneau and Y. Chevalier. "Modelling poroelastic multilayered material for aircraft insulation". In: *First European Forum-Materials and Products for Noise and Vibration Control In Machinery and Transportation*. Technical Centre for Mechanical Industry (CETIM). Senlis, France, 2001.

[98] S. C. Langer. "Schalltransmission durch Isolierverglasung". Braunschweiger Schriften zur Mechanik Nr. 41-2001, Mechanik-Zentrum, TU Braunschweig. PhD thesis. 2001.

[99] F. Langfeldt and W. Gleine. "Improved Sound Transmission Loss of Glass Wool With Acoustic Metamaterials". In: *Proceedings of the 26th International Congress on Sound and Vibration (ICSV26)*. International Institute of Acoustics and Vibration. Montreal, Canada, 2019.

[100] John Lataire and Tianshi Chen. "Transfer function and transient estimation by Gaussian process regression in the frequency domain". In: *Automatica* 72 (2016), pp. 217–229.

[101] R. Lerch, G. Sessler and D. Wolf. *Technische Akustik - Grundlagen und Anwendungen*. Springer, 2009.

[102] T. Lu and F. Xin. *Vibro-acoustics of lightweight sandwich structures*. Springer, 2014.

[103] S. Malek and L. Gibson. "Effective elastic properties of periodic hexagonal honeycombs". In: *Mechanics of Materials* 91 (2015), pp. 226–240, 2015.

[104] V. Mallardo et al. "An accelerated BEM for simulation of noise control in the aircraft cabin". In: *Aerospace Science and Technology* 23.1 (2012), pp. 418–428, 2012.

[105] M. H. Marcus. *An Improved Method for Solving Systems of Linear Equations in Frequency Response Problems*. Tech. rep. Naval Research Lab Washington DC Physical Acoustics Branch, 2004.

[106] T. Marker. *Development of Improved Flammability Criteria for Aircraft Thermal Acoustic Insulation*. Tech. rep. Federal Aviation Administration Technical Center Atlantic City NJ, 2000.

[107] T. Mary. "Block Low-Rank multifrontal solvers: complexity, performance, and scalability". Performance [cs.PF]. Université Paul Sabatier – Toulouse III. English. NNT: 2017TOU30305 . tel-01929478. PhD thesis. 2017.

[108] V. Mellert et al. "Impact of sound and vibration on health, travel comfort and performance of flight attendants and pilots". In: *Aerospace Science and Technology* 12.1 (2008), pp. 18–25, 2008.

[109] A. Mertins. *Signaltheorie*. Springer, 2013.

[110] G. Meurant. *Computer solution of large linear systems*. Vol. 28. Elsevier, 1999.

[111] R. D. Mindlin. "Influence of rotatory inertia and shear on flexural motions of isotropic, elastic plates". In: *ASME Journal of Applied Mechanics* 18 (1951), pp. 31–38, 1951.

[112] C. Moeser, A. Peiffer and S. Tewes. "FEM Schalldurchgangsrechnung einer Doppelwandstruktur". In: *Fortschritte der Akustik – DAGA 2008*. Deutsche Gesellschaft für Akustik e.V. (DEGA). Dresden, Germany, 2008.

[113] M. Möser. *Technische Akustik*. Springer, 2012.

[114] U. C. Mueller and M. J. Weber. "Cabin Noise Prediction for Propeller Aircraft in an Early Design Phase using Parametric FEM Geometry Models and Simplified Propeller Loads". In: *INTER-NOISE and NOISE-CON Congress and Conference Proceedings*. Institute of Noise Control Engineering. Hong Kong, China, 2017.

[115] G. Müller and M. Möser. *Handbook of Engineering Acoustics*. Springer, 2013.

[116] *MUMPS: MUltifrontal Massively Parallel sparse direct Solver*. Accessed: 6th Dec 2020, `http://mumps.enseeiht.fr`.

[117] N. L. Nagda et al. "Aircraft cabin air quality: a critical review of past monitoring studies". In: *Air Quality and Comfort in Airliner Cabins*. ASTM International, 2000.

[118] A. C. Nilsson and B. L. Liu. *Vibro-Acoustics, Volume I*. Springer, 2016.

[119] A. C. Nilsson and B. L. Liu. *Vibro-Acoustics, Volume III*. Springer, 2016.

[120] M. C.-Y. Niu. *Airframe structural design: practical design information and data on aircraft structures*. Hong Kong Conmilit Press, 1988.

[121] M. C.-Y. Niu. *Composite airframe structures: practical design information and data*. Hong Kong Conmilit Press, 1992.

[122] C. Olivier. *Airbus A350 XWBFamily & New Technologies*. Presentation at Hochschule für Angewandte Wissenschaften Hamburg, 2007, accessed: 22nd Oct 2019, `fzt.haw-hamburg.de/pers/Scholz/dglr/hh/text_2007_09_20_A350XWB.pdf`.

[123] M. Omais, J. Biedermann and M. Wandel. "From engine integration to cabin noise: drivers to accurate interior noise evaluations". In: *INTER-NOISE and NOISE-CON Congress and Conference Proceedings*. Institute of Noise Control Engineering. Hamburg, Germany, 2016.

[124] U. Orrenius, V. Cotoni and A. Wareing. "Analysis of sound transmission through aircraft fuselages excited by turbulent boundary layer or diffuse acoustic pressure fields". In: *INTER-NOISE and NOISE-CON Congress and Conference Proceedings*. Institute of Noise Control Engineering. Ottawa, Canada, 2009.

[125] U. Orrenius et al. "Wave modelling in predictive vibro-acoustics: Applications to rail vehicles and aircraft". In: *Wave Motion* 51.4 (2014), pp. 635–649, 2014.

[126] H. K. Ozcan and S. Nemlioglu. "In-cabin noise levels during commercial aircraft flights". In: *Canadian Acoustics* 34.4 (2006), pp. 31–35, 2006.

[127] R. Panneton. "Comments on the limp frame equivalent fluid model for porous media". In: *Journal of the Acoustical Society of America* 122.6 (2007), EL217–EL222, 2007.

[128] R. Panneton et al. *Validation of the inverse method of acoustic material characterization*. Tech. rep. SAE Technical Paper, 2003.

[129] *ParMETIS – Parallel Graph Partitioning and Fill-reducing Matrix Ordering*. Accessed: 2nd Aug 2021, `http://glaros.dtc.umn.edu/gkhome/metis/parmetis/overview`.

[130] A. Peiffer. "Full frequency vibro-acoustic simulation in the aeronautics industry". In: *Proceedings (Keynote) of ISMA 2016 including USD 2016 International Conference on Uncertainty in Structural Dynamics*. Leuven, Belgium, 2016.

[131] A. Peiffer et al. “Zeitoptimierte Berechnung des Schalldurchgangs durch Wandstukturern mittels FEM”. In: *Fortschritte der Akustik – DAGA 2005*. Deutsche Gesellschaft für Akustik e.V. (DEGA). München, Germany, 2005.

[132] A. Peiffer et al. “FE-, SEA- und hybride Simulation des Innenlärms von Propellerflugzeugen”. In: *Fortschritte der Akustik – DAGA 2011*. Deutsche Gesellschaft für Akustik e.V. (DEGA). Düsseldorf, Germany, 2011.

[133] S. Pennig, J. Quehl and V. Rolny. “Effects of aircraft cabin noise on passenger comfort”. In: *Ergonomics* 55.10 (2012), pp. 1252–1265, 2012.

[134] J. Poblet-Puig and A. Rodríguez-Ferran. “The block gauss–seidel method in sound transmission problems”. In: *Journal of Computational Acoustics* 18.01 (2010), pp. 13–30, 2010.

[135] R. Radespiel and W. Heinze. “SFB 880: fundamentals of high lift for future commercial aircraft”. In: *CEAS Aeronautical Journal* 5.3 (2014), pp. 239–251, 2014.

[136] M. Rescheleit et al. “On the simulation of acoustical properties of an aircraft cabin”. In: *Aircraft System Technologies, AST 2011*. Hamburg, 2011.

[137] H. J. Rice and P. Göransson. “A dynamical model of light fibrous materials”. In: *International journal of mechanical sciences* 41.4-5 (1999), pp. 561–579, 1999.

[138] J. Rieke. “Bewertung von CFK-Strukturen in einem multidisziplinären Entwurfsansatz für Verkehrsflugzeuge”. German institute of aircraft design and lightweight structures, TU Braunschweig, CFF-research report 2013-02, Cuvillier Verlag, Göttingen. PhD thesis. 2013.

[139] J. Rocha, A. Suleman and F. Lau. “Prediction of turbulent boundary layer induced noise in the cabin of a BWB aircraft”. In: *Shock and Vibration* 19.4 (2012), pp. 693–705, 2012.

[140] K. Rohwer. “Improved transverse shear stiffness for layered finite elements”. In: *For-schungsbericht – Deutsche Forschungs- und Versuchsanstalt fur Luft- und Raumfahrt* (1988).

[141] U. Römer et al. “An adaptive sparse grid rational Arnoldi method for uncertainty quantification of dynamical systems in the frequency domain”. In: *International Journal for Numerical Methods in Engineering* 122.20 (2021), pp. 5487–5511, 2021.

[142] P. Rong and O. von Estorff. “A new preconditioner for the iterative solution of the systems describing the vibro-acoustics of multi-layered panels”. In: *Fortschritte der Akustik – DAGA 2012*. Deutsche Gesellschaft für Akustik e.V. (DEGA). Darmstadt, Germany, 2012.

[143] N. B. Roozen. “Quiet by design: Numerical acousto-elastic analysis of aircraft structures”. Technische Universiteit Eindhoven. PhD thesis. 1992.

[144] J. C. Rotta. *Über die Theorie der turbulenten Grenzschichten*. Max-Planck-Inst. f. Strömungsforschung, 1950.

[145] R. Roy et al. “Characterization of Nomex honeycomb core constituent material mechanical properties”. In: *Composite Structures* 117 (2014), pp. 255–266, 2014.

[146] Y. Saad. *Iterative methods for sparse linear systems*. SIAM, 2003.

[147] Y. Saad and M. H. Schultz. “GMRES: A generalized minimal residual algorithm for solving nonsymmetric linear systems”. In: *SIAM Journal on scientific and statistical computing* 7.3 (1986), pp. 856–869, 1986.

[148] H. Scheel. “Next generation aircraft – A challenge for Interior Acoustics Developments”. In: *INTER-NOISE and NOISE-CON Congress and Conference Proceedings*. Institute of Noise Control Engineering. Hamburg, Germany, 2016.

[149] J. Schultz. *Lösungsstrategien für lineare Gleichungssysteme vibroakustischer Problemstellungen*. Studienarbeit, Institute for Engineering Design, TU Braunschweig. 2019.

[150] H. Schürmann. *Konstruieren mit Faser-Kunststoff-Verbunden*. Springer, 2004.

[151] G. Serhat. “Comparison of vibro-acoustic performance metrics in the design and optimization of stiffened composite fuselages”. In: *INTER-NOISE and NOISE-CON Cong-ress and Conference Proceedings*. Institute of Noise Control Engineering. Hamburg, Germany, 2016.

[152] V. Tarnow. “Measured anisotropic air flow resistivity and sound attenuation of glass wool”. In: *Journal of the Acoustical Society of America* 111.6 (2002), pp. 2735–2739, 2002.

[153] V. Tarnow. “Dynamic measurements of the elastic constants of glass wool”. In: *Journal of the Acoustical Society of America* 118.6 (2005), pp. 3672–3678, 2005.

[154] *Technisches Datenblatt – Epoxidharz-Serie HP-E3000RI*. Accessed: 22nd Mar 2020, `hp-textiles.com/TDS/DE/Epoxi/Infusionsharz/GTDS_RI.pdf`.

[155] C. Thomas and N. Atalla. *Optimization of Noise Control Treatments for Aircraft's Sidewalls*. Tech. rep. SAE Technical Paper, 2016.

[156] C. Thomas and H. Scheel. "Kabinenakustik in der Luftfahrtforschung". In: *Deutscher Luft-und Raumfahrtkongress*. Vol. 4. 6. 2018.

[157] T. C. T. Ting. "Positive definiteness of anisotropic elastic constants". In: *Mathematics and Mechanics of Solids* 1.3 (1996), pp. 301–314, 1996.

[158] R. Vaicaitis, F. W. Grosveld and J. S. Mixson. "Noise transmission through aircraft panels". In: *Journal of Aircraft* 22.4 (1985), pp. 303–310, 1985.

[159] R. J. H. Wanhill. "Carbon fibre polymer matrix structural composites". In: *Aerospace materials and material technologies*. Springer, 2017, pp. 309–341, 2017.

[160] C. Werner-Westphal, W. Heinze and P. Horst. "Multidisciplinary integrated preliminary design applied to unconventional aircraft configurations". In: *Journal of Aircraft* 45.2 (2008), pp. 581–590, 2008.

[161] J. F. Wilby. "Aircraft interior noise". In: *Journal of Sound and Vibration* 190.3 (1996), pp. 545–564, 1996.

[162] R. Winter, J. Biedermann and M. Norambuena. "High-Resolution Vibration Measurement And Analysis Of The Flight-LAB Aircraft Fuselage Demonstrator". In: *INTER-NOISE and NOISE-CON Congress and Conference Proceedings*. Institute of Noise Control Engineering. Chicago, IL, United States, 2018.

[163] R. Winter et al. "Experimental characterization of vibro-acoustic properties of an aircraft fuselage". In: *Proceedings of ISMA 2014 International Conference on Noise and Vibration Engineering, USD 2014 International Conference on Uncertainty in Structural Dynamics*. Vol. 15. 2014.

[164] P. Zeller. *Handbuch Fahrzeugakustik – Grundlagen, Auslegung, Berechnung, Versuch*. Vol. 3. Springer, 2018.

[165] Y. Zhou et al. "Effect of phenolic resin thickness on frequency-dependent dynamic mechanical properties of Nomex honeycomb cores". In: *Composites Part B: Engineering* 154 (2018), pp. 285–291, 2018.

[166] Y. Zhu and A. H. Sameh. "How to generate effective block jacobi preconditioners for solving large sparse linear systems". In: *Advances in Computational Fluid-Structure Interaction and Flow Simulation*. Springer, 2016, pp. 231–244, 2016.

[167] F. Ziegler. *Mechanics of Solids and Fluids*. Springer, 1995.

[168] O. C. Zienkiewicz. "Achievements and some unsolved problems of the finite element method". In: *International Journal for Numerical Methods in Engineering* 47.1-3 (2000), pp. 9–28, 2000.

[169] O. C. Zienkiewicz, R. L. Taylor and J. Z. Zhu. *The finite element method: its basis and fundamentals*. Elsevier, 2005.

[170] *ZOLTEK PX35*. Accessed: 22nd Mar 2020, `zoltek.com/products/px35/`.

List of figures

List of tables

A Appendix

Experiments on linearity of CFRP plates

In order to proof linearity for the measured CFRP plates, the excitation amplitude is doubled for plate 6. In Fig. A.1, the mean squared admittance for plate 6 is not changing significantly due to this change in amplitude. As the admittance is not varying, linearity can be assumed for this measurement. Additionally, linearity is assumed for all six plates as plate 6 is the thinnest plate for which non-linearities are most likely expected.

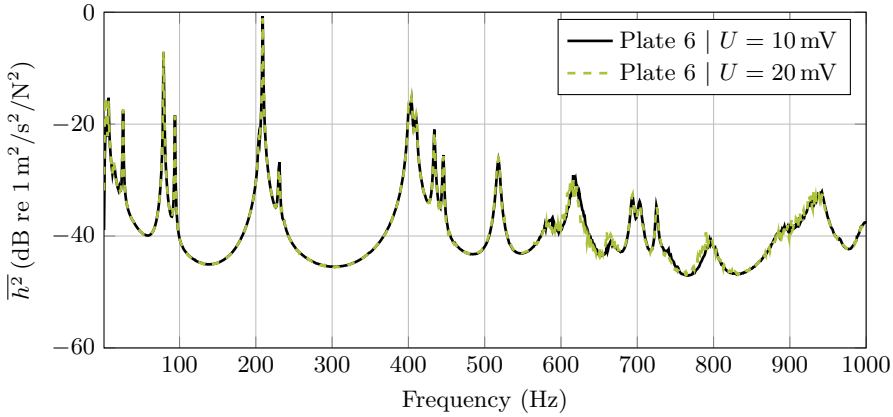

Figure A.1: Experimental results for the mean squared admittance $\overline{h^2}(f)$ of curved CFRP plate 6 with two different amplitudes (maximum input voltage U at electrodynamic shaker)

Experiments on measurement repeatability of CFRP plates

The measurement of CFRP plate 1 is conducted two times while the measurement setup has been redone. In Fig. A.2, the dynamic response of the same plate is shown for the two measurements. The two curves show clearly a high accordance of the repeated measurement. This fact suggests a low uncertainty of the measurement setup and allow differences between two nominal identical plates to be ascribed to

manufacturing tolerances.

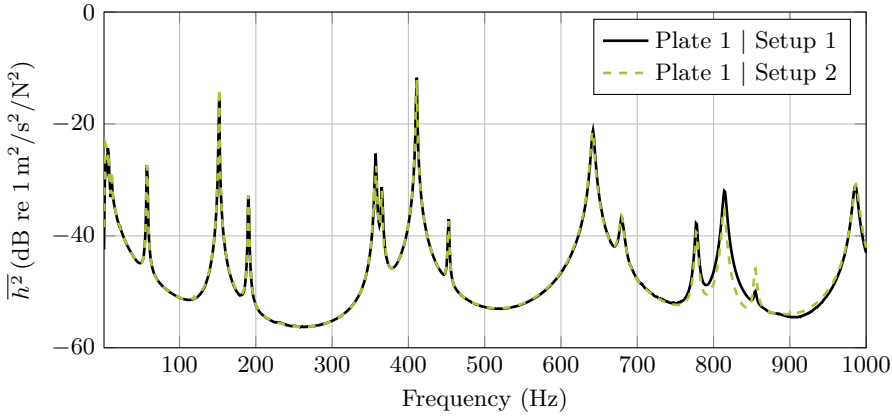

Figure A.2: Experimental results for the mean squared admittance $\overline{h^2}(f)$ of curved CFRP plate 1 for two repeated identical measurement setups

Experiments on linearity of the honeycomb sandwich plate

In order to proof linearity for the measured honeycomb sandwich plate, the excitation amplitude is halved for the measurement of surface 1. In Fig. A.3, the mean squared admittance is not changing significantly due to this change in amplitude.

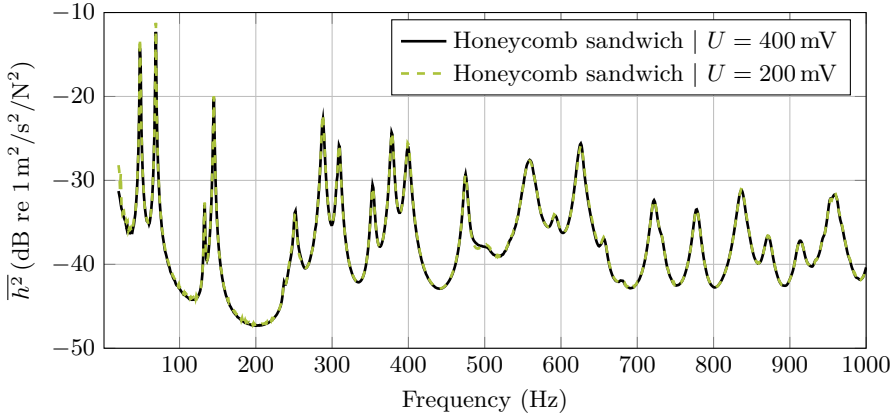

Figure A.3: Experimental results for the mean squared admittance $\overline{h^2}(f)$ of the honeycomb sandwich plate (surface 1) with two different amplitudes (maximum input voltage U at electrodynamic shaker)

Experiments on measurement repeatability of the honeycomb sandwich plate

The measurement of the honeycomb sandwich plate is conducted two times while the measurement setup has been redone. In Fig. A.4, the dynamic response of the same plate is shown for the two measurements. The two curves show clearly a high accordance of the repeated measurement indicating a highly deterministic measurement setup.

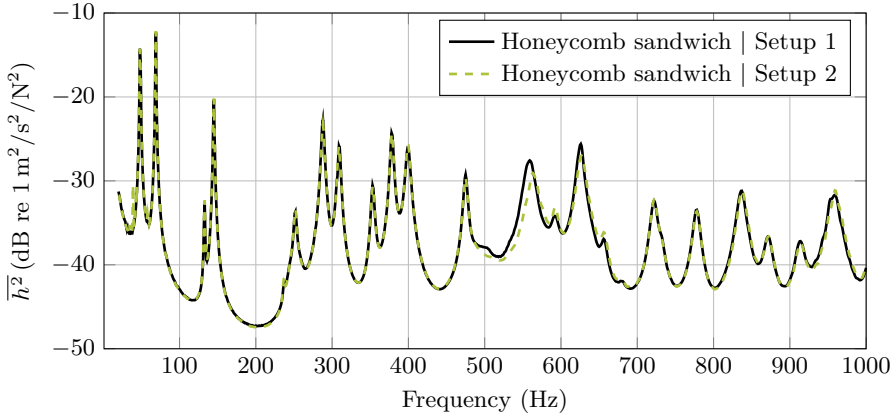

Figure A.4: Experimental results for mean squared admittance $\overline{h^2}(f)$ of the honeycomb sandwich plate (surface 1) for two repeated identical measurement setups

Initial numerical results of the honeycomb sandwich plate in comparison to experiments

In Fig. A.5, the initial dynamic response (no parameter fitting) of the 6 mm honeycomb plate is depicted in comparison to the experiment.

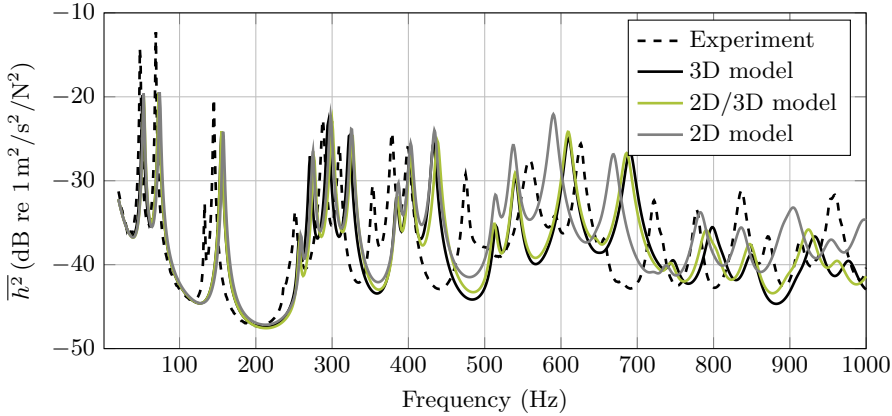

Figure A.5: Numerical results for the mean squared admittance $\overline{h^2}(f)$ of the 6 mm honeycomb plate – Comparison of three modelling approaches with initial material parameters to experimental results of side 1

Equivalent fluid parameters for aircraft seat cushions

Equivalent fluid domain parameters are shown in Fig. A.6. Experimentally determined flow resistivities σ serve as input basis for the Delany-Bazley model.

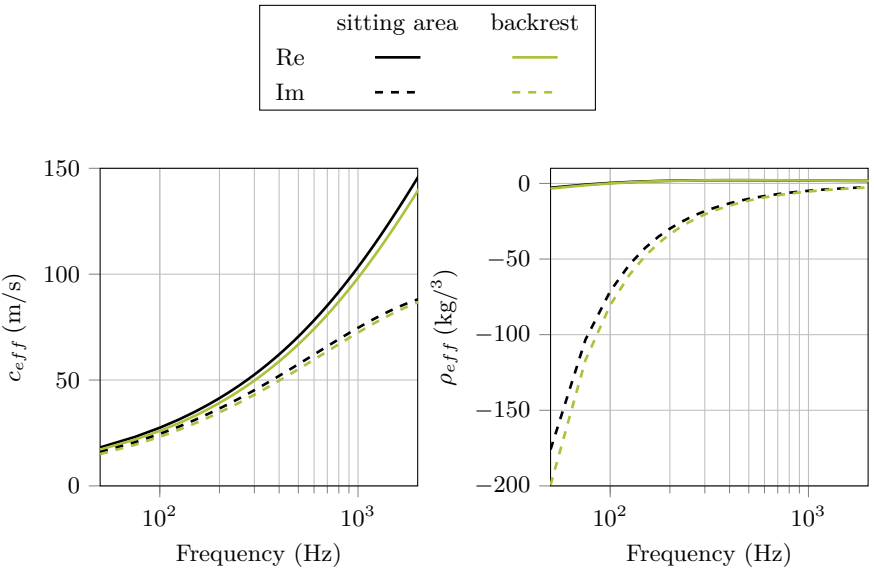

Figure A.6: Complex input parameters of an equivalent fluid model for aircraft seat cushions based on the Delany-Bazley model

Preliminary investigations of the BLR parameter in MUMPS

In Fig, A.7 and A.8, the BLR parameter ϵ is studied for mesh "5" and mesh "6", respectively. Based on the measured solution times and memory requirements, effective parameters are identified.

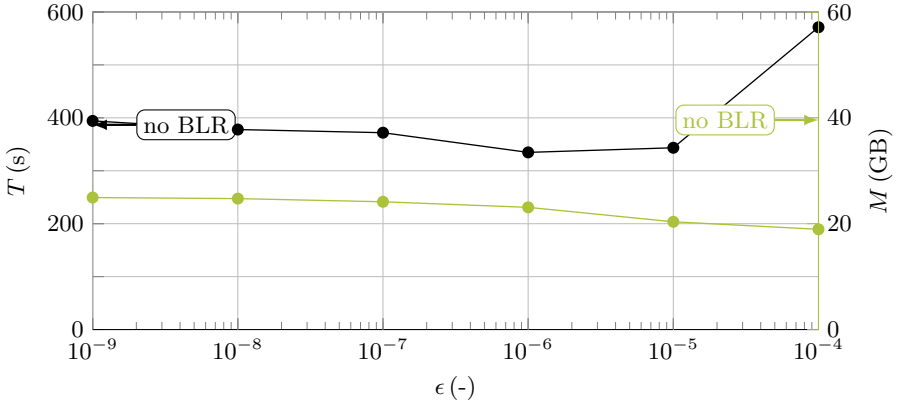

Figure A.7: Computational costs for the solution of the core model (mesh "5") with GMRES and block jacobian preconditioner (LU+LU with activated block low rank (BLR) feature) under variation of the dropping parameter ϵ

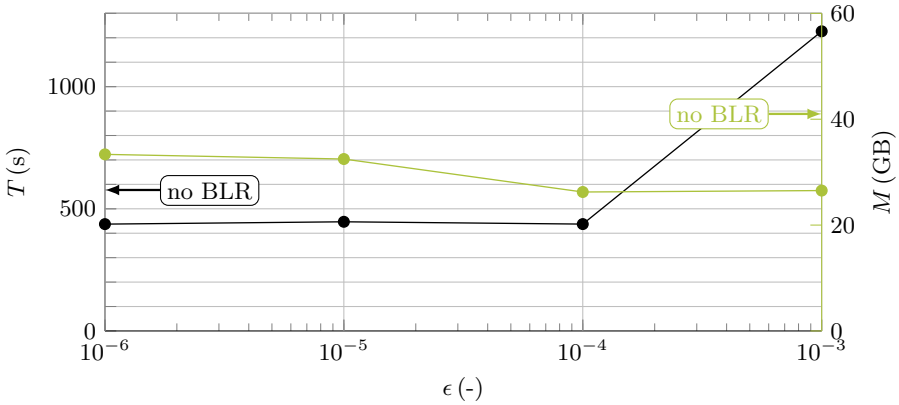

Figure A.8: Computational costs for the solution of the core model (mesh "6") with GMRES and LU preconditioner with activated block low rank (BLR) feature for the cabin only under variation of the dropping parameter ϵ